Universität Zürich

PHYSIK - INSTITUT

www.physik.unizh.ch

Wissenschaftlicher Jahresbericht

April 2003 - März 2004

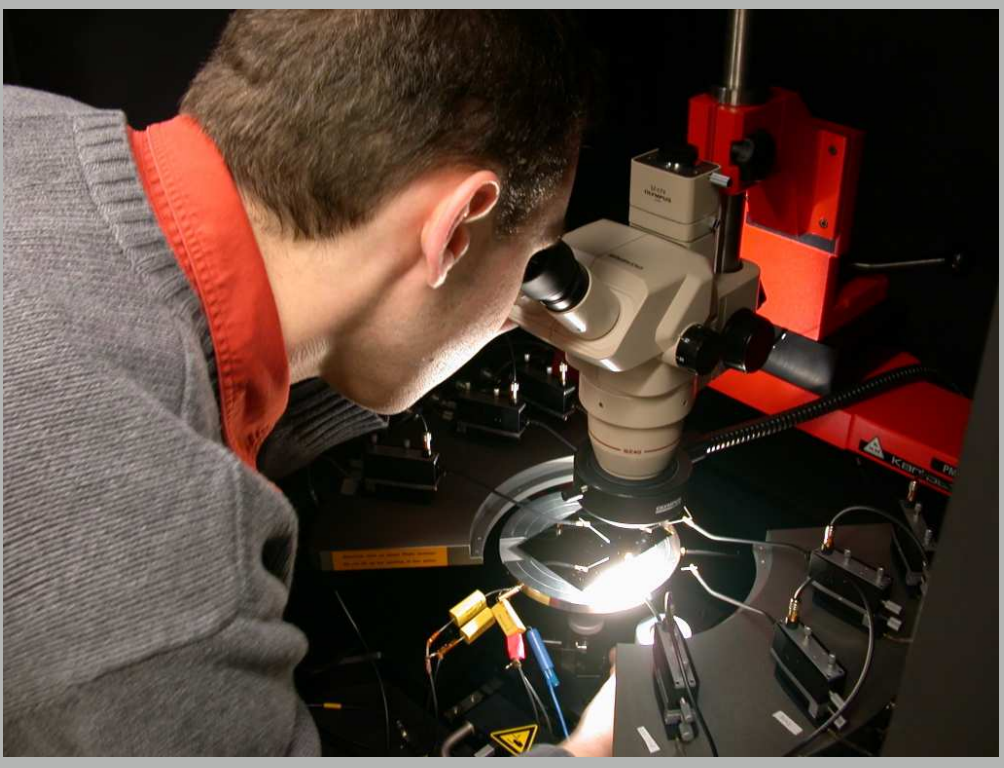

Winterthurerstrasse 190, CH-8057 Zürich/Schweiz

Universität Zürich

PHYSIK - INSTITUT

Wissenschaftlicher Jahresbericht

April 2003 - März 2004

Winterthurerstrasse 190, CH-8057 Zürich/Schweiz www.physik.unizh.ch

The picture on the cover shows Matt Siegler, summer student from Cornell, testing silicon sensors at the manual probe-station of the LHCb group (see Sec. 4).

Sekretariat	01 635 5721	secret@physik.unizh.ch
Prof. C. Amsler	01 635 5784 022 767 2914	amsler@cern.ch
Prof. H.-W. Fink	01 635 5801	hwfink@physik.unizh.ch
Prof. H. Keller	01 635 5748	keller@physik.unizh.ch
Prof. P.F. Meier	01 635 4016	pfmeier@physik.unizh.ch
Prof. J. Osterwalder	01 635 5827	osterwal@physik.unizh.ch
Prof. A. Schilling	01 635 5791	schilling@physik.unizh.ch
Prof. U.D. Straumann	01 635 5768	strauman@physik.unizh.ch
Prof. P. Truöl	01 635 5777	truoel@physik.unizh.ch

The annual reports are available on the internet: http://www.physik.unizh.ch/reports.html.

Begleitwort

Mit seinen sieben Professuren deckt das Physik-Institut ein breites, national und international vernetztes Spektrum experimenteller Forschung ab, das von den Eigenschaften biologischer Makromoleküle bis zu jenen der elementaren Bestandteile des Universums in seiner Frühphase reicht. In den beiden etwa gleich starken Hauptbereichen, Physik der kondensierten Materie und Physik fundamentaler Systeme, finden sich Gruppen in der Bio-, der Oberflächen-, der Festkörper- und der Elementarteilchenphysik. Die mit dem Rücktritt von Prof. Roland Engfer im Februar 2001 freigewordene Professur in Kern- und Teilchenphysik ist seit dem 1.4.2003 durch Prof. Andreas Schilling im Bereich Physik der kondensierten Materie besetzt. Die Forschungsgruppen des Physik-Instituts werden durch insgesamt fünfzehn Nationalprojekte unterstützt. Unter anderem ist das Physik-Institut an den Nationalen Forschungskompetenzzentren (NCCR) MaNEP (Materials with novel electronic properties, H. Keller, A. Schilling) und Nanoscale Science (Impact on life sciences, sustainibility, information and communication technology, H.W. Fink) beteiligt und gehört zu den Mitgründern des Swiss Institute of Particle Physics (CHIPP) (C. Amsler, U. Straumann). Vom 1.9.2002 bis 30.6.2003 war Prof. Zhi-Xun Shen (Stanford University, U.S.A.) am Physik-Institut als Gastprofessor tätig. Zwischen ihm und den Forschungsgruppen der Physik der kondensierten Materie hat in dieser Zeit ein fruchtbarer wissenschaftlicher Austausch statt gefunden.

Die Aufbau- und Installationsphase der Biophysik-Gruppe von H.-W. Fink ist abgeschlossen und die Forschung der Gruppe hat ihre Schwerpunkte nun auf vier Projekte konzentriert. Gemeinsames Ziel aller Projekte ist es, die Eigenschaften einzelner Objekte im Nanometerbereich zu erforschen und sie sich nutzbar zu machen. Ein besonderes Interesse gilt dabei den Eigenschaften und Funktionen einzelner Bio-Moleküle. Die experimentellen Methoden reichen von der Fluoreszenz-Mikroskopie zur direkten Beobachtung einzelner Moleküle in wässrigen Lösungen, über die Feldionen-Mikroskopie mit atomarer Auflösung bis zur Holografie mit kohärenten Elektronenwellen. Zur Strukturierung von Oberflächen und dünnen Filmen im Nanometerbereich steht seit Sommer 2003 ein fokussierter Gallium Ionenstrahl zu Verfügung.

Nanostrukturen in Form von ultradünnen Schichten, Quantendrähten oder Quantenpunkten werden in der Gruppe von J. Osterwalder mit Methoden der Oberflächenphysik kontrolliert hergestellt und charakterisiert. Die in solchen Strukturen dominierenden Grenzschichten werden mit atomarer Auflösung auf ihre Güte getestet. Wo nötig werden dazu bestehende Messmethoden verbessert oder es werden neue entwickelt. Das Ziel ist es, durch Strukturierung gezielt elektronische, magnetische und auch katalytische Eigenschaften von Oberflächen zu beeinflussen.

Die Gruppe von H. Keller untersucht fundamentale Eigenschaften von unkonventionellen Supraleitern und verwandten magnetischen Systemen mit dem Ziel den noch immer unverstandenen Mechanismus der Hochtemperatur-Supraleitung zu klären. Mit Hilfe von Untersuchungen des sogenannten Isotopen-Effektes ist es der Forschungsgruppe gelungen, zu zeigen, dass neben der Elektron-Elektron-Korrelation auch die Elektron-Phonon-Wechselwirkung wichtig für das Verständnis der Hochtemperatur-Supraleitung ist. Diese wichtige Erkenntnis wurde bis anhin von den meisten Wissenschaftern in der Modellierung dieser neuartigen Materialien nicht in Betracht gezogen.

Seit April 2003 ist die neue Forschungsgruppe von A. Schilling am Physik-Institut tätig. In dieser Zeit wurden neue Apparaturen evaluiert und beschafft und zwei Doktoranden in die Gruppe aufgenommen. Die neue Forschungsgruppe wird sich der Untersuchung von elektronischen Phasenübergängen in Metallen und Supraleitern und des thermischen Transportes in niedrigdimensionalen Systemen, sowie der Synthese und Charakterisierung von neuen Materialien widmen.

Die Gruppe Computerassistierte Physik von P.F. Meier untersucht mit der Methode der Dichtefunk-

tionale die elektronische Struktur von Materialien, die Hochtemperatur-Supraleitung aufzeigen. Die berechneten Grössen wie z.B. elektrische Feldgradienten, Hyperfeinfelder und chemische Verschiebungen ermöglichen die Interpretation der mit Kernresonanzspektroskopie gemessenen Daten.

Die Teilchenphysikgruppen sind in Beschleunigerexperimenten am CERN in Genf, am DESY in Hamburg, und am BNL auf Long Island engagiert, und zwar sowohl in laufenden Experimenten, als auch in der Vorbereitung neuer Projekte. Die Gruppe von U. Straumann ist verantwortlich für den inneren Spurdetektor des LHCb-Detektors (CERN LHC), bei dem grossflächige Silizium Sensoren zum Einsatz kommen werden. Silizium-Pixel Detektoren plant die Gruppe C. Amsler mit ihren Kollegen vom PSI im inneren Spurdetektektor des CMS-Detektors (CERN LHC) einzusetzen. Die Mitarbeiter von P. Truöl planen das Vetosystem für den KOPIO-Detektor (AGS Brookhaven). In diesen drei Experimenten steht die Erforschung der Ursachen der beobachteten Teilchen-Antiteilchen Asymmetrie im Vordergrund, sei es im *beauty* oder im *strange* Quark Sektor. Von den laufenden Experimenten gibt es Evidenz für ein neues Baryon (ein *Pentaquark* mit einem *anti-charm* Quark als Baustein) zu vermelden sowie die ersten Ergebnisse aus der Streuung polarisierter Elektronen am Proton bei höchsten Energien (H1-Experiment am DESY, Gruppen Straumann und Truöl). Die ATHENA Kollaboration hat die erfolgreiche Beobachtung von Antiwasserstoffatomen durch weitere experimentelle Fakten untermauert. Am PSI und am Brookhaven AGS sind die Grenzen für zwei Leptonzahlerhaltung verletzende Zerfälle weiter reduziert worden.

Alle Forschungsgruppen profitieren von der tatkräftigen Unterstützung der mechanischen und elektronischen Werkstätten, sowie des technischen Personals und des Sekretariats. Alle helfen mit einen reibungslosen Ablauf in Forschung und Lehre auf hohem Niveau zu garantieren.

Die beträchtlichen Lehraufgaben der Physik-Dozenten schliessen die fakultätsübergreifende physikalische Grundausbildung für viele Studienrichtungen und die zum Teil mit derjenigen anderer Schweizer Hochschulen verbundene Spezialausbildung der Physik-Studierenden ein. In Zusammenarbeit mit Studierenden, Assistierenden und Kollegen aus der Mathematik und theoretischen Physik hat U. Straumann das neue, dem dreistufigen Studienmodell (*Bologna*) angepasste Curriculum festgelegt. Die Ausbildungsinhalte und -methoden sind dabei angepasst worden mit dem Ziel, ein attraktives Studium mit intensiver persönlicher Betreuung der Studierenden anbieten zu können. Mit der neu etablierten Kursvorlesung "Physik auf der Nanometerskala" und einem begleitenden Praktikumsexperiment ist dieses junge Forschungsgebiet aus der Physik der kondensierten Materie nun auch in der Lehre vertreten.

Im September 2003 wurde das Physik-Institut von einem internationalen Team von renommierten Experten evaluiert. Es wurden die Leistungen in der Lehre und in der Forschung durch die typischen Indikatoren internationale Präsenz, Publikationen und eingeworbene Drittmittel beurteilt und als im internationalen Vergleich überdurchschnittlich gut bewertet.

Ende August 2003 ist Peter Truöl als Institutsdirektor zurück getreten, um sich seiner neuen Aufgabe als Dekan der Mathematisch-naturwissenschaftliche Fakultät voll zu widmen. Wir wünschen P. Truöl alles Gute für die erfolgreiche Ausübung dieser neuen Herausforderung und danken ihm für sein enormes Engagement für das Physik-Institut, das er kompetent und fair geleitet hat.

Zürich, im Mai 2003
Prof. Dr. Hugo Keller

Contents

1 Production and Spectroscopy of Antihydrogen

C. Amsler, A. Giacomin, A. Glauser, O. Iannarelli, I. Johnson, H. Pruys, C. Regenfus, and J. Rochet

in collaboration with:
CERN, University of Aarhus, Brescia, Genoa, Pavia, RIKEN, Rio de Janeiro, Swansea, Tokyo

(ATHENA Collaboration)

The first observation of cold antihydrogen ($\bar{H}$) was reported in 2002 by the ATHENA collaboration [1]. This breakthrough has stimulated renewed interest in the field of low energy antimatter, and comparisons of the properties of antimatter with those of matter. For future laser spectroscopy experiments the temperature and quantum state of the $\bar{H}$ atom have to be controlled. In 2003 we therefore concentrated on the mechanism underlying the formation of $\bar{H}$, when low energy antiprotons are merged with a dense and cold positron plasma. We have also begun installing a laser system that allows specific $\bar{H}$ states to be addressed.

Antihydrogen is formed in a nested Penning trap by mixing 10^4 antiprotons with a positron plasma containing up to 10^8 particles at a temperature of 15 K. Low energy antiprotons from the CERN antiproton decelerator (AD) are moderated and captured in a Penning trap and are cooled to the ambient temperature of 15 K (1.3 meV) by a preloaded electron plasma. The capture efficiency is about 0.4 %, mainly determined by energy straggling in the absorber. Antihydrogen begins to form after the overlap of the antiprotons with the positrons, with initial production rates in excess of 300 Hz. The characteristics of the positron plasma such as the number of particles, the dimensions (typically 2 cm in length, 2 mm in width) and the density (10^8-10^9 cm^{-3}) can be obtained with a non-destructive method based on a measurement of the low-order axial electrostatic modes of the plasma [2]. The raw experimental data are the resonant frequencies of the first two modes (dipole and quadrupole), and the equivalent inductance of the plasma. The plasma diagnostic, coupled with radio-frequency heating, can be used to monitor and control changes in the plasma temperature. Antihydrogen formation at 15 K will be called "cold mixing" while positron-antiproton mixing with a positron plasma heated to $\approx$3000 K will be referred to as "hot mixing".

The neutral $\bar{H}$'s are not confined by the electric and magnetic fields and therefore migrate to the trap walls where they annihilate. These events are monitored by the $\bar{H}$ detector built by the University of Zurich [3]. The detector consists of two layers of double-sided silicon strip detectors to register the charged annihilation pions and to reconstruct the annihilation vertex. Antihydrogen is detected by requiring the spatial and temporal coincidence of the vertex with two back-to-back 511 keV γ's produced by the annihilation of the positron. The γ's are detected by a high granularity electromagnetic detector comprising 192 CsI crystals with avalanche photodiode readout. A comprehensive description of the ATHENA apparatus can be found in ref. [4].

1.1 Antihydrogen production efficiency

The observation of cold $\bar{H}$ was based on a complete reconstruction of its annihilation, in which both antiprotons and positrons were detected via their annihilation products. We reported 131 ± 22 "golden events" [1]. However, the detection efficiency was low ($\simeq$ 0.2%), mainly due to the 20% detection efficiency for each of the two 511 keV photons, and stringent software cuts. In a further analysis [5] we show that the trigger rate during cold mixing is due to two sources: $\bar{H}$ production itself

comprises over 85% of the triggers at the beginning of mixing, and declines with a time constant of several seconds. Antiproton annihilation on positive ions or on rest gas (with a slowly decreasing rate) comprises the remainder of the triggers. During a complete cold mixing cycle $\bar{H}$ production accounts for (65 $\pm$ 5)% of the total integrated trigger rate. Thus in 2002 almost 500,000 $\bar{H}$ atoms were produced.

In Fig. 1.1 (left) we show the photon energy spectrum for cold mixing and for antiprotons only, normalized to the same number of annihilation vertices. No peak is observed at 511 keV for the annihilation of antiprotons only. This is good news since we feared earlier that the background from positron annihilation from high energy showers in the surrounding coils would be much more severe. The difference plot (Fig. 1.1, right) shows the 511 keV line from positron (antihydrogen) annihilation, together with a pure positron (no $\bar{p}$) annihilation spectrum. Peak position and resolution agree.

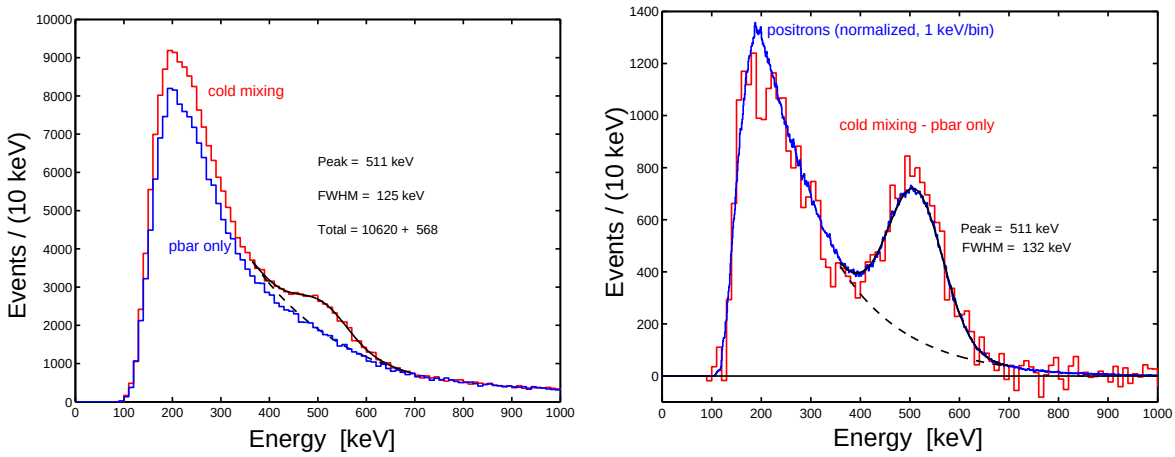

Figure 1.1: *Left: photon spectrum (sum of the 162 best crystals) for cold mixing and antiprotons only. Right: difference plot and annihilation spectrum from a pure positron plasma superimposed.*

1.1.1 Orthopositronium production

The detection of antihydrogen relies on the reconstruction of two back-to-back 511 keV photons. However, orthopositronium could be produced when positrons annihilate on the trap walls. The contribution from orthopositronium (which decays into 3γ) is unknown since it depends on a possible frozen gas layer on the trap electrode surface at cryogenic temperatures. A large production rate could lead to an underestimate of our antihydrogen formation rate.

A dedicated measurement with positrons only was therefore performed to determine the relative rates of the 2γ and 3γ decay modes of e^+e^- annihilations for antihydrogen atoms interacting with the electrode surfaces [5]. The electrostatic well holding the positrons was modified so that the radial outward transport of positrons onto the trap electrodes was strongly enhanced. The photons produced in positron annihilations at the surface of the electrodes were detected in the photon detector. The trigger condition required the detection of at least two photons with an energy greater than 150 keV each. For events containing two or three photons, the total energy E_{tot} and the total momentum P_{tot} were determined. Figure 1.2a shows the clear signal from 2γ events at $E_{tot} = 2m_ec^2$ and $P_{tot} < 200$ keV/c. The accumulation of events at $P_{tot} = E_{tot}$ stems from 2γ events for which one γ escaped detection, while the other underwent Compton scattering in the first crystal before being absorbed by the second adjacent crystal. This process also accounts for most detected 3γ events, stemming from

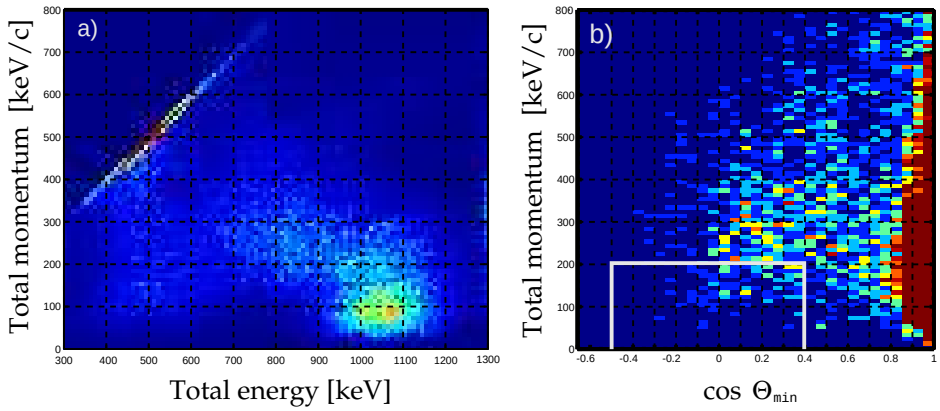

Figure 1.2: *a) P_{tot} vs. E_{tot} for 2γ-events; b) P_{tot} vs. cosine of the minimum 2γ-opening angle for 3γ events. The box shows the expected region for orthopositronium annihilation.*

2γ events, for which one γ is Compton scattered in a first and detected in a second crystal. Figure 1.2b shows a distribution for 3γ events satisfying the condition $|E_{tot} - 2m_e c^2| < 200$ keV. The total momentum of the 3γ is plotted versus the smallest of the three angles between any 2γ. Compton scattered photons accumulate at small angles. The box indicates the expected orthopositronium signal region. The detection probabilities for the two decay modes were evaluated by Monte Carlo simulation. From the observed number of events we could conclude that 2γ events account for at least 95% of all e^+e^- annihilations.

1.1.2 Optimization of $\bar{H}$ Rate

Combining hot and cold mixing data we have produced so far in excess of 2 million $\bar{H}$ atoms. However, this corresponds only to about 17% of the antiprotons injected into the trap. Possibilities to increase this formation rate were studied in 2003. For example, positron plasma compression can be achieved using the so-called "rotating wall" method in which the plasma is spun by applying a rotating electric field of several hundred kHz to a segmented trap electrode. The segmented Faraday cup detector in the positron accumulator was replaced with a phosphor screen and an auxiliary low-noise CCD camera. This enables a more accurate measurement of the position and size of the positron plasma (Fig. 1.3) before it is transferred to the ATHENA mixing trap located inside the main 3T magnet. We achieved plasma densities of up to 10^{10} e^+ cm^{-3}, which is the highest density positron plasma achieved worldwide to date.

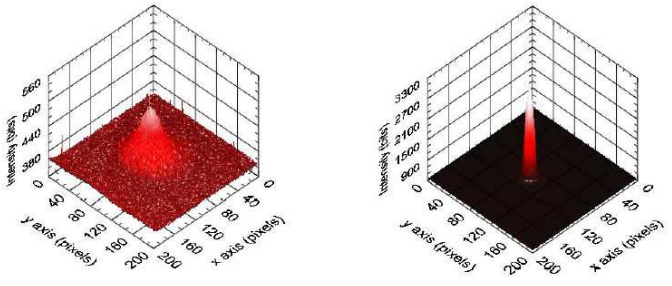

Figure 1.3: *CCD images of the position and size of the positron plasma dumped on the phosphor screen in the positron accumulator without (left) and with (right) rotating wall compression.*

Attempts were also made to increase the number of positrons available for $\bar{H}$ formation by stacking successive shots of positrons from the positron accumulator in the mixing trap. Figure 1.4 shows the number of stacked positrons in the main magnet versus the number of transfers. In this way we were

able to reach positron plasmas containing 1.2 $\times$ 10^9 positrons, again the highest number of stored positrons achieved anywhere to date.

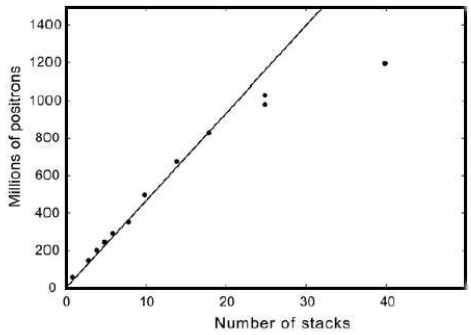

Figure 1.4: *Stacking successive shots of positrons from the positron accumulator. The line is a fit to the data up to 20 stacks and shows the linear behaviour. The fit shows that 50 million positrons per stack were captured.*

Modifications to the ATHENA trap are being carried out to implement the so-called "side band excitation" of the radial $\bar{p}$ motion to reduce the $\bar{p}$ plasma size and increase the overlap with the e^+ cloud: due to the degrader foil, captured antiprotons have large initial axial, magnetron, and modified-cyclotron amplitudes. While the axial and cyclotron motions are quickly damped through collisions with electrons, the large magnetron radii of the confined antiprotons are retained throughout the entire stacking, transfer, and measurement cycle. This leads to both reduced transfer efficiency and reduced $\bar{H}$ production due to poor radial overlap with the positron plasma. The two independent radial motions carried out by charged particles, the magnetron motion and the modified cyclotron motion, can be resonantly excited by azimuthal radio-frequency electric fields. Quadrupolar excitation at the sum frequency of the two modes (the true cyclotron frequency, 45 MHz in ATHENA) leads to a coupling and energy exchange between them. In the absence of a cooling mechanism, this can be used to transform low-frequency, low-energy magnetron motion into high-frequency, high-energy cyclotron motion. In the presence of a cooling mechanism the modified cyclotron motion would be quickly damped and the total radial motion centered. No significant improvement in the $\bar{H}$ production rate was achieved so far. This issue will be pursued in 2004.

1.2 Dynamics of antihydrogen formation

We have measured the antiproton energies during cooling and while $\bar{H}$ is efficiently formed [6]. Figure 1.5 shows the measured antiproton energy spectra at various times during the mixing cycle and Fig. 1.6 the W-shaped nested penning trap potential with the positrons in the middle. The antiprotons were ejected from the entrance well and their intensity measured as a function of electric potential. The antiproton potential energy is divided into three regions (labeled I-III in Fig. 1.5. Region I corresponds to $\bar{p}$ energies larger than positron energies, region II to $\bar{p}$'s within the positron space charge, whilst in the lowest energy region III antiprotons no longer have sufficient kinetic energy to penetrate the positron cloud.
The antiprotons ejected from the left well under cold mixing conditions begin to cool rapidly and after about

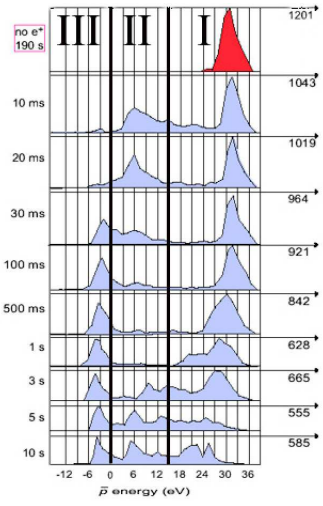

Figure 1.5: *Antiproton energy spectra for different interaction times, shown on the left. The maximum number of events per channel in each distribution is indicated on the right. The vertical thick lines divide the three energy regions (see text)*

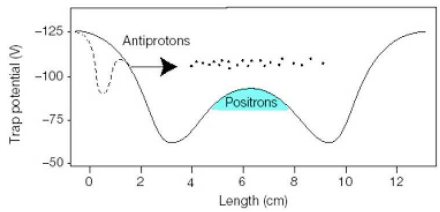

Figure 1.6: *Nested Penning trap potential*

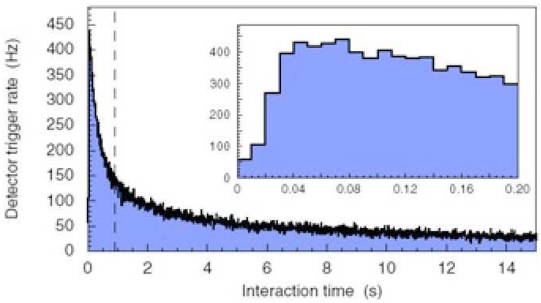

Figure 1.7: *Trigger rate vs. time for cold mixing. The inset shows an expansion of time between 0 and 0.2 seconds illustrating the onset of $\bar{H}$ production at about 20 ms.*

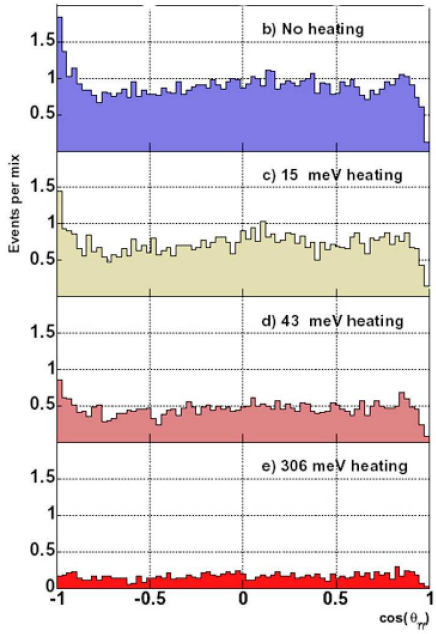

Figure 1.8: *Cosine of the opening angle distribution for different positron plasma temperatures $\sim$ 15 K, 190 K, 515 K and 3500 K (top to bottom, normalized to the mixing of 10'000 $\bar{p}$ with 7$\times$ 10^7 e^+). The peak at -1 is due to e^+e^- annihilation of $\bar{H}$ atoms hitting the electrodes.*

20 ms a significant fraction ($\simeq$ 40%) reach energies close to the bottom of the positron well. It is here that they are moving slowest as they traverse the positron cloud, and under these conditions one might expect $\bar{H}$ to form. This is borne out by the data shown in Fig. 1.7 where the $\bar{H}$ detector trigger rate shows a dramatic increase after 20 ms. On longer time scales, though $\bar{H}$ is still copiously formed, there are many antiprotons that retain kinetic energies close to those on injection. This indicates only weak coupling to the positron plasma, possibly due to poor radial overlap. There is also a slow transfer of antiprotons into region III, since antiprotons are present in both the left and right wells at longer times. The precise manner in which the antiprotons cool below the lowest positron energy is not yet clear, but may involve field ionisation of weakly bound $\bar{H}$. A measurement without positrons is included in Fig. 1.5 and, as expected, no antiproton cooling is apparent.

We have also measured the temperature dependence of $\bar{H}$ formation [7]. The two processes that lead to $\bar{H}$, radiative combination (in which a photon removes the binding energy) and three-body combination (in which a second positron removes the excess energy), lead to different n-state distributions. The former populates mainly the low n states and the latter mainly the high n states. The $\bar{H}$ production rate has also a different dependence on temperature, $T^{-1/2}$ for the former and $T^{-9/2}$ for the latter.

As explained above, the positron plasma temperature could be changed in a controlled way by radio-frequency excitation. The minimum measurable temperature increase was about 15 meV ($\sim$ 175 K). The electrode temperature of 15 K was the lower limit for the unheated plasma, and this was adopted as the unperturbed temperature. Mixing was carried out at different positron plasma temperatures including the cold mixing data (15 K) and three other high statistics hot mixing samples at 190 K, 515 K and 3500 K. The measurements were analyzed in a variety of ways by measuring (a) the 2γ opening angle excess enhancement, (b) the number of triggers for all samples and (c) the peak trigger rates for the high statistics samples. The 2γ opening angle distribution is shown in Fig. 1.8.

One observes from the enhancement at low $\cos\Theta_{\gamma\gamma}$ that $\bar{H}$ production decreases with temperature, but is still produced at room temperature. This favours radiative over three-body combination.
The temperature dependence of $\bar{H}$ is shown for the three methods in Fig. 1.9. One observes a clear decrease of the $\bar{H}$ production with positron plasma temperature. However, a simple power law does not fit the data. The three-body temperature dependence ($T^{-9/2}$) is not consistent with data. Again this favours radiative over three-body recombination. However, the radiative rate prediction is not obviously compatible with our data, being an order of magnitude lower. More work is necessary to definitively clarify the underlying mechanism.
We also measured the spatial distribution of the emerging $\bar{H}$ atoms which can also provide insights into dynamics of the formation process and the distribution of initial atomic states. Figure 1.10 shows the measured distribution compared to a set of model distributions. The model that best matches the measurements is a slightly anisotropic distribution with a small radial excess. The near-isotropic nature of the distribution suggests that $\bar{H}$ is mostly formed when the antiprotons are diffusing randomly in the positron plasma. Calculations suggest that weakly bound states (populated mostly by the three-body mechanism) would emerge along the lines of the magnetic field. Therefore, the observed isotropic emergence suggests that three-body combination may not be the dominant $\bar{H}$ formation mechanism in ATHENA, in accord with the temperature measurements discussed above.

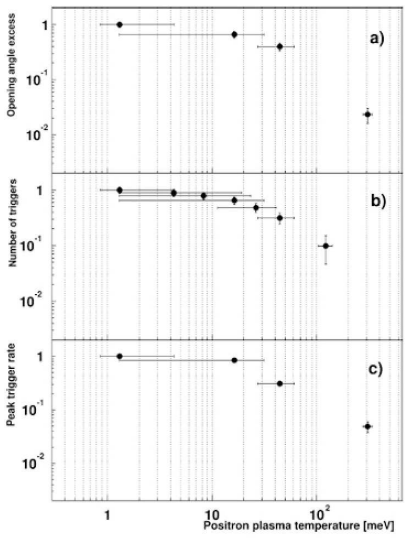

Figure 1.9: *Temperature dependence of $\bar{H}$ production (a) for the opening angle excess, (b) the number of triggers, and (c) the peak trigger rates. Data are normalised to the 15 K sample.*

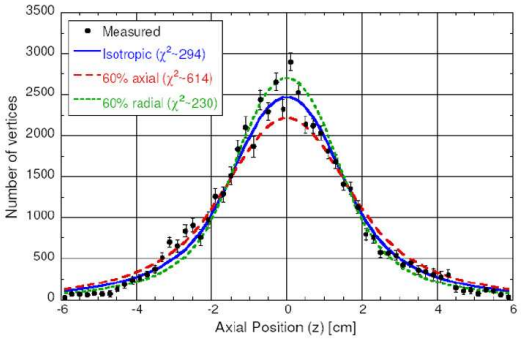

Figure 1.10: *Comparison between isotropic, axially and radially enhanced axial vertex distributions of $\bar{H}$ annihilations. A typical plasma length of 32 mm was used. The data are almost compatible with isotropic emission (blue curve).*

1.3 Measurements and improvements on detector performances

Improvements to the detector readout were made to enhance the sensitivity and extend the capabilities of the ATHENA apparatus. The 32 Si μstrip modules of the detector are now read out in a zero suppressed mode so that the detector can be read out at a much higher rate of 200 Hz. One consequence is a substantial increase in baseline fluctuations in the raw crystal data. At readout rates near 200 Hz electronic baselines of the crystals can fluctuate by more than 5 times the average noise. The readout chips are the cause of these fluctuations, since each row of 12 crystals is read out by one readout chip and baselines of crystals within each row move together. Figure 1.11 illustrates the row-by-row correlation of the baseline fluctuations. New row-by-row baselines for each event are calculated by

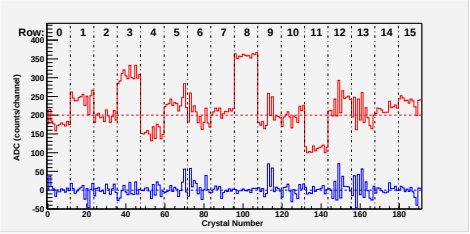

Figure 1.11: *ADC versus crystal channel distributions for a typical readout rate near 200 Hz. Upper distribution: before common-mode-noise correction (artificially offset from 0 by 200 ADC counts). Note the common offsets for rows of 12 crystals connected to the same amplifier chip. Lower distribution: after a row-by-row common-mode-noise correction.*

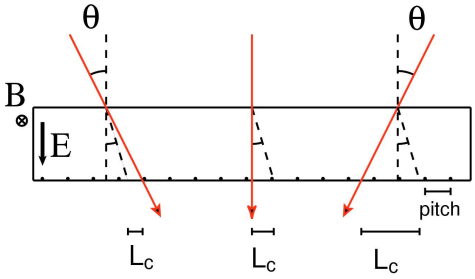

Figure 1.12: *The Lorentz angle λ leads to different cluster lengths L_c that depend on the incident angle θ.*

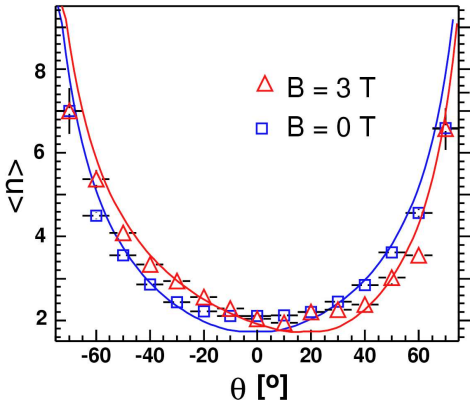

Figure 1.13: *Cluster size distribution for tracks in the plane perpendicular to the detector axis as a function of θ.*

averaging the ADC values of the groups of 12 crystals (ignoring of course crystals with signals). The new row-by-row baselines are subtracted from the data to obtain ADC distributions that oscillate around zero, see Fig. 1.11.

1.3.1 Measurement of the Lorentz angle

In the presence of the 3 T field the charge carriers (the holes in our detector) do not migrate radially along the electric field but are deflected by the Lorentz angle. Hence the cluster size of the collected charge is modified and its centroid displaced on the readout side. Under the drift along the Lorentz angle λ, the cluster lengths L_c is shortened for tracks that traverse the silicon at angles in the direction of the Lorentz deflection, and increased for tracks that cross in the opposite direction (Fig. 1.12).
Our sensors are oriented around two cylinders. The propagation direction of the holes is inward for the inner layer and outward in the outer layer. This results in opposite Lorentz angle displacements that can substantially modify the helix parameterization of the tracks and deteriorate the determination of the annihilation vertex.
We therefore measured the Lorentz deflection angle λ at 130 K. Measurements were made with cosmic rays with field off and on. Figure 1.13 shows for example the average cluster size (number of adjacent hit strips) for tracks in the plane perpendicular to the detector axis ($\phi \simeq 0$) and traversing the silicon layer under the angle θ. The symmetry about θ = 0 in the field off data indicates that charge is propagating along the electric field perpendicular to the plane of the silicon, as expected, while the asymmetry in the distribution of the 3 T data clearly indicates that the holes propagate along a non-zero Lorentz angle.
Since the cluster size also depends on the total charge deposited and hence on the track inclination ϕ along the detector axis, the data were subdivided in ϕ intervals and fits were performed for each bin to determine λ. The strip pitch (139.5 μm) and detector thickness (380 μm) were fixed to their known values, while the charge detection threshold was left as a free parameter. The results shown in Fig. 1.14 do not depend on ϕ, as expected. We obtain a Lorentz angle λ = (18.8 $\pm$ 0.5) $^\circ$ for holes at 130 K and 3 T, while for the field off data λ was consistent with zero.
In order to correct for the displacement caused by the drift along the Lorentz angle, all cluster positions were then shifted by -64.5 μm in the $\vec{E} \times \vec{B}$ direction. This led

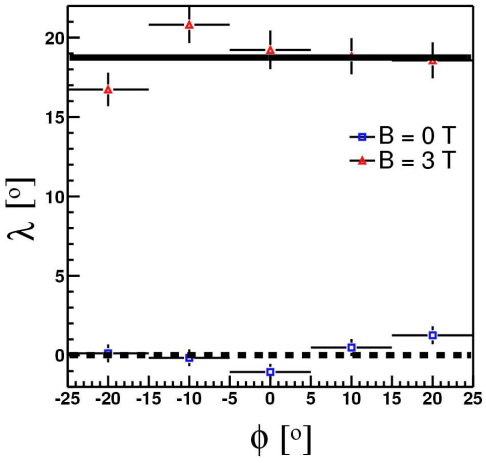

Figure 1.14: *Distribution of the Lorentz angle λ vs. ϕ (track angle along the detector axis) for field on and off.*

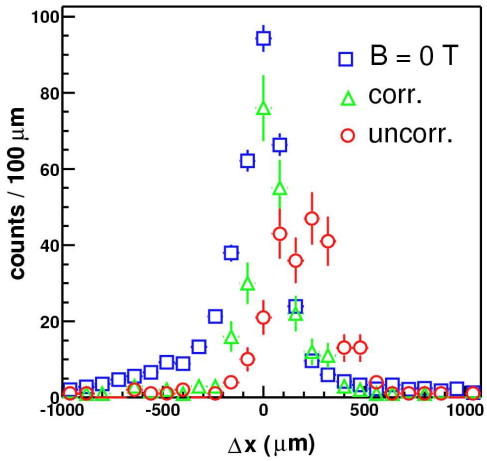

Figure 1.15: *Shift in the reconstructed position of traversing cosmic rays for field on (red) and off (blue). The shifts after correction are shown in green.*

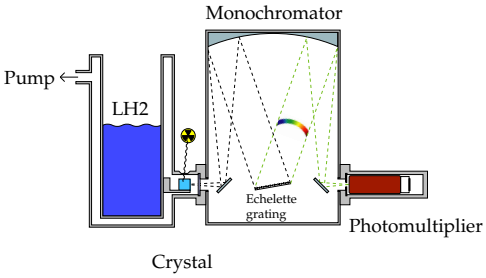

Figure 1.16: *Optical spectrometer to measure the light yield of scintillator crystals as a function of temperature and wavelength.*

to a significant improvement in the residuals for traversing cosmic rays which are now in good agreement with the unaffected field off distributions (Fig. 1.15).

1.3.2 R & D on CsI crystals

Pure CsI was chosen in ATHENA because of the excellent light yield at low temperature [8]. Initially, the crystals were coupled to pn photodiodes, but their performances deteriorated with time, due to corrosion from the iodine of CsI. We therefore replaced them with avalanche photodiodes (APD) which have gains and hence much better signal-over-noise ratios. A systematic study of the response of SINTEF and avalanche photodiodes as a function of temperature and wavelength was performed with an optical spectrometer based on an Echelette grating [9].
In 2003 we modified this facility to measure the light emission spectrum of scintillation crystals as a function of wavelength and temperature. Figure 1.16 shows the apparatus. A 50 MBq ^{90}Sr electron source irradiates a CsI crystal kept at liquid nitrogen temperature. The monochromator is equipped with a spherical mirror to image the entrance slit with parallel light to the exit slit after the grating. The crystal is located on a cold finger (see Fig. 1.17) at the focus of the monochromator.

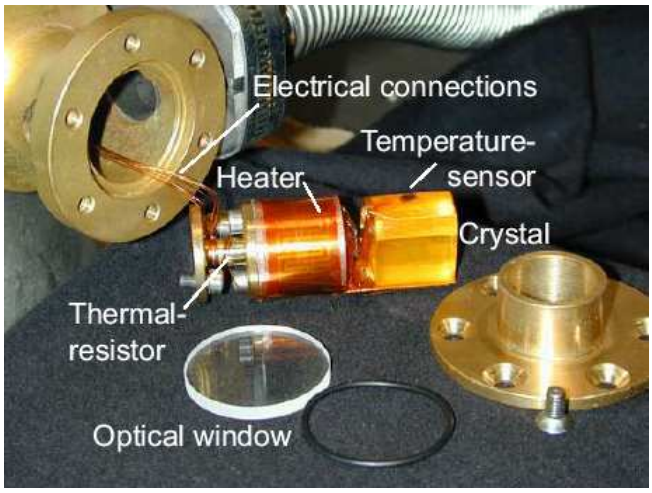

Figure 1.17: *Cold finger and vacuum chamber. The crystal is attached to the copper support with a capton tape. The brass piece on the right is used to press the optical window to the gasket ring and fits into the entrance slit of the monochromator.*

To reach liquid nitrogen temperatures a good vacuum is needed to prevent heat flow through the short

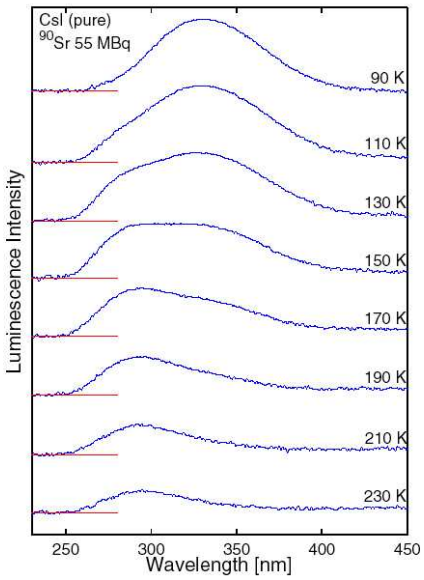

Figure 1.18: *Emission spectra from pure CsI crystal at different temperatures. The logarithmic vertical scale is in arbitrary units.*

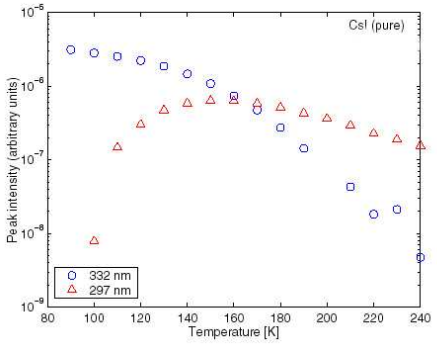

Figure 1.19: *Intensity of the emission lines at 332 nm and 297 nm as a function of temperature.*

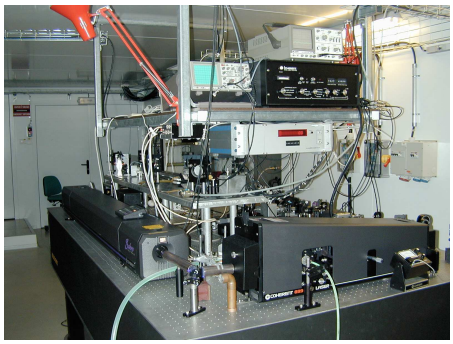

Figure 1.20: *Photograph of the krypton and dye lasers on the optical bench.*

distance (1 mm) between the cold finger and the wall of the chamber at room temperature. A turbo vacuum pump is used and a vacuum below $2\times\ 10^{-6}$ mbar can be achieved. The Echelette grating is slowly rotated while the light intensity is measured with a photomultiplier. The current of the photomultiplier is integrated and measured with an electrometer.

Data were taken in temperature steps of 10 K between 90 and 230 K for wavelengths between 240 and 450 nm. The emission spectrum contains two lines (Fig. 1.18) which were fitted with gaussians and a smooth background. The relative intensities of the fitted emission lines at 297 and 332 nm are shown in Fig. 1.19 as a function of temperature. The presence of two emission lines in pure cold CsI was already known before [10]. However, our measured intensity distributions are much more precise.

1.4 R&D for laser spectroscopy

In 2003 our group group was involved in the preparation of the spectroscopy phase, namely the construction of a laser system to generate 243 nm light for 1s-2s two-photon spectroscopy in antihydrogen [11]. We used the well known non-linear technique to generate 243 nm light from a laser source of longer wavelength. The laser system consists of a Kr^+ ion laser that emits 4 W in the range 406 nm to 415 nm. The (up to 6 W) Kr^+ ion laser pumps a dye laser which emits in the range 460 nm to 516 nm. The dye laser is tuned to a wavelength of 486 nm which is twice the wavelength of the two-photon 1s-2s transition in (anti)hydrogen. Most of the equipment was provided by the University of Aarhus. A photograph of the two lasers is shown in Fig. 1.20.

The light from the dye laser is sent into an external frequency doubling cavity containing a nonlinear crystal. The second harmonic generation power in the crystal is maximum when the refractive indices n for the fundamental and the second harmonics are equal. Since the refractive index depends on frequency, a birefringent crystal with a suitably oriented optical axis is used, in which the ordinary ray is chosen for the fundamental frequency and the extraordinary ray for the second harmonic, i.e. $n_o(\omega) = n_e(2\omega)$. Losses are reduced by using a crystal cut such that the light with fundamental frequency traversing the crystal penetrates the crystal under the Brewster angle. Under this angle the polarisation parallel to the plane formed by the incident beam and the normal to the crystal surface is not reflected but transmitted into the crystal. The wavelength can be measured accurately with a Michelson interferometer with moving mirrors, calibrated on a He-Ne laser.

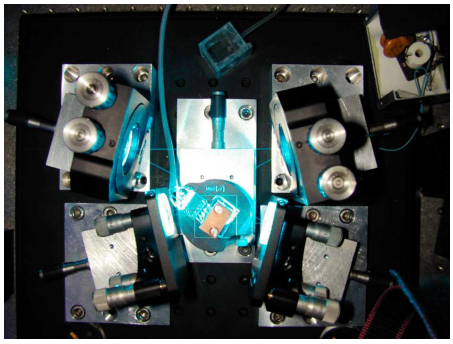

Figure 1.21: *Photograph of the lasing cavity. The crystal is mounted inside the temperature stabilized copper block in the center of the picture.*

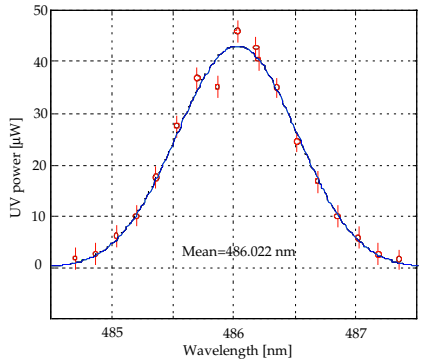

Figure 1.22: *Tuning the dye laser to 486 nm (input power 45 mW).*

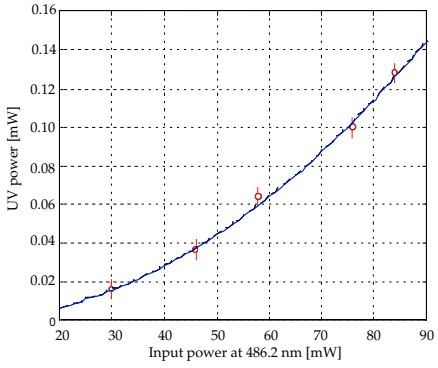

Figure 1.23: *The 243 nm cavity output power as a function of 486 nm input power. The curve shows the expected quadratic dependence.*

The cavity - Fig. 1.21 - consists of a Brewster cut rhomb shaped beta barium borate (BBO) crystal of dimensions $5 \times 5 \times 8$ mm^3. The light from the dye laser enters from the right. The convex mirrors have a reflection coefficient of 100 % for the first harmonic and a transmission coefficient of 95 % for the second harmonic. One of the mirrors is mounted on piezoelectric crystal to vary the optical path-length in the cavity. The beam is sent to a photodiode for cavity locking. The cavity was developed by the Zurich team and the mechanical stability of the piezo was investigated in details [11]. The support structure and temperature stabilized crystal holder (to better than 0.1°) were built in the mechanical workshop of our institute.

Figure 1.22 shows the tuning of 486 nm light from the dye laser. Unfortunately the specified output power of the dye laser (360 mW of power at 486 nm for 3 W input power) could not yet be achieved. The power output is an order of magnitude smaller than expected. However, second harmonic generation of 243 nm UV light was achieved in the BBO cavity. Figure 1.23 shows the output power at 243 nm as a function of input power at 486 nm. The measurement agree with the prediction that the second harmonic power increases with the square of the input power (curve).

[1] M. Amoretti *et al.*, Nature **419** (2002) 456.
[2] M. Amoretti *et al.*, Phys.Rev.Lett.**91** (2003) 055001.
[3] C. Regenfus, Nucl.Instr.Meth.**A 501** (2003) 65.
[4] M. Amoretti *et al.*, Nucl.Instr.Meth.**A 518** (2004) 679.
[5] M. Amoretti *et al.*, Phys.Lett.**B 578** (2004) 23.
[6] M. Amoretti *et al.*, submitted to Phys.Lett.**B**.
[7] M. Amoretti *et al.*, Phys.Lett.**B 583** (2004) 59.
[8] C. Amsler *et al.*, Nucl.Instr.Meth.**A 480** (2002) 494.
[9] A. Glauser, Diplomarbeit, Universität Zürich, 2003.
[10] H. Nishimura *et al.*, Phys.Rev.**B 51** (1995) 2167.
[11] O. Iannarelli, Diplomarbeit, Universität Zürich, 2004.

2 Rare Kaon Decays at Brookhaven AGS

H. Kaspar (visiting scientist), P. Robmann, A. van der Schaaf,
S. Scheu, A. Sher and P. Truöl

Our research program at the Brookhaven National Laboratory's Alternating Gradient Synchrotron (AGS) focuses on rare kaon decays. Only at the AGS sufficiently intense low-momentum neutral and charged kaon beams are still available today. Experiment BNL E-865 finished data-taking in 1998, and the last results from the analysis of a high-statistics sample of rare semi-leptonic charged kaon decays are being presented. The KOPIO-experiment has been approved for funding by the U.S. National Science Foundation, and its planning concentrates now on the construction of detector prototypes and development of a suitable neutral kaon beam.

2.1 BNL E-865: a search for lepton flavor violation in K^+ decay

in collaboration with:
Paul–Scherrer–Institut, CH-5234 Villigen; Brookhaven National Laboratory, Upton, NY-11973, USA; University of New Mexico, Albuquerque, NM-87131, USA; University of Pittsburgh, Pittsburgh, PA-15260, USA; Yale University, New Haven, CT-06511, USA; Institute for Nuclear Research, Academy of Sciences 117 312 Moscow, Russia

The final results obtained by experiment E865 concern the search for the lepton flavor number violating (LFNV) decay $K^+ \to \pi^+\mu^+e^-$ ($K_{\pi\mu e}$), i.e. the decay for which the experiment was primarily set up. The proposal had aimed for a sensitivity level reaching down to a branching ratio below 10^{-11}. With finite neutrino masses established LFNV is no longer forbidden. The standard model extended to incorporate neutrino masses still predicts this decay to occur at an unobservably low level. Several extensions of the standard model, however, allow lepton family number violation at a much higher rate (as high as 10^{-10}). Hence, if the search for the decay is successful, it signals non-standard model physics, if not, parameters of the extension models are constrained. We can illustrate this taking the example of the extended technicolor model (ETC) [1], where the transitions between the leptons of different generations can be mediated by a horizontal ETC boson. Due to the similarity between $K_{\pi\mu e}$ decay and the familiar decay $K_{\mu 3}$ ($K^+ \to \pi^0\mu^+\nu_\mu$) the branching ratios can be compared to give an approximate mass of the ETC boson (M_H)

$$\frac{B(K_{\pi\mu e})}{B(K_{\mu 3})} = 16\frac{1}{\sin^2\theta_c}\left(\frac{g_H}{g}\right)^4\left(\frac{M_W}{M_H}\right)^4 ,$$

where θ_c is the Cabbibo angle, g and g_H are the weak and ETC coupling constants, and M_W is the mass of the W boson.

The existing limit on the branching ratio for $K_{\pi\mu e}$ of $2 \cdot 10^{-10}$ [2] was lowered with E865's 1995/6 data to $2.8 \cdot 10^{-11}$ [3]. The analysis of the 1998 data, which was the thesis project of Aleksey Sher [4] has by itself improved the limit to $2.2 \cdot 10^{-11}$. A combination of all the above results then leads to $1.2 \cdot 10^{-11}$ or, with $g_H \approx g$, to

$$M_H \approx 150\,\mathrm{TeV}\left[\frac{10^{-12}}{B(K_{\pi\mu e})}\right]^{1/4} \geq 80\,\mathrm{TeV} .$$

In order to reach this result a time-consuming and difficult analysis had to be brought to conclusion. One difficulty refers to the total amount data, which Aleksey Sher had to handle. During a period of

seven months $1.5 \cdot 10^9$ K-decays were registered in the detector, corresponding to 500 Exabyte tapes with approximately 4.5 Gbyte each or 2 Tbyte of raw data. The first analysis step, which reduced the amount of data by about a factor of five, selected events with three charged tracks coming from a reconstructible vertex and took eight months on a cluster of Linux workstations at BNL working around the clock. This cumbersome part was followed by the selection of candidates based on the reconstructed momenta using kinematics, proper particle identification, the decay vertex and the event timing. The blind analysis philosophy was followed here, i.e. all conceivable sources of background were investigated first and criteria were developed to suppress them, before the small volume in the multi-parameter space, in which the real events were expected, the so-called *box*, was looked at.

Three types of background had to be dealt with:

- decays in which one or two of the products decayed, too, yielding the correct $K_{\pi\mu e}$ final particles, for example the K_τ decay sequence $K^+ \to \pi^+\pi^+\pi^-$; $\pi^+ \to \mu^+\nu_\mu, \pi^- \to e^-\bar{\nu}_e$,
- decays in which one or two of the decay products were misidentified, for example again K_τ with a π^- misidentified as an e^- and a π^+ as a μ^+, and
- accidental overlap of two kaon decays simulating a real decay.

The detector [5] resided in a 6 GeV/c unseparated K^+ beam and featured a high resolution magnetic charged particle spectrometer with four large multi-wire proportional chambers, two of them built by us in Zürich, a finely segmented electromagnetic calorimeter of shashlyk type, a muon range filter equipped with proportional tubes, and two large atmospheric pressure gas Čerenkov counters within the spectrometer magnets. Calorimeter and Čerenkov counter information was used for e versus π discrimination. Only 0.2 event from these two types of backgrounds were expected in the signal region. In order to reach this prediction extensive Monte Carlo simulations were necessary, with the experimentally and independently determined detector efficiencies properly adapted to the high rate running conditions of 1998. The acceptance for $K_{\pi\mu e}$ events and the two monitor decays from pre-scaled minimum bias trigger events $K_{\rm Dal}$ ($K^+ \to \pi^+\pi^0$; $\mu^+\pi^0\nu_\mu$; $e^+\pi^0\nu_e$; $\pi^+\pi^0\pi^0$; $\pi^0 \to e^+e^-\gamma$) and K_τ had to be calculated. Figures 2.1 and 2.2 illustrate how well the simulation represents the measured quantities.

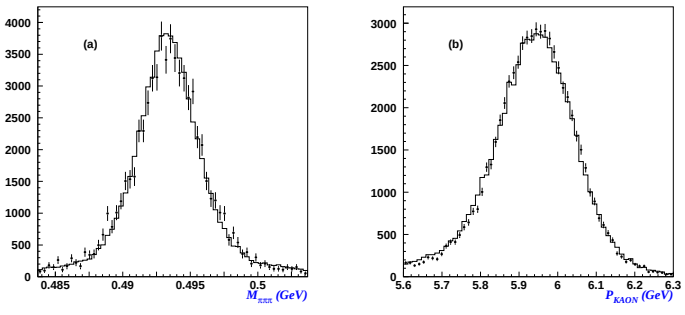

Figure 2.1: *Distributions of (a) 3π invariant mass and (b) K^+ momentum for K_τ (see text). Full histograms: simulation; crosses: measured data.*

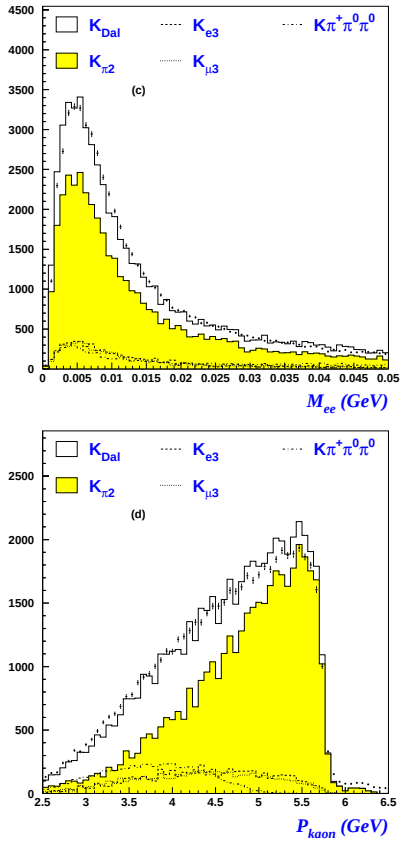

Figure 2.2: *Distributions of (top) e^+e^- - invariant mass and (bottom) K^+ momentum for K decays into e^+e^- pairs. Full histograms: simulation; crosses: measured data.*

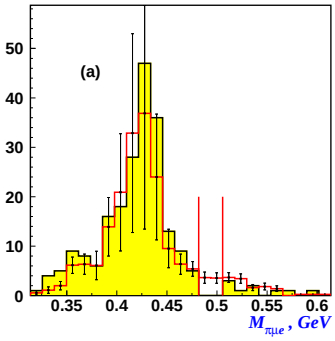

Figure 2.3:
*Three particle invariant mass for $K_{\pi\mu e}$ candidates. The signal region (*box*) is indicated. Full histogram: predicted background from misidentified K_τ and $K_{\rm Dal}$ decays and accidental background; crosses: measured data.*

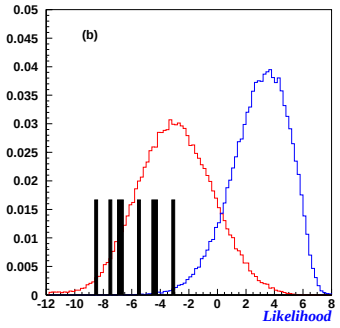

Figure 2.4:
Expected log-likelihood distributions for signal (blue curve) and background (red curve) events. The position of the eight events found in the K^+ mass window are indicated.

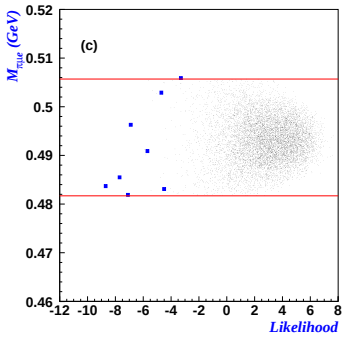

Figure 2.5:
Three particle invariant mass versus log-likelihood. Points: Monte Carlo generated signal events; squares: measured data.

The most problematic background source turned out to be accidental coincidences, e.g. from the decay $K^+ \to \pi^+\pi^0$; $\pi^0 \to e^+e^-\gamma$ with detected π^+ and e^- and a μ^+ from the beam halo or another decay, which survived the selection criteria. The analysis of the side bins in the event timing distributions and of those events, to which the reconstruction assigned a kaon momentum above 6.9 GeV/c led to an expectation of 8.2 ± 1.9 such events in the *box* (see Fig. 2.3). Eight events were indeed found, when the *box* was opened, to all of which the maximum likelihood analysis assigned a low probability to be signal events (see Fig. 2.4 and Fig. 2.5).
The flexibility of the E865 apparatus allowed also to obtain high statistics event samples on other rare final states, where existing data were scarce, namely:

- $\mu^+e^+e^-\nu_\mu$
- $e^+e^+e^-\nu_e$ ($K_{\ell\nu\gamma^*}$)
- $\pi^+\pi^-e^+\nu_e$ (K_{e4})
- $\pi^0e^+\nu_e$ (K_{e3})
- $\pi^+e^+e^-$
- $\pi^+\mu^+\mu^-$.

Several publications have appeared concerning these decay branches in the past, the last two in 2003 [6; 7]. The analysis of the K_{e4} data (400'000 events) allowed to measure low energy s-wave $\pi\pi$ scattering phase shifts and K-decay form factors with high precision, from which a new value for the s-wave $\pi\pi$ scattering length was extracted [6]. These results are often cited, because they provide stringent constraints for chiral QCD perturbation theory (ChPT) parameters. In a dedicated low intensity run in 1998 we also collected 70'000 K_{e3} events to afford a precise measurement of the branching ratio for this decay, which along with that for the analogous decay of the neutral kaon is the primary source for the determination of the CKM quark mixing matrix element V_{us}. In our experiment the π^0 was detected via its Dalitz decay $\pi^0 \to e^+e^-\gamma$ and the K_{e3} branching ratio was measured relative to the sum of all other decays involving π^0 [7]. We have reported on the significance of this result for testing unitarity relations in CKM-matrix [8] last year.

[1] E. Farhi, and L. Susskind, Phys. Rep. **74**, 277 (1981).

[2] A.M. Lee *et al.*, Phys.Rev.Lett.**64**, 165 (1990).

[3] R. Appel *et al.* (E865-coll.), Phys.Rev.Lett.**85**, 2450 (2000).

[4] *An improved limit on the decay* $K^+ \to \pi^+\mu^+e^-$,
Aleksey Sher, PhD. Thesis, University of Zürich, 2003;
http://www.physik.unizh.ch/people/truoel/e865/sherthesis.pdf.

[5] *A large acceptance, high resolution detector for rare* K^+*-decay experiments*,
R. Appel *et al.* (E865-coll.), Nucl.Instr.Meth.**A479**, 349 (2002).

[6] *High statistics measurement of* K_{e4} *decay properties*, S. Pislak *et al.* (E865-coll.), Phys.Rev.**D67**, 072004-1 (2003); Phys.Rev.Lett.**87**, 221801-1 (2001).

[7] *High statistics measurement of the* $K^+ \to \pi^0 e^+ \nu_e$ (K^+_{e3}) *branching ratio*,
Alexandre Sher *et al.* (E865-coll.), Phys.Rev.Lett.**91**, 261802-1 (2003).

[8] H. Abele *et al.*, Eur.Phys.J.**C33**, 1 (2004).

2.2 KOPIO: a study of the CP-violating rare decay $K_L^0 \to \pi^0\nu\overline{\nu}$

in collaboration with:
Brookhaven National Laboratory, University of Cincinatti, INR Moscow, KEK, Kyoto University of Education, Kyoto University, University of New Mexico, INFN University of Perugia, Stony Brook University, Thomas Jefferson National Accelerator Facility, TRIUMF/UBC, University of Virginia, Virginia Polytechnic Institute & State University, and Yale University.

The aim of the experiment as formulated in the proposal and detailed in the technical design report [1], a measurement of the branching ratio of the decay $K_L^0 \to \pi^0\nu\overline{\nu}$ with a single-event sensitivity around 6×10^{-13} (corresponding to $\approx 50 \pm 20$ observed events for the SM prediction), remains unchanged.

The combined MECO/KOPIO project at BNL is part of the US National Science Foundations (NSF) Major Research Equipment (MRE) program and funding of construction and operation will start in October 2005. Until that date some USD 6 million will be available for planning and design activities.

Within the Standard Model the $K_L^0 \to \pi^0\nu\overline{\nu}$ decay amplitude is directly proportional to the CP-violating phase in the CKM matrix. In contrast to the interpretation of the value of ϵ'/ϵ theoretical uncertainties can be neglected. Whereas the Standard Model makes no quantitative prediction for this phase the comparison with the result obtained in the B-meson sector would allow a sensitive test of the Standard Model.

The KOPIO-experiment will use an intense low momentum, time structured K_L^0 beam available only at the AGS. This way the momentum of the kaon can be determined from the time of flight which will allow the full reconstruction of the π^0 mass and momentum in the K_L^0 center-of-mass system. Kinematical cuts and an elaborate veto counter system are designed to nearly eliminate all background from K_L^0 decay modes with additional π^0 or charged particles. The observation of about 40 to 50 events (at SM prediction level) with a signal to background ratio of 2:1 would correspond to a measurement of the area of the CKM unitary triangle with an accuracy of about 10% .

Our group has taken on the responsibility for the design and construction of the charged particle veto counters, which are of crucial importance for a variety of background sources, e.g. from $K_L^0 \to \pi^- e^+ \gamma \nu_e$ and $K_L^0 \to \pi^-\pi^+\pi^0$. The energy of the PSI $\pi^\pm$ beams is ideally suited for testing prototypes, a program which we started in 2000.

2.2.1 CP violation in the quark sector: SM and beyond

Within the SM CP violation in the quark sector arises from a single complex phase in the CKM mixing matrix [2]. In the Wolfenstein parametrisation the violation results from a non-zero value of the parameter η which manifests itself in two CKM elements:

$$\begin{aligned} V_{ub} &= |V_{ub}|e^{-i\beta} = A\lambda^3(\rho - i\eta) \\ V_{td} &= |V_{td}|e^{-i\gamma} = A\lambda^3(1-(1-\lambda^2/2)(\rho+i\eta)) \approx A\lambda^3(1-\rho-i\eta) \end{aligned}$$

The decay $K_L^0 \to \pi^0\nu\overline{\nu}$ has major contributions from penguin and box diagrams with up-type quarks in the intermediate state. Since the transition amplitude scales with the quark mass the top contribution dominates by far and $A(K_L^0 \to \pi^0\nu\overline{\nu}) \propto V_{td}^* V_{ts} - V_{ts}^* V_{td} \propto i\eta$. As a result $B(K_L^0 \to \pi^0\nu\overline{\nu}) \propto \eta^2$. The corresponding charged decay mode does not require CP violation but gives a circular constraint around $\rho = 1.3, \eta = 0$: $B(K^+ \to \pi^+\nu\overline{\nu}) \propto (\rho - 1.3)^2 + \eta^2$.

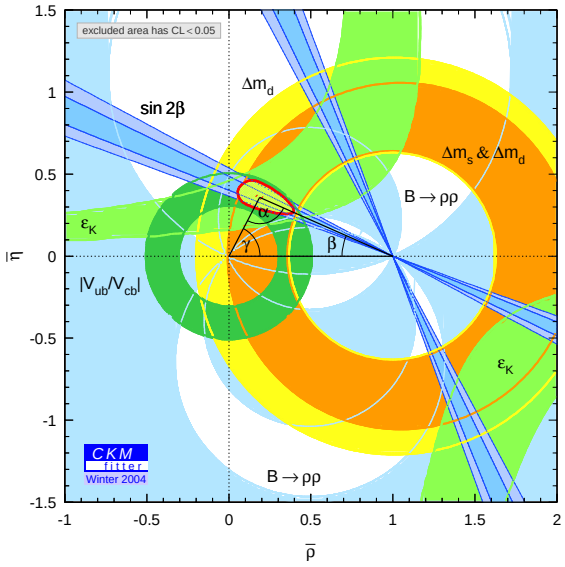

Present situation (95% confidence regions)

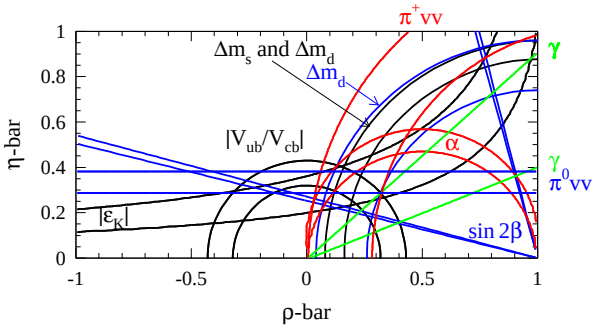

Possible situation in 2010

Figure 2.6: *The constraints from various K and B decays on the Wolfenstein parameters $\overline{\rho}$ and $\overline{\eta}$. Results from the CKMfitter working group*[2].

Ultimately these two decay modes together will give a complete picture of CP violation in the K system with negligible theoretical uncertainties. Figure 2.6 shows how various observables in K and B decays contribute to our knowledge of $\overline{\eta} \equiv (1-\lambda^2)\eta$ and $\overline{\rho} \equiv (1-\lambda^2)\rho$.

Physics beyond the SM generally allows additional CP-violating phases [3] and as a result the SM description with a universal set of Wolfenstein parameters for K and B would break down. It is very fortunate that we may expect significant improvements in the experimental constraints in both areas during the next decade so that meaningful tests can be made.

A recent theoretical analysis [4] links the observed $B \to \pi\pi$ rates using SU(3) flavour-symmetry and plausible dynamical assumptions to the $B \to \pi K$ rates and determines the CKM angle γ in accordance with the usual fits. The analysis of the $B \to \pi K$ system in the SM yields good agreement with the experimental picture, with the exception of those observables that are significantly affected by electroweak penguins, thereby suggesting new physics (NP) in this sector. Indeed, a moderate enhancement of these topologies and a large CP-violating NP phase allows then to describe any currently observed feature and to predict the CP-violating $B_d \to \pi^0 K_S$ observables. In the specific scenario where NP enters only through Z^0 penguins, one obtains a link to rare K and B decays, where the most spectacular NP effects are an enhancement of the $K_L \to \pi^0\nu\bar{\nu}$ rate by one order of magnitude with $B(K_L \to \pi^0\nu\bar{\nu}) \approx 4B(K^+ \to \pi^+\nu\bar{\nu})$.

[2] http://www.slac.stanford.edu/xorg/ckmfitter/ckm_results_winter2004.html

2.2.2 The KOPIO experiment

The decay $K_L^0 \to \pi^0 \nu\overline{\nu}$ will be distinguished from other more likely decay modes on the basis of the following signature:

- Two photons are observed with a common vertex inside the decay region and an invariant mass equal to m_{π^0}.
- No simultaneous charged particles or additional photons are observed.
- The energy $E^*_{\pi^0}$ of the reconstructed π^0 in the K_L^0 rest frame (using the K^0 time of flight through the beam line) and the photon energy sharing do not coincide with the regions populated by the background of the decay $K^0 \to 2\pi^0$ remaining after test 2.

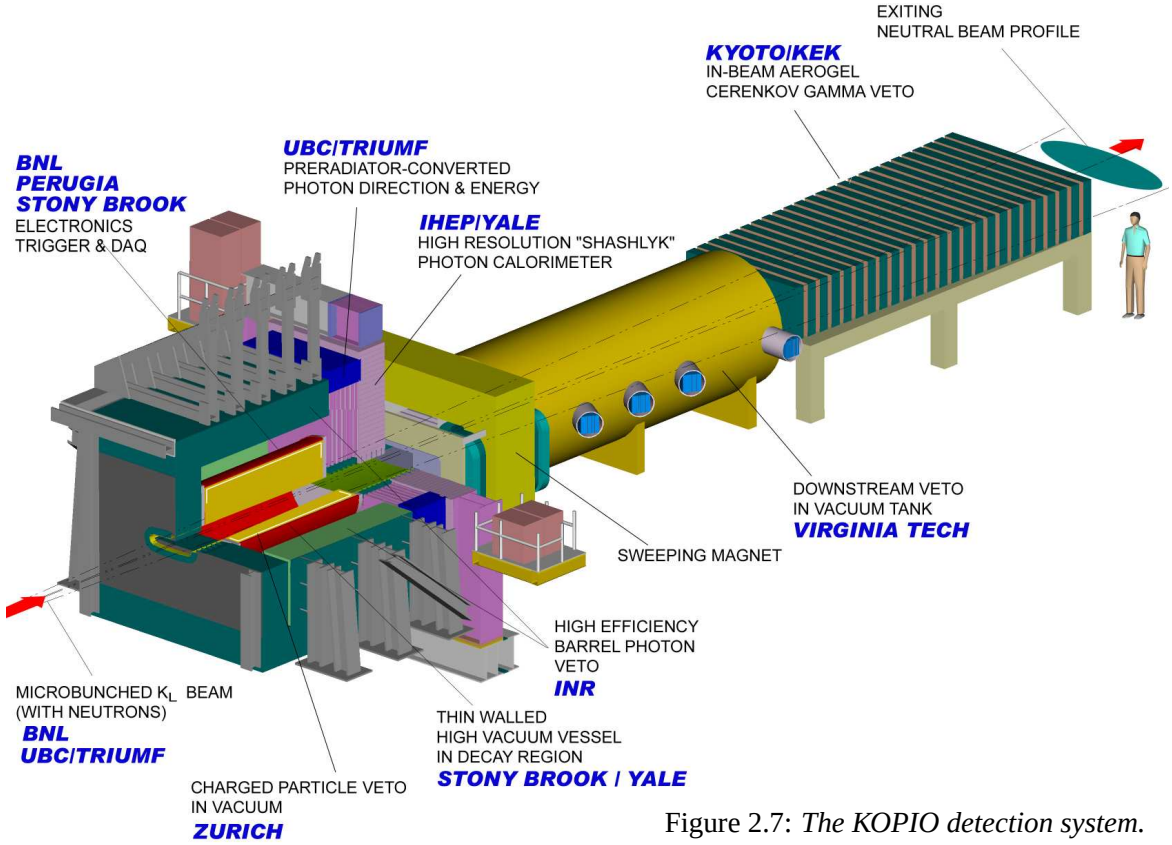

Figure 2.7: *The KOPIO detection system.*

Figure 2.7 shows the planned setup. The π^0 detector consists of a highly segmented pre-radiator followed by an electromagnetic calorimeter. All remaining detectors serve as veto counters for charged particles and photons. Particularly problematic are the detectors for particles and photons moving along the beam which contains $O(10^{11})$ s^{-1} neutrons. Charged particles are bend out of the beam with the help of a sweeping magnet situated right behind the π^0 detector.

The Zürich group took over the responsibility for the main charged-particle veto system situated directly around the decay region. Additional veto systems situated further downstream should detect charge particles escaping through the beam pipe. The purpose of the charged-particle veto systems is the efficient identification of background processes in which an apparent $\pi^0 \to 2\gamma$ decay inside the decay volume is accompanied by charged particle emission. Examples of such background processes are, (i) $K_L^0 \to \pi^+\pi^-\pi^0$, (ii) $K_L^0 \to e^+\pi^-\nu\gamma$ in which the positron creates a second photon through Bremsstrahlung or annihilation in flight, (iii) $K_L^0 \to e^+\pi^-\nu$ again followed by $e^+ \to \gamma$ whereas the

π^- creates a photon through $\pi^- p \rightarrow \pi^0 n$. In all cases two particles with opposite electrical charge emerge. The events may also produce signals in other detector elements, like the barrel veto system.

As discussed already in the proposal simulation shows that **detection efficiencies** of 99.99% or better are required to keep these backgrounds below a few events in the final sample. Our 2001 studies at PSI[5] have shown that the **dead layer** in front of the veto system (which includes wrapping material and possibly a window separating the detector from the high-vacuum decay region) should be kept below 20 mg/cm^2 and that a **detection threshold** of ≈ 75 keV (corresponding to ≈ 0.3 mm scintillator thickness) should be reached. Minimising dead material in front of the detector mainly helps to reduce the inefficiency for π^- caused by nuclear reactions.

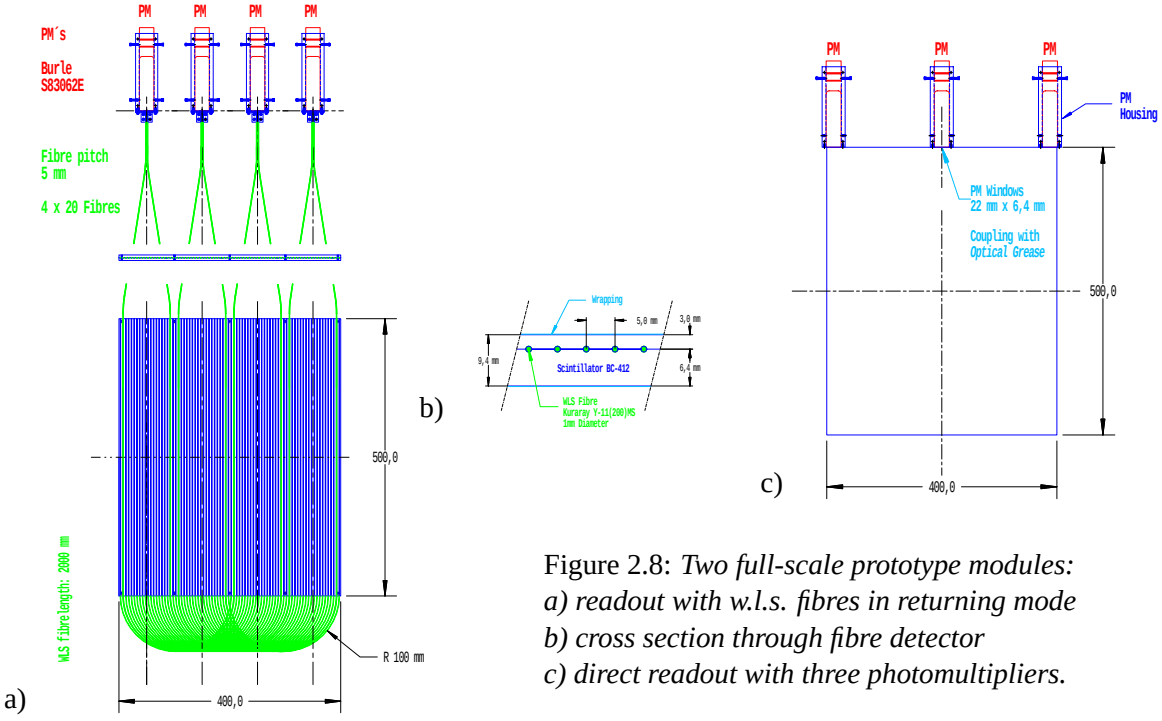

Figure 2.8: *Two full-scale prototype modules:*
a) readout with w.l.s. fibres in returning mode
b) cross section through fibre detector
c) direct readout with three photomultipliers.

During a two weeks beam period at PSI in July 2003 full-scale (400 mm x 500 mm) prototypes of the two light-collection schemes of interest were studied (see Fig.2.8). In addition prototypes for the downstream charged particle veto system and for the scintillator planes of the pre-radiator detector were tested. All measurements were done with 500 MeV/c π^-. Two xy MWPC's were used to determine the impact position on the scintillator.

In Table 2.1 the observed photoelectron yields are compared with our 2002 results for elements with dimensions 200 x 250 mm^2. As can be seen from the table direct readout may give almost ten times more photoelectrons for a given energy deposit then observed with embedded wavelength shifting fibres. Our new results with full-scale prototypes indicate that it should be possible to reach a threshold of ≈ 10 keV with a $\pm 5\%$ homogeneity over the detector surface. For this reason direct readout was chosen in our present design (see Fig. 2.9).

The remaining decisions are on the detector thickness and the type of photomultiplier or possibly Geiger-mode avalanche photodiode. As can be seen from Tab. 2.1 3 mm thick counters still give 200 photoelectrons for minimum-ionising particles so 1-2 mm thickness should be sufficient. Reducing the thickness results in less sensitivity to neutrons and photons and in less dynamic range which in turn improves the double-pulse resolution. Reducing the thickness also reduces the cathode

Table 2.1: *Photoelectron (p.e.) yields of various light collection schemes. Scintillator: BC-412 by BICRON, photomultipliers: Burle 83062E (Ø 22 mm).*

	size [cm^2]	thickness [mm]	version		wrapping	nr. of PMT's	p.e.	p.e. in 10 mm
			fiber	geometry				
w.l.s. fibers	20x25	2x6.4	Bicron[a]	straight[c]	Tyvek[d]	4	110	90
		⋮	Kuraray[b]	⋮	⋮	⋮	130	110
	40x50	6.4+3.0	⋮	returning[c]	VM2000[e]	⋮	115	125
			width of windows	grease				
direct readout	20x25	6.4	10 mm	no	black paper	4[f]	130	200
		⋮	⋮	⋮	Tyvek[d]	⋮	260	400
	40x50	⋮	⋮	⋮	⋮	4[g]	130	200
		⋮	22 mm	⋮	⋮	⋮	220	340
		⋮	⋮	yes	⋮	⋮	410	640
		⋮	⋮	⋮	VM2000[e]	⋮	520	810
		3.0	⋮	⋮	⋮	⋮	200	670
		6.4	⋮	⋮	⋮	3[g]	500	780
		⋮	⋮	⋮	⋮	2[g]	330	520

[a] BCF-92MC
[b] Y-11(200)MS
[c] read from both ends
[d] DuPont trademark
[e] radiant mirror film produced by 3M
[f] mounted at opposite sides
[g] mounted at one side

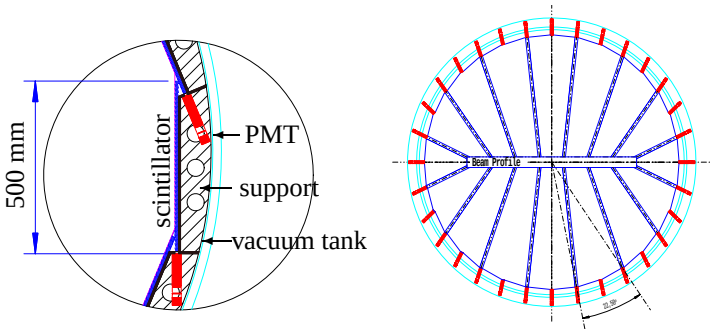

Figure 2.9:
Present design of the main charged-particle veto system. Left: sector of a cross section perpendicular to the beam. Along the beam there would be ≈ 10 modules with overlap to avoid dead space.
Right: endcap detectors.

area required. As a result the newly-developed Geiger-mode photodiodes become an interesting alternative to photomultipliers. These devices are presently available with an area of 3×3 mm^2 and an effective efficiency (geometric times quantum efficiency) around 20%. Contrary to photomultipliers significant improvements can be expected in the near future. Advantages are much smaller dimensions, lower price (so one can afford more of them), ease of operation and immunity to magnetic field. Compared to standard APD's they do not require large electronic amplification which makes them both faster and less noisy.

[1] *Rare Symmetry Violating Processes, KOPIO section*, Technical design report submitted to the National Science Foundation to construct the MECO and KOPIO experiments, June 2001; available at *http://www.physik.unizh.ch/people/truoel/kopio/kopiotdr.pdf*.
The proposal (1999) is available at *http://pubweb.bnl.gov/people/rsvp/proposal.ps*

[2] *Flavour physics and CP violation in the SM*, A. Buras, Proceedings of KAON 2001, eds. F. Constantini, G. Isidori and M. Sozzi, (Frascati Physics Series Vol.XXVI), pp. 15-43.

[3] *Flavour physics and CP violation beyond the SM*, A. Masiero, Proceedings of KAON 2001, eds. F. Constantini, G. Isidori and M. Sozzi, (Frascati Physics Series Vol.XXVI), pp. 45-58.

[4] A.J. Buras, R. Fleischer, S. Recksiegel, and F. Schwab, Preprint CERN-PH-TH-2004-020, TUM-HEP-540-04, MPP-2004-14, hep-ph/0402112 (February 2004).

[5] KOPIO Technical Note TN027, *Measurements on the response of plastic scintillator to charged pions at 185-300 MeV/c*, H. Kaspar, P. Robmann, A. v.d.Schaaf, S Scheu, P. Truöl, J. Egger, M. Blecher, 31 October 2001.

3 Particle Physics at DESY/HERA (H1)

J. Becker, Ilaria Foresti, N. Keller, H. Klehr, J. Kroseberg (until May 2003),
L. Lindfeld, Katharina Müller, P. Robmann, S. Schmitt, C. Schmitz, U. Straumann,
P. Truöl, M. Urban, Nicole Werner and Stefania Xella Hansen

in collaboration with:
S. Baumgartner, N. Berger, W. Erdmann, C. Grab, B. List, S. Mangano, D. Meer, A. Schöning and R. Weber, Institut für Teilchenphysik der ETH, Zürich; S. Egli, R. Eichler, K. Gabathuler, M. Hildebrandt, and R. Horisberger, Paul–Scherrer–Institut, Villigen, and 34 institutes outside Switzerland

(**H1**–Collaboration)

3.1 Electron–proton collisions at a centre of mass energy up to 320 GeV: overall status of the project

The analysis of the data taken in 1999/2000 ($\mathcal{L} = 91$ pb^{-1}), combined in some cases with the pre–1999 data ($\mathcal{L} = 50$ pb^{-1}) continued vigorously leading to 14 publications ([1]-[14]) and 27 papers contributed to the 2003 high–energy physics conferences [15] ([16]-[42]), addressing the following subjects:

- Neutral and charged electroweak current cross sections, proton structure functions and parton densities (extensions into lower and higher Q^2 regimes, use of QED–Compton scattering events) [3; 16; 17; 18; 44; 45];
- Search for states and interactions outside the Standard Model: unexpected event topologies [2; 41], compositeness [4], squarks [12], gravitinos [42], leptoquarks [39], single top [7], charged Higgs [40], anomalous lepton pairs [6; 8], magnetic monopoles [40] and heavy stable charged particles [13];
- Photo– and electro–production of di– and multi–jets [2; 9; 10; 24; 25; 27];
- Photo– and electro–production of exclusive final states: π^0 [14], ρ [32], J/Ψ [5; 34], antideuterons [13];
- Production of open charm and beauty: anti–charmed baryon state [11], inclusive charm [20; 21; 22; 23], inclusive beauty [26];
- Diffractively produced final states: inclusive [28; 29; 30; 31; 36], π^0 [14], jets [27], ρ, $f_0(980)$, and $f_2(1270)$ [32], J/Ψ [5; 34], high p_t photons [35];
- Photon structure [19] and deeply virtual Compton scattering [37].

3.2 Status of the HERA accelerator

Since the end of the HERA shutdown in September 2003 the vacuum and background situation has significantly improved. This was achieved by the installation of an additional ion getter pump, in-

creased pumping power and a lead shield around the beam pipe for better synchrotron radiation protection.

From January to end of April 2004 HERA–II has continuously delivered data up to an integrated luminosity of 37.2 pb^{-1}. The produced integrated luminosity as a function of time is shown in Fig. 3.1 together with the luminosity recorded with H1. The slope of the curve for 2004 is similar to that in the year 2000 with higher specific luminosity but lower duty cycle. The maximum instantaneous luminosity achieved up to end of April was $3.5 \cdot 10^{31}$ cm^2/s. Both beam intensities and specific luminosity have thus reached the HERA-II upgrade design values. However, there is still room for improvements in the reliability of various technical elements of the accelerators, in order to increase the duty cycle of the machine.

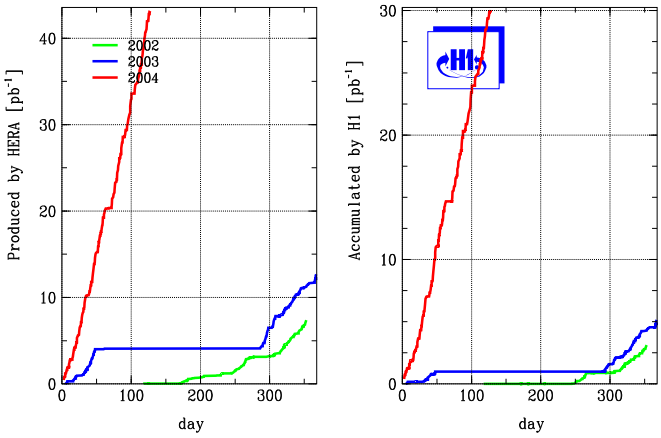

Figure 3.1:
Left: integrated luminosity produced by HERA–II as a function of time.
Right: integrated luminosity accumulated by H1 as a function of time.

3.3 Commissioning and first operation of the new z–vertex trigger

3.3.1 Repair of the CIP2k frontend electronics

In summer 2003 we had the chance to access the front–end electronics of the CIP2k chamber and repair some broken channels. After removing the SpaCal calorimeter and disconnecting the beam–pipe the CIP2k chamber was retracted by about 50 cm and the front–end electronics was removed and repaired. Boards which could not be repaired were replaced. The new/repaired electronics was tested using a three–step procedure:

- Check the response of each single channel with a special test board.
- Connecting to the standard readout and slow control system and doing pedestal and noise runs.
- Connecting each board to the standard readout again after attaching it to the chamber.

All 40 boards passed these tests and the chamber was put back in place. A second cooling ring was installed, and the heat conduction improved, in order to prevent the front–end electronics from over–heating.

3.3.2 Performance of the new z–vertex trigger

Since the synchrotron radiation background increased with the upgrade the quality of the vacuum in the beam pipe degraded, in particular in the backward region (incoming proton direction) of the

detector. Thus, background from collisions between protons and rest gas nuclei increased. These are observed as hadronic showers coming from the backward direction.

To cope with this higher background rate a dead time free trigger system was developed for the H1 experiment that is able to distinguish between beam background events and true ep interactions. This CIP2k z–vertex trigger recognises particle tracks, calculates a histogram of their origins along the beam axis and derives a trigger decision by evaluating this histogram.

The system has been described in detail in earlier annual reports. It is based on a set of five cylindrical multi–wire proportional chambers (CIP2k) of 2 m length and 40 cm diameter, with a cathode readout granularity of 16 in azimuth angle ϕ and 120 along the beam axis. A total of about 8,500 channels are amplified, digitised and synchronised to the accelerator clock (10.4 MHz) immediately on the detector. The resulting binary data is optically transmitted to the trigger logic in the counting house.

The pipelined H1 trigger system requires a dead time free calculation of the trigger response, which has to be available 2.3 μs after the event occurred. We use large FPGAs (APEX20k400) both for the trigger calculation and for the storage of the complete binary data for later readout by the data acquisition system. Due to their embedded memory these FPGAs are very well suited for the implementation of ring buffers with 32 bunch crossings for pipelined data acquisition storage. The complete trigger and storage functionality for one of the 16 ϕ–sectors fits into two FPGAs. The trigger calculation runs synchronously with the accelerator clock and its latency amounts to 960 ns.
Tests with minimum ionising particles have been performed after the repair efforts in summer 2003 using cosmic ray muons in order to check the performance of the system. To ensure the correct timing of the data in the pipelines the trigger decision derived by the trigger system was compared to the results of a complete software simulation of the trigger system, based on the readout of the corresponding bunch crossing. Furthermore correlations between tracks recognised in the drift chamber of the H1 detector and tracks triggered by the CIP2k system have been studied. The deviation of the vertex position found by the CIP2k trigger from the vertex position reconstructed offline is shown in Fig. 3.2. The position resolution is found to be 16.7 cm in agreement with expectations. The single track efficiency in the trigger is better than 95%..

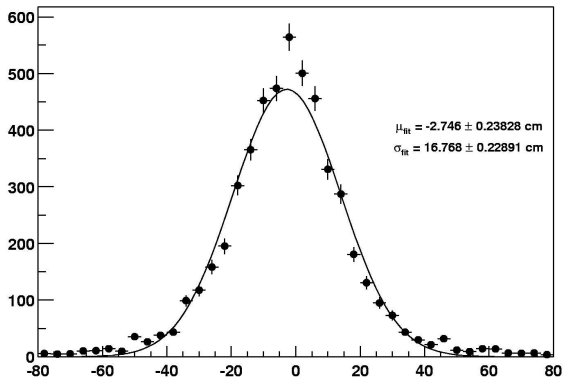

Figure 3.2: *Deviation of the vertex position found by the CIP2k trigger from the vertex position reconstructed offline.*

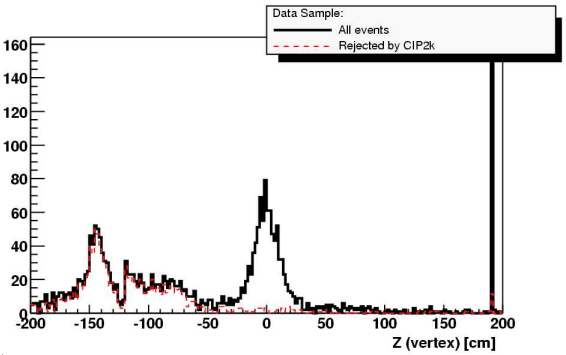

Figure 3.3: *Rejection power of the CIP2k system. Shown is the z–vertex position of all events including the background coming from the backward direction, i.e. negative z values (full line) and the events which are rejected by the CIP2k trigger (dashed line).*

First events taken in ep collisions, provided by HERA–II since October 2003, were used to tune details of the behaviour of the CIP2k trigger. An excellent rejection power against proton beam background of the CIP2k trigger system was established as can be seen in Fig. 3.3. Presently the

CIP2k trigger is routinely used to reject background events and to provide precise timing information in most H1 physics trigger combinations. Further improvements of the performance for triggering selected physics channels are ongoing. This new trigger system was the thesis project of Max Urban who received his Ph.D. recently [43].

3.3.3 Reimplementation of the old z–vertex trigger

In addition to the upgrade of the z–vertex trigger we reimplemented the old readout and z–vertex trigger system parallel to the new system. The new CIP2k trigger fills a z–vertex histogram by a projective geometry of five readout layers at small radii, whereas the old system used the two layers of the two separated chambers CIP and COP (central outer proportional chamber). Due to the roughly 50 cm long lever arm between CIP and COP, the old z–vertex histogram has a better resolution in z compared to the new histogram. Moreover, the longer lever arm allows to cut off very low momentum tracks from the trigger. For instance, heavy flavour triggers use the track multiplicity given by the old z–vertex trigger.

The interesting and rare high p_t (Sec. 3.5.3) and charged current (Sec. 3.6.1) events with an undetectable neutrino in the final state rely on an efficient triggering of missing transverse energy in the detector. This can be improved by the combination of information delivered by the old z–vertex trigger and by the liquid argon calorimeter using *Big Rays* pointing from tracks of charged particles to corresponding areas of the calorimeter. The sensitivity of the calorimeter and therefore the efficiency for triggering on events with small energy deposits is limited by the noise in the calorimeter cells. The coincidence of *Big Rays* pointing to energy depositions in the calorimeter allows to lower the threshold values locally and thus leads to higher trigger efficiencies for events with low tranverse energy. Both, the old z–vertex trigger and the *Big Ray* system, were originally built by our group (theses of S. Eichenberger (1993) and H. P. Beck (1996)).

In order to feed the readout of the old CIP with signals from the CIP2k a hardware interface was realised in 2003. The signals of the innermost two layers of the new CIP2k are de–multiplexed, shaped and logically combined to enter the old receiver cards. After the signals are matched in time with the COP signals the old z–vertex trigger system delivers the trigger elements to the first trigger level as it was before 2001. The system is still being optimised with Linus Lindfeld acting as the person mainly responsible.

3.3.4 Steering of the CIP2k

During the 2003 summer shutdown and the successive test operation period, the slow control software for the CIP2k was implemented in PVSS (Prozess Visualisierungs– und Steuerungs–Software). PVSS is a software package allowing the efficient development of control software for complex technical systems. It features a variety of control features like alarms, data logging, redundancy, automatic reporting and others. The system was chosen by the H1DCM (H1 detector control management) project group as the standard slow control software for H1, it is also foreseen to be used in most LHC projects.

The high voltage control was unified for all tracking detectors by the H1DCM group using PVSS. For all other control tasks of the CIP2k as are the data acquisition system, the trigger, the front–end and the temperature monitoring a PVSS application was developed by Hannes Klehr. About 60 distinct parameters for multiple hardware components are monitored and adjusted. The graphical user interface allows quick access to all parameters. Procedures for standard tasks, e.g. programming the front–end

electronics have been implemented. During the first data taking periods with cosmic ray muons and with electron–proton collisions the user friendly interface helped optimising the parameters quickly for an efficient operation. The interface is documented in a user manual.

3.4 Activities of the Polarimeter group

The Polarimeter group at DESY consists of members of H1, HERMES, ZEUS and DESY. The group is responsible for the operation of the HERA–II electron beam polarimeters (transverse and longitudinal polarimeter, TPOL and LPOL). Stefan Schmitt is acting as the speaker of this group. Apart from coordinating the group activities the main focus of his work in the polarimeter group [46] is the operation of the TPOL and the analysis of the TPOL data. The polarimeters are based on Compton scattering of laser light and the electron beam. The scattered Compton photons are detected in a small calorimeter.

The TPOL is located in the HERA tunnel far from spin rotators, where the lepton polarisation is transverse. It measures the polarisation by detecting the energy and vertical position of single Compton photons at a rate of 50–100 kHz. The laser light is coming from a 10 W cw laser. The calorimeter is divided into two halves to give sensitivity to the spatial coordinate. The lepton polarisation is determined from the asymmetry in the spatial coordinate when comparing the cross section for left– and right–circular polarised laser light.

The LPOL is located in the HERA tunnel near the HERMES experiment, between a pair of spin rotators where the lepton polarisation is longitudinal. The polarimeter measures the polarisation by detecting the mean energy of about 1000 Compton photons, scattered from a single bunch using a high–power pulsed laser with a repetition rate of about 100 Hz. The energy of the photons is averaged because their showers overlap in the same calorimeter. The lepton polarisation is determined by the asymmetry in the mean energy when comparing left– and right–circular polarised laser light.

In the summer shutdown 2003 a Fabry–Perot cavity was installed near the existing LPOL interaction point. It is fed by a 1W cw laser. The power stored inside the cavity can be amplified by a factor of 5000. Using the high photon density inside the cavity, it is possible to produce Compton photons at a rate of 10 MHz (the HERA bunch crossing rate). By recording the energy spectra of these photons the single differential cross section is accessible and the beam polarisation can be measured with ultimate precision. The LPOL cavity is still in the phase of commissioning.

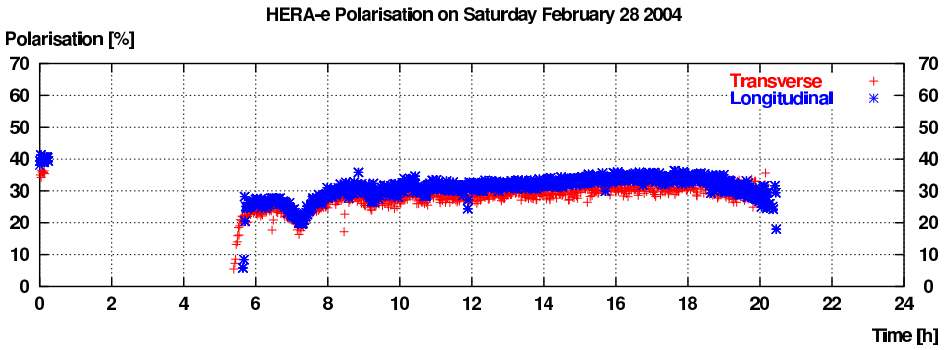

Figure 3.4: *Lepton polarisation measured by LPOL and TPOL during a typical HERA fill.*

During 2003 the two lepton polarimeters were fully operational whenever HERA was running. Figure

3.4 shows the lepton polarisation measured by LPOL and TPOL during a typical HERA fill. Typical polarisation values reached by HERA are up to 40% during luminosity operation. The polarisation is subject to constant tuning by the HERA operators. The expected maximum polarisation with three spin rotators is up to 60%. The main challenge for the Polarimeter group is to get a correct calibration of the absolute scale of both polarimeters.

3.5 Results from recent analyses

3.5.1 Evidence for a new anti–charmed baryon state

We have observed a narrow resonance in the $D^{*-}p$ and $D^{*+}\bar{p}$ invariant mass combinations in the analysis of deep inelastic scattering events ($1 < Q^2 < 100$ GeV^2) recorded between 1996 and 2000 ($\mathcal{L} = 75$ pb^{-1}, 88 % e^+ and 12 % e^-) [11]. The resonance has a mass of $(3099 \pm 3\,(\text{stat.}) \pm 5\,(\text{syst.}))$ MeV and a measured Gaussian width of $(12 \pm 3\,(\text{stat.}))$ MeV, compatible with the experimental resolution. We interprete this new state as an anti–charmed baryon with a minimal constituent quark composition of $uudd\bar{c}$, together with its charge conjugate.

The analysis was motivated by the fact that several experiments have recently reported the observation of a narrow resonance with a mass near 1540 MeV, decaying to K^+n or $K^0_s p$ (see [11] for references). The latter state has both baryon number and strangeness of $B = S = 1$, such that its minimal composition in the constituent quark model is $uudd\bar{s}$ (*pentaquark* Θ^+). Various models have been put forward to explain the nature of these states and the structure of the multiplet that contains them, many of which naturally also call for extensions into the charm sector.

Through the boson–gluon fusion mechanism states with open and hidden charm are produced copiously and the most efficient way to tag them is via the detection of the $D^{*\pm}$ decay chains [47]

$$D^{*-} \to \bar{D}^0\pi^-_s \to K^+\pi^-\pi^-_s,$$
$$D^{*+} \to D^0\pi^+_s \to K^-\pi^+\pi^+_s\,.$$

This signal is easily detectable in the distribution of the mass difference variable $\Delta M_{D^*} = m(K\pi\pi_s) - m(K\pi)$ (see Fig. 3.5). The resonance is observed when combining $D^{*-} \to \bar{D}^0\pi^-_s \to K^+\pi^-\pi^-_s$ candidates with protons and $D^{*+} \to D^0\pi^+_s \to K^-\pi^+\pi^+_s$ candidates with anti–protons (see Fig. 3.6). The resonance is also observed in an

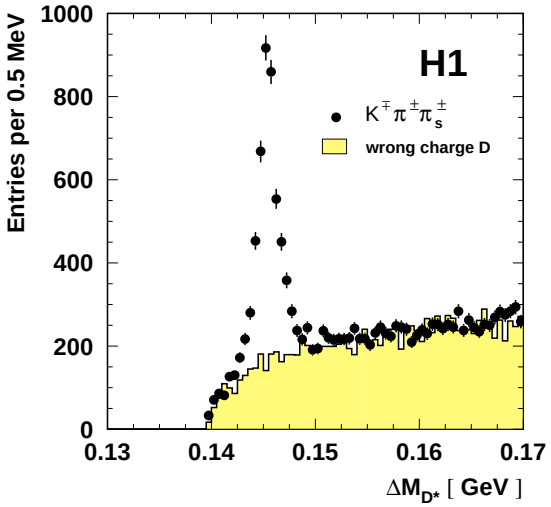

Figure 3.5: *ΔM^*_D mass distribution for $K^{\mp}\pi^{\pm}\pi^{\pm}_s$ combinations. Wrong charge combinations refer to those events where K and π have the same charge and invariant mass near $m(D^0)$.*

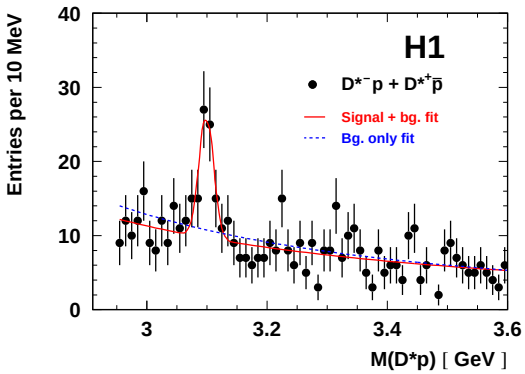

Figure 3.6: *$M(D^*p)$ mass distribution from opposite charge D^*p combinations compared with the results of a fit in which both signal and background components are included (solid line) and with the result of a fit in which only the background is included (dashed line).*

independent photoproduction data sample. The identification of protons and anti–protons is aided by the specific energy loss derived from the mean of the inverse square root of the charge collected by all wires of the central drift chamber showing a signal ($\sigma(dE/dx)/(dE/dx) \approx 8\%$). Approximately half of the events in the narrow peak observed for the opposite–charge combinations at $M(D^*p)$ near 3100 MeV arise from either protons or anti–protons. The distribution for the same–charge combinations $K^-\pi^+\pi_s^+p$ and $K^+\pi^-\pi_s^-\bar{p}$ does not show such a signal.

Fits to the $M(D^*p)$ distribution (opposite charge combinations) have been carried out to evaluate the peak position, width and statistical significance. Assuming the measured width to be dominated by the experimental resolution, a Gaussian distribution is used for the signal, with the peak position, the width and the normalisation as free parameters. The background is parameterised with a power law. The results quoted above are derived from a fit in the range $2950 < M(D^*p) < 3600$ MeV, and are compared with the data in Fig. 3.6. The signal contains 50.6 ± 11.2 events, corresponding to roughly 1 % of the total D^* production rate in the kinematic region studied. The systematic uncertainty on the mass of the peak is 5 MeV, estimated from the reconstructed masses of known states, such as the J/Ψ. The probability that the background distribution fluctuates to at least produce the signal has been evaluated to 4×10^{-8}. To arrive at this result the observed number of events was compared with background estimates for a window spanning $3075 < M(D^*p) < 3123$ MeV, corresponding to $\pm 2\sigma$ around the peak position. The total number of events in this interval is 95. The background contribution estimated using the fit described above is 45.0 ± 2.8 (stat.) events. A consistent number of background events is obtained with a parameterisation using a two–component background model. This model uses wrong charge D ($K^\pm\pi^\pm$) combinations to describe non–charm related background, and Monte Carlo generated events for real D^* background. In our publication several tests are described which concern the particle identification, the possibility for kinematical reflections faking such a signal as well as the consistency of different subsets of the data. The region of $M(D^*p)$ in which the signal is observed contains a richer yield of D^* mesons and exhibits a harder proton candidate momentum distribution than it is the case for side bands in $M(D^*p)$.

3.5.2 Inclusive Beauty production

Muons with a relatively large transverse momentum with respect to the axis of the hadronic jet to which they belong, a distinguishable secondary decay vertex or at least tracks with a large distance of closest approach to the primary vertex in the event are the signatures which are exploited to measure beauty production. The latter technique based on the longer lifetime of the hadrons with open beauty was pioneered in the thesis of J. Kroseberg [49] for the pre–1997 data. Now two analyses are available which extend these methods to the data taken in 1999/2000. The first comprises an integrated luminosity of $\mathcal{L} = 50$ pb^{-1} and contains events with at least one jet with a transverse momentum $p_t^{jet} > 6$ GeV and pseudo–rapidity $|\eta^{jet}| < 2.5$ and a muon associated to this jet with $p_t^\mu > 2.5$ GeV and $-0.75 < \eta^\mu < 1.15$. Differential jet–muon cross sections are evaluated for the first time, namely in the region of photon virtuality $2 < Q^2 < 100$ GeV^2 and inelasticity $0.1 < y < 0.7$. Figures 3.7 and 3.8 illustrate the separation technique and give some of the results. Within the albeit large statistical and systematic

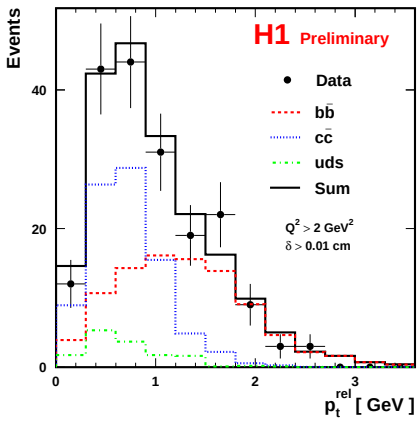

Figure 3.7: *Transverse muon momentum $p_t^{rel,\mu}$ distribution for events with impact parameters $\delta > 100$ μm with the light, charm and beauty quark contributions indicated.*

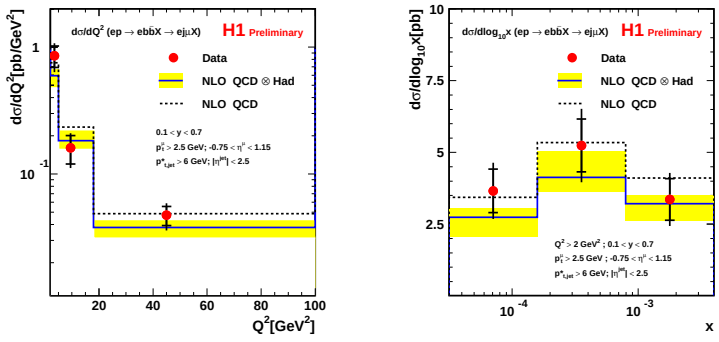

Figure 3.8: *Differential dijet muon production cross sections $d\sigma/dQ^2$ and $d\sigma/dx$ $(ep \rightarrow eb\bar{b}X \rightarrow ej\mu X)$. The inner error bars show the statistical error, the outer include the systematic uncertainty added in quadrature. The results for next–to–leading order perturbative QCD calculation [53] at parton (dashed line) and hadron (solid line) level are also shown.*

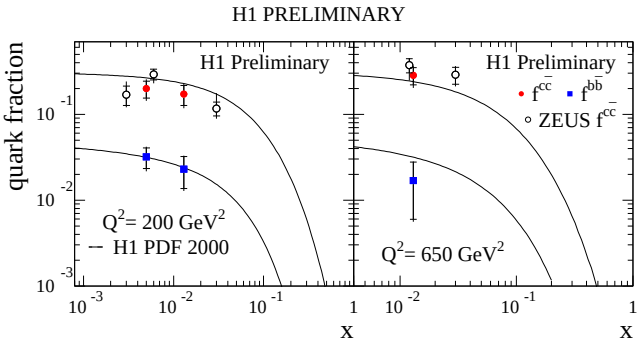

Figure 3.9: *The ratio $f^{c\bar{c}} = F_2^{c\bar{c}}/F_2$ and $f^{b\bar{b}} = F_2^{b\bar{b}}/F_2$ as a function of Bjorken–x for two different values of Q^2. The solid lines represent predictions derived from a next–to–leading order QCD fit to inclusive H1 data [3].*

uncertainties the agreement with next–to–leading order perturbative QCD predictions [53] is satisfactory. The second analysis concentrates on high momentum transfer events $Q^2 > 150$ GeV^2 and inelasticity $0.1 < y < 0.7$ and uses solely the distance of closest approach to the primary vertex reconstructed from tracks observed in the silicon vertex detector to enhance the beauty fraction. Beauty, charm and light quark contributions are separated by fitting the observed distributions to Monte Carlo simulations. The data could be divided into three bins in x and Q^2. The results, expressed as the ratio $f^{c\bar{c}} = F_2^{c\bar{c}}/F_2$ and $f^{b\bar{b}} = F_2^{b\bar{b}}/F_2$ are given in Fig. 3.9. Again the results are in satisfactory agreement with theoretical expectations but also (for charm) with ZEUS results.

3.5.3 High p_t data from HERA II

With the HERA accelerator complex finally reaching its post–upgrade expectation it is gratifying to see the first results arriving from data taken early this year. An analysis based on an integrated luminosity of $\mathcal{L} = 17$ pb^{-1} of high transverse momentum events including isolated leptons, multi–electrons and large missing transverse momentum has been prepared for the spring conferences in 2004 [48]. The analysis makes use of the techniques described in references [1] and [6]. For example ten di–electron and two tri–electron events are observed, compared to the Standard Model expectation of 15.8 ± 1.7 and 3.0 ± 0.4, respectively. Two electron events with missing transverse momentum above 25 GeV are observed while the Standard Model (dominated by real W–boson production) predicts 0.3 events. One of these events is shown in Fig. 3.10.

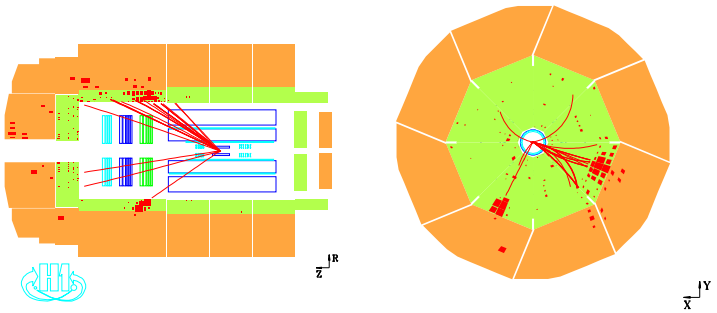

Figure 3.10: *An event with an isolated electron, missing transverse momentum and a prominent hadronic jet observed during the HERA II run 2004.*
The transverse momenta are 37, 44 and 29 GeV/c for the electron, the missing neutrino and the hadronic jet, respectively.

3.6 Progress of Zürich analysis projects

3.6.1 High Q^2 charged current data

In deep–inelastic lepton–proton scattering processes a boson emitted by the lepton interacts with particles inside the proton and causes its dissociation. In the Standard Model of particle physics the interaction can be mediated by four different bosons, namely the electromagnetically interacting photon, γ, and the three weakly interacting bosons, Z_0, and $W^{\pm}$. Two of them, the electrically neutral γ and Z_0, occur in Neutral Current (NC) ep interactions $ep \rightarrow eX$. In NC events the scattered electron and a system of hadrons X form the final state that is observed in the detector. Through the exchange of the charged $W^{\pm}$ boson Charged Current (CC) $ep \rightarrow \nu_e X$ interactions are mediated. The crucial characteristic of CC events is the neutrino, ν_e, in the final state which cannot be detected with the H1 detector. However, the missing transverse momentum can be measured. It is the main observable for the selection of CC events.

An important feature of CC interactions is that they are of weak nature exclusively. The charge of the W boson as well as its sensitivity to the parton helicities make CC interactions particularly well suited to study parton distributions and weak interactions within the Standard Model. The u– and d–quark densities are directly accessible in $e^- p \rightarrow \nu_e X$ and $e^+ p \rightarrow \bar{\nu}_e X$ scattering, respectively. The longitudinally polarised lepton beam which is now available for HERA–II (see Sec. 3.4) provides a new opportunity to test the weak sector of the Standard Model. In CC interactions a positively polarised incoming positron results in a right handed antineutrino. Due to angular momentum conservation the negatively polarised positrons would have to result in left handed anti–neutrinos which do not exist in the Standard Model. Thus, the CC cross section is expected to vanish for negatively polarised positrons. Cross section measurements with longitudinally polarised positrons in combination with the measurement without polarisation could demonstrate the expected linear dependence on polarisation. A measured significant discrepancy from this prediction would be a sign for new physics beyond the Standard Model.

During the upgrade phase for HERA–II a new H1 software environment H1OO based on object oriented programming in C^{++} was designed and implemented. The main goal of this sophisticated change from already established FORTRAN software tools to new software is to provide a modern and extendable framework with standardised physics algorithms that can be incorporated and supported by all H1 physics analyses. The new charged current measurement presented in the recent thesis [44] of Nicole Werner uses this new framework. Another significant change with respect to former measurements is that it is based on reprocessed data, i.e. data with improved track and vertex reconstruction. Figure 3.11 shows the measurement of the single differential charged current

cross section as function of the four momentum transfer squared Q^2. The results are compared to the Standard Model prediction and to the published H1 measurement [3] using the same data sample of 1999/2000 data, corresponding to an integrated luminosity of 65.25 pb^{-1}. The results of both measurements are found to be in good agreement. Due to improvements of the vertex reconstruction and a better simulation of the parton distributions the new result seems to be better described by the Standard Model prediction.
The comparison with the earlier measurement based on the old FORTRAN environment is a vital cross check of whether both analysis frameworks are consistent with each other. Moreover, the development of the programming code for the new measurement was a crucial preparation for the measurement of the charged current cross section with longitudinally polarised leptons. First results of the cross section measurement based on 15.3 pb^{-1} of new HERA–II data with positively polarised positrons are shown in Fig. 3.12 [54]. Despite of its limited statistics the result is in good agreement with the Standard Model prediction. A measurement for negatively polarised positrons is ongoing.

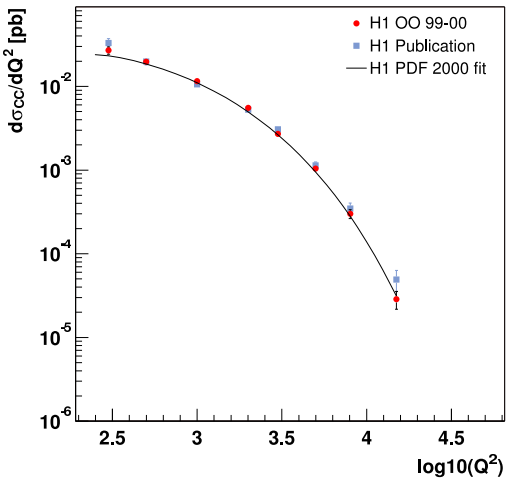

Figure 3.11: *The CC cross section as a function of Q^2. The new measurement based on the new object oriented programming framework (circles) is compared to the H1 publication based on the FORTRAN framework (squares) and to the Standard Model prediction.*

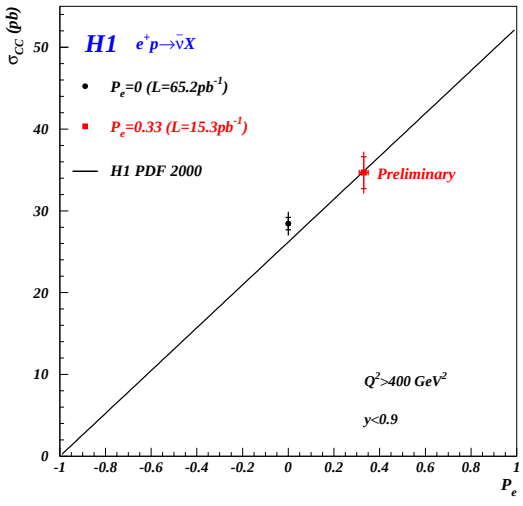

Figure 3.12: *The total CC cross section as a function of longitudinal positron polarisation. Shown are the HERA–I data point without polarisation, the new HERA–II data point measured with positively polarised positrons and the linear curve of the Standard Model prediction.*

3.6.2 Isolated high–p_T τ leptons

Considerable progress has been made this last year in the analysis of isolated, high–p_T τ leptons in events with missing transverse momentum.
Recently Stefania Xella, together with colleagues prepared the first preliminary results for the spring conferences [55]. This analysis is the first H1 analysis on τ leptons and it is a very important parallel result to the previous H1 publications on electron and muon final states where an excess with respect to the total Standard Model expectation was observed at high transverse momentum of the event p_X^T (defined as the total transverse momentum of the event excluding the transverse momentum of the τ candidate).

The current results, for time reasons, are based on a simple τ identification algorithm, exploiting only

one of the various variables which characterise τ jets, namely the jet radius or energy weighted radius of all cells in the τ jet candidate. The final τ identification procedure (to be used for publication later on in the year) will be most probably based on a multi–variable analysis, exploiting fully the different shapes of τ and QCD (background) jets, both longitudinally and transversely, and will provide a better signal over background ratio.

At the current stage of the analysis, H1 does not see any significant excess of data with respect to the Standard Model expectation in the isolated, high–p_T τ lepton analysis, in contrast to what has been seen in the electron and muon channel and in the ZEUS analysis with τ leptons. No events are selected on the 110 pb^{-1} data sample in the region of $p_X^T > 25$ GeV with an expectation of 0.53 events from Standard Model processes. The distribution for the whole p_X^T range is shown in Fig. 3.13 where the number of data selected by all cuts is 5 for a Standard Model expectation of 5.81. In the figure the anomalous top production is also shown scaled to an arbitrary number in order to clearly indicate the region in p_X^T where it would be. Anomalous top production has been considered as one of the possible explanations for the excess at high p_X^T observed in the electron and muon channel. Statistical and systematic errors are currently being investigated, but conservatively should range between 20–30%. This means that the total number of events observed is less than a sigma away from the expectation.

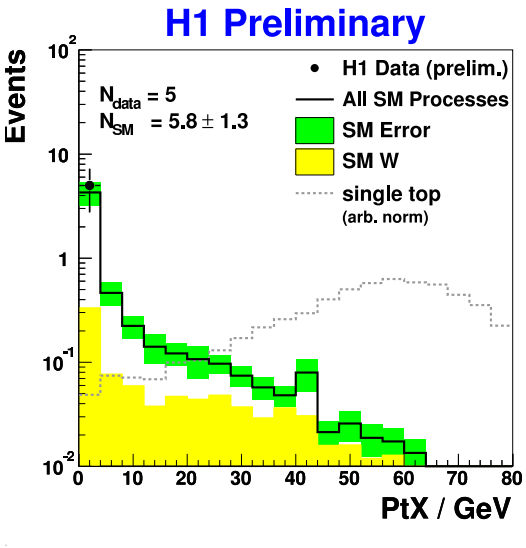

Figure 3.13: *p_X^T of the events selected by the isolated high–p_T τ analysis. In grey is the expected distribution for anomalous top production process, considered as one of the possible interpretations for the excess observed in the electron and muon channel (histogram for top production is scaled to an arbitrary number)*

3.6.3 Prompt photon production

High energy ep collisions at HERA are dominated by electron scattering at small angles with a quasi real photon interacting with the proton (γp collisions). These interactions can also lead to the emission of photons - so called prompt photons - from the hard QCD process, which makes them sensitive both to the partonic structure of the proton and the photon. Though the cross section is very low, this measurement has the advantage that no corrections due to hadronisation or fragmentation processes are necessary.

The prompt photon analysis uses the full integrated luminosity of 133 pb^{-1} from the years 96–00. Prompt photons are identified in the H1 liquid argon calorimeter (LAR) by a compact electromagnetic cluster with transverse energy 5 GeV$< E_T^\gamma <$ 10 GeV in the pseudo–rapidity region $-1 < \eta^\gamma < 0.9$. No track is allowed to point to the candidate. The main experimental difficulty is the separation from hadronic background. The signal from neutral mesons (π^0 or η^0) at high energies is very similar to the signal of a photon since the decay photons cannot be resolved in the calorimeter. The neutral mesons are predominantly produced in jets. Therefore an isolation requirement is applied to the photon

candidate: The transverse energy in a cone of radius one in the (η, ϕ)–plane around the candidate has to be less than $0.1 \cdot E_T^\gamma$. This cut reduces also higher order processes such as events with a photon radiated off the outgoing quark. Events with an identified electron are removed. Furthermore a cut on the inelasticity $y = 1 - E'_e/E_e$ is applied to remove background from DIS events with a badly measured scattered electron. The range of y ($0.2 < y < 0.7$) corresponds to a $\gamma - p$ centre of mass energy of $142 < W < 266$ GeV.

After all selection cuts the background is still of the same size as the signal. The signal is extracted by a detailed analysis of the shower shape.

The results on the inclusive measurement of the prompt photon cross section as a function of transverse energy and pseudo–rapidity were shown at EPS03 [15; 19]. The measurement was now extended to events with an isolated photon and a hadronic jet in the kinematical range $E_T^{jet} > 4.5$ GeV, $-1 < \eta^{jet} < 2.3$. The shape of the inclusive cross section as a function of E_T^γ and η^γ is well described by LO PYTHIA simulation but the MC normalisation is 30% low. The NLO–QCD calculation describes the data well with a tendency to overshoot the data at large η^γ. Cross sections for a prompt photon and a jet are shown in Fig. 3.14 as a function of $E_T^\gamma, \eta^\gamma, E_T^{Jet}, \eta^{Jet}, x_\gamma$ and x_p, the energy fraction, pseudo–rapidity and Bjorken–x of the parton in the proton and the photon, respectively.

The results can be compared with the PYTHIA Monte Carlo and a NLO–QCD calculation. The NLO corrections are significant at low x_p and low x_γ, thus affecting mainly the resolved photon. Multiple interactions are accounted for in NLO calculations by corrections as expected by PYTHIA simulations. The data are well described by the NLO calculation. The results are currently being finalised for publication.

The measurement will be extended into the region of high E_T photons and high η^γ (forward region). At high E_T^γ the photon signal in the calorimeter is hardly distinguishable from the neutral mesons. Therefore the background rejection entirely relies on simulations. This as well as the extension in the forward region requires additional studies on the detector description in the simulation.

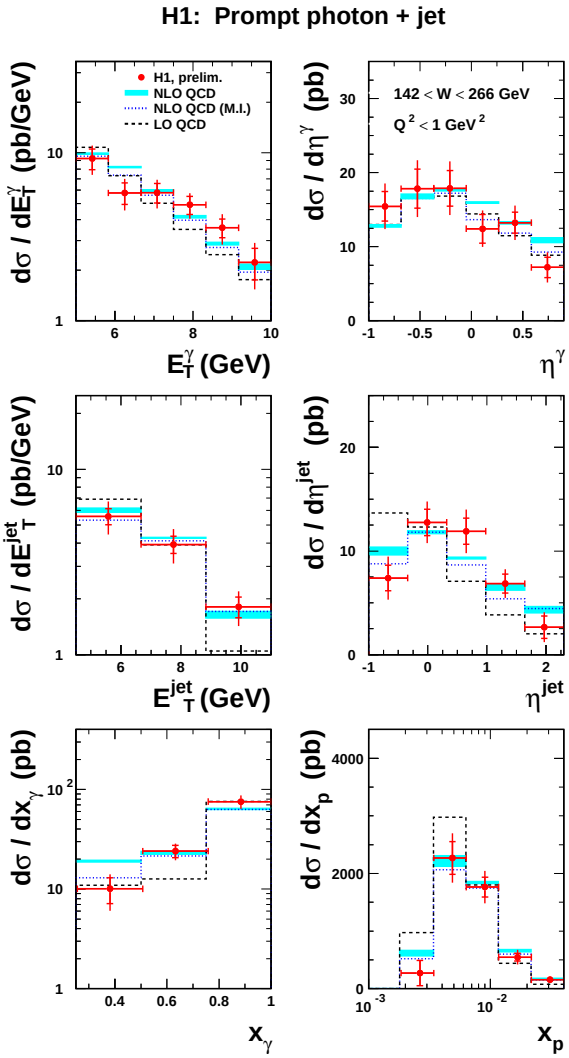

Figure 3.14: *Cross section for prompt photon events with an additional jet as a function of E_T^γ, η^γ, E_T^{Jet}, η^{Jet}, x_γ and x_p. The result is compared to LO Monte Carlo (dashed) and NLO(full) calculation. The dotted line shows the NLO calculation corrected for multiple interactions as determined with PYTHIA simulation.*

A new analysis has started (PhD Thesis Carsten Schmitz) which measures the photon content of jets. The goal is to identify photons inside a hadron jet and measure the photonic energy fraction of the jet. This allows to determine the quark–to–photon fragmentation which is not yet measured in the

kinematic regime of HERA and cannot be estimated by QCD calculations due to its non–perturbative component. The result will be needed for the simulation of physics processes at LHC. The analysis is very challenging because of the photon identification which is hampered by the hadronic environment in the jet and by misidentification of neutral mesons.

3.6.4 QED Compton Scattering

QED Compton events are ep scattering events with a hard photon radiated off the scattered electron. The 4–momentum transfer (Q^2) is very low, hence these events probe the region of very low Q^2 where perturbative QCD models are not valid anymore and phenomenological models have to be tested.

The aim of the analysis is to measure the differential cross section of the QED Compton process. This can be used to determine the structure function F_2 at low Q^2, the transition region between deep–inelastic scattering and real photoproduction, which was so far not accessible with HERA data.

A further motivation is an experimental test of the so called collinear approximation. It is used by several authors to calculate the QED Compton cross section. The approach neglects the transverse momentum of the exchanged photon and treats the photon as a parton of the proton with a structure function describing the photon–parton content of the proton.

- *Event signature:*
  Both the outgoing lepton and the photon are detected in the backward region (wrt the p–beam direction) of the H1 detector almost back–to–back in azimuth. The main difficulty of the analysis is the lepton–photon identification. Roughly 50% of the photons convert before they reach the backward calorimeter (Spacal) and the backward drift chamber (BDC) because all the readout cables and most of the readout electronics of the central tracking chambers are situated in the backward area. The identification of photons and positrons therefore relies on central tracking chambers, namely on the backward silicon detector (BST) in the inner region of the Spacal and the central inner proportional chamber (CIP) in the outer region. The hadronic final state is boosted in the forward direction and can only be measured for inelastic events, which implies that there is no well determined event vertex for most of the events. Therefore a vertex reconstruction using the signals of the scattered lepton in the BST, CIP and BST was used for all events. The analysis is based on a data sample recorded in 1997 with a luminosity of roughly 9 pb^{-1}.

- *Background:*
  Several classes of events can mimic QEDC events, their influence on the cross section measurement was studied. Electron–positron pair production, which is one of the dominant background sources is suppressed by a cut on the total energy in the Spacal and the photon–lepton identification. Photoproduction events with the scattered lepton escaping through the beam–pipe can mimic a QEDC event if several hadronic particles point into the backward region. One of the most significant contributions after the analysis cuts are DIS events with a backward going hadron (typically a π^0) faking a photon. These events were suppressed by a cut on the angular distribution of the hadrons. Deeply virtual Compton scattering, a diffractive process, has the same final state particles as QED Compton scattering and cannot be separated. Its contribution is subtracted, using MC events.

  MC studies showed that the background is well suppressed by the cuts on the total Spacal energy and a maximum angle of clusters in the liquid argon calorimeter. The remaining contribution is estimated by MC studies.

The measurement on the structure function determined with QEDC events was shown at the 2003 conferences [15; 18]. The measurement gives access to the kinematic range down to $Q^2 = 0.1\ GeV^2$ (Fig. 3.15) which was not covered by inclusive measurements at HERA. It is in good agreement with fixed target data.
Nicolas Keller has contributed in his thesis work to this QEDC analysis and recently received his Ph.D. [45].

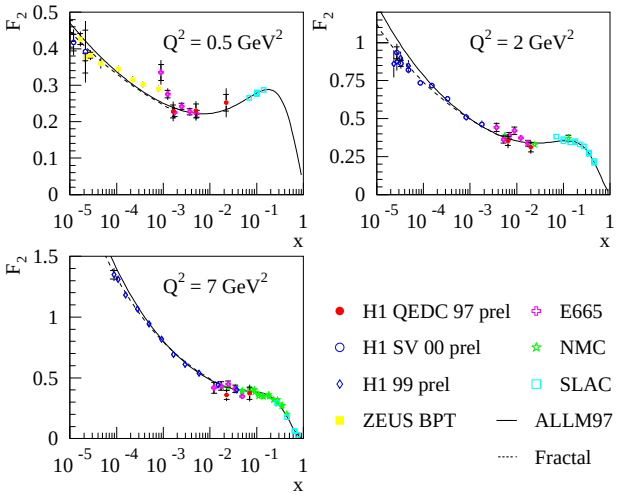

Figure 3.15: *Structure function F_2 as measured with QEDC events for two different Q^2 regions.*

[1] *Isolated Electrons and Muons in Events with Missing Transverse Momentum at HERA*, H1-Coll., V. Andreev *et al.*, DESY 02 – 224, hep-ex/0301030, Phys.Lett.**B561** (2003), 241 - 257.

[2] *Measurement of Inclusive Jet Cross Sections in Photoproduction at HERA*, H1-Coll., C. Adloff *et al.*, DESY 02 – 225, hep-ex/0302034, Eur.Phys.J.**C29** (2003), 497 - 513.

[3] *Measurement and QCD Analysis of Neutral and Charged Current Cross Sections at HERA*, H1-Coll., C. Adloff *et al.*, DESY 03 – 038, hep-ex/0304003, Eur.Phys.J.**C30** (2003), 1 - 32.

[4] *Search for New Physics in $e^{\pm}q$ Contact Interactions*, H1-Coll., C. Adloff *et al.*, DESY 03 – 052, hep-ex/0305015, Phys.Lett.**B568** (2003), 35 - 47.

[5] *Diffractive Photoproduction of J/Ψ Mesons with Large Momentum Transfer at HERA*, H1-Coll., A. Aktas *et al.*, DESY 03 – 061, hep-ex/0306013, Phys.Lett.**B568** (2003), 205 - 218.

[6] *Multi-electron Production at High Transverse Momentum in ep Collisions at HERA*, H1-Coll., A. Aktas *et al.*, DESY 03 – 082, hep-ex/0307015, Eur.Phys.J.**C31** (2003), 17 - 29.

[7] *Search for Single Top Quark Production in $e^{\pm}p$ Collisions at HERA*, H1-Coll., A. Aktas *et al.*, DESY 03 – 132, hep-ex/0310032, Eur.Phys.J.**C33** (2004), 9 - 22.

[8] *Muon Pair Production in ep Collisions at HERA*, H1-Coll., C. Aktas *et al.*, DESY 03 – 159, hep-ex/0311015, Phys.Lett.**B583** (2004), 28 - 40.

[9] *Inclusive Dijet Production at Low Bjorken-x in Deep Inelastic Scattering*, H1-Coll., A. Aktas *et al.*, DESY 03 – 160, hep-ex/0310019, Eur.Phys.J.**C33** (2004), 477 - 493.

[10] *Measurement of Dijet Production at Low Q^2 at HERA*, H1-Coll., A. Aktas *et al.*, DESY 03 – 206, hep-ex/0401010, Eur.Phys.J.**C** (2004), in print.

[11] *Observation of a Narrow Anti-Charmed Baryon State*, H1-Coll., A. Aktas *et al.*, DESY 04 – 038, hep-ex/0403017, Phys.Lett.**B588** (2004), 17.

[12] *Search for Squark Production in R-Parity Violating Supersymmetry at HERA*, H1-Coll., A. Aktas *et al.*, DESY 04 – 025, hep-ex/0403027, Eur.Phys.J.**C** (2004), in print.

[13] *Measurement of Anti-Deuteron Photoproduction and a Search for Heavy Stable Charged Particles in at HERA*, H1-Coll., A. Aktas *et al.*, DESY 04 – 032, hep-ex/0403056, Eur.Phys.J.**C** (2004), in print.

[14] *Forward π^0 Production and Associated Transverse Energy Flow in Deep-Inelastic Scattering at HERA*,
H1-Coll., A. Aktas *et al.*, DESY 04 – 051, hep-ex/0404009, Eur.Phys.J.**C** (2004), in print.

[15] Contributed papers to Int. Europhysics Conf. on High Energy Physics (EPS03), Aachen, Germany (July 2003), and Int. Conf. on Lepton-Photon Interactions (LP03), Fermilab, Chicago, USA (August 2003). Only those papers are listed, which have not yet been submitted to journals; H1-Coll., unless otherwise noted.

[16] *Measurement of the Deep Inelastic Scattering Cross Section at $Q^2 \approx 1$ GeV^2 with the H1 Experiment* (EPS0082, LP165), [15].

[17] *Determination of F_L at Low Q^2* (EPS0083, LP166), [15].

[18] *F_2-measurements at Very Low Q^2 using QED-Compton Events* (EPS0084, LP167), [15].

[19] *Measurement of Prompt Photon Production in γp Interactions* (EPS0093, LP176), [15].

[20] *D^*-μ Correlations in ep Scattering at HERA* (EPS0095, LP177), [15].

[21] *Inclusive D-meson Production in Deep Inelastic Scattering at HERA* (EPS0096, LP178), [15].

[22] *Photoproduction of D^* Mesons at HERA* (EPS0097, LP179), [15].

[23] *D^* Mesons and Associated Jet Production in Deep Inelastic Scattering* (EPS0098, LP180), [15].

[24] *Forward Jet Production at HERA* (EPS0109, LP189), [15].

[25] *Two-Jet and Three-Jet Differential Event Shapes in Deep Inelastic Scattering* (EPS0111, LP191), [15].

[26] *Measurements of Beauty Production using Semi-muonic Decays* (EPS0117, LP194), [15].

[27] *Diffractive Photoproduction of Jets at HERA* (EPS0087, LP170), [15].

[28] *Measurement of the Diffractive DIS Cross Section at low Q^2* (EPS0088, LP171), [15].

[29] *Measurement and NLO DGLAP QCD Interpretation of Diffractive Deep Inelastic Scattering at HERA* (EPS0089, LP172), [15].

[30] *Measurement of the Inclusive Diffractive Cross Section $\sigma_r^D(3)$ at high Q^2* (EPS0090, LP173), [15].

[31] *Diffractive Dissociation in Photoproduction at HERA* (EPS0091, LP174), [15].

[32] *Elastic Electroproduction of ρ-mesons at High Q^2* (EPS0092, LP175), [15].

[33] *Inclusive ρ, $f_0(980)$, $f_2(1270)$, and η Photoproduction* (EPS0107, LP187), [15].

[34] *Elastic Photoproduction of J/ψ Mesons* (EPS0108, LP188), [15].

[35] *Diffractive Photoproduction of High p_t Photons at HERA* (EPS0110, LP190), [15].

[36] *Comparison at NLO between Diffractive Final State Observables and Predictions from Fits to F_2^D* (EPS0113, LP192), [15].

[37] *Deeply Virtual Compton Scattering Cross Section Measurement at Medium and Small Photon Virtualities* (EPS0115, LP193), [15].

[38] *Search for Doubly Charged Higgs Production at HERA* (EPS0104, LP184), [15].

[39] *A Search for Leptoquarks at HERA* (EPS0105, LP185), [15].

[40] *A Search for Magnetic Monopoles at HERA* (EPS0106, LP186), [15].

[41] *General Search for New Phenomena at HERA* (EPS0118, LP195), [15].

[42] *Search for Superlight Gravitinos at HERA* (LP196), [15].

[43] *A New z–Vertex Trigger for H1*, Max Urban, PhD Thesis, University of Zürich (2004).

[44] *Measurement of the Charged Current Cross Section in Positron–Proton Scattering at HERA*, Nicole Werner, PhD Thesis, University of Zürich (2004).

[45] *A Measurement of the QED Compton Cross Section in Electron-Proton Scattering with the H1*

Experiment at HERA,
N. Keller, PhD Thesis, University of Zürich (2003).

[46] *A New Analysis for the Transverse Polarimeter at HERA II*,
T. Behnke, J. Böhme, B. List, and S. Schmitt (EPS0120), [15].

[47] S. Aid *et al.*, H1-Coll., Nucl. Phys. **B472** (1996), 32; C. Adloff *et al.*, H1-Coll., Nucl. Phys. **B545** (1999), 21; C. Adloff *et al.*, H1-Coll., Phys.Lett.**B528** (2002), 199.

[48] *High P_T analysis of HERA II data*, H1-report H1prelim-04-063, see [52] .

[49] *A Measurement of Beauty Production in High-Energy Positron-Proton Scattering*,
J. Kroseberg, PhD thesis, University of Zürich (2003).

[50] *Measurement of Beauty Production in Deep Inelastic scattering at HERA*,
H1-report H1prelim-04-071, see [52].

[51] *Measurement of $F_2^{c\bar{c}}$ and $F_2^{b\bar{b}}$ at High Q^2*,
H1-report H1prelim-04-072, see [52].

[52] available at http://www-h1.desy.de/publications/H1preliminary.short_list.html.

[53] B.W. Harris, and J. Smith, Nucl. Phys. **B452** (1995), 109.

[54] *Measurement of Polarised Charged Current Total Cross Section at HERA II*,
H1-report H1prelim-04-041, see [52].

[55] *Search for Events with τ-leptons in ep Collisions at HERA*,
H1-report H1prelim-04-061, see [52].

4 High-precision CP-violation Physics at LHCb

R.Bernet, R.P.Bernhard, Y.Ermoline, J.Gassner, St.Heule, F.Lehner, C.Lois, M.Needham, M.Siegler, P.Sievers, O.Steinkamp, U.Straumann, A.Vollhardt, D.Volyanskyy

in collaboration with:
the silicon tracking group of LHCb: University of Lausanne; Max Planck Institute, Heidelberg, Germany; University of Santiago de Compostela, Spain; Budker Institute for Nuclear Physics (INP), Novosibirsk, Russia and Ukrainian Academy of Sciences, Kiev, Ukraine.

The full LHCb collaboration consists of 51 institutes from Brazil, China, Finland, France, Germany, Italy, The Netherlands, Poland, Romania, Russia, Spain, Switzerland, Ukraine, and the United Kingdom.

(LHCb)

The main goal of the LHCb experiment is to perform systematic measurements of CP violating processes and rare decays in the B meson systems, with unprecedented precision. Measuring CP violation in many different decay modes of B_d^0 and B_s^0 mesons and comparing the results with predictions from the Standard Model of particle physics, the experiment will also search for new physics beyond the Standard Model. Our group concentrates on the development, construction, operation and data analysis of the LHCb Silicon Tracker as well as on physics analyses.

4.1 The LHCb experiment

The LHCb experiment [1] has been designed to exploit the large $b\bar{b}$ production cross section at the Large Hadron Collider (LHC) at CERN in order to perform a wide range of precision studies of CP violating phenomena and rare decays in the B meson systems. The experiment will use a moderate luminosity of $2 - 5 \times 10^{32}\text{cm}^{-2}\text{s}^{-1}$ and will be fully operational at the startup of the LHC, which is foreseen for 2007.

In particular, the copious production of B_s^0 mesons, combined with the unique particle-identification capabilities of the LHCb detector, will permit the experiment to perform sensitive measurements of CP violating asymmetries in a variety of decay channels that are beyond the reach of the current generation of CP-violation experiments.

Since the production of b quarks in proton-proton collisions at LHC is strongly peaked towards small polar angles with respect to the beam axis, the LHCb detector is layed out as a single-arm forward spectrometer. Its acceptance extends out to 300 mrad in the horizontal bending plane of the 4 Tm dipole magnet and to 250 mrad in the vertical plane. The forward acceptance of the experiment is limited by the LHC beam pipe that passes through the detector and follows a 10 mrad cone pointing back to the p-p interaction region.

In 2002, the LHCb collaboration decided to revise the layout of the LHCb detector in general, and of the tracking system in particular. The goal of this revision was to further improve the physics potential of the experiment by reducing the material budget of the detector and by improving the performance of the Level-1 trigger. A large part of the year 2003 was dedicated to studying the physics potential of the revised detector and to working out the technical design of the revised detector components. The results of these efforts are summarised in the so-called "LHCb re-optimised detector Technical

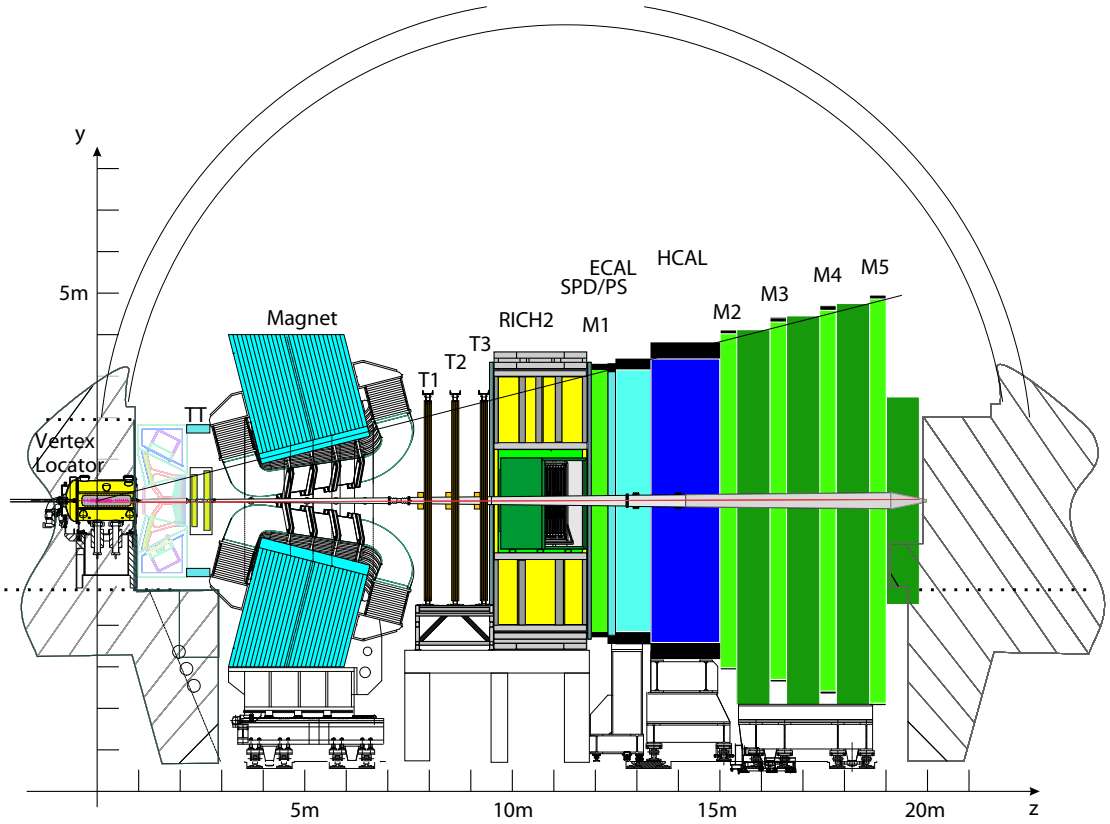

Figure 4.1: *Vertical cross section through the revised LHCb detector.*

Design Report" [2] that was submitted to the CERN LHCC committee in September 2003. It was well received by the committee and has been recommended for approval.

A vertical cut through the revised LHCb detector is shown in Fig. 4.1. The tracking system consists of four planar tracking stations (TT and T1-T3), complemented by the Vertex Detector (VELO) that surrounds the p-p interaction region.

4.2 Silicon tracker

Our group has taken a leading rôle in the development, production and operation of the Silicon Tracker. The Silicon Tracker project is led by U. Straumann and O. Steinkamp (deputy). It consists of two detectors that both employ silicon microstrip technology but differ in important details of the technical design: The Inner Tracker covers the innermost region around the beam-pipe in the three large tracking stations T1-T3 downstream of the spectrometer magnet; the Trigger Tracker (TT) is located upstream of the spectrometer magnet and covers the full acceptance of the experiment.

The technical design of the Inner Tracker is described in the Inner Tracker Technical Design Report [3]. After the submission of the Inner Tracker TDR in November 2002, a large fraction of our efforts over the year 2003 was taken up by design work and R&D for the TT station. The resulting technical design of the TT station is described in Chapter 5, written by O. Steinkamp, of the "LHCb re-optimised detector TDR" [2] and in a subsequent technical note [4]. Furthermore, our group is responsible for the development of the optical digital readout link for Inner Tracker and TT station.

A full prototype link using final components has been set up and tested in the laboratory. Several irradiation tests of critical components have been carried out during the last year.

4.3 TT station

The Trigger Tracker (TT station) fulfills a two-fold purpose: First, it will be used in the Level-1 trigger to assign transverse-momentum information to large-impact parameter tracks. Secondly, it will be used in the offline analysis to reconstruct the trajectories of low-momentum particles that are bent out of the acceptance of the experiment before reaching tracking stations T1-T3.

The TT station consists of four detection layers. Its active area is approximately 160 cm wide and 130 cm high and will be covered entirely by silicon micro-strip detectors. The layout of a detection layer is illustrated in Fig. 4.2. The areas above and below the beam pipe are each covered by a single seven-sensor long silicon ladder, the areas to the left and to the right of the beam pipe are covered by seven or eight staggered 14-sensor long ladders. Electronically, each ladder is split into several readout sectors, indicated by different shadings in Fig. 4.2. All readout electronics and associated mechanics are located at the top end or the bottom end of a ladder, outside of the acceptance of the experiment. The inner readout sectors are connected to their readout electronics via approximately 39 cm long Kapton interconnect cables. An isometric drawing of the basic detector unit, consisting of seven silicon sensors, a Kapton interconnect, and two staggered front-end readout hybrids, is shown in Fig. 4.3. The 14-sensor long ladders that cover the areas to the left and to the right of the beam pipe are assembled from two such detector units that are joined together at their ends. A readout strip pitch of 183 μm will be employed everywhere. In simulation studies, M. Needham has demonstrated that this layout provides adequate spatial resolution and acceptably low detector occupancies. For four detection layers, the TT station employs 896 silicon sensors, arranged in 128 modules and 256 readout sectors. It covers a total sensitive area of approximately 8 m^2 and counts 131k readout channels.

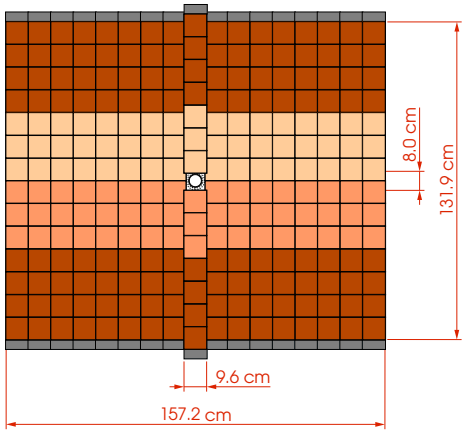

Figure 4.2: *Layout of one detection layer of the TT station. Readout sectors are indicated by different shading.*

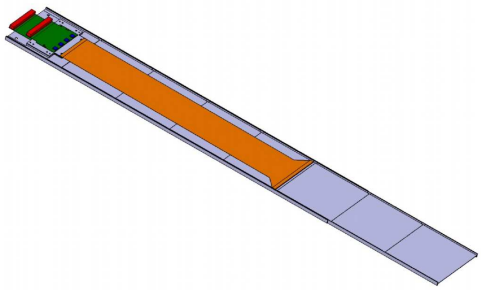

Figure 4.3: *Drawing of a silicon module, consisting of seven silicon sensors, a Kapton interconnect cable and two staggered readout hybrids attached at one end of the module.*

A substantial R&D effort has been carried out in our group in order to validate this layout and develop the mechanical design of the long detector modules and of the station frames.

Key issues in our R&D effort have been the optimisation of silicon sensors and the design of the interconnect cables. The long readout strips and interconnect cables employed in the TT station result in expected load capacitances of up to 55 pF at the input of the front-end readout amplifier. In order to maintain sufficiently high signal-to-noise ratios for full particle detection efficiency, thicker sensors have to be used for the TT station than for the shorter ladders of the Inner Tracker. Several proto-

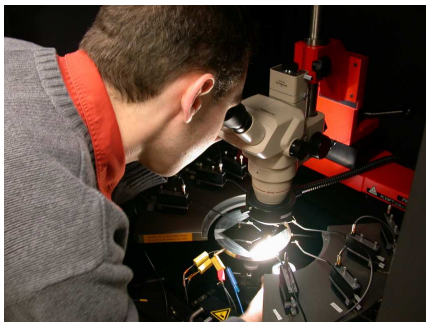

Figure 4.4:
Manual probe-station.

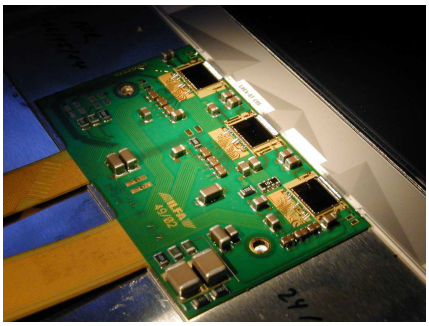

Figure 4.5: *Readout hybrid with Beetle 1.2 chips.*

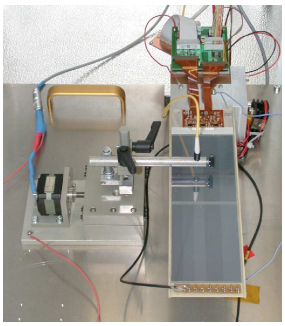

Figure 4.6:
Laser test stand.

type ladders were constructed from 320 μm, 410 μm and 500 μm thick silicon sensors. Before being assembled into ladders, all sensors were characterised by C.Lois, using manual (see Fig. 4.4) and automatic probe-stations in our laboratory [5]. Each prototype ladder consisted of three silicon sensors bonded in series, for a total readout strip length of approximately 30 cm. All ladders were equipped with a prototype version of the LHCb front-end readout chip, called Beetle 1.2. A photograph of a front-end readout hybrid carrying three Beetle 1.2 chips and bonded to one of the prototype ladders is shown in Fig. 4.5.

Initial tests on the prototype ladders were performed in an infra-red laser test stand [6] that has been set up in our laboratory by P.Bernhard, St.Heule and A.Vollhardt. A photograph of the setup is shown in Fig. 4.6. It employs a focussed 1064 nm laser beam to generate charges at well-defined locations in the silicon bulk and permitted systematic studies of signal pulse shapes as a function of various operation parameters of the detector and of the location of the charge deposition. A detailed description of the setup and the results obtained in the laser tests is given in [6].

Further measurements were then performed at the X7 test-beam facility at CERN, in collaboration with our colleagues from Lausanne and Heidelberg. The analysis of the collected data was coordinated by M.Needham. A detailed description of the test-beam setup and the obtained results is given in [7]. As shown in Fig. 4.7, for all prototype ladders a significant drop of the charge collection efficiency was observed in the central region in between two readout strips. The effect was observed both in the laser setup and in the test-beam and confirmed an earlier result from measurements on Inner Tracker prototype ladders [3]. It was also reproduced in a detector simulation developed by St.Heule as part of his Diploma thesis in our group [8]. It is mainly attributed to a loss of charge carriers at the

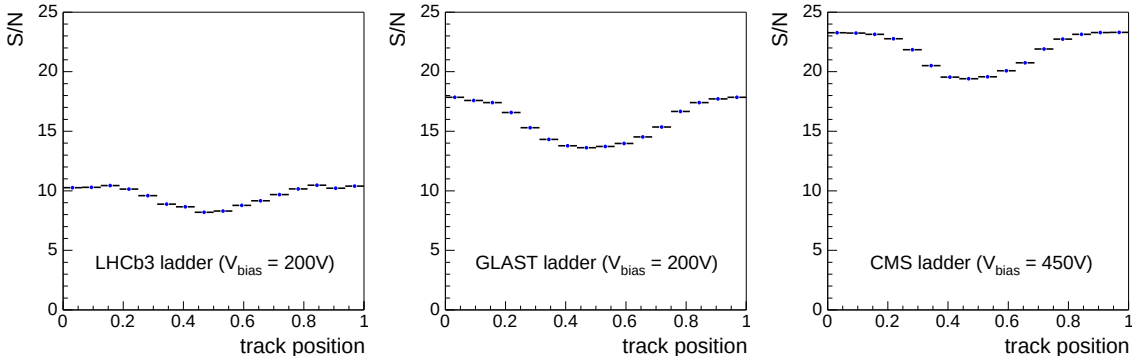

Figure 4.7: *Most probable signal-to-noise ratios as a function of the relative interstrip position of the charge deposition.*

boundary between the silicon bulk and the silicon oxide layer in between the two readout strips.
For the ladder built from 320 μm thick silicon sensors, this charge loss led to a significant loss of particle detection efficiency in the central region in between two strips. For the ladders using 410 μm and 500 μm thick silicon sensors a particle detection efficiency in access of 99.8% was maintained over the full interstrip gap. Readout strips in the TT station will be slightly longer than those on the prototype ladders and in order to ensure a robust operation of the detector it was decided to employ 500 μm thick silicon sensors for the TT station.
Low-mass interconnect cables of approximately 39 cm in length will be employed in order to connect the inner readout sectors on a ladder to their front-end readout hybrid. The design of these cables is the resonsibility of J.Gassner. Several prototype cables were developed in collaboration with the company Dyconex, Bassersdorf, and characterised in our laboratory. A prototype ladder has then been constructed consisting of three 500 μm thick silicon sensors, a 39 cm long interconnect cable and a readout hybrid carrying three Beetle 1.2 chips. Laboratory measurements on this prototype ladder, using the infra-red laser setup, are ongoing and show promising results. Further tests on this prototype ladder will be performed in a test-beam at CERN later this year.

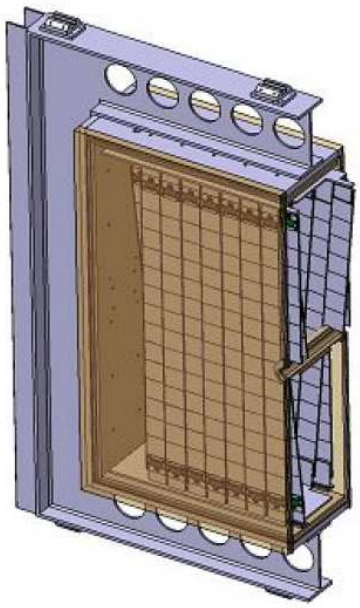

Figure 4.8: *Isometric drawing of one half of the TT station.*

The mechanical design of the silicon ladders for the TT station and of the station frames is advancing well, in close collaboration with the engineers and the mechanical workshop at the Physik-Institut. An isometric drawing of a silicon module is shown in Fig. 4.3, a drawing of one half of the TT station is shown in Fig. 4.8.
The production of the complete TT station, including all silicon modules and station mechanics is the responsibility of our group. The preparation of production and test facilities has started under the supervision of F.Lehner, a detailed production plan and quality assurance procedures are being defined.

4.4 Optical readout link

The Beetle front-end chip samples detector data at the LHC bunch crossing frequency of 40 MHz and stores the analog data for the latency of the Level-0 trigger. At a trigger accept, the analog data are multiplexed, read out, digitised and transmitted to the LHCb electronics barrack. Here, the data are processed and transmitted to the higher-level triggers and the data acquisition system.

The L0 Trigger operating at a maximum accept rate of 1.1 MHz, up to 2.6 Tbit/s of digitised detector data have to be transmitted for the Silicon Tracker. A low-cost digital optical link using commercially available components is being developed for this purpose by A.Vollhardt as part of his PhD thesis work in our group. A full prototype link using final components has been set up and is working in the laboratory [9]. Similar developments are underway for other LHCb subsystems and the formation of a common working group has been initiated by A.Vollhardt. He organizes regular group meetings, in which common solutions are discussed and the selection of commercial components is coordinated.

Some components of the readout link are located close to the detector, where an accumulated radiation dose of up to 10 kRad is expected after ten years of LHCb operation at nominal luminosity. All relevant components have been radiation qualified by A.Vollhardt and Y.Ermoline in total ionizing dose irradiation campaigns at PSI and in a neutron irradiation at the Prospero nuclear reactor at CEA Valduc, France [10].

First components of the Low-Voltage supply system for the Silicon Tracker have been received and characterised [11] by A.Vollhardt and A.Gafner, the latter working in our group as a technical student.

4.5 Event simulation

The group has played a major part in simulation studies of the LHCb tracking system performance that were described in the LHCb reoptimized detector TDR [2]. In particular, M.Needham has shown that the proposed detector design leads to high tracking efficiency, low ghost-rates and good momentum resolution. In addition the proposed design has been shown to be robust in the case the simulation of the detector is overly optimistic. For the forthcoming LHCb data challenge (DC '04) M.Needham has provided software to encode and decode the data in the format that it is expected to come from the detector.

4.6 Physics studies

In preparation for Physics data taking the group has recently started to work on physics simulation studies. Such studies are important in order to understand the CP reach of LHCb, to investigate possible sources of systematic uncertainty and to optimize the performance of the trigger. In the area of B_s decays which are beyond the reach of the current generation of B factories LHCb will make a large impact. Therefore, we have chosen to study the decay mode $B_s \rightarrow J/\psi\eta'$. This decay mode can be used to measure the CKM angle, χ via a time dependent CP asymmetry measurement. A high precision measurement of this angle is an important check of the standard model [12]. Under the supervision of M.Needham and as part of his Ph.D. thesis work in our group, D.Volyanskyy currently works to develop an analysis for this decay mode and to determine the annual expected yield and signal-to-background ratio. These numbers will then be used to investigate the physics sensistivity of LHCb for this decay mode. In April 2004, M.Regli will join this project as a Diploma student.

4.7 Summary and outlook

R&D and design work for the TT station of the LHCb Silicon Tracker has been the major occupation of our group over the last year. Successful prototype tests have been performed in the laboratory and in test-beams and a mechanical design of the station has been developed. Preparations for the production of the detector are ongoing, a pre-series production is scheduled to begin in Autumn 2004, series production will commence beginning of 2005. The detector is foreseen be installed and fully commissioned before the startup of LHC, foreseen for 2007.

The digital optical readout link is operational in the laboratory and all relevant components have been radiation qualified.

In preparation for Physics data taking, the group has started to work on simulation studies, studying the decay mode $B_s \rightarrow J/\psi\eta'$. These studies will continue over the next years and will permit the group to build up experience for Physics analyses.

[1] *LHCb technical proposal*, CERN/LHCC 998-4.

[2] *LHCb Reoptimised Detector Technical Design Report*, CERN/LHCC 2003-030.

[3] *LHCb Inner Tracker Technical Design Report*, CERN/LHCC 2002-029.

[4] J.Gassner, M.Needham, O.Steinkamp, *Layout and expected performance of the LHCb TT station*, LHCb-2003-140.

[5] J.Gassner *et al.*, *Capacitance Measurements on Silicon Micro-Strip Detectors for the TT Station of the LHCb Experiment*, LHCb-2003-081.

[6] R.Bernhard *et al.*, *Measurements of Prototype Ladders for the Silicon Tracker with Laser*, LHCb-2003-075.

[7] M.Agari *et al.*, *Test-Beam Measurements on Prototype Ladders for the LHCb TT Station and Inner Tracker*, LHCb-2002-032.

[8] St.Heule, *Simulation und Messung von Silizium-Streifen-Detektoren*, Diplomarbeit, Universität Zürich, 2003;
see also: St.Heule and F.Lehner, *Simulation of Signal Generation in Silicon Micro-strip Detectors for the Silicon Tracker of the LHCb Experiment*, LHCb-2003-159.

[9] A.Vollhardt, *A Prototype for the LHCb Silicon Tracker Data Readout System*, LHCb-2003-045.

[10] A.Vollhardt, *Neutron Irradiation Results for the LHCb Silicon Tracker Data Readout System Components*, LHCb-2003-049.

[11] A.Vollhardt and A.Gafner, *Characterization and Sample Testing of the LHC4913 Positive Voltage Regulator for the LHCb Silicon Tracker*, LHCb-2003-049.

[12] J.P.Silva and L.Wolfenstein, Phys.Rev.**D 55** (1997) 5331.

5 The DØ experiment at the Tevatron $p\bar{p}$ collider: Search for rare decays of B_s-mesons and a new silicon detector layer

Ralf Bernhard and Frank Lehner

The full DØ collaboration consists of 80 institutes from 18 countries: Argentina (1), Brazil (3), China (1), Czech Republic (3), Colombia (1), Ecuador (1), France (7), Germany (6), India (3), Ireland (1), Korea (1), Mexico (1), Netherlands (3), Russia (5), Sweden (4), United Kingdom (3), United States of America (35) and Vietnam (1)

(DØ Collaboration)

Until LHC at CERN starts its operation in 2007 the Tevatron at the Fermi National Accelerator Laboratory, Batavia, USA, is the world's highest energy accelerator with an available center of mass energy of 2 TeV. The so-called Run II of the $p\bar{p}$ collider has started in 2001 and addresses some of the most important questions in particle physics. The most recent physics results involve direct searches for as yet unknown particles and forces, including both those predicted or expected (like the Higgs boson and supersymmetry) and those that would come as a surprise. Other important aspects of this programme are precise measurements of the top quark properties and new accurate determinations of the mass of the W boson and the couplings of the electroweak bosons. Moreover, numerous measurements of various B meson decay modes have already allowed the investigation of B meson properties that are not accessible at other colliders as well as searches for CP-violating effects. A recent overview of the latest B physics results from DØ is presented in [1].

Because of the tantalizing physics prospects a high integrated luminosity run will bring, a second phase of Tevatron running, that will cover the years 2006 until 2009, is presently being prepared. The innermost layer of silicon detectors situated close to the beampipe will be replaced [2] since it will suffer from the harsh radiation environment and might lose efficiency.

After the DØ detector became fully operational for Run II and about 300 pb^{-1} of $p\bar{p}$ collision data have been taken until now, we started with our physics analysis programme of rare B_s decay searches. The study of the B_s meson is unique to hadron colliders since the particle can not be produced at the $\Upsilon(4S)$ resonance at which e^+e^- B-Factories like BaBar and Belle are running. So far we have focused on the flavor-changing neutral current decay $B_s \to \mu^+\mu^-$, which is forbidden at tree level. This decay channel is a very clean and attractive probe for physics beyond the Standard Model (SM) since it has a very small SM branching ratio of $3.5 \cdot 10^{-9}$ and many supersymmetric extensions of the SM could enhance it significantly [3]. Especially at high $\tan\beta$ any model with an extended Higgs sector leads to rates which may already now be observable at the Tevatron.

So far, we have analyzed about 180 pb^{-1} of DØ data and optimized the event selection in the invariant mass regions next to the signal region (the "box") which has been left to avoid any bias (see Figure 5.1). We expect 7.3 ± 1.3 background events in the box which corresponds to an upper limit of $1 \cdot 10^{-6}$ at 95% confidence level assuming no signal [4], almost a factor three lower than the Run I limit of CDF [5].

Our plan is to open the signal box for the ICHEP conference in August 2004. By then we will have doubled the statistics which will start to constrain the parameter space of certain supersymmetric models at high $\tan\beta$.

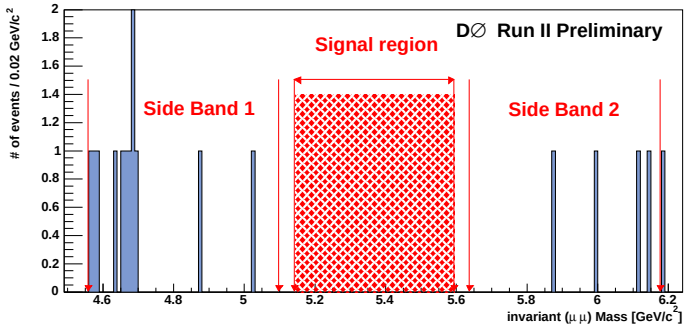

Figure 5.1: $\mu^+\mu^-$ *invariant mass distribution around the region of interest. The latter has not yet been looked at.*

We are also involved in the construction of the new DØ silicon detector layer which will be put in operation in 2005. We have worked on the specifications, the design and the quality assurance procedures for the silicon sensors which have been ordered by now [6]. In addition we have designed a long low-mass cable with a very fine pitch to route the analog signals from the innermost silicon detector layer to the readout electronics. Together with the Swiss company Dyconex [7] several cable prototypes were developed and characterized. The production of those cables has just started.

[1] *Recent Results from B Physics at DØ* , talk presented by F. Lehner at the XII International Workshop on Deep Inelastic Scattering, DIS 2004, Strbske Pleso, Slovakia, April 14-18, 2004.

[2] The DØ Run IIb silicon detector collaboration: *DØ Run IIb silicon detector upgrade, Technical Design Report*, http://d0server1.fnal.gov/projects/run2b/Silicon/www/smt2b/Layer00/l0html.

[3] A. Dedes, H. Dreiner and U. Nierste, Phys. Rev. Lett. **87**, 251804, 2001.

[4] R. Bernhard and F. Lehner: *Sensitivity analysis of the rare decay $B_s \to \mu^+\mu^-$ with the DØ detector*, DØ note 4377.

[5] F. Abe *et al.* [CDF Collaboration], Phys. Rev. D **57**, 3811 (1998).

[6] A. Bean *et al., Silicon Sensor Quality Assurance for the* DØ *RunIIb Silicon Detector: Procedures and Equipment*, DØ note 4120, see also `http://www.physik.unizh.ch/~lehnerf/dzero/run2b.html`.

[7] Dyconex advanced circuit technologies, Zurich, Switzerland.

6 Particle Physics with CMS at LHC

C. Amsler, V. Chiochia, A. Dorokhov, C. Hörmann, K. Prokofiev, H. Pruys,
C. Regenfus, P. Robmann, T. Speer, and S. Steiner

in collaboration with:
ETH-Zürich, Paul Scherrer Institut (PSI), Universität Basel and the CMS Collaboration.

(CMS Collaboration)

During 2003 our group continued to design and test the pixel sensors and readout chips for the innermost vertex detector of the CMS experiment. We are also involved in the charged particle reconstruction software and the workshop of our institute is developing the support structure and service tube for the pixel detector.

The CMS (Compact Muon Solenoid) at the Large Hadron Collider (LHC) will start operating at CERN in 2007. Our group will concentrate on physics involving the b- and t-quarks quark, e.g. b-quark production associated with the formation of Higgs bosons. The most interesting events at LHC will contain one or several b-jets originating from the decay of B mesons, with typical decay lengths of a few mm. To allow for efficient tagging of B mesons among the large background of light quark and gluon jets, the detection system has to trace back particles towards the primary vertex. The silicon pixel detector we are developing is the closest detector to the interaction point, located only 4 cm from the beam-beam interaction point. The extremely high particle flux near the primary vertex ($\approx$ 1000 particles every 25 ns) requires the innermost tracking layers to be composed of pixel devices delivering 3D coordinates with high resolution and no ambiguity.

The barrel pixel detector consists of three concentric cylindrical layers, 53 cm long with radii of 4.4, 7.3 and 10.2 cm. The layers contain some 3×10^7 silicon pixels. The pixel modules consist of thin, segmented sensor plates with highly integrated readout chips connected by indium bump bonds (Fig. 6.1). The final pixel size will be $100 \times 150\,\mu\mathrm{m}^2$. The analogue signals are read out to determine the coordinates more accurately, using charge sharing between adjacent pixels.

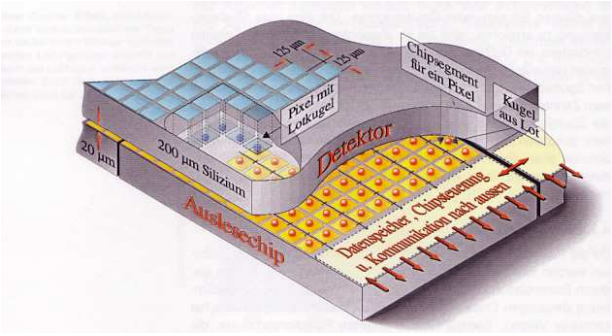

Figure 6.1: *Schematic view of a pixel detector element. Each sensor pixel is connected through an indium solder bump to a pixel unit cell on the readout chip which amplifies and processes the signal. The data are stored on the edge of the chip where they wait for trigger confirmation.*

6.1 Development of pixel sensors

The CMS pixel sensors are manufactured using the "n-on-n" technique consisting of n^+-structures on n-bulk silicon. This allows the partially depleted operation of highly irradiated sensors after type inversion, but also requires inter-pixel isolation. Two isolation techniques were considered for our

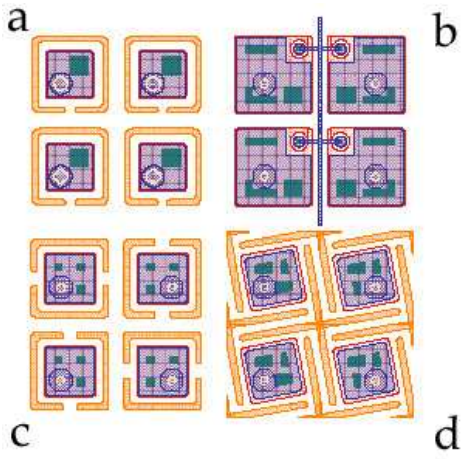

Figure 6.2: *Some of our favorite designs for the pixel sensors. Open p-stop rings (a and c), p-stop crosses (d) and p-spray with bias grid (b).*

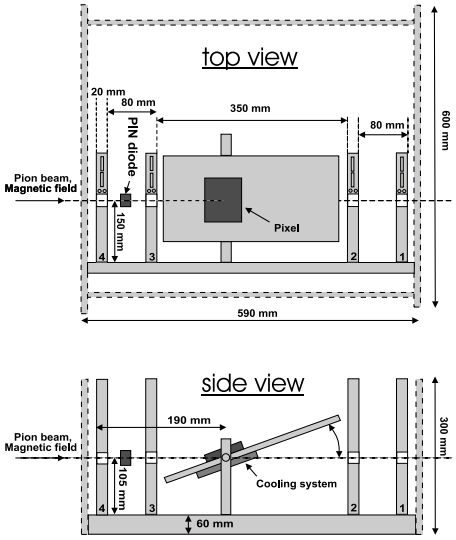

Figure 6.3: *Top and side views of the beam telescope.*

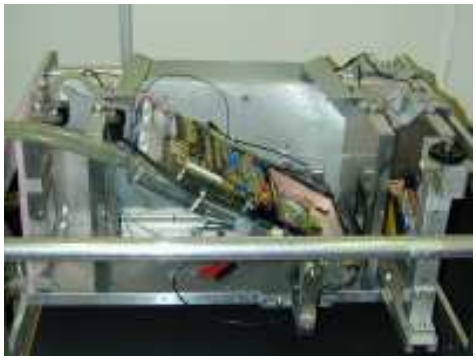

Figure 6.4: *Beam telescope setup.*

latest prototypes: p-spray [1], for which a uniform average dose of p-impurities ($\approx 10^{12}$ cm^{-2}) covers the whole structured surface, and p-stop rings ($\approx 10^{13}$ impurities cm^{-2}) which surround the n^+-implants (Fig. 6.2). Possible failures of the pixel bump-bonds require a method to evacuate the charge. This is achieved with a bias grid and punch-through structures for the p-spray detectors and by openings in the rings for the p-stop detectors.

Test measurements were performed in the H2 beam line of the CERN SPS in June and September 2003 using 150-225 GeV pions. The test devices contained 22×32 pixels with a total sensitive area of 2.75×4 mm^2, and a thickness of 280 μm. The readout pitch was still of the old design, 125 μm $\times$ 125 μm. Some of these devices had been previously irradiated in a 24 GeV proton beam at the CERN PS. The sensors received total particle fluences of 3.3×10^{14} n_{eq}/cm^2, 8.1×10^{14} n_{eq}/cm^2 and 1.1×10^{15} n_{eq}/cm^2. They were bump bonded to non-irradiated readout chips of the DMILL type.

The hit coordinates in the pixel detector were determined accurately with our silicon reference telescope [2]. The beam telescope consisted of 4 modules, each with two orthogonal 300μm thick single-sided silicon detectors (32×30 mm^2) with a strip pitch of 25 μm and a readout pitch of 50 μm. The resulting intrinsic resolution of the beam telescope was around σ = 1 μm.

The pixel sensor with the readout chip was mounted on a rotating support positioned between the second and the third module (Figs. 6.3 and 6.4). A trigger signal was generated by a PIN diode. The data acquisition system and slow control (temperature and bias voltage) were written in LabView and LabWindows CVI (National Instruments) running on a PC. The analog signals were digitized in a VME based readout system by FADCs. The setup was located in an open 3 T Helmholtz magnet with magnetic field parallel to the beam. The pixel sensors were cooled with water cooled Peltier elements. Similar measurements were performed earlier by our group [3; 4] but irradiated sensors could not be tested reliably because they were not cooled down to the -10° C foreseen for the CMS tracker. A more detailed discussion of the latest beam test results can be found in ref. [8].

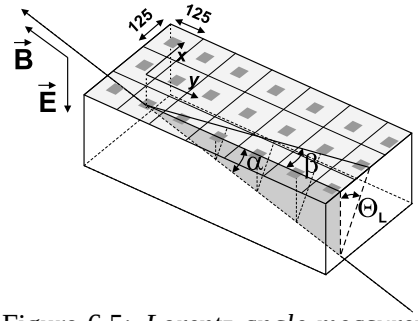

Figure 6.5: *Lorentz angle measurement with the grazing angle method.*

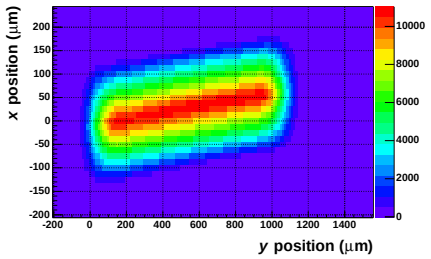

Figure 6.6: *Deflection of the drifting charge in a 3 T magnetic field.*

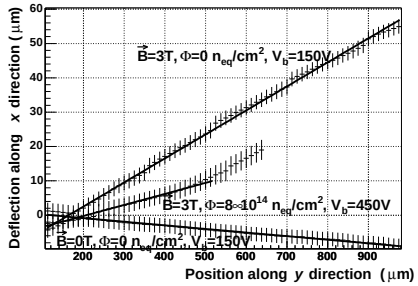

Figure 6.7: *Deflection of the collected charge as a function of the y-position. The solid line is the fit.*

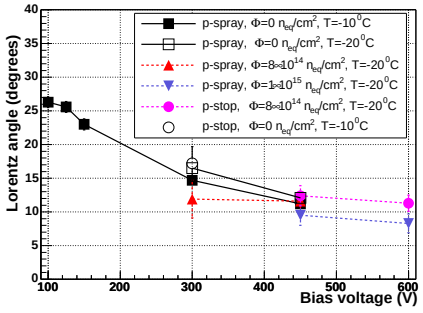

Figure 6.8: *Lorentz angle as a function of bias voltage for a magnetic field extrapolated to 4 T.*

6.1.1 Lorentz angle measurements

The Lorentz angle was obtained by the direct measurement of the charge drift in the magnetic field using the grazing angle method [4]. The pion beam which was in direction of the magnetic field entered the sensor surface at a shallow angle $\alpha = 15°$ (Fig. 6.5). The deposited charge drifts according to the combined electric and magnetic forces, resulting in a deflection of the particle track projection on the surface by the angle β from which the Lorentz angle Θ_L could be obtained. The deflection observed at 3 T magnetic field is illustrated in Fig. 6.6 for the non-irradiated p-spray sensor.
The angle β was measured by slicing the histogram perpendicularly to the y-axis. The x position of the charge center is shown in Fig. 6.7 as a function of y. A measurement without magnetic field is used to correct for detector misalignment with respect to the beam (bottom line). For the irradiated device there are two regions with different slopes, and hence two different Lorentz angles. This behaviour can be explained by the non-linear behaviour of the electric field in the irradiated devices (see next section). Since most of the signal charge is collected from the region close to the pixel implant, this region was used to determine the Lorentz angle.
Figure 6.8 shows the measured Lorentz angles for non-irradiated and irradiated sensors, extrapolated to 4 T. One observes a strong dependence of the Lorentz angle on the bias electric field, which is weakly affected by irradiation and does not depend strongly on sensor design. For the non-irradiated sensors a Lorentz angle of $26°$ can be reached at a bias voltage of 100 V, while irradiated sensors have to be operated at much higher bias voltages, where the Lorentz angle drops to roughly $10°$. Our results are in a good agreement with other measurements and simulations [5].

6.1.2 Charge collection in irradiated sensors

Following irradiation, the amount of collected charge decreases due to charge trapping and partial depletion of the sensor. Measurements of the charge collection efficiency as a function of sensor depth were performed using the grazing angle method, this time with magnetic field off. The charge collected in non-irradiated and irradiated p-spray sensors as a function of depth is shown in Fig. 6.9. In the non-irradiated sensor the charge is collected uniformly across the whole sensor depth, while

the irradiated devices exhibit a different behaviour. At low bias voltages charge is also collected from the side opposite to the pixel implants which could indicate that the depletion starts from both sides of the detector, due to the non-linear behaviour of the electric field. The fraction of collected charge for different designs and irradiation doses is shown in Fig. 6.10 as a function of bias voltage. Charge collection also depends on the position of the incident particle with respect to the pixel implant since the gaps between pixels have a reduced sensitivity. The average charge collected is shown in Fig. 6.11 as a function of position for non-irradiated and irradiated sensors. The signal-to-noise ratio decreases from 65 to 35 after irradiation. Thus the CMS pixel detector will operate up to the maximum expected irradiation dose. Note that the area with reduced charge collection between pixels is larger for the p-stop design.

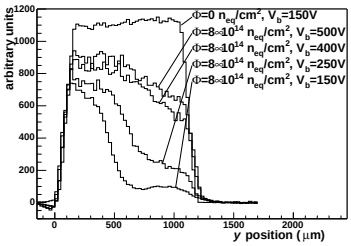

Figure 6.9: *Charge collected for different bias voltages.*

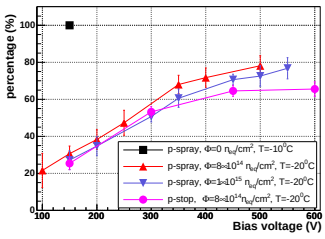

Figure 6.10: *Total collected charge normalized to non-irradiated device.*

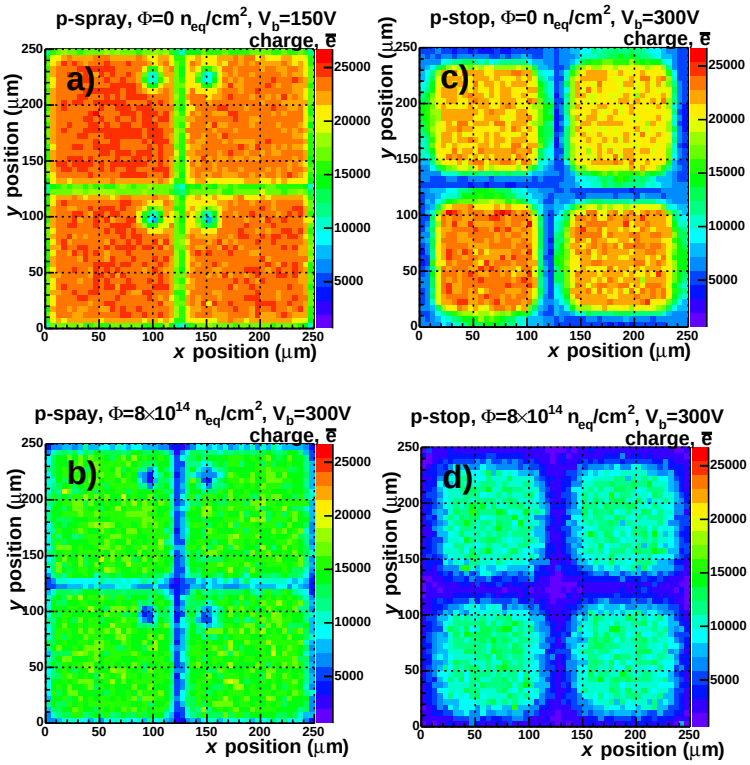

Figure 6.11: *Distribution of charge collected in the pixels. The top plots show the non-irradiated p-spray (a) and p-stop designs (c), the bottom plots the respective irradiated sensors.*

6.2 Development of the pixel readout chip

We collaborate with PSI in the design of the readout chip (ROC) [6]. The prototype (PSI46) in quarter micron technology DSM (Deep Sub Micron) was submitted and delivered by the manufacturer in 2003. The previous chips had been processed in radiation hard DMILL technology. DSM technology is a well known standard process, significantly cheaper than DMILL which was especially developed for radiation hard devices. However, DSM designs can also be radiation hard. We expect a better yield with DSM than with DMILL and, indeed, the preliminary yield is 80% for DSM, compared with 20% for our previous DMILL chips (PSI43). Power consumption is also lower in DSM which requires only half of the supply voltage and half of the current, hence a quarter of the total power consumption.

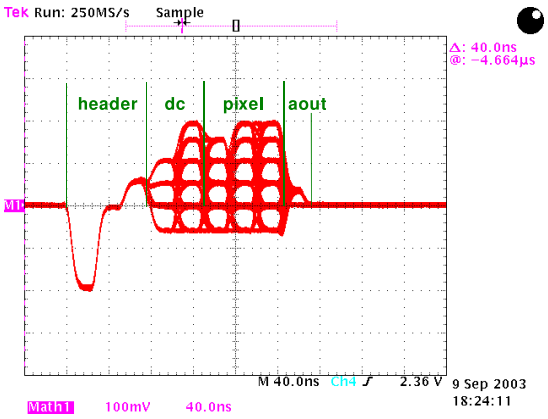

Figure 6.12:
Event readout structure of PSI46 (see text).

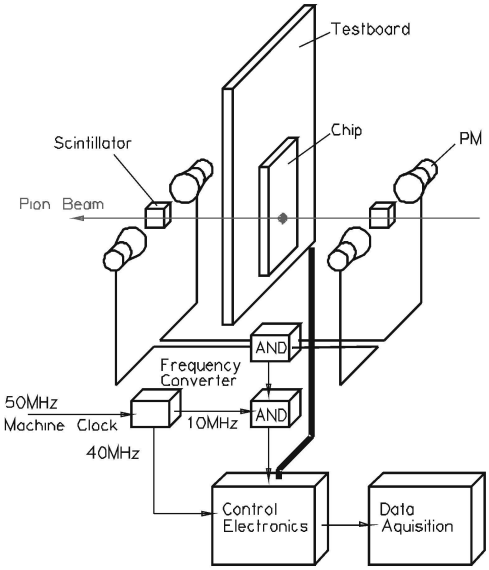

Figure 6.13: *Test beam setup.*

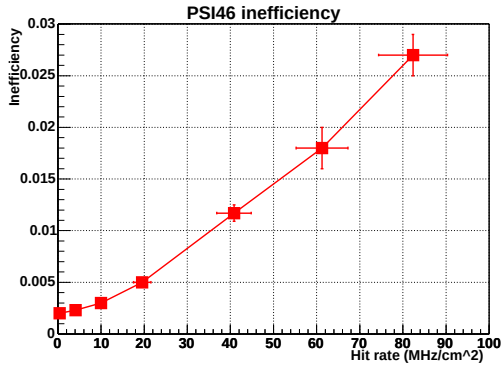

Figure 6.14: *Data loss measured with test pions.*

DSM technology also offers new possibilities in designing chips and improving their performances. There are five metal layers available for routing instead of only two, and the smallest feature size is 0.25 μm, compared to 0.8 μm for DMILL. Hence more complex circuits can be designed to cope with the updated requirements at LHC: the three layers of pixel detectors will now be operated at high luminosity, including the innermost at 4 cm from the interaction vertex. In DMILL technology, however, we would have an unacceptable fraction of lost data.

The wafer submitted to the manufacturer in 2003 contained four versions of the ROC which differ essentially in the power decoupling scheme (to minimize cross talk and therefore allow lower comparator thresholds) and the total area of metal insulator metal capacitors. Test circuits for internal measurements at points that are not accessible in the ROC were also foreseen in the wafer. In particular, we designed a circuit to investigate single event upsets, see below.

The analog readout of the ROC was tested in the laboratory (Fig. 6.12). The first three cycles are used for the header, the next two for the double column address and the following three for the pixel addresses. The addresses are coded by six analog levels which are clearly distinguishable in Fig. 6.12. The last cycle is the analog pulse height. The cycles for the address of the double column, the pixel address and the pulse height are repeated for each hit. The readout frequency is 40 MHz.

The ROC was tested on the 300 MeV/c πE_1 beamline at PSI. One of the goals was to investigate the data loss under LHC equivalent intensities. The beam intensity varied up to 8×10^7 pions/cm^2 which corresponds to the expected track density at CMS for the middle layer of the pixel detector. The experimental layout is shown in Fig. 6.13. The trigger signal was generated by scintillators and reduced to 10 kHz by coincidence with the random signal of a radioactive source. The ROC was operated with a synchronized 40 MHz frequency which corresponds to the bunch crossing frequency at LHC.

The inefficiency versus fluence is shown in Fig. 6.14. The data loss of PSI46 (2.5 % at the maximum luminosity) is about an order of magnitude smaller than that of PSI43, but still some-

what higher than expected. Hence the translation of the ROC from DMILL to DSM was successful and the new chip is much more performant. Some minor improvements are, however, still necessary.

Single event upsets (SEU) occur during high energy deposits in a small sensitive volume of the electronics circuit, leading to unwanted bit flips. SEU events are due to hadronic interactions with nuclei on the lattice. This is a known problem, e.g. in space applications, which has also to be taken seriously at LHC. SEU is more dangerous in DSM technology due to smaller node capacities, faster circuits and lower supply voltages, and is a serious problem for detector control functions. For example, the analog converter values and trimbits for the thresholds are stored in memory cells. In order to deal with the SEUs, one has to reload permanently the storage cells, which causes unnecessary data traffic.

In our measurements we investigated the effects of capacitors as protections against SEUs. The SEU test structures designed in DSM technology consisted of shift registers protected by capacitors. The shift registers were filled with 1 or 0 and read out every 5 minutes to count the flipped bits. The cross sections for bit flips are shown in figure 6.15 as a function of supply voltage. The cross sections for SEU are roughly two orders of magnitude smaller with protective capacitor.

Another interesting result is the asymmetry in the probabilities for 1 to 0 flips and 0 to 1 flips. The ratio of probabilities $0 \rightarrow 1 \,/\, 1 \rightarrow 0$ is about 120. Figure 6.16 shows the spatial distribution of SEUs after 160 readouts of 5 minutes each, at a supply voltage of 1.5 V. The upper row shows the spatial distribution of SEUs in the unprotected shift registers and the lower row shows the distribution for the protected cells.

By histogramming the number of SEUs after each readout one obtains a Poisson distribution. This is a hint for independent single pixel upsets and no clusterisation of SEUs. The ratio of SEU cross sections for π^+/π^- is 1.6. The ratio for π^+/p (~ 5) was also measured using 500 MeV/c protons. This is an important measurement since most investigations for space applications were done with protons.

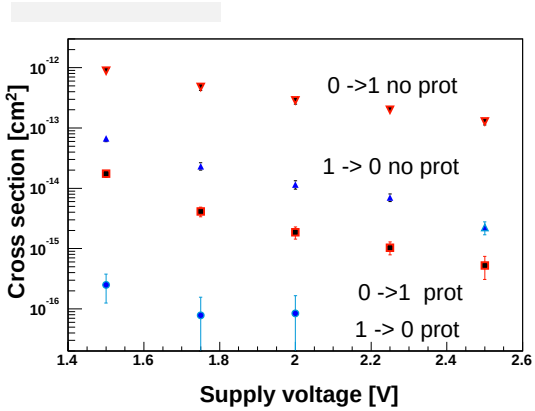

Figure 6.15: *SEU cross sections for 300 MeV/c π^+ on the SEU test structures for various supply voltages.*

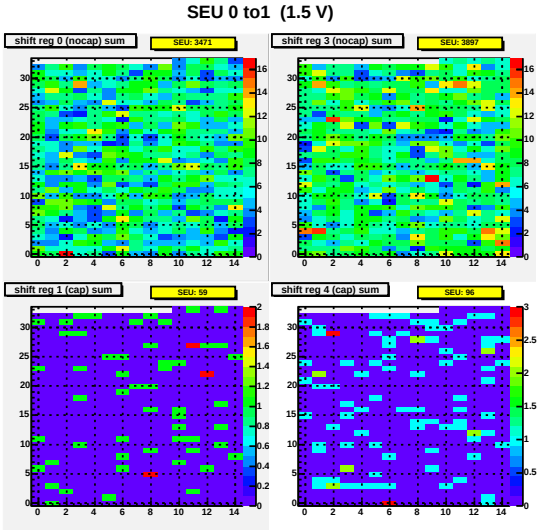

Figure 6.16: *Accumulated spatial distribution of SEUs after 160 readouts for four shift registers in parallel. The upper row shows the distribution of two unprotected shift registers and the lower one the distribution for two protected shift registers.*

6.3 Event reconstruction software

We are developing techniques to reconstruct the interaction vertex in CMS within the object-oriented reconstruction framework (ORCA). After having implemented in ORCA a single-vertex fit algorithm using the Kalman filter formalism (see last year's annual report and ref. [7]), we are now developing an algorithm based on a the so-called Gaussian sum filter.

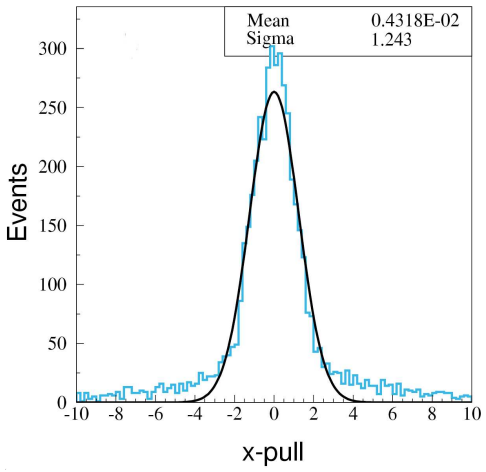

Figure 6.17: *Pull of the reconstructed vertex x-coordinate.*

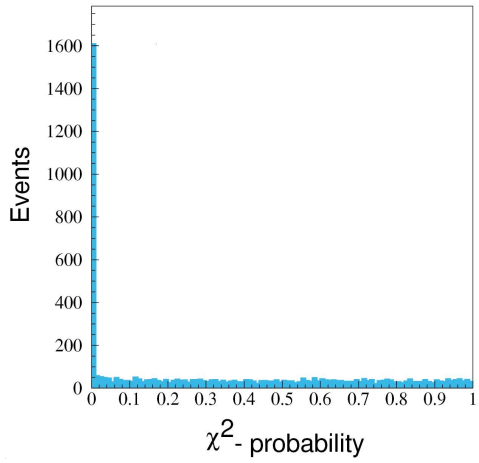

Figure 6.18: *χ^2-probability distribution for the Kalman filter.*

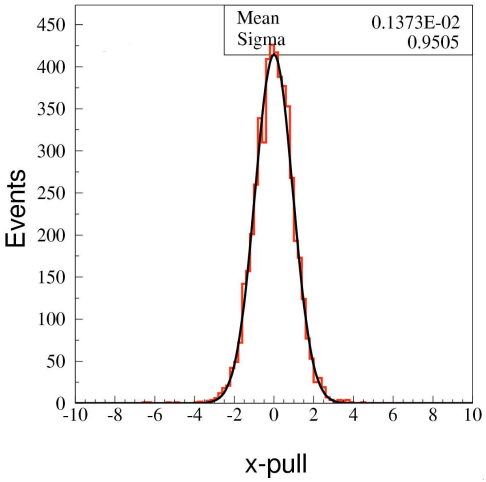

Figure 6.19: *Pull of the reconstructed vertex x-coordinate.*

The usual vertex reconstruction algorithm is the Kalman filter based on a least square minimization, which hence assumes that the track measuring errors follow a normal distribution. However, a non-Gaussian noise (due e.g. to δ-electrons) is always present. One method that takes non-Gaussian effects into account is the Gaussian-sum filter (GSF) in which the measurement errors are modeled by a superposition of several (mostly two) Gaussians which we shall refer to as *components*. It is a non-linear estimator, in which the weights of the components depend on the measurements.

In an iterative procedure, the estimate of the vertex is updated with one track at the time. The vertex consists of several solutions calculated with all possible components of the tracks. When one track is added to the vertex, each solution for the vertex is combined with each component of the new track, using the Kalman filter. The final vertex estimate is then calculated as the weighted average of all solutions. Since the number of solutions increases exponentially, it has to be limited to an acceptable number. This is achieved by merging solutions which are close enough.

To investigate the performance of a such an algorithm we made a simulation using vertices leading to four-tracks. No track reconstruction was performed but track parameters were smeared according to a two-component Gaussian model. The component modeling the non-Gaussian tails had a standard deviation ten times larger than that of the core component and their relative weights were 9:1.

For a fit with the Kalman filter, for which only one component is used, the distributions of the vertex pulls (difference between simulated and reconstructed values divided by the measurement error) show a Gaussian core with tails (Fig. 6.17) and a large fraction of the fitted events have a very small χ^2-probability (Fig. 6.18).

In the GSF method the two components are used, each with the correct weight and variance. The pulls have a resolution closer to unity when fitted with a Gaussian, the tails vanish (Fig. 6.19) and the peak at low χ^2 disappears (Fig. 6.20). This indicates that the error estimates and component weights were reasonable. These encouraging tests demonstrate the power of the algorithm and its efficiency in the presence of non-Gaussian noise.

We are also developing a kinematic fit using the Lagrange multiplier method which incorporates additional constraints into the vertex fit. Additional constraints such as masses of decaying particles, energy and momentum conservation, will improve the resolution. A further constraint of interest would require the momentum of the reconstructed B meson to be parallel to the vector pointing from the primary to the secondary vertex (pointing constraint).
As an example, consider the decay $B_s \rightarrow J/\psi\ \phi \rightarrow K^+K^-\mu^+\mu^-$. The invariant mass of the four tracks after the vertex fit but without any additional constraint is shown in Fig. 6.21. The distribution has a Gaussian width of about 40 MeV and the average mass is displaced by some 13 MeV compared to the table value. This is due to the large error on the muon momentum measurement in the CMS detector.
However, the invariant mass distribution becomes significantly narrower and correctly centered when the four-momentum of the two-muon system is constrained to match the J/ψ mass (Fig. 6.22). This constraint is applicable due to the very small width of the J/ψ compared to the measurement uncertainties of typically 10 MeV.

[1] R. H. Richter *et al.*, Nucl.Instr.Meth.**A 377** (1996) 412.

[2] C. Amsler *et al.*, Nucl.Instr.Meth.**A 480** (2002) 501.

[3] R. Kaufmann, PhD Thesis, Universität Zürich, 2001.

[4] B. Henrich and R. Kaufmann, Nucl.Instr.Meth.**A 477** (2002) 304.

[5] V. Bartsch *et al.*, Nucl.Instr.Meth.**A 478** (2002) 330.
V. Bartsch *et al.*, Nucl.Instr.Meth.**A 497** (2003) 389.

[6] M. Barbero *et al.*, Nucl.Instr.Meth.(in print).

[7] R. Frühwirth, K. Prokofiev, T. Speer, P. Vanlaer and W. Waltenberger, Nucl.Instr.Meth.**A 502** (2003) 699.

[8] A. Dorokhov *et al.*, to appear in Nucl.Instr.Meth.**A** preprint physics / 0311050;
T. Rohe *et al.*, submitted to IEEE-TNS 7, preprint physics / 0312009.

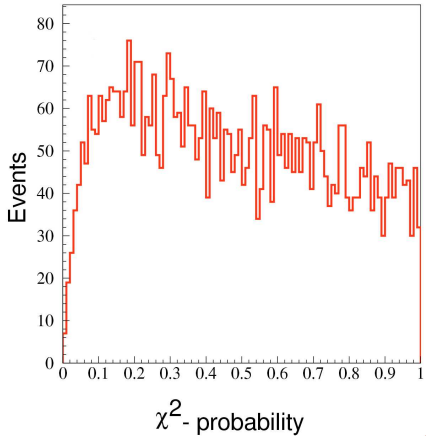

Figure 6.20: *χ^2-probability distribution for the GSF (see text).*

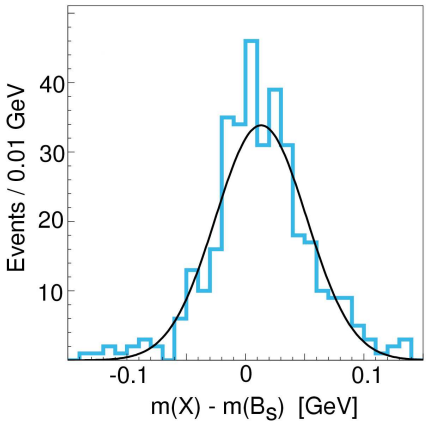

Figure 6.21:
$K^+K^-\mu^+\mu^-$ invariant mass in $B_s \rightarrow J/\psi\ \phi \rightarrow K^+K^-\mu^+\mu^-$ without J/ψ mass constraint.

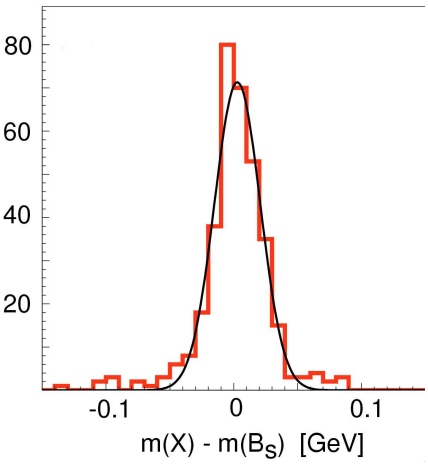

Figure 6.22:
Distribution as in Fig.6.21 but with J/ψ mass constraint.

7 Superconductivity and Magnetism

M. Angst (till November 2003), M. Bruun (till November 2003), D. Di Castro,
D.G. Eshchenko, H. Keller, R. Khasanov, S. Kohout, M. Mali (till November 2003),
J. Roos, A. Shengelaya, S. Strässle (since Mai 2003),
M. Eremin (visiting scientist), V.A. Ivanshin (visiting scientist), B. Kochelaev (visiting scientist),
T. Schneider (Titularprofessor), and K.A. Müller (Honorarprofessor)

in collaboration with:
ETH Zürich (K. Conder, J. Karpinski), Paul Scherrer Institute (PSI) (E. Morenzoni), IBM Rüschlikon Research Laboratory (J.G. Bednorz), Université de Genève (Ø. Fischer), University of Birmingham (E.M. Forgan), University of St. Andrews (S.L. Lee), University of Rome (A. Bianconi), Kazan State University (A. Dooglav, M.V. Eremin, B.I. Kochelaev), University of Belgrade (I.M. Savić), Institute of Low Temperature and Structure Research, Polish Academy of Sciences, Wroclaw (P.W. Klamut), Institute of Physics, Polish Academy of Sciences, Warsaw (R. Puzniak, A. Wisniewski), University of Tokyo (K. Kishio, T. Sasagawa, H. Takagi), Northern Illinois University, DeKalb (B. Dabrowski).

Our last years research activities were again aimed at the fundamental physical properties of non-conventional superconductors such as cuprate high-temperature superconductors (HTS) and magnesium diboride (MgB_2).

A main focus was put on the role of the electron-phonon interaction in the basic physics of these systems by investigating the effects of isotope substitution and hydrostatic pressure on the relevant superconducting parameters. Furthermore, new aspects related to charge inhomogeneity as a possible intrinsic property of the novel superconductors were explored by studying finite-size effects and signatures of an electronic phase separation. Applying the combination of microscopic techniques [*muon-spin rotation (conventional μSR and low energy LEμSR), nuclear magnetic resonance (NMR), nuclear quadrupole resonance (NQR), electron paramagnetic resonance (EPR)*] and bulk-type measurements [*SQUID and torque magnetometry, resistivity*] proved to be of great advantage in our investigations, which are described in more detail in the following.

7.1 Studies of isotope effects in novel superconductors

7.1.1 Direct observation of the oxygen isotope effect on the magnetic field penetration depth in optimally doped $YBa_2Cu_3O_{7-\delta}$

A direct way to explore the role of the electron-phonon interaction in HTS is to investigate the isotope effect on the in-plane penetration depth λ_{ab} [1; 2; 3]. We used the advantages of the low-energy μSR (LEμSR) technique, developed recently at the Paul Scherrer Institute (PSI) [4], for the direct measurement of the oxygen isotope ($^{16}O/^{18}O$) effect (OIE) on λ_{ab} in optimally doped $YBa_2Cu_3O_{7-\delta}$ films [5]. The principle of λ determination by using LEμSR is shown schematically in Fig. 7.1. Low-energy muons of tuneable energy can be implanted at a different and controllable depth z beneath the surface of the superconductor in the Meissner state. Due to the random nature of the muon scattering process, the implantation depths are distributed over a nanometer scale, and the implantation depth profile $n(z)$ depends on the muon energy [Fig. 7.1(a)]. Knowing the value of the mean implantation depth $\overline{z}$ the magnitude of the local field $B(\overline{z})$ is obtained from the muon spin precession frequency.

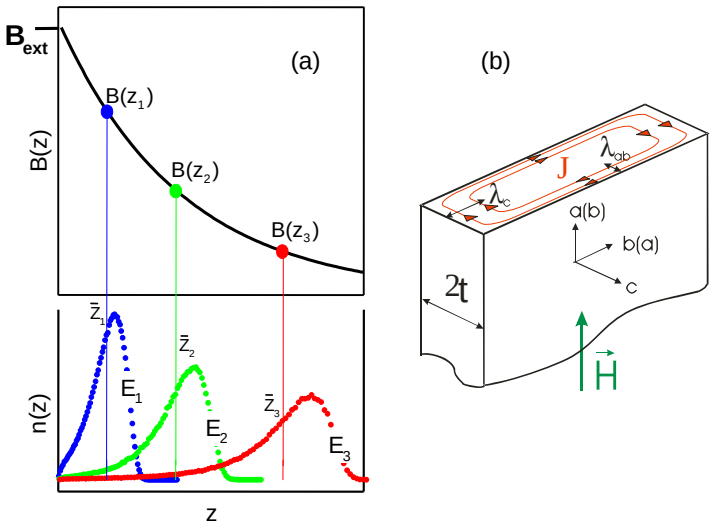

Figure 7.1:
(a) The principle of λ determination using LEμSR. By tuning the energy E of the incident muons they are implanted at controllable distances $\overline{z}$ beneath the surface of the superconductor in the Meissner state. The local magnetic field $B(\overline{z})$ is determined from the muon precession frequency using μSR. (b) Schematic distribution of the screening current J in a thin anisotropic superconducting slab of thickness $2t$ in a magnetic field applied parallel to the flat surface.

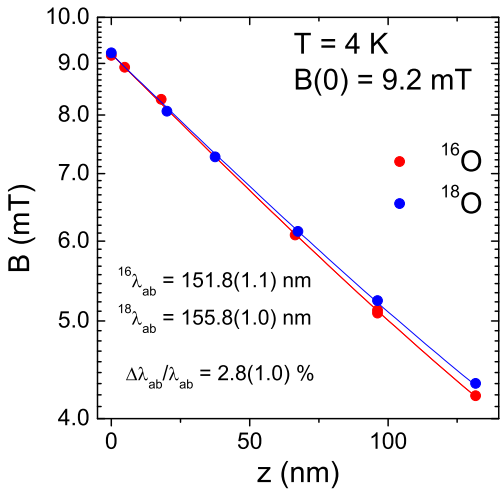

Figure 7.2: *Magnetic field penetration profiles $B(\overline{z})$ on a logarithmic scale for an ^{16}O substituted (red circles) and an ^{18}O substituted (blue circles) $YBa_2Cu_3O_{7-\delta}$ film measured in the Meissner state at 4 K and an external field of 9.2 mT, applied parallel to the surface of the film. The data are shown for implantation energies 3, 6, 10, 16, 22, and 29 keV starting from the surface of the sample. Solid curves are best fits by Eq. (7.1).*

The measurements of the in-plane magnetic penetration depth λ_{ab} were performed on a 600 nm thick epitaxial $YBa_2Cu_3O_{7-\delta}$ film in the Meissner state. A weak external magnetic field of 9.2 mT was applied parallel to the film surface after cooling in zero magnetic field from a temperature above T_c to 4 K. In this geometry (the thickness of the sample is negligible in comparison with the width), currents flowing in the ab-planes determine the magnetic field profile along the crystal c-axis inside the film [see Fig. 7.1(b)]. Spin-polarized muons were implanted at a depth ranging from 20-150 nm beneath the surface of the film by varying the energy of the incident muons from 3 to 30 keV. The muon implantation depth profile $n(z)$ for the given implantation energy was calculated using the Monte-Carlo code TRIM.SP [6]. The reliability of the calculated $n(z)$ was demonstrated by previous LEμSR experiments on thin metal layers [7].

For each implantation energy the average value of the magnetic field $\overline{B}$ and the corresponding average value of the stopping distance $\overline{z}$ were extracted. The value of $\overline{B}$ was taken from the fit of the μSR time spectrum assuming a Gaussian relaxation function. The value of $\overline{z}$ was taken as the first moment of the emulated $n(z)$ distribution. Results of this analysis for the ^{16}O and ^{18}O substituted $YBa_2Cu_3O_{7-\delta}$ films are shown in Fig. 7.2. The data points for the ^{18}O film are systematically lower than those for the ^{16}O film, showing that $^{16}\lambda_{ab} < {}^{18}\lambda_{ab}$. The solid lines represent a fit to the $B(\overline{z})$ data by the function:

$$B(z) = B_0 \frac{\cosh[(t-z)/\lambda_{ab}]}{\cosh(t/\lambda_{ab})}\,, \tag{7.1}$$

where $B(0)$ is the field at the surface of the superconductor, and $2t$ is the film thickness. Fits of Eq. (7.1) to the extracted ${}^{16}B(\overline{z})$ and ${}^{18}B(\overline{z})$ yield ${}^{16}\lambda_{ab}(4K) = 151.8(1.1)$ nm and ${}^{18}\lambda_{ab}(4K) = 155.8(1.0)$ nm. Taking into account an ^{18}O content of 95%, the relative shift was found to be $\Delta\lambda_{ab}/\lambda_{ab} = 2.8(1.0)\%$ at 4 K.

To confirm that the observed OIE on λ_{ab} is intrinsic, additional measurements of the Meissner fraction in fine powder samples with an average grain size compatible to λ_{ab} were performed. Analyzing the data using the procedure described in Ref. [1] gives $\Delta\lambda_{ab}/\lambda_{ab} = 2.7(1.0)\%$, in agreement with the LEμSR results. It was pointed out [1; 2; 3; 5] that the OIE on λ_{ab} arises mainly from the oxygen-mass dependence of the in-plane effective mass m^*_{ab}. Therefore, our finding implies that even in optimally doped HTS for which only a small isotope effect on T_c is observed, the supercarriers are strongly coupled to the lattice.

[1] G.M. Zhao *et al.*, Nature (London) **385**, 236 (1997).

[2] J. Hofer *et al.*, Phys. Rev. Lett. **84**, 4192 (2000).

[3] R. Khasanov *et al.*, J. Phys.: Condens Matter **15**, L17 (2003).

[4] E. Morenzoni *et al.*, J. Appl. Phys. **81**, 3340 (1997).

[5] R. Khasanov *et al.*, Phys. Rev. Lett. **92**, 057602 (2004).

[6] W. Eckstein, Computer Simulations of Ion-Solid Interactions (Springer-Verlag, Berlin, 1992).

[7] E. Morenzoni *et al.*, Nucl. Instrum. Methods B, **192**, 254 (2002).

7.1.2 Site-selective oxygen isotope effect on the penetration depth in $Y_{0.6}Pr_{0.4}Ba_2Cu_3O_{7-\delta}$

The observation of an OIE on λ_{ab} in HTS indicates an unusual (e.g., non-adiabatic) coupling of the electrons to phonon modes involving the movement of the isotope substituted atoms. It is important to identify the relevant phonon modes responsible for this effect. This can be achieved by investigating the site-selective oxygen-isotope effect (SOIE). We used transverse-field μSR to study the SOIE on T_c and λ_{ab} in underdoped $Y_{0.6}Pr_{0.4}Ba_2Cu_3O_{7-\delta}$ powder samples [1].

In order to prepare oxygen site-selective samples a two-step exchange process was applied [2]. The following site-selective samples were prepared: ${}^{16}O_{pac}$, ${}^{18}O_{pac}$, ${}^{16}O_p^{18}O_{ac}$, and ${}^{18}O_p^{16}O_{ac}$ where indexes p, a and c denote planar (within CuO_2 planes), apical and chain oxygen, respectively. The site-selectivity of the oxygen exchange was checked by Raman spectroscopy confirming that the site-selective oxygen substitution is almost complete in all the samples. The μSR measurements were performed at PSI using the

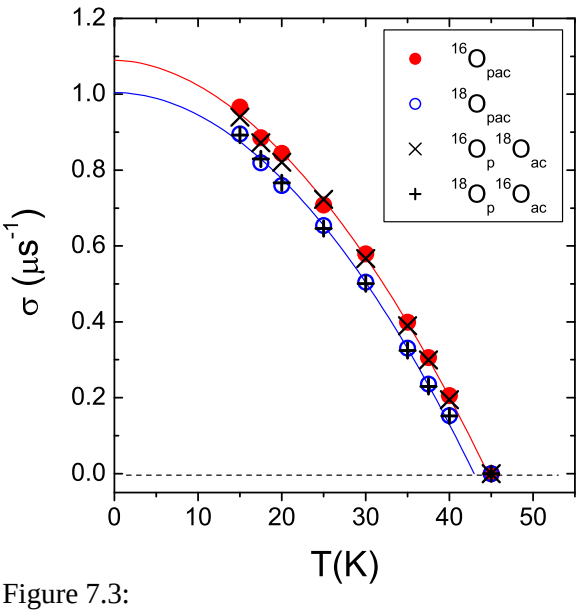

Figure 7.3:
Temperature dependence of the depolarization rate in site-selective $Y_{0.6}Pr_{0.4}Ba_2Cu_3O_{7-\delta}$ samples (200 mT, FC). The solid lines correspond to fits to the power law $\sigma(T)/\sigma(0) = 1 - (T/T_c)^n$ for the ${}^{16}O_{pac}$ and ${}^{18}O_{pac}$ samples.

πM3 beam line. The samples were cooled from far above T_c in a magnetic field of 200 mT. In a highly anisotropic layered superconductor the in-plane penetration depth λ_{ab} can be extracted from the muon-spin depolarization rate $\sigma(T) \propto 1/\lambda_{ab}^2$ which probes the second moment of the probability distribution of the local magnetic field function $p(B)$ in the mixed state [3]. The depolarization rate σ was extracted from the μSR time spectra using a Gaussian relaxation function. Figure 7.3 shows the temperature dependence of σ for the four $Y_{0.6}Pr_{0.4}Ba_2Cu_3O_{7-\delta}$ site-selective samples. It is evident that a remarkable oxygen isotope shift of T_c as well as of λ_{ab} is present. More importantly, the data points of the site-selective $^{16}O_p^{18}O_{ac}$ ($^{18}O_p^{16}O_{ac}$) samples coincide with those of the $^{16}O_{pac}$ ($^{18}O_{pac}$) samples. Therefore, our results show unambiguously that the OIE on both the transition temperature T_c and the in-plane magnetic penetration depth λ_{ab} comes from the oxygen within the superconducting CuO_2 planes and not from the apical and chain oxygen. Noting that the lattice parameters remain essentially unaffected by the isotope substitution [4], our results show the existence of a strong coupling of the electronic subsystem to phonon modes involving movements of the oxygen atoms in the CuO_2 plane, while suggesting that modes involving apical and chain oxygen are less strongly coupled to the electrons.

[1] R. Khasanov *et al.*, Phys. Rev. B **68**, 220506 (2003).

[2] K. Conder, Mater. Sci. Eng. **R32**, 41 (2001).

[3] P. Zimmermann *et al.*, Phys. Rev. B **52**, 541 (1995).

[4] F. Raffa *et al.*, Phys. Rev. Lett. **81**, 5912 (1998).

7.1.3 Finite-size and oxygen isotope effect in $Y_{0.6}Pr_{0.4}Ba_2Cu_3O_{7-\delta}$

Only in the ideal case superconductors can be considered as homogenous. For HTS there is increasing evidence that inhomogeneity is even an intrinsic property. Suppose that HTS are granular, consisting of spatial superconducting domains, embedded in a non-superconducting matrix and with spatial extent L_a, L_b and L_c along the crystallographic a, b and c-axes. The correlation length ξ_i in direction i, which increases strongly when T_c is approached, cannot grow beyond L_i. Consequently, for finite superconducting domains, thermodynamic quantities like the specific heat and penetration depth are smooth functions of temperature. As a remnant of the singularity at T_c these quantities exhibit a so-called finite size effect [1], namely a maximum or an inflection point at $T_{p_i(i=a,b,c)}$ (see Fig. 7.4). Knowing the value of T_{p_c} (see Fig. 7.4) and the values of the in-plane magnetic penetration depth λ_{ab} at $T = T_{p_c}$ the value of the domain size along c-direction L_c can be easily calculated[2]:

$$L_c = \frac{16\pi^3 k_B T_{p_c}}{\Phi_0^2} \frac{1}{\lambda_{ab}^{-2}(T_{p_c})} , \qquad (7.2)$$

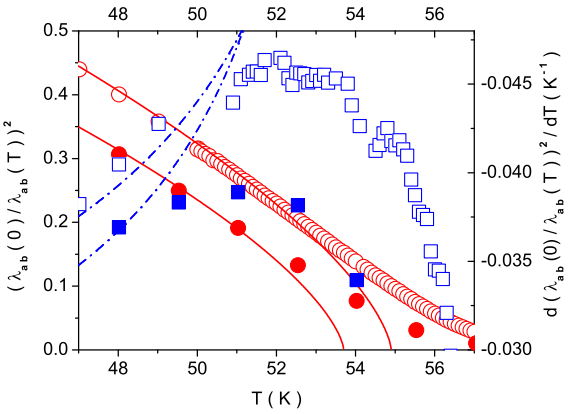

Figure 7.4: *Temperature dependence of the normalized $\lambda_{ab}^{-2}(T)/{}^{16}\lambda_{ab}^{-2}(0)$ in the vicinity of T_c for the ^{16}O – open circles and ^{18}O – closed circles $Y_{0.7}Pr_{0.3}Ba_2Cu_3O_{7-\delta}$ samples. Closed and open squares represent the temperature behavior of the first derivative $d\left(\lambda_{ab}^{-2}(T)/{}^{16}\lambda_{ab}^{-2}(0)\right)/dT$ for ^{16}O and ^{18}O substituted samples, respectively. The extrema in the first derivative around $T \approx 52.1(2)\,K$ and $51.0(2)\,K$ for ^{16}O and ^{18}O, respectively, clearly reveal the existence of an inflection point, characterizing the occurrence of a finite size effect in $1/\lambda_{ab}^2$. The solid and dashed lines indicate the leading critical behavior of a homogenous system with $L_c \sim \infty$.*

where Φ_0 is the flux quantum. The results of the finite size effect analysis in $^{16}O/^{18}O$ substituted $Y_{1-x}Pr_xBa_2Cu_3O_{7-\delta}$ ($x = 0.0$, 0.2, 0.3) samples are presented in Fig. 7.5, where the size of super conducting domains along the $c-$axis, L_c, versus the "inflection" temperature, T_{p_c}, are plotted. Two important points should be mentioned. (i) The domain size increases with decreasing T_{p_c} (T_c). This can be taken as an evidence for the shrinkage of limiting length scales upon change of doping, stemming from the behavior close to the quantum superconductor to insulator transition where T_c vanishes [3]. Here the cuprates become essentially two dimensional and correspond to a stack of independent slabs [4]. (ii) For a fixed Pr concentration the lattice parameters remain essentially unaffected by isotope substitution [5]. Accordingly, an electronic pairing mechanism, not taking into account coupling to local lattice distortions and anharmonic phonons, would imply $\Delta L_c = 0$. On the contrary, a significant change of L_c upon oxygen exchange uncovers the coupling to local lattice distortions and anharmonic phonons, involving the oxygen lattice degrees of freedom.

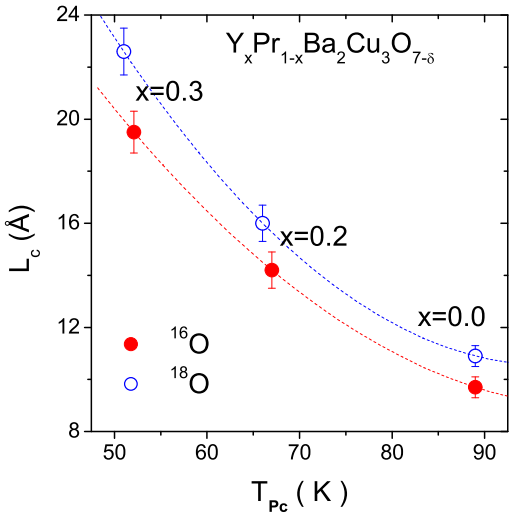

Figure 7.5: *Domain size L_c versus "inflection" temperature T_{p_c} for oxygen isotope $^{16}O/^{18}O$ substituted $Y_{1-x}Pr_xBa_2Cu_3O_{7-\delta}$ (x =0.0, 0.2, 0.3) samples. The dashed lines are guides to the eye.*

[1] M. E. Fisher and M. N. Barber, Phys. Rev. Lett. **28**, 1516 (1972).
[2] T. Schneider *et al.*, J. Phys.: Condens. Matter **15**, L763 (2003).
[3] T. Schneider, cond-mat/0210697.
[4] T. Schneider, Europhys. Lett. **60**, 141 (2002).
[5] F. Raffa *et al.*, Phys. Rev. Lett. **81**, 5912 (1998).

7.1.4 Isotope effect studies in magnesium diboride

The anomalous superconducting properties of MgB_2 such as, for example, specific heat and unusual behavior of the superconducting anisotropies, were explained by the existence of two sets of bands (π and σ) with different dimensionality and pairing strength. It was proposed [1; 2] that MgB_2 is a non-adiabatic superconductor, because of the strong coupling of the electrons to the E_{2g} phonon mode and the small Fermi energy. This would lead to the break-down of the *Migdal* adiabatic approximation, in which the density of states at the Fermi level, the electron-phonon coupling constant, and the effective supercarrier mass m^* are all independent of the mass M of the lattice atoms. To clarify this point, we continued a study of the boron isotope effect (BIE) on the magnetic penetration depth λ, a physical quantity directly related to the carriers effective mass m^*: $1/\lambda^2 \approx [\mu_0 e^2/c^2](n_s/m^*)$. Last year we obtained a BIE compatible with zero within the experimental error. To check the reproducibility of this result and to show that they are intrinsic for MgB_2, we repeated the experiment on samples of higher quality. To measure λ, we used again the μSR technique. For $Mg^{11}B_2$ and $Mg^{10}B_2$ isotope samples, we measured the temperature dependence of the muon spin depolarization rate σ, which is proportional to the second moment of the magnetic field distribution, and, under certain conditions, to the superfluid density $\sigma \propto 1/\lambda^2 \propto n_s/m^*$.

Therefore, a shift in $1/\lambda^2$ due to the isotope substitution would lead to a shift in m^*, since n_s does not change on isotope substitution.
In Fig. 7.6 the temperature dependence of σ for the new $Mg^{11}B_2$ and $Mg^{10}B_2$ isotope samples is reported. The data were fitted with the two-gap equation [3]:

$$\sigma(T) = \sigma(0) - w \cdot \delta\sigma(\Delta_1, T) - (1-w) \cdot \delta\sigma(\Delta_2, T), \tag{7.3}$$

with $\delta\sigma(\Delta,T)=\frac{2\sigma(0)}{k_B T}\int_0^\infty f(\varepsilon,T)\cdot[1-f(\varepsilon,T)]d\varepsilon$. Δ_1 and Δ_2 are the zero temperature large and small gaps, respectively, w is the relative contribution of the large gap to $\sigma(0)$, and $f(\varepsilon,T)$ is the Fermi distribution. For the temperature dependence $\Delta(T)$ of the gaps we used the conventional *BCS* gap function.

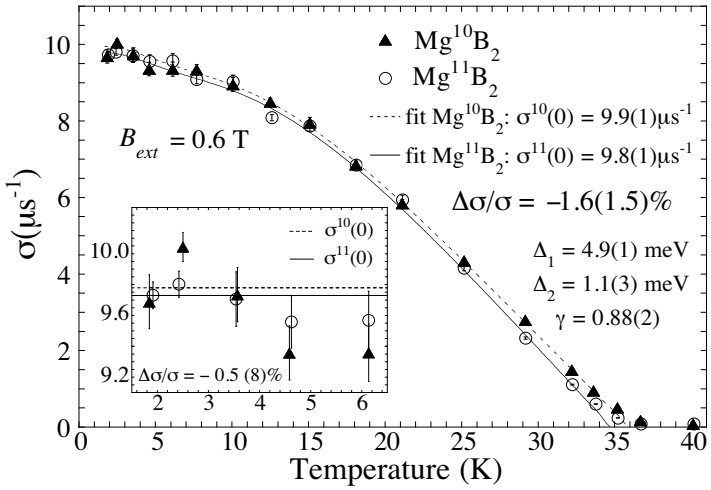

Figure 7.6: *Temperature dependence of the muon spin depolarization rate σ at $B_{\rm ext} = 0.6\,{\rm T}$ for the two isotope samples $Mg^{10}B_2$ (▲) and $Mg^{11}B_2$ (○). The solid ($Mg^{10}B_2$) and dotted ($Mg^{11}B_2$) lines are fits using Eq. (7.3). The inset shows the low-temperature region on a larger scale. The solid and dotted horizontal lines represent the weighted average values of $\sigma(0)$ for $T < 7.5\,{\rm K}$ for $Mg^{10}B_2$ and $Mg^{11}B_2$, respectively.*

From the fit we found $\Delta\lambda^2(0)/\lambda^2(0) = -1.6(1.5)\%$[3]. This result is in agreement with the previous one on samples of lower quality, showing that there is a negligible BIE on $\lambda^2(0)$. This is in contrast to the substantial oxygen isotope effect observed in the non-adiabatic cuprate HTS [4; 5]. Our results imply that polaronic or non-adiabatic effects in MgB_2 are absent or negligibly small. With this work we establish an upper limit to any theoretical prediction of such effects[1; 2].

[1] A. S. Alexandrov, Physica C **363**, 231 (2001).
[2] E. Cappelluti *et al.*, Phys. Rev. Lett. **88**, 117003 (2002).
[3] D. Di Castro *et al.*, cond-mat/0307330.
[4] J. Hofer *et al.*, Phys. Rev. Lett. **84**, 4192 (2000).
[5] R. Khasanov *et al.*, J. Phys.: Condens. Matter **15**, L17 (2003).

7.2 Studies of pressure effects in novel superconductors

7.2.1 Pressure effect on the penetration depth in $YBa_2Cu_4O_8$

Previous studies[1; 2; 3; 4] showed a substantial OIE on the in-plane penetration depth λ_{ab}, which indicates a non-adiabatic coupling of the electrons to phonon modes involving the movement of the isotope substituted atoms. Another way to study lattice effects are pressure experiments. The squeezing of the crystal lattice by external pressure changes the lattice parameters, the phonon spectrum and consequently the electron-lattice coupling. Surprisingly, the pressure effect on the magnetic field penetration depth has not attracted much attention so far.

Recently we performed the first measurements of the in-plane magnetic penetration depth λ_{ab} under high hydrostatic pressure (up to 11.5 kbar) in $YBa_2Cu_4O_8$. The temperature dependence of λ_{ab}^{-2} was extracted from Meissner fraction measurements at low magnetic field. A pronounced pressure effect on both the transition temperature T_c and $\lambda_{ab}^{-2}(0)$ is observed. Both quantities increase with increasing pressure. The pressure shift on $\lambda_{ab}^{-2}(0)$ can be attributed to (i) the pressure induced charge carrier transfer from chains to the planes and (ii) the decreasing of the in-plane charge carrier mass m_{ab}^*. However, it is demonstrated that the effect mainly ($\sim 2/3$) arises from the pressure dependence of m_{ab}^*.

[1] G.M. Zhao *et al.*, Nature (London) **385**, 236 (1997).

[2] J. Hofer *et al.*, Phys. Rev. Lett. **84**, 4192 (2000).

[3] R. Khasanov *et al.*, J. Phys.: Condens Matter **15**, L17 (2003).

[4] R. Khasanov *et al.*, Phys. Rev. Lett. **92**, 057602 (2004).

7.2.2 Pressure effect on the penetration depth in MgB_2

The pressure effect on the superconducting critical temperature T_c of MgB_2 has been studied at large. A linear pressure dependence was found, with dT_c/dP = 1.11(2) K/GPa [1]. It was attributed to the pressure induced lattice stiffening (increase of the phonon frequency) [2], rather than to the decrease in the electronic density of states. Comparison with theoretical calculations support the view that MgB_2 is a *BCS* superconductor with moderately strong electron-phonon coupling.
Apart from T_c, the most relevant superconducting parameter is the magnetic field penetration depth λ. A study of the pressure effect on $\lambda^{-2}(T=0)$, the so-called superfluid density, can give important information on how the electronic degrees of freedom are affected by lattice modifications and, therefore, on the nature of the electron-phonon coupling. In the cuprate HTS $YBa_2Cu_4O_8$, a large pressure effect on $\lambda^{-2}(0)$ was found (see section 7.2.2). Part of it can be attributed to the strong renormalization of the effective mass, due to the non-adiabatic coupling of the electrons to the lattice [3]. We studied the pressure effect on the magnetic penetration depth in the MgB_2 superconductor. The temperature dependence of $\lambda^{-2}(T)$ was extracted from the Meissner fraction measured in low magnetic field, and is plotted in Fig. 7.7 for two different pressures.

In analogy to our previous work [4], we fitted the experimental data at low temperature to a two-gap equation. The fit yields a very small pressure effect on $\lambda^{-2}(0)$: $\frac{\Delta\lambda^{-2}}{\lambda^{-2}} = -1.9(1.4)\%$. Our simple theoretical calculation of the pressure effect on λ [$\frac{\Delta\lambda^{-2}}{\lambda^{-2}} = -1.1\%$] confirms the experimental results, attributing the small pressure effect to a change in the stiffness of the Fermi velocity at low pressures. These results also confirm the adiabatic-like nature of the electron-phonon coupling, as it was revealed by the study of the boron isotope effect on $\lambda^{-2}(0)$ in MgB_2[4].

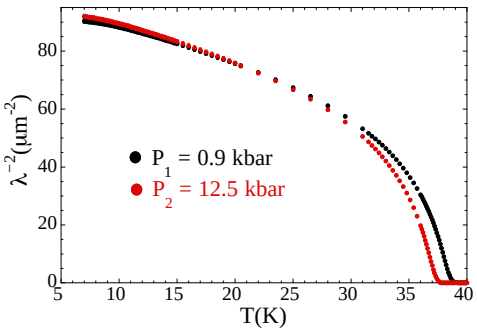

Figure 7.7: λ^{-2} *as a function of temperature for P = 0.09 GPa and 12.5 GPa.*

[1] T. Tomita *et al.*, Phys. Rev. B **64** (2001) 092505.

[2] F. Goncharov, Phys. Rev. B **64**, 100509(R) (2001).

[3] C. Grimaldi, E. Cappelluti, and L. Pietronero, Europhys. Lett. 42 , 667 (1998).

[4] D. Di Castro *et al.*, cond-mat/0307330.

7.3 Spectroscopic studies of novel superconductors

7.3.1 Low temperature NQR studies of $YBa_2Cu_4O_8$

In collaboration with the NMR group of the Kazan State University we continued our NQR study of the temperature dependent plane ^{63,65}Cu spin-lattice relaxation in superconducting $YBa_2Cu_4O_8$. In normal conducting $YBa_2Cu_4O_8$ the plane-copper spin-lattice relaxation is predominantly of magnetic origin caused by spin fluctuations and its temperature dependence is controlled by the spin-pseudogap phenomenon [1]. In the superconducting phase this magnetic contribution to the relaxation diminishes due to the opening of the superconducting gap. In previous measurements we have shown that with decreasing temperature this reduced relaxation changes its character and gets predominantly quadrupolar below 5 K with an unexpected temperature dependence [2]. The cause for this behavior is the appearance of new low frequency charge fluctuations at low temperatures. As a consequence of these new findings we extended the temperature range of our NQR spin-lattice relaxation measurements into the milli-Kelvin region. Fig. 7.8 shows the experimental results we obtained for ^{16}O and ^{18}O exchanged $YBa_2Cu_4O_8$.

Below 5 K the temperature dependence of the quadrupolar spin-lattice relaxation is characterized by a rate maximum at about 300 mK. This is a clear sign of a slowing-down of the dynamics of conjectured new charge inhomogeneities as e.g. stripe-like electronic structures. In a tentative model we can quantitatively describe the observed behavior by a distribution of charge fluctuation correlation times. Assuming thermally activated underlying processes it may be related to a distribution of energy barriers. A possible oxygen isotope effect on the details of the rate maximum is obscured by the errors of the data.

The slowing-down of dynamics is accompanied by a progressive reduction in the observed signal intensity of plane Cu nuclei (see Fig. 7.9). For the fully stoichiometric $YBa_2Cu_4O_8$ this phenomenon is observed for the first time. It seems similar to the so-called "wipe-out effect" observed in the LaSrCuO system (see e.g. [3]) but occurs at much lower temperatures. More detailed investigations are needed to clarify the origin of charge inhomogeneities in $YBa_2Cu_4O_8$ and have been started with a study of the temperature dependence of the plane Cu NQR relaxation behavior at very low temperatures in Ca doped $Y_{0.938}Ba_{1.962}Ca_{0.1}Cu_4O_8$.

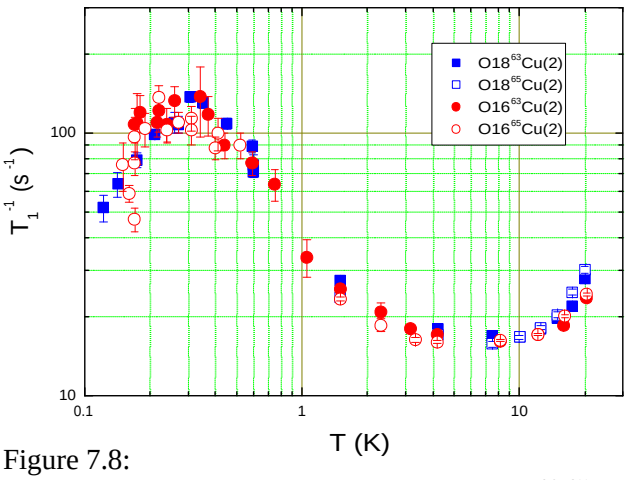

Figure 7.8:
Low temperature behaviour of the plane-^{63,65}Cu spin-lattice relaxation in ^{16}O and ^{18}O exchanged $YBa_2Cu_4O_8$.

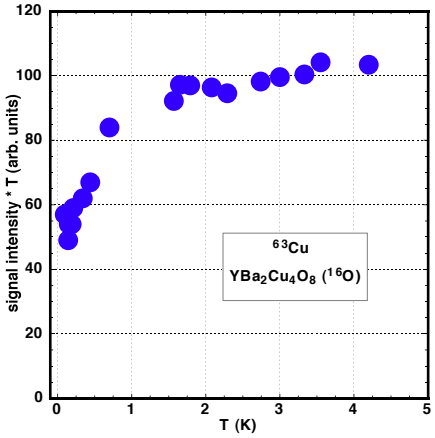

Figure 7.9:
Low temperature behaviour of the normalized plane ^{63}Cu NQR signal intensity of ^{16}O $YBa_2Cu_4O_8$.

[1] F. Raffa *et al.*, Phys. Rev. Lett. **81**, 5912 (1998).
[2] M. Mali *et al.*, Journal of Superconductivity: Incorporating Novel Magnetism **15**, 511 (2002).
[3] A. W. Hunt *et al.*, Phys. Rev. Lett. **82**, 4300 (1999).

7.3.2 NMR investigation of a MgB_2 single crystal

So far NMR investigations of MgB_2 have been performed exclusively by using polycrystalline samples. Regarding the superconducting phase in MgB_2 ($T_c = 39\,\mathrm{K}$), it is therefore very difficult to obtain reliable information on NMR parameters (particularly the relaxation rates) [1] due to the random orientation of crystallites with respect to the applied magnetic field and the strong critical field anisotropy [2]. Because high-quality single crystals of MgB_2 of sub-millimeter size became available recently [3] we started a single crystal MgB_2 investigation using quadrupole perturbed ^{11}B NMR. The measurements were performed from 250 K down to 9 K in a field of 9 T, applied along the boron planes, and revealed a transition temperature $T_c(9\,T) \approx 23\,\mathrm{K}$. An adapted micro-coil version of the resonant circuit was built in order to overcome the sensitivity limitations due to the unfavorably small size of the crystals. In normal conducting MgB_2 the electric field gradient (EFG) and the magnetic shift tensors at the boron site were determined. Whereas our experimental values for the EFG are in agreement with available literature data, we can now provide first reliable values for the magnetic shift components parallel and perpendicular to the boron layer, which are not available from powder sample investigations.

The ^{11}B spin-lattice relaxation rate (see Fig. 7.10) and the nuclear dipolar coupling were measured in the whole temperature range. In the normal conducting phase the relaxation rate is slightly anisotropic and it shows the well-known *Korringa* temperature behavior. In the superconducting phase it decreases exponentially with decreasing temperature due the opening of the larger of the two superconducting gaps. Within experimental errors no evidence for a coherence peak (*Hebel-Slichter*-peak) [4] in the relaxation rate was found. This is in contrast to published results obtained in powder sample investigations [5].

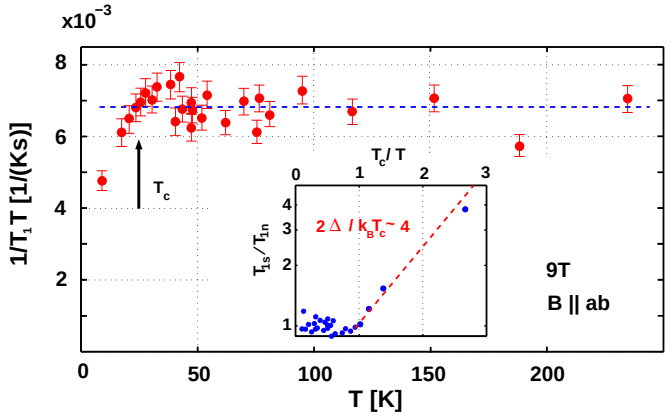

Figure 7.10: *Temperature dependence of the spin-lattice relaxation rate per unit temperature,* $1/T_1T$*. Insert: Plot of the ratio of* T_1 *in the superconducting phase and the normal phase against* T_c/T *showing the opening of the superconducting gap.*

[1] S.H. Baek *et al.*, Phys. Rev. B**66**, 104510 (2002).
[2] M. Angst *et al.*, Physica C**385**, 143 (2003).
[3] J. Karpinski *et al.*, Supercond. Sci. Technol. **16**, 221-230 (2003).
[4] L.C. Hebel and C.P. Slichter, Phys. Rev. **113**, 1504 (1959).
[5] H. Kotegawa *et al.*, Phys. Rev. Lett. **87**, 127001 (2001).

7.3.3 EPR study of lightly doped LaSrCuO

It is known that high-temperature superconductivity is achieved when a moderate density of conducting holes is introduced in the CuO_2 planes. At a critical concentration of doping $x_{cr} \approx 0.06$, superconductivity appears. However, it is still an unresolved issue how the electronic structure evolves with hole doping from the antiferromagnetic (AF) insulator to the paramagnetic metallic and superconducting state. While most of the theoretical models assume that the holes are homogeneously doped into CuO_2 planes, there is an increasing number of experiments pointing towards a highly nonuniform hole distribution leading to a formation of hole-rich and hole-poor regions [1]. This electronic phase separation is expected to be mostly pronounced at low hole concentrations. The Coulomb interaction limits the spatial extension of the electronic phase separation to hole-rich and hole-poor regions to a microscopic scale [2]. Therefore it is important to use a local microscopic method to study the electronic phase separation in cuprates. EPR is one of such methods.

We performed a thorough EPR investigation of the $La_{2-x}Sr_xCuO_4$ (LSCO) cuprate in the lightly doped range $0.01 \leq x \leq 0.06$, i.e. below x_{cr}. In order to observe the EPR signal, LSCO was doped with 2% of Mn^{2+} ions which replace the Cu ions in the copper-oxygen layer and serve as an EPR probe. The first important observation is that the EPR spectra consist of two lines. We found that they can be well fitted by a sum of two Lorentzian components with different linewidths: a narrow and a broad one.

Figure 7.11 shows the temperature dependence of the EPR intensity for the x=0.03 sample. One can see that the two EPR lines follow a completely different temperature dependence. The qualitatively different behavior of the broad and narrow EPR signals indicates that they belong to distinct regions in the sample. First we notice that the broad line vanishes at low temperatures. This can be explained by taking into account the AF order present in samples with very low Sr concentration [3]. In contrast to the broad line, the narrow signal appears at low temperatures and its intensity increases with decreasing temperature. This indicates that the narrow signal is due to the regions where the AF order is supressed. It is known that the AF order is destroyed by the doped holes, and above x = 0.06 AF fluctuations are much less pronounced [4]. Therefore, it is natural to relate the narrow line to regions with locally high carrier concentration and high mobility. Since we relate the narrow line to hole-rich regions, an exponential increase of its intensity at low temperatures indicates an energy gap for the existence of these regions.

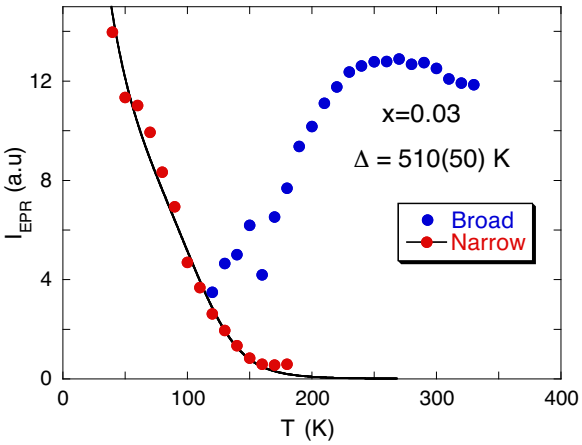

Figure 7.11: *Temperature dependence of the narrow and broad EPR signal intensity in* $La_{2-x}Sr_xCu_{0.98}Mn_{0.02}O_4$ *with* x = *0.03. The solid line represents a fit using the model described in the text.*

We propose a model where this microscopic phase separation is driven by the elastic interactions between the holes. This interaction is highly anisotropic being attractive for some orientations and repulsive for others [5]. The attraction between holes may result in a pair formation when holes approach each other closely enough. The pair formation can be a starting point for the creation of hole-rich regions by attracting additional holes. Because of the highly anisotropic elastic forces these regions are expected to have the form of stripes. Therefore the pair formation energy Δ can

be considered as an energy gap for the formation of hole-rich regions. The solid line in Fig. 7.11 represents a fit using this model. For the pair formation energy we obtained Δ = 460(50) K, which is practically doping-independent. This value agrees very well with the value of Δ obtained from the analysis of inelastic neutron-scattering and Raman data in cuprate HTS [6].

To summarize, performed EPR experiments provide a very important information about the electronic structure of the lightly-doped LSCO. First, we obtained a clear indication of the electronic phase separation into microscopic hole-rich and hole-poor regions. This shows that metallic domains exist in LSCO starting from very small carrier concentrations. A second important observation is the gap related with the formation of the metallic regions. The gap value extracted from our experiments is nearly the same as that deduced from other experiments for the formation of bipolarons [6], pointing to the origin of the metallic regions.

[1] See, for instance, *Phase separation in Cuprate Superconductors*, edited by K.A. Müller and G. Benedek (World Scientific, Singapore, 1993).
[2] V. J. Emery and S. A. Kivelson, Physica C **209**, 597 (1993).
[3] J. H. Cho *et al.*, Phys. Rev. Lett. **70**, 222 (1993).
[4] Ch. Niedermayer *et al.*, Phys. Rev. Lett. **80**, 3843 (1998).
[5] B. I. Kochelaev *et al.*, Mod. Phys. Lett. B**17**, 415 (2003).
[6] V. V. Kabanov and D. Mihailovic, Phys. Rev. B**65**, 212508 (2002).

7.3.4 Tri-layer Y123/Pr123/Y123 studies by means of LEμSR

There are several motivations behind the study of high-T_c multilayered structures. First, there is a technological need for heterostructures containing superconductors and insulating (or metallic) layers, for instance in the fabrication of Josephson and proximity effect junctions. Second, multilayers have been demonstrated in the past to be very powerful tools for studying the basic physics of semiconductors [1] and metals [2].

The low-energy-muon technique available at PSI is well suited for such a multilayer study: slow muons of tunable energy between 1 keV and 30 keV can be implanted at a very small and controllable depth below the surface of a sample. This allows all the advantages of standard μSR to be obtained in thin samples, near surfaces, and as a function of depth below surfaces [3]. We started the project with the simplest system of a 33 nm/50 nm/ 115 nm $YBa_2Cu_3O_7$/$PrBa_2Cu_3O_7$/$YBa_2Cu_3O_7$ (Y123/ Pr123/ Y123) structure grown at the Université de Genève. Our first μSR measurements in zero magnetic field are presented in Fig. 7.12.

Implantation energies of incoming muons were tuned to stop most of the muons in the appropriate layer (3 keV/12.5 keV/30 keV). In the top Y123 layer, we observed a slowly relaxing signal (due to the copper nuclear moments). The precession signal seen in the intermediate layer indicates that Pr123 is in an antiferromagnetic state with an internal field $B_{int} \sim 150$ G. We see no significant change in the internal field measured at T=110 K (which is above the superconducting transition for bulk Y123) and at T=5 K, respectively. The value observed is similar to the internal magnetic field known for bulk Pr123 at $T \sim 100$ K. At 30 keV most of the muons stop inside the last Y123 layer and give rise to the slow relaxing signal. The small additional precession signal seen in this spectrum corresponds to a small part of the muons which are still stopped in the antiferromagnetic intermediate layer. Zero field measurements confirmed the good quality of the tri-layer film and demonstrate the capability of the low-energy-muon technique. We also started measurements in a weak ($H < H_{c1}$) external

field applied parallel to the surface of the film. A preliminary analysis shows that the magnetic field measured inside both of the Y123 layers is screened better than it is estimated for separated Y123 layers in the Meissner state. This finding requires further experimental study. In particular we are planing experiments in single thin films of Pr123 and Y123.

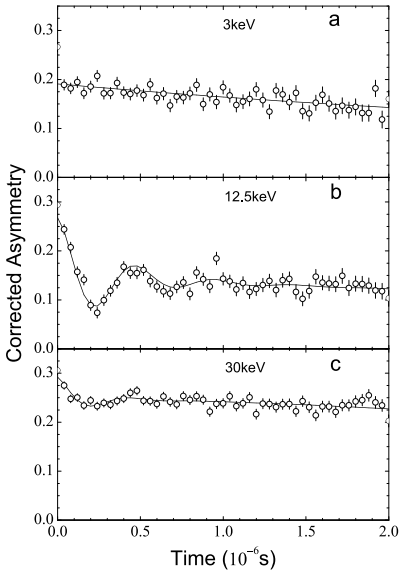

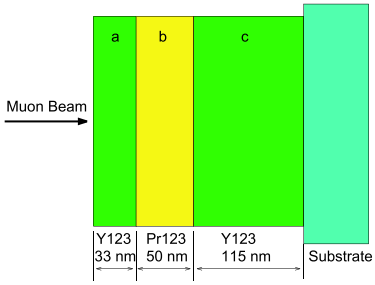

Figure 7.12: *Experimental μSR spectra measured at $T = 25\,K$ in zero magnetic field in:*
a) first $YBa_2Cu_3O_7$ layer;
b) intermediate $PrBa_2Cu_3O_7$ layer;
c) second $YBa_2Cu_3O_7$ layer.

[1] L. Esaki in *Synthetic Modulated Structures*, ed. by L.L. Chang and B.C. Giessen (Academic Press, New York, 1985), ch. 1.

[2] C.M. L. Falco and I.K. Schuller in *Synthetic Modulated Structures*, ed. by L.L. Chang and B.C. Giessen (Academic Press, New York, 1985), ch. 9,10.

[3] Morenzoni *et al.*, J. Appl. Phys. 81, 3340 (1997).

7.4 Magnetometry of cuprate superconductors

7.4.1 Doping dependence of superconducting properties of LaSrCuO by torque measurements

In continuation of our former projects we are working on the measurement of oxygen isotope effects in cuprate single crystals. As the isotope exchange occurs by diffusion of the oxygen within the sample, crystals used for this kind of study need to be very small (on the order of $150\,\mu m$ along each direction) to ensure a complete exchange. This rises the need for very sensitive equipment capable of measuring the small effects (below $5\,\%$) associated with isotope exchange experiments. In this case the torque magnetometer developed in our group specifically for this purpose is used. In a torque experiment a magnetic sample is exposed to an external magnetic field and the mechanical torque is measured as a function of temperature, and the applied field's magnitude and direction. Due to their anisotropy cuprate superconductors are well suited for this kind of study. Depending on the used theoretical models several superconducting properties such as the critical temperature T_c, the magnetic penetration depth λ, the correlation length ξ or the anisotropy parameter γ can be calculated from appropriate torque measurements.

Our interest lies in the investigation of the cuprate superconductor $La_{2-x}Sr_xCuO_4$ covering the whole doping regime from underdoped to overdoped samples with critical temperatures ranging from $18\,$K to $35\,$K. The field dependent measurements at a fixed field orientation (angle between the magnetic field and the samples main axis $\theta = 45°$) collected up to now can be used to extract some superconducting properties, but more measurements at different angles are needed to reliably determine all properties of interest. As an example the in-plane correlation length ξ_{ab} is shown in Fig. 7.13 as a function of temperature for the differently doped single crystals. The divergence close to T_c is well visible.

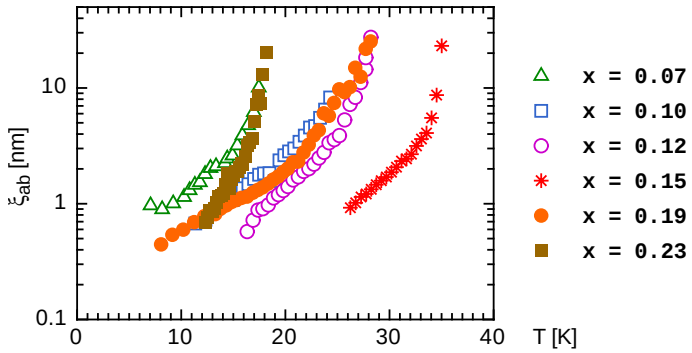

Figure 7.13:
Temperature dependence of the in-plane correlation length ξ_{ab} of $La_{2-x}Sr_xCuO_4$ for different doping levels x.

7.4.2 Anisotropy and internal field distribution of MgB_2 in the mixed state at low temperatures

The two-band superconductivity in MgB_2 leads to an array of unusual superconducting properties, particularly to a very unusual behavior of the superconducting anisotropies [1]. For example, a pronounced temperature dependence of the anisotropy γ_H of the upper critical field H_{c2}, directly related to the coherence length ξ, was observed [2] and calculated based on the two-band model [3]. In comparison, calculated values of the low field penetration depth anisotropy, γ_λ, are much lower, with an opposite temperature dependence [4]. This was experimentally confirmed as well by measurements of H_{c1} [5] and investigations by small-angle neutron scattering [6]. However, experiments indicate that, γ_λ is close to isotropicin the limit of very low fields, whereas it is soon rising strongly with increasing field H [6].

The behavior of the anisotropies of the superconducting length scales in the mixed state $H_{c1} < H < H_{c2}$ still needs to be clarified. Therefore, to study the field dependence of the anisotropy at low temperature, we analyzed SQUID and torque magnetization data, obtained from a MgB_2 single crystal with very low pinning, and μSR data, measured on unaligned MgB_2 powder. We determined the field dependence of the magnetic penetration depth, which is obtained from the field or angle dependence of the bulk magnetization (SQUID/torque), as well as from the average variation of the internal field (μSR).

The results from SQUID and μSR measurements are consistent in showing a rapid decrease of the superfluid density, $1/\lambda^2$, with the field H increasing below about 10 kOe (see Fig. 7.14). Moreover, both SQUID and torque data agree on the anisotropy γ_λ, increasing strongly with H as shown in Fig. 7.15. The analysis of the torque data further suggests that the coherence length anisotropy is not very different from the one of the penetration depth in any given field.

These findings are consistent with the decrease of the contribution to super-

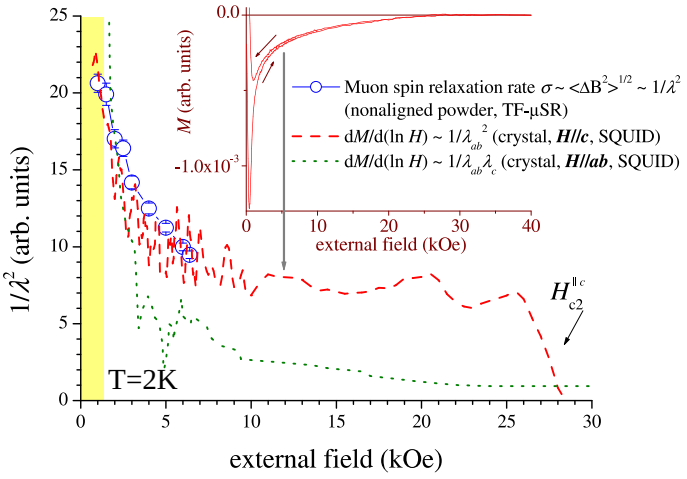

Figure 7.14: *Comparison of λ^{-2} vs H obtained from $dM/dlnH$ from SQUID measurements on a single crystal with $H//c$ (dashed curve) and $H//ab$ (dotted curve) and from the muon spin depolarization rate measured on unaligned powder (open circles). The shaded box indicates fields close to or lower than H_{c1}. Inset: $M(H)$ measured on the crystal with $H//c$.*

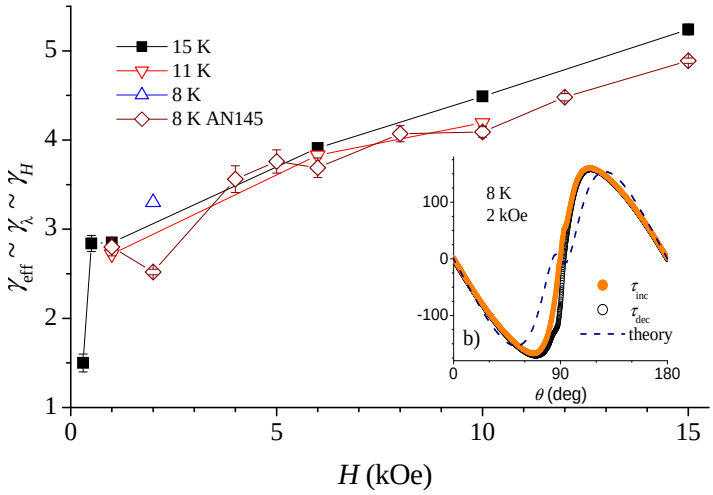

Figure 7.15: *Anisotropy as determined from an analysis of angle dependent torque data at various low temperatures, as a function of the applied field. Inset: Angle dependence of torque in 2 kOe at 8 K. The dashed line is a theoretical description, assuming* $\gamma_\lambda \ll \gamma_H$.

conductivity of the more isotropic π band, which has lower intrinsic H_{c2}^{π} in respect of the anisotropic σ band. The data presented indicate that H_{c2}^{π} is manifested by a rather broad crossover.

[1] M. Angst and R. Puzniak, in Focus on Superconductivity Research 2003, edited by B. P. Martines (Nova Publishers, New York, 2004), Chap. 1, preprint on cond-mat/0305048.

[2] M. Angst *et al.*, Phys. Rev. Lett. **88**, 167004 (2002).

[3] A. A. and A. E. Koshelev, Phys. Rev. B **68**,104503 (2003).

[4] V. G. Kogan, Phys. Rev. B **66**, 020509 (2002).

[5] L. Lyard *et al.*, Phys. Rev. Lett. **92**, 057001 (2004).

[6] R. Cubitt *et al.*, Phys. Rev. Lett. **91**, 047002 (2003).

8 Phase transitions, thermal transport and new materials

A. Schilling, M. Reibelt, and R. DellAmore

in collaboration with:
Paul Scherrer Institute (Ch. Rüegg), University of Bern (K. Krämer), Bhaba Atomic Research Center (G. Ravikumar), Forschungszentrum Karlsruhe (Th. Wolf, C. Meingast), Iowa State University (P. Canfield), ETH Zürich (J. Karpinksi).

In our new research group that started activity in April 2003 we are mainly investigating phase transitions, thermal transport, and the physical properties of new materials.

The study of phase transitions of vortex matter in conventional and high-temperature superconductors is a continuation of our work that we have done at the University of Karlsruhe (Germany). The physics of magnetic flux lines (vortices) in high-temperature superconductors has been a matter of very active research because of its high relevance for the technical applications of these materials [1]. Details in the magnetic phase diagrams of the vortex lattices in other classes of type-II superconductors have also become of growing interest [2; 3; 4]. However, no thermodynamic data on the different vortex phases and respective phase transitions in these systems are available. There are possibilities to circumvent known problems associated with vortex pinning [5; 6], and it is therefore likely that corresponding experiments will eventually be successful.

The main mechanisms for the transport of heat in simple three dimensional solids are quite well understood, and the corresponding contributions to the thermal conductivity by lattice vibrations (phonons) and nearly-free electrons in simple metals are standard subjects in all solid-state physics textbooks. By contrast, little is known about the mechanism for the heat transport in lower dimensional systems. The application of theoretical microscopic models for the heat transport in one and two dimensional atomic lattices, for example, gives surprising results. Fourier's law is expected to be violated in reduced dimensions, and the thermal conductivity should diverge with increasing system size [7; 8]. There are indeed a variety of real systems, where such deviations from standard three dimensional phonon heat transport can be expected, and we aim to perform thermal-conductivity experiments on such systems.

[1] G. Blatter *et al.*, Rev. Mod. Phys. **66**, 1125 (1994).
[2] V.G. Kogan *et al.*, Phys.Rev.B **55**, R8693.
[3] M.R. Eskildsen *et al.*, Phys.Rev.Lett.**78**, 1968 (1997).
[4] C.E. Sosolik *et al.*, Phys.Rev.B **68**, 140503 (2003).
[5] M. Willemin *et al.*, Phys.Rev.B **58**, R5940 (1998).
[6] E.H. Brandt and G.P. Mikitik, Phys.Rev.Lett.**89**, 027002 (2002).
[7] A. Lippi and R. Livi, J. Stat. Phys. **100**, 1147 (2000).
[8] O. Narayan and S. Ramaswamy, Phys.Rev.Lett.**89**, 200601 (2002).

8.1 Phase transitions in superconductors

8.1.1 Magnetocaloric effects and vortex phases in V_3Si

The magnetic phase diagram of the type-II superconductor V_3Si in the superconducting state has been previously studied by DC magnetisation measurements. In external magnetic fields in the mixed

state above $\mu_0 H$ = 1 T, the magnetisation M shows a pronounced hysteretic peak effect that defines two distinct magnetic fields: the peak field B_P where the hysteresis width is largest, and the onset field B_{HF} where the large peak in the hysteresis loop opens (see Fig. 8.1, upper figures). This onset has been shown to depend on the magnetic history of the sample and is sharpest after repeated fields cycles below B_{HF}. The magnetic region right below B_{HF} is believed to exhibit long-range order of the vortex lattice, while the peak region very likely corresponds to a disordered glass-like state.

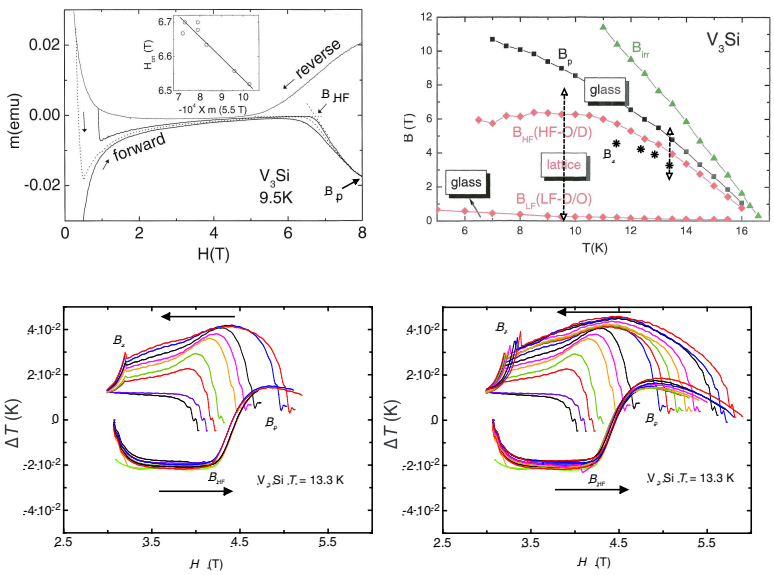

Figure 8.1:
Phase diagram and magnetocaloric effect in V_3Si (see text).

We have investigated the magnetic phase diagram of V_3Si using a differential calorimeter to detect possible thermodynamic phase transition between the different vortex phases. Our main result is shown in Fig. 8.1 (lower figures), where we have plotted the magnetocaloric effect on the sample temperature T in a differential setup with finite heat links. In the steady state, the temperature difference ΔT to a copper reference sample corresponds, to first approximation, to the variation of $\tau \frac{dH}{dt} \left(\frac{\partial M}{\partial T}\right)_H \frac{T}{C}$ of V_3Si, where τ is the thermal relaxation time of the sample due to the finite heat link to the surrounding heat reservoir, $\frac{dH}{dt}$ is the rate of the field variation, and C is the sample heat capacity. In such an experiment, the thermodynamic quantity $\left(\frac{\partial M}{\partial T}\right)_H$ is probed, which is usually inaccessible in magnetisation experiments due to the large hysteresis effects on M.

We have performed numerous experiments by varying the magnetic history of the sample below B_{HF}. We could not detect any feature that would indicate a thermodynamic phase transition at B_{HF} within the resolution of the experiment. However, we have measured a large self-heating effect as soon as the magnetic field enters the peak region from below, which we interpret as the onset of a dissipative process that reflects the destruction of the long-range ordered vortex lattice. Cycling the magnetic field back to low fields is again a dissipative process, and the amount of the produced heating power depends on the width of the magnetic loop. In addition, a distinct, first-order like feature develops at a field B_x, where an approximately constant amount of heat is suddenly released, leading to an immediate increase in sample temperature (see Fig. 8.1, lower figures). This field B_x does not depend on the magnetic history as long as the backward magnetic cycles start below B_P. Cycling down from a field above this peak value, however, results in a history dependence of the location of the heat-releasing field B_x. We believe that in a small magnetic-field cycle, starting at low fields and entering the peak region at B_{HF} but reversing the sign of $\frac{dH}{dt}$ below B_P, a metastable and perhaps incomplete glassy state is established in the peak region that discontinuously transforms back to a regular ordered solid at a well defined magnetic field B_x by releasing a finite amount of heat. Larger cycles that exceed the peak field B_P seem to produce disordered vortex configurations that transform back at different transformation fields B_x, depending on the width of the respective cycles.

These investigations show that a variety of thermal effects in V_3Si can be ascribed to the formation of different vortex phases. Most of these phases are not in thermodynamic equilibrium. To study these

glass-like phases in more detail we are now using external transverse AC-field coils that have been shown to be effective to drive non-equilibrium vortex states into a thermodynamic equilibrium [1; 2].

8.1.2 The effect of twin-boundary and intrinsic pinning on flux-lattice melting in single crystals of REBa$_2$Cu$_3$O$_{7-\delta}$ (RE = Y, Nd)

Some characteristic features of high-temperature superconductors, such as the magnetic-field-broadened resistive transition, have made pinning a central issue in the study of these materials. The presence of a melting transition for $H//c$ in untwinned $YBa_2Cu_3O_{7-\delta}$ crystals, in contrast to its absence in twinned crystals at low magnetic fields, indicates that twin boundaries play a major role in determining the vortex structure and its dynamics for this magnetic field orientation. Measurements of the magnetization on $YBa_2Cu_3O_{7-\delta}$ [3] and $NdBa_2Cu_3O_{7-\delta}$ [4] and transport measurements on $YBa_2Cu_3O_{7-\delta}$ [5] have indicated that for $H//ab$, strong commensurability effects between the vortex lattice and the crystal lattice occur, and the phase-transition line separating the vortex solid from the vortex liquid can be expected to strongly deviate from continuum-theory expectations. In fact an oscillatory melting temperature of the vortex smectic phase as a function of magnetic field has been measured by [3; 4; 5].

Every inhomogeneity of the material that weakens superconductivity can cause pinning. Pinning centers are, for example, grain boundaries, twin boundaries, dislocations, impurities and even the crystal structure itself in the case of layered superconductors. When the magnetic field is applied parallel to the superconducting CuO_2-planes in cuprates, Josephson vortices can form, with their axes along the weakly superconducting intermediate layers. These intermediate layers are effective pinning centers with respect to vortex motion perpendicular to the planes, but the vortices are still able to easily move parallel to the layers. This behaviour reminds of a smectic liquid crystal phase and is therefore called "vortex smectic phase". This phenomenon causes commensurability between the vortex lattice and the layered crystal structure when the condition $l = kd$ is satisfied [6; 7]. Here k is an integer number, $l = [\sqrt{3}\phi_0/(2\gamma B)]^{1/2}$ is the vortex distance along the c axis, and γ is the anisotropy parameter. The oscillations in the melting temperature as a function of magnetic field are a direct consequence of the difference between the confinement strengths in commensurate and incommensurate smectic vortex states. The commensurate states experience a stronger confinement potential and hence melt at higher temperatures than the incommensurate states. Figure 8.2 shows possible arrangements of the vortices in different commensurate and incommensurate states.

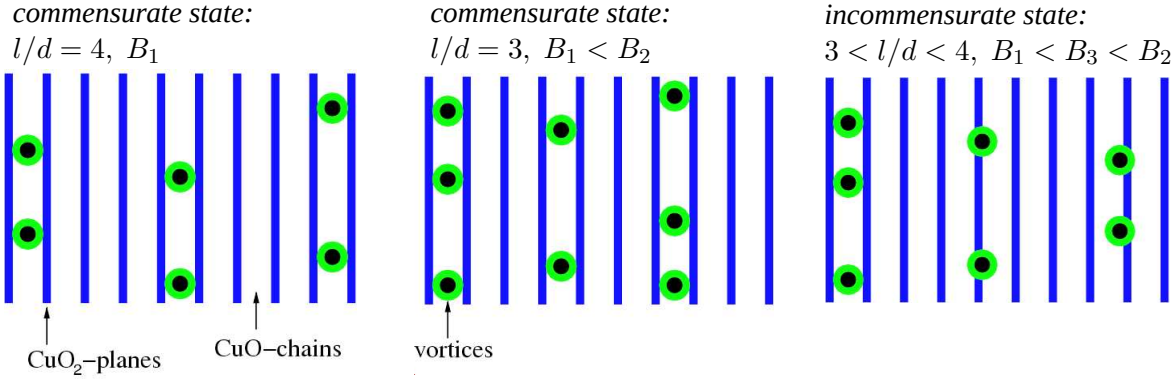

Figure 8.2: *Possible arrangements of the vortices in different commensurate and incommensurate states (see text).*

We have done a series of experiments to investigate these commensurability oscillations of the melting transition by specific-heat measurements, which has not been carried out before. Transport measurements indicated that the freezing of the vortex liquid into a smectic phase is a first-order transition, but a final confirmation requires measurements of thermodynamic quantities. We first investigated a twinned $NdBa_2Cu_3O_{7-\delta}$ ($T_c \approx 96.8$ K) single crystal. We used a high-accuracy differential thermal analysis (DTA) method [8], and attached a small laser-setup on the rotation axis to achieve a high angular resolution. Although we used the same single crystals as in [4], our experiments indicated that the pinning due to the strong twinning of the crystal makes a distinction between a continuous glass-to-liquid transition from the predicted continuous smectic-phase-to-liquid transition for $H//ab$ very difficult.

We decided to repeat these measurements on an oxygen depleted $NdBa_2Cu_3O_{7-\delta}$ single crystal with $T_c \approx 65$ K. It is known that such crystals exhibit a relatively large electronic anisotropy, which favours the formation of a vortex smectic phase already in moderate magnetic fields [5]. However, we again did not detect any distinct signal due to the expected phase transition, which we attribute to considerable random (chemical) disorder in the considered sample, thereby reducing the difference in the effectiveness of pinning between commensurate and incommensurate vortex states.

[1] M. Willemin *et al.*, Phys.Rev.B **58**, R5940 (1998).
[2] E.H. Brandt and G.P. Mikitik, Phys.Rev.Lett.**89**, 027002 (2002).
[3] A. A. Zhukov *et al.*, Phys.Rev.B **59**, 11213 (1999).
[4] H. Küpfer *et al.*, Phys.Rev.B **66**, 064512 (2002).
[5] S. N. Gordeev *et al.*, Phys.Rev.Lett.**85**, 4594 (2000).
[6] B. I. Ivlev and N. B. Kopnin, Phys.Rev.Lett.**64**, 1828 (1990).
[7] L. Bulaevskii and J. R. Clem, Phys.Rev.B **44**, 10234 (1991).
[8] A. Schilling and O. Jeandupeux, Phys.Rev.B **52**, 9714 (1995).

8.2 Thermal transport

8.2.1 Thermal-conductivity measurements on the quasi one dimensional $S = \frac{1}{2}$ quantum spin system $TlCuCl_3$

We performed thermal-conductivity measurements on the quantum spin system $TlCuCl_3$. This material has a monoclinic structure (space group $P2_1/c$) and shows changes of the spin state, that depend on the temperature T as well as on the applied magnetic field H.

The magnetic properties are determined by the $S = \frac{1}{2}$ exchange interactions between the Cu^{2+} ions, which are arranged in dimer pairs within Cu_2Cl_6-clusters. These planar dimers are stacked on the top of one another to form infinite double chains parallel to the crystallographic a-axis [1]. These double chains are located at the corners and the center of the unit cell in the $b-c$ plane, and are separated by Tl^+.

The magnetic ground state of $TlCuCl_3$ is a non-magnetic spin singlet, that is separated from the first excited triplet state by an excitation gap $\Delta = 0.65$ meV in zero magnetic field. The magnitude of the spin gap Δ was evaluated by previous magnetization and ESR measurements [2]. Inelastic neutron-scattering measurements revealed that the spin gap is due to the strong antiferromagnetic interaction $J = 5.68$ meV in the planar dimer of Cu_2Cl_6. The neighboring dimers are coupled by strong inter-dimer interactions along the double chain and in the (1 0 -2) plane [3; 4]. These 3D interactions play an important role concerning the quantum regime of this compound. The critical field H_c is defined as

the magnetic field corresponding to the gap energy $\Delta = g\mu_0\mu_B H_c$. When a magnetic field H larger than H_c is applied, the energy gap vanishes and the system can undergo a three dimensional magnetic ordering. The process of closing the spin excitation gap drives a quantum phase transition, which separates the quantum disordered singlet ground state from the 3D ordered ground state. The critical field for $TlCuCl_3$ is $\mu_0 H_c \approx 5.5$ T at $T = 0$ K [2]. The ordering temperature increases with increasing magnetic field for $H > H_c$. These features were interpreted and qualitatively well described in terms of the Bose-Einstein condensation (BEC) of spin triplets (magnons) [5]. The coherent superposition of the singlet and the $S_z = +1$ triplet components throughout the Cu^{2+}-dimers generates the condensate (S_z denotes the the quantum number for the spin component along the quantization axis) [6]. The spin structure in the ordered state has been determined by elastic neutron-scattering measurements. The spins lie in the $a - c$ plane, with $H||b$. They are arranged in parallel along a leg in the double chain and form an angle α = 39 ° with the a-axis. The transverse spin components are long-range ordered [7].

Our thermal-conductivity measurements are motivated by the above mentioned quantum phase transition and the possibility to detect thermal signatures due to the presence of a Bose-Einstein condensate. We measured the thermal conductivity with a conventional steady state method along the crystallographic a-axis, and applying a magnetic field H up to $\mu_0 H$ = 9T along the direction of the heat flux $\parallel a$. An enhancement of κ at lower temperatures is observable (see Fig. 8.3). With increasing magnetic field the absolute values of κ decrease in this temperature region. At higher temperatures the thermal conductivity is magnetic field independent. Further measurements of the thermal conductivity along other directions, especially along and perpendicular to the ordered spin vectors, are planned.

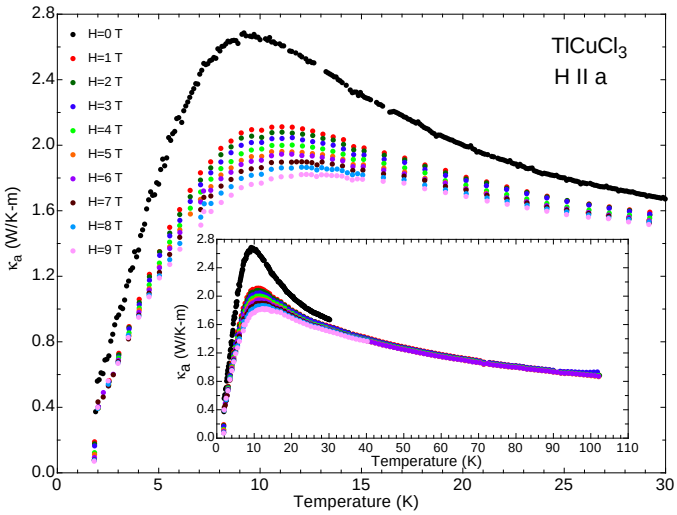

Figure 8.3: *The thermal conductivity of $TlCuCl_3$ along the crystallographic a-axis. The inset shows an extended temperature range.*

[1] K. Takatsu *et al.*, J. Phys. Soc. Jpn. **66**, 1611 (1997).
[2] A. Oosawa *et al.*, J. Phys.: Condens. Matter. **11**, 265 (1999).
[3] N. Cavadini *et al.*, Phys.Rev.B **63**, 172414 (2001).
[4] A. Oosawa *et al.*., Phys.Rev.B **64**, 094426 (2002).
[5] T. Nikuni *et al.*, Phys.Rev.Lett.**84**, 5868 (2000).
[6] Ch. Rüegg *et al.*, Nature **423**, 62 (2003).
[7] A. Oosawa *et al.*, J. Phys. Soc. Jpn. **72**, 1026 (2003).

9 Surface Physics

T. Greber, M. Hengsberger, J. Wider, M. Hoesch, W. Auwärter, M. Muntwiler, A. Tamai, A. Dolocan, M. Corso, C. Cirelli, T. Gresch, Ch. Schlepütz, M. Klöckner, W. Deichmann, J. Osterwalder

The surface physics laboratory is well equipped for the preparation and characterization of clean surfaces, ultrathin films and nanostructures under ultrahigh vacuum (UHV) conditions. Experimental techniques available to us include x-ray photoelectron spectroscopy (XPS) and diffraction (XPD), angle-resolved photoemission spectroscopy (ARPES), two-photon photoemission (2PPE) using femtosecond laser pulses, low-energy electron diffraction (LEED) and scanning tunneling microscopy (STM). At the nearby Swiss Light Source we have built up two more photoemission spectrometers, one for spin-resolved Fermi surface mapping and one for near-node photoelectron holography.

The research carried out during the report period can be grouped into four topics:

- *Surface states on clean metal surfaces*
  The close-packed (111) surfaces of several face-centred-cubic metals (e.g. Au, Ag, Cu, Ni) exhibit so-called Shockley surface states that propagate almost freely within the surface plane, and which have wave functions that decay exponentially both into the vacuum and into the bulk of the crystal. They thus exemplify a two-dimensional gas of nearly-free electrons (2DEG), which manifests itself in parabolic energy dispersion relations. On Au(111), this 2DEG is subject to spin-dependent momentum shifts due to the Rashba effect. We have measured these momentum shifts and the detailed spin structure in reciprocal space (Section 9.1). On vicinal Cu(111) surfaces we could show that the wavefunction of this 2DEG can localize on individual terraces, while photoemission matrix element effects still make the measured dispersion look free-electron-like (Section 9.2).

- *Monolayer films of hexagonal boron nitride on metal surfaces*
  The preparation of well-defined monolayer-thick films permits us to study the structural, electronic and magnetic properties at an interface between two different materials. In the nanosciences, such knowledge is essential for the understanding of how nanoscale structures and devices function. We have continued to study single monolayers of hexagonal boron nitride (*h*-BN) on transition metal surfaces as well-defined model cases for metal-insulator junctions. A new and more convenient precursor molecule was demonstrated to produce high quality films on Ni(111) (Section 9.3). On Rh(111) the *h*-BN film self-assembles into a remarkable nanostructure in the form of a two-layer nanomesh (Section 9.4), while on Pd(110) a variety of Moiré patterns is found (Section 9.5).

- *Adsorbed molecules*
  Molecular monolayers offer a highly interesting route to prepare functionalized surfaces. Chemists provide molecules with suitable chemical anchors and with the desired functional groups that are to be exposed at the surface. We are working on methods that can measure the bonding geometry of the molecules on the substrate, and we study the electronic properties of molecular layers that have a high degree of self-organized crystalline order within the layer. For C_{60} molecules on Ag(111) we find a strong dependence of the molecular orientation on the degree of potassium doping of the layer (Section 9.6). In Section 9.7 a new and efficient procedure is presented for unraveling the presence of several molecular orientations in such monolayers and quantifying their relative abundances. For a C_{60} layer on *h*-BN/Ni(1 1 1) a new type of phase transition is revealed where the charge transfer to the molecules changes due to a thermally excited rocking motion of the molecules (Section 9.8). In Section 9.9 the adsorption geometry of tartaric acid on Cu(110) is measured by a new generation XPD experiment that makes use of the high-brightness tuneable

synchrotron radiation of the SLS. The XPD patterns display directly the chiral character of the molecule when single enantiomers are adsorbed, as well as the conformation changes due to the interaction with the metal substrate.

- *Time-resolved electron diffraction*
  The setup of our picosecond time-resolved electron diffraction experiment is complete, and we have seen the first temporal correlation signals between laser pump pulses and electron probe pulses. This was achieved by aiming the electrons through a fine pinhole in a metal plate while hitting the entrance of the pinhole with the laser pulses (Section 9.10). The space charge produced by the laser light acts like a time-dependent valve for the electron pulse. This relatively simple setup can now be used in order to establish spatial and temporal overlap of the two pulses on a sample surface.

9.1 The spin-structure of the Shockley surface state on Au(111)

in collaboration with:
V.N. Petrov, St. Petersburg Technical University, Russia and L. Patthey, M. Shi and M. Falub, Swiss Light Source, Paul Scherrer Institut, 5232 Villigen, Switzerland

The reduced symmetry of a two-dimensional electron gas confined by asymmetric boundaries can result in a spin-splitting of the electronic levels in momentum space (Rashba splitting). Such a separation of up- and down-spins in k-space might be useful as a source of polarized electrons in future spintronic devices. The fundamental physics governing the strength and the detailed behaviour of the splitting have been investigated. The (111) surface of gold accommodates a Shockley-type surface state. This two-dimensional quasi-free electron gas is a model case; it displays a strong spin-orbit splitting proportional to the in-plane momentum of the electrons [1; 2; 3].

The spin-resolved photoelectron spectrometer COPHEE installed at the Surface and Interface Spectroscopy (SIS) beamline at the Swiss Light Source was used to investigate in detail the Fermi surface of the surface state on Au(111). For the first time a complete spin-resolved angular mapping of the photoelectrons emitted with linear polarized VUV radiation was performed. Such a mapping allows to determine the individual contributions to the Fermi surface from electrons of opposite spin. For the two-dimensional free-electron gas the Rashba model predicts the spins to lie in the surface plane, with a momentum shift for spins pointing in a counterclockwise (clockwise) direction tangential to the Fermi surface. Therefore we chose the tangential direction as the reference direction for spin-up and spin-down. An out-of-plane component of the spin-polarization is only expected if the electrons interact with the nuclear charge in such a way that an electrical field component parallel to the surface plane is experienced. Figure 9.1 shows the measured momentum distribution pattern of the surface state photoelectrons (a) and the tangential (b) and out-of-plane (c) components of the spin-polarization. The sample was cleaned by repeated sputtering and annealing cycles and held at $\approx$150 K during the measurements. The data were acquired in a 7 hrs. long continuous scan. In the polarization maps the modulation of the polarization components can be studied. From the intensity (a) and the in-plane polarization (b), which is obviously the dominant component, the spin-resolved intensities for spin-up (d) and spin-down (e) were calculated. Note the two individual Fermi surfaces with different radii (Fermi wave vectors). A detailed analysis of the polarization modulations for both the in-plane and the out-of-plane component was performed. Any modulation must reflect the three-fold symmetry of the surface. It was found that the polarization follows the tangent to the circular Fermi surface. No modulation could be observed within the detection limit of 2% (electron polariza-

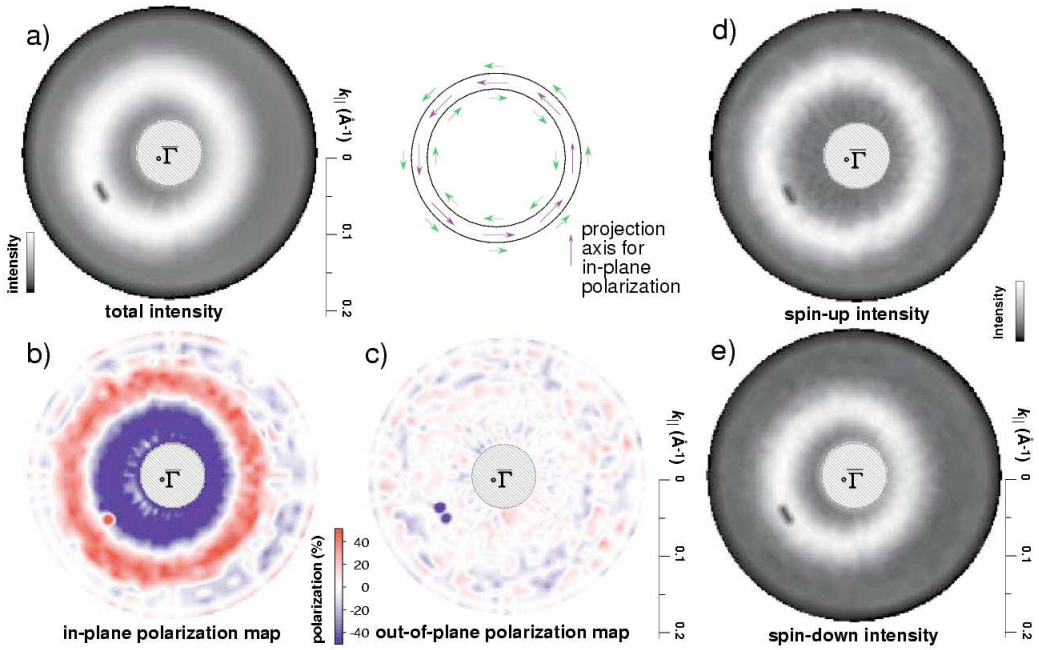

Figure 9.1: *Spin-resolved momentum distribution maps near the Fermi surface (E_B=170 meV) measured with UV-light of $\hbar\omega = 21.1$ eV.*
a) Total intensity map and a sketch of the Fermi surface and the predicted spin structure (guide to the eye). Purple arrows indicate the projection axes for in-plane polarization.
b) and c) Polarization maps in a color-scale representation for the in-plane component (b) and for the out-of-plane component (c) of the polarization vector. The in-plane polarization (b) is a projection on the tangents to the circular Fermi surface. Red (blue) indicates a counter-clockwise (clockwise) spin orientation.
d) and e) Individual spin-up and-spin down intensity maps derived from a) and b).

tion value). This allows the conclusion that the electrons experience on the average an electrical field perpendicular to the surface and the free-electron picture applies very well to the description of the surface state, including its spin structure.

[1] S. LaShell, B.A. MacDougall, E. Jensen, Phys.Rev.Lett.77 (1996) 3419.
[2] G. Nicolay, F. Reinert, S. Hüfner, P. Blaha,Phys.Rev.B 65 (2001) 33407.
[3] M. Muntwiler, M. Hoesch, V. N. Petrov, M. Hengsberger, L. Patthey, M. Shi, M. Falub, T. Greber, and J. Osterwalder, J. Electron Spectrosc. Relat. Phenom. in press (2004).

9.2 Localization of surface states in disordered step lattices

in collaboration with: L. Patthey, M. Shi and J. Krempasky, Swiss Light Source, Paul Scherrer Institut, 5232 Villigen, Switzerland

Real single crystal surfaces contain a variety of more or less complex defects. Isolated monoatomic steps are the most frequent imperfections on clean surfaces. It is known that such defects have a profound influence on many surface-related phenomena, such as heterogeneous catalysis, heteroepitaxy or self assembly of molecular super-structures. However, the underlying changes of the electronic

structure in the presence of defects are still poorly understood. As a model system, we have investigated the electronic structure of several vicinal Cu surfaces that can be obtained by cutting a single crystal under a small angle with respect to the dense (111) planes. Suitably prepared, these surfaces exhibit hexagonally close packed terraces of a few atomic spacings width, bounded by a monoatomic step lattice, where the lattice constant may be chosen by varying the miscut angle. Since the repulsive interactions between steps are comparable with thermal energies, fluctuations in the lattice positions, mediated by diffusion of atoms along the step edges, are unavoidable. Thus, step positions oscillate around their nominal lattice points, analogous to thermal vibrations in an atomic lattice. However, the frequencies of these oscillations are much lower than those of lattice vibrations, and the amplitudes reach values which would cause a single crystal to melt. It is thus natural to ask whether electronic states still propagate under such conditions or whether they tend to localize, as expected for amorphous or liquid condensed matter. This allows to study electronic properties in a unique structural regime, hardly accessible otherwise.

We used the free-electron-like Shockley surface state as an electronic probe of the disordered step–lattice. This state has been shown to remain free-electron like on vicinal Cu(111) surfaces with small step–step separations (< 15Å). In this regime, the step–lattice is well ordered and thus can be treated as a one–dimensional super–lattice which causes a slightly anisotropic dispersion of the surface state, but does not cause localization. Increasing the terrace width to a critical value of half of the surface state Fermi wave length, we recently found the opening of super–lattice band gap, which clearly demonstrates that a description of the step arrays as super–lattice is appropriate [1]. On the other hand, recent experiments of Mugarza *et al.* revealed that surface states on vicinal Au(111) fully localize perpendicular to the step direction for terrace widths > 30Å, while they remain free-electron-like along the steps [2]. This result was in contrast to earlier experiments on vicinal Cu, which always showed free-electron-like dispersing states, also for terrace lengths where a super–lattice description is inappropriate. Analyzing our recent experiments carried out at the SIS beamline of the Swiss Light Source, we could show that the roughly parabolic band of high intensity observed previously in photoemission from vicinal Cu is not indicative of propagating states, but is fully consistent with the assumption of lateral quantum well states localized on single terraces [3]. This is illustrated in Fig. 9.2, where we simulated photoemission This is illustrated in Fig. 9.2, where we simulated photoemission

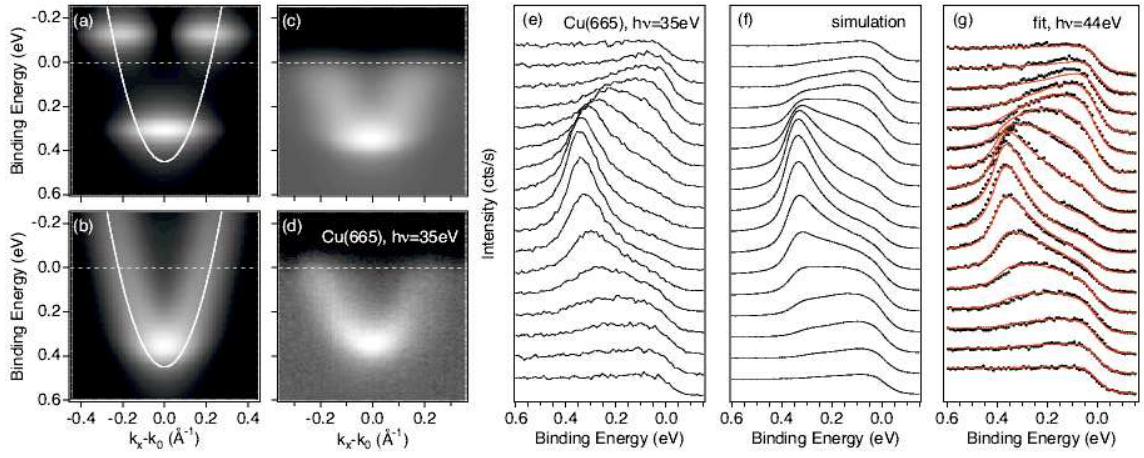

Figure 9.2: *Simulation of photoemission data from the Shockley surface state on Cu(665). a) Intensity distribution for isolated quantum wells of 25Å width, assuming a line width of 90meV. b) same for a Gaussian distribution of the well–width. c) Simulated intensity distribution from (b) with a constant background and multiplied with a Fermi function. d) Photoemission data from Cu(665). e),f) EDCs from c) and d). g) Fit to a refined model (for details see Ref. [3]).*

data expected from single decoupled lateral quantum wells, and from a distribution of quantum wells with different widths, as found on vicinal surfaces with large step–step separations. The apparently parabolic band, which closely resembles the experimental data, arises as a consequence of the strong momentum dependence of the matrix element in conjunction with the averaging over different terrace sizes.

[1] F. Baumberger, M. Hengsberger, M. Muntwiler, M. Shi, J. Krempasky, L. Patthey, J. Osterwalder, and T. Greber, Phys.Rev.Lett.**92**, 016803 (2004).

[2] A. Mugarza, A. Mascaraque, V. Pérez–Dieste, V. Repain, S. Rousset, F.J. García de Abajo, and J.E. Ortega, Phys.Rev.Lett.**87**, 107601 (2001).

[3] F. Baumberger, M. Hengsberger, M. Muntwiler, M. Shi, J. Krempasky, L. Patthey, J. Osterwalder, T. Greber, Phys.Rev.Lett., in press.

9.3 Synthesis of one monolayer of hexagonal boron nitride on Ni(111) from B-trichloroborazine $(ClBNH)_3$

in collaboration with: H.U. Suter, Physik Institut der Universität Zürich, and H. Sachdev, Institut f. Anorg. Chemie, Universität des Saarlandes, D-66041 Saarbrücken, Germany

Single layer h-BN films may be grown on Ni(111) by using B-trichloroborazine $(ClBNH)_3$ as a molecular precursor [1]. This way of producing stoichiometric, ultimately thin h-BN layers is an alternate route to the use of borazine $(HBNH)_3$ [2; 3]. The handling of borazine, a reactive liquid, is not very simple, whereas B-trichloroborazine sublimates from the solid phase. The decomposition reaction of the molecules to form the h-BN film proceeds at 1000 K via the path $(ClBNH)_3$ + Ni(111) $\rightarrow$ h-BN/Ni(111) + 3(HCl). Scanning tunneling microscopy (STM) experiments show that high quality films can be grown, as for the more established method that uses borazine [4] (see Fig. 9.3). The h-BN growth patterns indicate a reaction mechanism proceeding via ring opening of these cyclic BN molecules. A set of density functional calculations for B-trichloroborazine, borazine and N-trichloroborazine yields bond energies and bond lengths in these molecules and helps rationalizing the similar film morphologies and defects irrespective of the use of $(HBNH)_3$ [4] or $(ClBNH)_3$ [1].

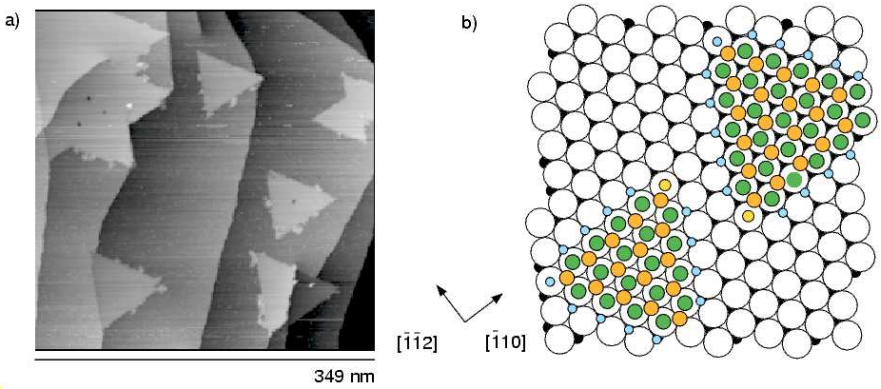

Figure 9.3: *Single layer h-BN islands on Ni(111). a) STM image from a partial coverage of h-BN on Ni(111) as formed from B-trichloroborazine (V_{sample}=-0.2V, I_t=0.5nA). The triangles with opposite orientations are h-BN islands with B on fcc and B on hcp sites, respectively. b) Corresponding hard sphere models for the two types of islands with hcp (left) and fcc (right) domains. From [1].*

[1] W. Auwärter, H.U. Suter, H. Sachdev and T. Greber, Chem. Mater. **16**, 343 (2004).
[2] A. Nagashima, N. Tejima, Y. Gamou, T. Kawai, and C. Oshima, Phys.Rev.B **51**, 4606 (1995).
[3] W. Auwärter, T.J. Kreutz, T. Greber, J. Osterwalder, Surf. Sci. **429**, 229 (1999).
[4] W. Auwärter, M. Muntwiler, J. Osterwalder and T. Greber, Surf. Sci. **545**, L735 (2003).

9.4 Boron nitride nanomesh

A new mesh-like nanostructure (Fig. 9.4a) is found when *h*–BN is deposited on the Rh(111) surface [1]. The large lattice mismatch of 6.7% between the two systems is likely the main reason leading to its formation. Due to its highly regular periodicity of 3 nm it is a unique link between the nano- and mesoscopic world, so that it can be easily used as a template to organize molecules into supramolecular structures. It is thermally stable up to 1000 K and resistant to air exposure.

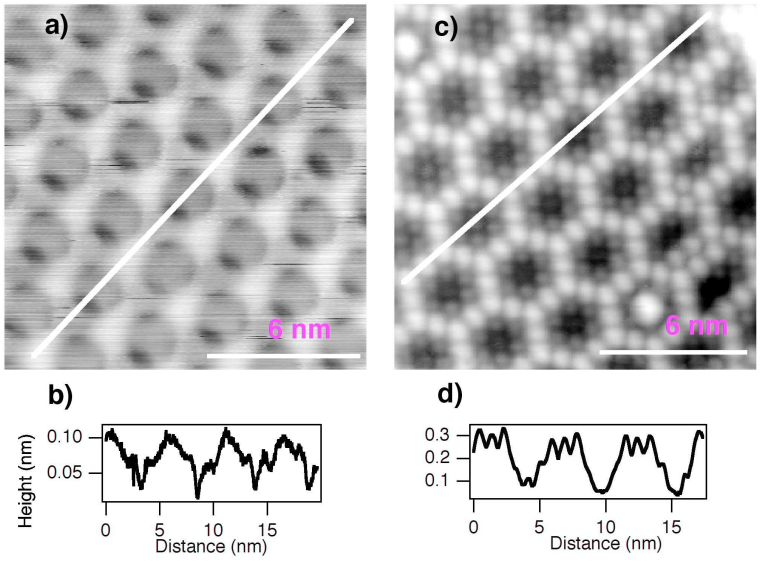

Figure 9.4:
a) Constant–current STM image (-2 V and 1.0 nA) of the h–BN nanomesh.
b) Cross–sectional profile along the white line in a).
c) Constant–current STM image (-2 V and 1.5 nA) of roughly one monolayer of C_{60} adsorbed on the nanomesh.
d) Cross–sectional profile along the white line in (c).

This structure self-assembles when the clean Rh(111) surface is kept at 1070 K during exposure to 40 L of borazine $(HBNH)_3$. From the calibration with x–ray photoelectron spectroscopy of the B1s and N1s signals with respect to Rh3s, a coverage of 1.5 ML of *h*–BN on Rh(111) is calculated. The analysis of STM images combined with LEED pattern information results in the following picture: the hexagonal nanomesh consists of two atomic mesh layers with a periodicity of 32 ± 2 Å which corresponds to 13×13 *h*–BN unit cells growing on top of 12×12 Rh unit cells. The hole diameter of the top layer is 24 ± 2 Å; it may be slightly smaller in the bottom one. The mesh wire width is 9 ± 2 Å. The two layers are offset in order to cover most of the metal surface. While the first layer sits flat on the substrate, the second one behaves like a corrugated sheet which follows the underlying topography: it is pulled into the first layer holes and pushed out when superimposed on the first layer wires. The real height of the nanomesh cannot be directly extracted from STM images such as the one in Fig. 9.4a. The line profile in Fig. 9.4b indicates that the step height from the Rh surface to the first *h*–BN layer as well as from the first to the second layer is only 0.5 Å. This is due to electronic effects, since the *h*–BN layer is an insulator (in the sense that there are no *h*–BN electronic states in the Rh–d band region and at the Fermi level), and the STM images thus reflect the lateral changes of the tunneling resistance through the nanomesh. The real corrugation can be observed when C_{60} molecules are deposited on the structure (Fig. 9.4c). They decorate the mesh and 11 to 13 molecules are found in each unit cell. The corrugation of the layer is here 2 Å (Fig. 9.4d), indicating *h*–BN step heights as on Ni(111) [2].

[1] M. Corso, W. Auwärter, M. Muntwiler, A. Tamai, T. Greber, J. Osterwalder, Science **303** (2004) 217.

[2] M. Muntwiler, W. Auwärter, F. Baumberger, M. Hoesch, T. Greber, J. Osterwalder, Surf. Sci. **472** (2001) 125.

9.5 *h*–BN/Pd(110): a hexagonal covalent network on a rectangular substrate

The properties of hexagonal boron nitride monolayers adsorbed on the Ni(111) surface have been studied for several years, because this system represents a model case for a perfect metal/insulator junction [1]. Due to the small compressive lattice mismatch of 0.4%, the *h*–BN forms large ordered terraces with a low corrugation of 0.1 Å. In the case of *h*–BN/Rh(111), the large tensile lattice mismatch of 6.7% between the two systems leads to the formation of the bilayer nanomesh discussed in the previous section. What happens when the *h*–BN unit cells aggregate on a non-hexagonal and incommesurate substrate?

On the Pd(110), the *h*–BN units do not find a unique way to register with the substrate. As a consequence, they form many different domains of Moiré patterns distributed randomly over the surface.

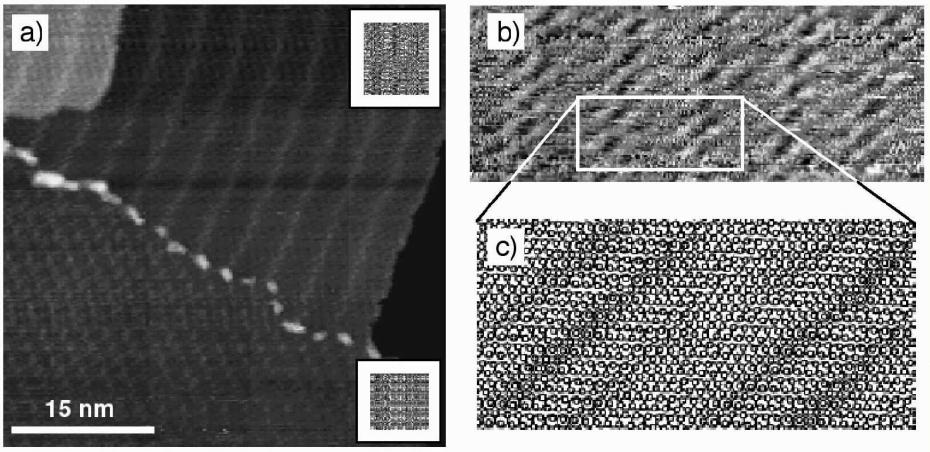

Figure 9.5:
a) Constant–current STM image (1.0 V and 1.0 nA) of h–BN/Pd(110) showing two different Moiré patterns separated by a domain boundary. The inset in the top right corner depicts an atomic model for the upper Moiré domain (see (b) and (c)), the one in the bottom right corner is an atomic model for the lower domain.
b) High resolution STM image for a region of the upper domain.
c) Atomic model for this same domain, where a layer of boron nitride, represented by nitrogen atoms only, is placed on the substrate, rotated clockwise by 5 degrees with respect to [001] crystallographic direction of the Pd(110) surface. In b) it can be seen that the STM images bright ridges along the darker Moiré stripes, leading to the continuous bright stripes in a) for this domain. This is believed to be due to an electronic effect.

The LEED patterns recorded over a wide energy range (from 50 to 300 eV) show that each palladium principal lattice spot is surrounded by a large circle. This indicates that the *h*–BN domains are oriented randomly with respect to the substrate surface. The radii of the circles correspond to the lattice constant of *h*–BN. The Moiré domains show clearly in STM images from monolayer films (Fig. 9.5a).

They are separated by domain boundaries that are decorated by white features of an apparent height of 1.8 ± 0.3 Å. The Moiré contrast can be understood with a simple atomic model placing a *h*–BN layer, represented by the nitrogen atoms alone, on top of the Pd(110) surface layer. By varying the azimuthal orientation between film and substrate, various domain patterns similar to those observed in STM images can be generated. This procedure is justified since it has recently been found that, under similar tunneling conditions, it is primarily the N atoms that are imaged by the STM [2]. Figure 9.5b shows a close-up STM image of the upper domain, with its characteristic Moiré stripes that are well reproduced by the model depicted in Fig. 9.5c.

[1] W. Auwärter, One Monolayer of Hexagonal Boron Nitride on Ni(111): an Atomically Sharp Interface, PhD thesis Universität Zürich (2003).

[2] G. B. Grad, P. Blaha, K. Schwarz, W. Auwärter, T. Greber,Phys.Rev.B **68** (2003) 085404.

9.6 Doping induced reorientation of C_{60} molecules on Ag(111)

in collaboration with:
Z.-X. Shen, Physik-Institut, Universität Zürich (while on Sabbatical) and Department of Applied Physics and Stanford Synchrotron Radiation Laboratory, Stanford University, Stanford, USA

Alkali–doped C_{60} compounds (fullerides) present a lot of interesting properties. Depending on the concentration of the dopant they display metallic or insulating behaviour, and they even become superconducting at temperatures as high as the best conventional superconductors. The variety of different electronic properties observed has been assigned to the simultaneous importance of electron-phonon and electron-electron interactions [1].

Only recently it became possible to measure the band dispersion of the partially filled lowest unoccupied molecular orbital (LUMO) in the electron doped C_{60}/K/Ag(111) system [2]. Density functional calculations (DFT) indicate that the electronic band dispersion is highly sensitive to the relative ori-

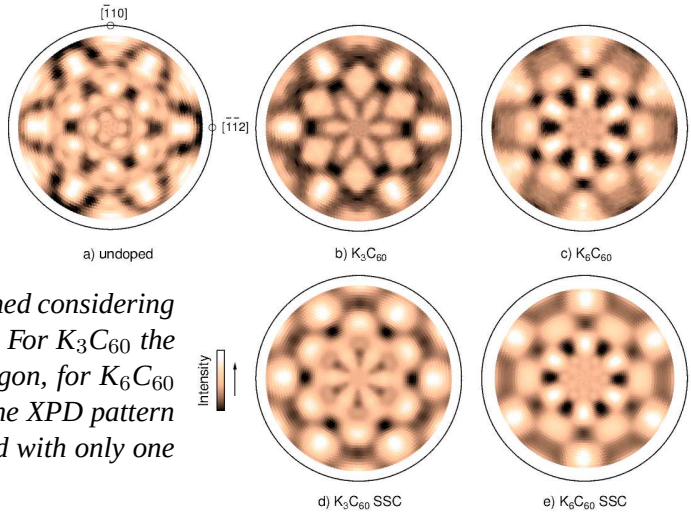

Figure 9.6:
C 1s XPD patterns from one monolayer of C_{60} on the Ag(111) surface.
a), b) and c) Experimental patterns for one undoped monolayer, K_3C_{60} and K_6C_{60}, respectively.
d) and e) Calculated SSC patterns obtained considering one inequivalent molecular orientation: For K_3C_{60} the molecule face the surface with the hexagon, for K_6C_{60} with the bond between two hexagons. The XPD pattern from the undoped layer cannot be solved with only one orientation of the molecule.

entation of neighboring molecules [2]. In order to determine experimentally the orientation of the C_{60} molecules on Ag(111) and to investigate the role of potassium as a dopant we used angle–scanned x–ray photoelectron diffraction (XPD). This technique has already shown to be a very powerful tool for measuring the orientation of C_{60} adsorbed on different metallic surfaces [3].

In Figs. 9.6a), b) and c) we show the experimental patterns for three doping levels. The pronounced differences reveal that potassium induces a change in the orientation of the molecule. In the undoped monolayer the experimental pattern corresponds to more than one defined orientation. Upon doping with potassium the layer gets ordered and two different orientations can be identified for K_3C_{60} and K_6C_{60}. The single–scattering cluster (SSC) calculations were obtained considering one orientation (Figs. 9.6d) and e)). They reproduce quite well the overall positions and shapes of the prominent forward-focusing maxima in the experimental patterns. When the LUMO is half-filled (K_3C_{60}) the molecules face the surface with a hexagon. When the LUMO is fully occupied (K_6C_{60}) they face it with a bond between two hexagons. An azimuthal rotation of the molecule away from the high symmetry crystal axes of the substrate is found for both doping levels. The orientation found in this analysis for K_3C_{60} is in reasonable agreement with that expected from the DFT calculations [2]. K2*p* XPD reveals the same change in the orientation of the molecules and gives indications for the dopant sites in both cases. The reorientation of C_{60} induced by potassium is important to understand the effects of doping on the electronic properties of fullerides.

[1] O. Gunnarsson, Rev. Mod. Phys. **69** (1997) 575.

[2] W.L. Yang et al., Science **300** (2003) 303.

[3] R. Fasel, P. Aebi, R.G. Agostino, D. Naumovic, J. Osterwalder, A. Santaniello, L. Schlapbach, Phys.Rev.Lett.**76** (1996) 4733.

9.7 Automated determination of coexisting inequivalent orientations of C_{60} molecules on Ag(111)

As is exemplified in the previous section, XPD has great potential for determining the orientation of large adsorbed molecules on metallic surfaces, especially in the case of C_{60}. Experimental XPD patterns are usually compared with simulated ones produced by single–scattering cluster (SSC) calculations. Using a vast trial–and–error structure search, it has even been possible to determine the relative abundance of two coexisting orientations of C_{60} on a Ag(001) surface [1]. Attempts to fit the pattern recorded from C_{60} molecules adsorbed on a Ag(111) surface (see Fig. 9.6a), however, provided no satisfactory conclusion concerning the molecular orientations. One plausible cause might be the limitation of the maximum number of coexisting inequivalent orientations in the available fitting routines.

The scope of this work has been to approach in a more general way the problem of fitting XPD patterns to a combination of simulated orientations. One would like to specify any arbitrary maximum number of coexisting orientations for the fit. The routine should be kept as material-unspecific as possible, thus allowing analysis of different molecular adsorbate systems. As in earlier procedures, the multipole expansion of the experimental pattern is compared with a linear combination of a limited set of calculated patterns representing inequivalent orientations. New features include minimization of a reliability factor via simulated annealing techniques, the rotation of the simulated patterns directly in the space of their multipole expansion coefficients, and automatic determination of the relative abundance of the present orientation through freely variable weight factors.

First tests have shown that the routine reliably reproduces arbitrary linear combinations of simulated patterns. The abundances of up to five different orientations with weight factors ranging from 0.04 to 0.45 have been correctly identified to within 0.1 percent of the total composition (see Fig. 9.7). The application to real experimental data has been hindered so far by issues concerning the intrinsic background of the measurements. A possible normalization procedure to counter this problem has been implemented, but is not yet fully operational.

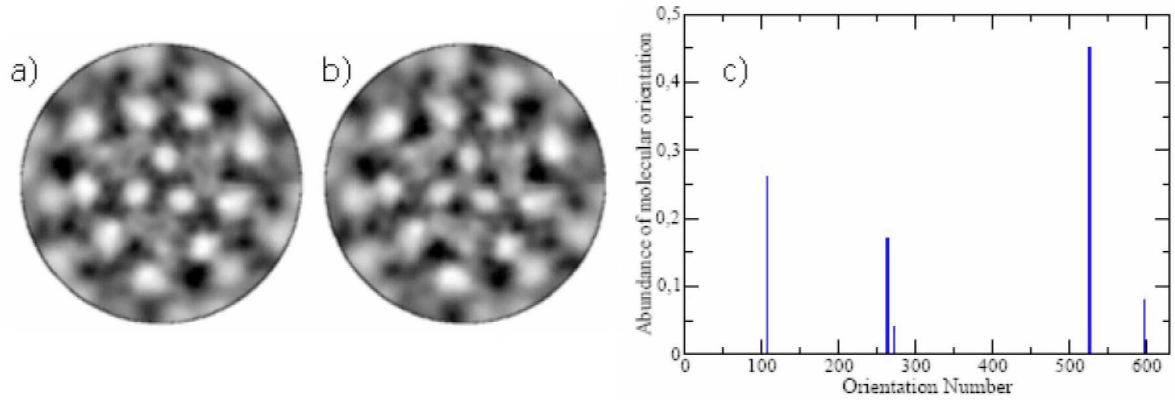

Figure 9.7: *First fitting results:*
a) simulated test pattern for C 1s emission from C_{60} molecules, representing the linear combination of 5 arbitrary inequivalent orientations,
b) the fit result for that test pattern and
c) the histogram showing the fitted orientation distribution.
For all but the correctly identified 5 orientations from the test pattern the weight factors are < 0.0002. The abundances of the five present orientations have been correctly identified to within 0.1% of the total composition.

[1] C. Cepek, R. Fasel, M. Sancrotti, T. Greber, J. Osterwalder, Phys.Rev.B **63** (2000) 125406.

9.8 Temperature-dependent charging of monolayer C_{60} on *h*-BN/Ni(1 1 1)

in collaboration with: A. Seitsonen, Physikalisch-Chemisches Institut der Universität Zürich

Monolayer hexagonal boron nitride (*h*-BN) on Ni(1 1 1) represents an atomically sharp insulating layer with well-known structure (see also Section 9.3) on a ferromagnetic substrate. With a metallic adsorbate deposited on top of it, it could form a model metal-insulator-metal interface for developing and testing charge and spin transport theory across magnetic heterojunctions. In contrast to elemental metals that either form three-dimensional clusters on top of *h*-BN or intercalate underneath, C_{60} forms a compact wetting layer on *h*-BN/Ni(1 1 1) [1]. C_{60} layers become metallic upon doping with alkali metals [2], and a C_{60}/*h*-BN/Ni(1 1 1) layer structure may thus represent such a model system.

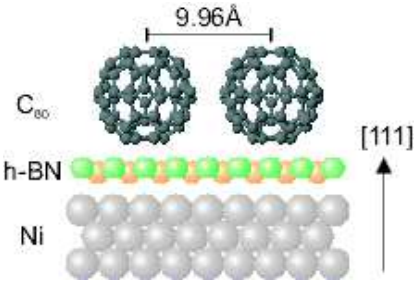

Figure 9.8:
Model of the adsorption geometry of monolayer C_{60} on h-BN/Ni(1 1 1) (side view).
The molecules arrange themselves in a commensurate 4×4 superstructure with a lattice constant of 9.96 Å.

In the line of known C_{60} monolayer systems, C_{60}/*h*-BN/Ni(1 1 1) can be ranged between C_{60} adsorbed on plain metals, where the molecules are spontaneously charged by 1–2 electrons per molecule [3], and insulators or semiconductors, where the molecules remain uncharged [2]. The film structure of C_{60}/*h*-BN/Ni(1 1 1) is illustrated in Fig. 9.8. The electronic properties of the system are illustrated in Fig. 9.9 showing He I_α excited photoemission spectra. The most prominent features of the spectra stem from the C_{60} valence shell, where the highest occupied molecular orbital (HOMO) is marked in

the graph. Comparing spectra at different temperatures, one notices that the C_{60} features are shifted to higher binding energies for the higher temperature, and that the leading edge of the spectrum moves above the Fermi level. This additional intensity arises due to the LUMO that is shifted closer to the Fermi level, thus producing spectral density that reaches into the region of occupied states. A careful analysis of the room-temperature spectra shows that the LUMO is occupied by 0.6 electrons per molecule, on the average.

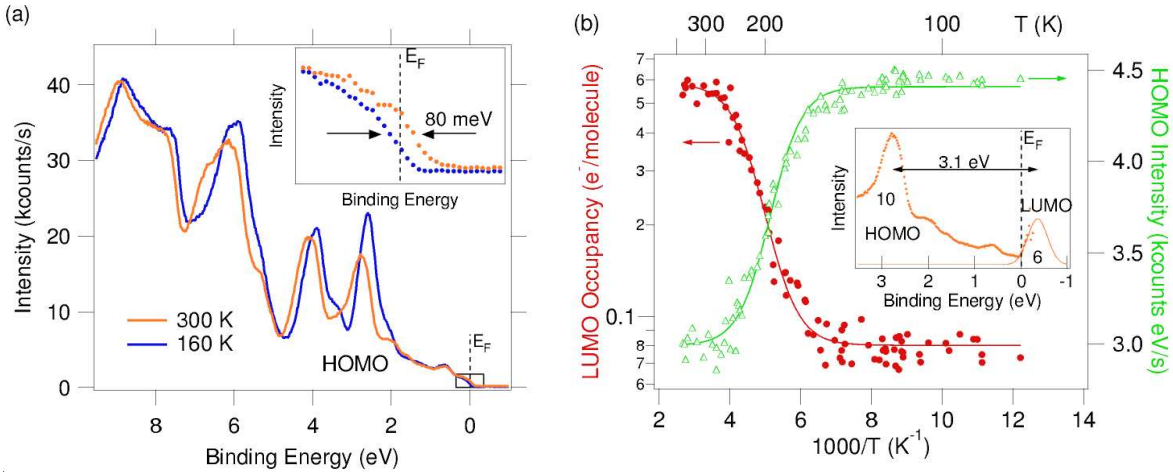

Figure 9.9:
a) Normal emission photoemission spectra ($h\nu = 21.22\,eV$) of the monolayer C_{60}/h-BN/Ni(1 1 1) system at two different temperatures. The inset zooms into the Fermi level region, where a considerable temperature-dependent shift of the leading edge is observed.
b) Calculated LUMO occupancy (red circles), and HOMO peak intensity (green triangles) versus inverse temperature. Both quantities show the same phase transition at around 200 K. The inset displays a measured room temperature spectrum divided by a Fermi-Dirac function, and a fitted Gaussian which indicates the position of the LUMO.

The temperature dependence of the LUMO occupancy (Fig. 9.9b) shows a sharp transition around 200 K. The shape of the curve, as well as the magnitude of the effect, cannot be accounted for by simple thermal activation. Rather, the transition is connected to a structural phase transition. This is further supported by angle-scanned photoelectron diffraction experiments [4], where the structural phase transition is observed in the HOMO intensity curve shown in Fig. 9.9b. From the HOMO intensity, recorded in normal emission, it is concluded that the structural phase transition induces rocking motion that leads to enhanced charge transfer onto the molecule. The magnitude of the charge transfer is unexpectedly high and poses questions that are addressed in continued experimental and theoretical investigations.

[1] W. Auwärter, *One monolayer of hexagonal boron nitride on Ni(111): an atomically sharp interface*, Dissertation, Universität Zürich (2003).
[2] P. Rudolf, M. S. Golden, P. A. Brühwiler, J. Electron Spectrosc. Relat. Phenom. 100 (1999) 409.
[3] C. Cepek, M. Sancrotti, T. Greber, J. Osterwalder, Surf. Sci. 454-456 (2000) 467–471.
[4] M. Muntwiler, *Nanostructured magnetic interfaces: Case studies and new experiment control software*, Dissertation, Universität Zürich (2004).

9.9 Direct determination of the absolute conformation of tartaric acid on Cu(110)

in collaboration with: R. Fasel and K.-H. Ernst, Swiss Federal Lab. for Materials Testing and Research (EMPA), Überlandstr. 129, 8600 Dübendorf, and C. Quitmann, Swiss Light Source, Paul-Scherrer Institut, 5232 Villigen

The interaction between molecules and solid surfaces can cause significant changes of the molecular shape. While in most cases the topological structure like the chirality remains intact, the conformation may change significantly and result in modified functionality of the molecular building blocks [1]. Such structural changes involve torsions of molecular bonds which are driven by the subtle energy balance between bonding to preferred substrate sites and stress induced strain and shear of the softest intramolecular bonds. For the example of Pasteur′s tartaric acid ($C_4H_6O_6$) adsorbed on Cu(110) we determined the absolute chirality and the conformation of the two bitartrate ($C_4H_4O_6$) enantiomers directly [2]. This is obtained by angle-scanned x-ray photoelectron diffraction (XPD) which measures the angles of molecular bonds with high accuracy. The experiment relies on an advanced synchrotron radiation source where a high signal-to-background ratio allows the structure determination of low density and low Z molecules in dilute adsorbate systems.

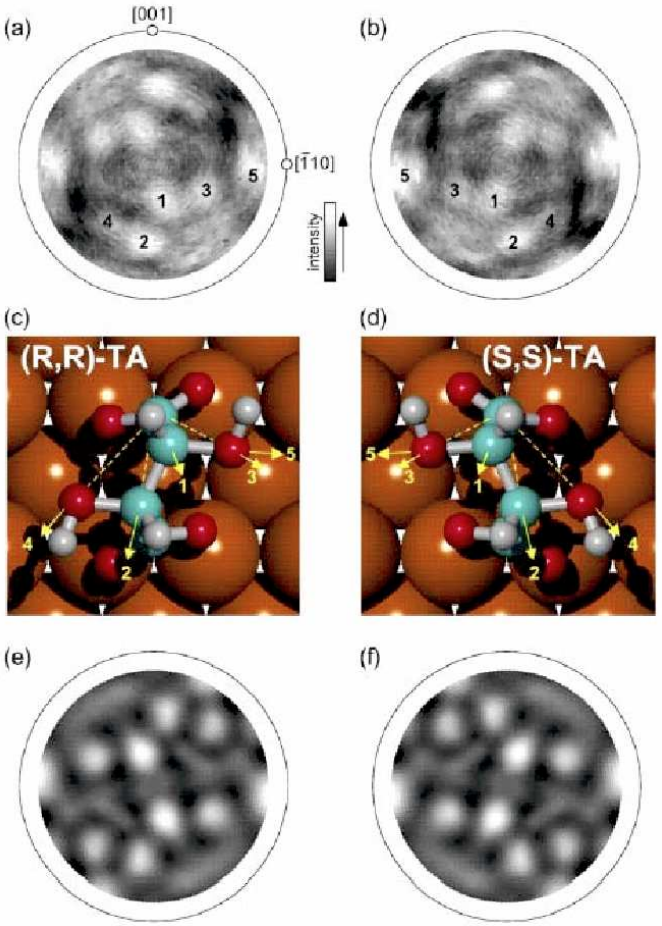

Figure 9.10:
a), b): Experimental C 1s XPD patterns from the (R,R)- and (S,S)-bitartrate adsorbed on Cu(110), respectively.
c), d): Molecular conformations from the geometrical evaluation of the positions of the prominent forward-focusing maxima labeled 1-5 in a) and b). As indicated by the arrows, each peak can be associated to photoelectron emission from one of the C-atoms and forward-focusing by a particular O or C atom.
e), f): Best-fit single-scattering cluster calculations for the (R,R)- and (S,S)-isomers, respectively. The simulations for the optimized molecular conformations accurately reproduce the experimental XPD patterns. From [2].

Figure 9.10 shows the experimental C 1s XPD patterns from the (R,R)- and (S,S)- bitartrate enantiomers adsorbed on the Cu(110) surface [2]. Ten prominent intensity maxima are observed in the patterns, and it is obvious that the patterns from the two enantiomers are mirror images with respect

to each other. Due to the fact that strong intensity maxima correspond to emitter-scatterer directions and that the emitters were selected to be the carbon atoms, the conformation of the carbon backbone and the positions of the hydroxyl-groups relative to the carbon-skeleton are easily determined from the XPD patterns by applying geometrical arguments. In addition to the absolute conformation that results from this straightforward geometrical triangulation, detailed structural parameters can be determined by comparing the experimental XPD pattern to those obtained via calculations, systematically optimizing the structural parameters. The conformation of the (R,R)- bitartrate enantiomer on Cu(110) as predicted from density functional theory (DFT) calculations that did not consider substrate reconstruction [3] is qualitatively similar to the one determined here, but with significantly smaller angular distortions.

[1] S.M. Barlow and R. Raval, Surface Sci. Rep. **50**, 201 (2003).
[2] R. Fasel, J. Wider, C. Quitmann, K.-H. Ernst and T. Greber, Angew. Chem. Int. Edit. (in press).
[3] L. A. M. M. Barbosa, P. Sautet, J. Am. Chem. Soc. **123**, 6639 (2001).

9.10 Time-resolved electron diffraction: space-charge dynamics as tool for characterization

The experimental setup for realizing a low-energy electron diffraction (LEED) experiment with electron pulses of a few picoseconds duration has been completed. First trial experiments on Ge(111) and Ag(111) failed, mainly due to difficulties in finding spatial and temporal overlap of electron and pump light pulses. To overcome this problem, and in order to characterize the electron pulses, a relatively simple electron and light pulse correlation experiment was developed. The setup is depicted in Fig. 9.11. The pulsed electron beam is aimed through a pinhole of 300 μm in diameter drilled into

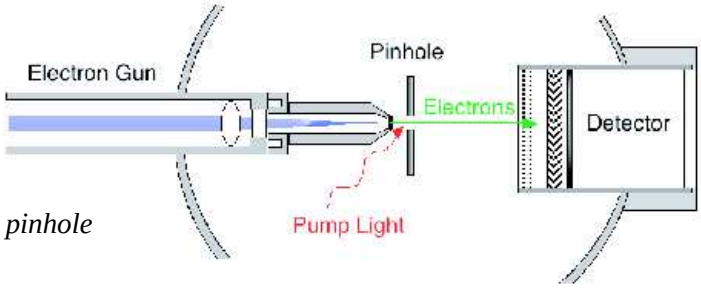

Figure 9.11: *Space-charge experiment: Experimental setup with electron gun, pinhole plate and detector.*

an aluminium plate (thickness 1 mm). Behind the pinhole, electrons are detected by a position sensitive resistive-anode detector with microchannelplate amplifier. Energy filtering is achieved by means of a single copper grid with negative bias voltage in front of the detector. The infrared pump beam (800 nm, fluence on the sample about 10 mJ/cm^2 at 250 kHz repetition rate) is focused into the pinhole creating space charge by the photoelectric effect. Photoelectron spectra, recorded with the same light source from an aluminium plate, showed a broad energy distribution due to multiphoton absorption, with a maximum kinetic energy of roughly 65 eV. The repulsive space charge potential felt by the electrons from the gun produces a negative lens decreasing the transmission through the pinhole. By recording the number of electrons passing through the pinhole as function of delay time between the pump pulse and the electron probe pulse, the temporal evolution of the space charge potential is measured, broadened by the finite time spread of the probing electron pulse. In order to minimize signal fluctuations due to instabilities of the laser, the pump light is chopped with a frequency of roughly 1 Hz. The signal measured with pump light is normalized by the signal without pump light. The experiments were carried out using two different electron guns, one designed for high time resolution

at low energies [1], the second one being a high-energy gun [2]. The guns are referred to hereafter as LEED–gun and MEED–gun, respectively. Electrons are produced in both guns by two-photon-photoemission with the second harmonic of the fundamental wavelength of the Ti:sapphire laser. In order to minimize the temporal broadening of the pulses in the rather long (30 cm) MEED–gun the lens potentials were optimized by means of ray-tracing calculations [3]. Briefly, immediately after emission from the cathode, the electrons are accelerated to energies of the order of 3 keV, and decelerated to their final kinetic energies at the end of the gun. By this optimization, the total flight time of the electrons from the cathode to the sample could be reduced from 48 ns to about 27 ns. The temporal broadening which should scale accordingly was estimated *a priori* to be of the order of 150 to 200 ps.

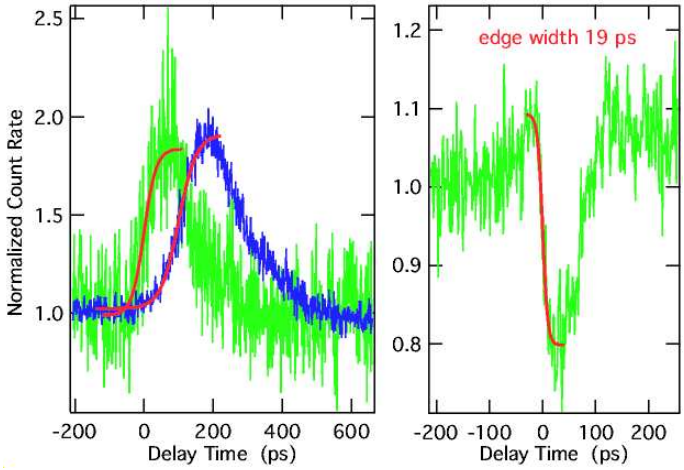

Figure 9.12: *Space-charge experiment: Left: Comparison of the results obtained for the two electron guns used (LEED–gun: green curve, MEED–gun: blue curve). The curves have been scaled to the same height and offset for the sake of clarity; the red lines denote fits to the leading edge.*
Right: Best result obtained so far using the LEED–gun, the edge has a total width of 19 ps.
All curves have been recorded using electron pulses of 200 eV energy.

Indeed, first measurements revealed sizeable effects as shown in Fig. 9.12. The transmission of 200 eV electrons shows a steep decrease by about 30% within 19 ps for electron pulses from the LEED–gun, followed by an exponential increase, fitted with a time constant of 54 ps. Edge and decay of the curves were fitted separatly due to the lack of an analytical function describing the temporal evolution of the space-charge potential. It is safe to conclude that the width of the leading edge of the dip represents an upper limit for the temporal spread of the electron pulses. The value of 19 ps is not far from the value of 5 ps which was the initial design goal [1]. It is interesting to note that the largest effects observed correspond to a transient *increase* in transmission through the pinhole, as plotted in Fig. 9.12 for selected measurements with both guns. The time scales of leading edge and exponential decay are larger than in the case of the dip. We obtain 50 to 70 ps for the leading edge with the LEED–gun indicating that the width of the edge is largely determined by the build-up of the space charge. The decay has a time constant of about 120 ps. The time constants obtained with the MEED–gun are comparable, 103 ps for the rise and 140 ps for the decay, consistent with a time-resolution of about 100 ps of the MEED–gun operated at 200 eV. The increase of transmission is likely to be caused by charges close to the border of the pinhole which produce a positive lens that focuses the incoming electron beam and, thereby, increases the transmission. This conjecture was supported by ray-tracing calculations. Furthermore, curves with different shapes like a peak following a dip and vice versa have been observed, but even a qualitative modeling of these complex shapes is beyond the scope of our research. In conclusion, this experiment allows to characterize the temporal and spatial overlap of electron probe and light pump pulses. Furthermore, the width of narrow features sets an upper limit for the temporal broadening of electron pulses. The method represents a simple and powerful tool for future time-resolved electron diffraction experiments.

[1] R. Karrer, H.J. Neff, M. Hengsberger, T. Greber, and J. Osterwalder, Rev. Sci. Instr. **72**, 4404 (2001).

[2] M. Aeschlimann, E. Hull, C.A. Schmuttenmaer, J. Cao,Y. Gao, D.A. Mantell, and H.E. Elsayed-Ali, Proc. SPIE **2521**,103 (1995).

[3] SIMION software package, Idaho NationalEngineering Laboratory, EG&G Idaho Inc., Idaho Falls.

10 Physics of Biological Systems

Cornel Andreoli, Conrad Escher, Hans-Werner Fink, Michael Krüger,
Tatiana Latychevskaia (since March 2004), Hiroshi Okamoto, Thomas Rusterholz,
Gregory Stevens (since November 2003), Sandra Pascale Thomann (since March 2004).

in collaboration with:
Jevgeni Ermantraut, Clondiag Chip Technologies (Germany), Pierre Sudraud, Orsay Physics (France), Roger Morin, CNRS Marseille (France), John Miao, Stanford University (USA), Dieter Pohl, University of Basel, Andreas Plückthun, Peter Lindner, Biochemistry Institute, University of Zurich, NCCR - National Center of Competence in Research Nano-Scale Science

A fair amount of dedicated equipment has been completed in the course of the past year and the group is now focusing on its scientific goals which remain to be in the exploration of nanometer-sized objects. The nanometer-scale is a unique scale for condensed matter physics in as much as it represents the transition between classical and quantum mechanical physics. At this scale, the transport of charges now relates to the transmission of waves in quantum wires. The de Broglie wavelength, respectively the value of Planck's constant and that of the electron mass, identify this unique length scale. Single electron effects become apparent only at the nanometer-scale which is directly related to the discrete nature and distinct value of the elementary charge of the electron. By using techniques like field ion microscopy and holography with low energy electrons, in combination with other more established tools, we are now in a position to address the above issues. A special emphasis of the group's efforts is related to biological systems. We have recently been able to quantitatively explore the energetics of individual DNA molecules in liquids as illustrated in some detail below. In our efforts to establish the LEEPS (Low Energy Electron Point Source) microscopy as a new tool for structural biology, we have made progress in fitting bacteriophages, that will eventually act as templates for imaging single proteins, onto nano-structured thin films. A focused ion beam machine, delivered in summer 2003, enables us to employ a 10 nm gallium ion beam for milling structures in silicon devices or other thin-film materials to create suitable structures for interfacing molecules.

10.1 Studies of single DNA molecule in liquids

The activation free energy governing the transition from the stretched to the random coil configuration of individual DNA molecules has quantitatively been determined. From the temperature dependence of the transition times it is apparent that the formation of the DNA random coil is a thermally activated process. A total of 420 observations have been made, which were carried out on 80 different individual DNA molecules covering the temperature range from -5 C$^\circ$ to $+60$ C$^\circ$. The data indicate that the observed transitions are in fact thermally activated, which is evident from an Arrhenius type behavior. From the Arrhenius plot an activation barrier of a good fraction of 1 eV has been determined. With this, the first direct determination of the energetics governing an individual DNA molecule in its natural liquid environment has been made.

The experiments have been performed using fluorescent video microscopy with a time resolution of 40 ms. This technique, pioneered by Steven Chu of Stanford University, is meanwhile employed by a few laboratories around the world to study the dynamics of single DNA molecules. However, to study the energetics of single molecules, some technical challenges had to be mastered. The main problem was the realization of thermal equilibrium conditions free from disturbances of the observation process itself, as well as the ability to change and measure the equilibrium temperature. Furthermore,

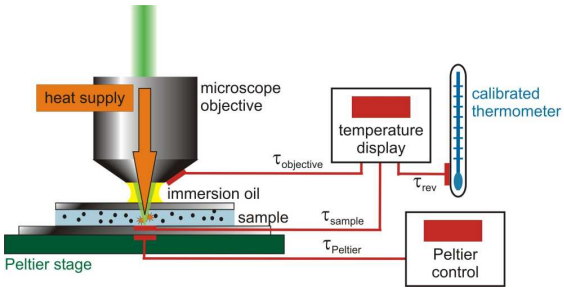

Figure 10.1: *Schematic of the set-up for measuring the energetics of single DNA molecules. Except for the objective lens, most of the optical- and data acquisition-system is not shown here. Four temperature sensors are employed to establish equilibrium in a thin water film. The temperature of the peltier element is adjusted to a fixed value by a PID controller. The temperature at the place where the scenario occurs is then calibrated against the peltier stage temperature, the heat sink, made up of the objective lens and the immersion oil drop, and the temperature of the surrounding air. - Conrad Escher*

in providing a proper distance reference, stretching the molecules in an electric field prior to re-establishing equilibrium and routine methods for anchoring the 16 μm long and 2 nm thick molecules at one end had to be developed. Attachment of the DNA at one end to a fixed position was essential for being able to derive sufficient statistics to obtain quantitative energy values. This has been achieved in a close collaboration with Clondiag Chip Technologies that provided us with state of the art molecular biology techniques for binding just one end of the molecule to a silicon oxide substrate. The experiment takes place in a liquid environment in which a single DNA molecule is embedded in just a few pico-liters of ultra pure water. It is part of a 10 μm thick water film which is sealed from the environment to avoid evaporation and associated erratic liquid flow which would perturb the equilibrium conditions, essential for deriving quantitative free energy data. A schematic of part of the apparatus is illustrated in Fig. 10.1.

10.2 Towards the limits of holography with low energy electrons

The use of a coherent single-atom electron source for low energy electrons has developed into a tool that appears to be particularly useful for investigating individual objects of nanometer-sized dimensions. The absence of radiation damage due to the low energy of the electrons and the high contrast in scattering by light atoms holds promise as a new tool for structural biology of individual molecules. The sensitivity to small electric and magnetic fields, combined with the high spatial and time resolution of the technique, will also be used to explore the properties of mesoscopic physics objects, such as quantum wires and single electron devices. This project aims at reaching the experimental resolution limit of this technique, which will then be made available to other projects, both inside and outside of our research group. The ultimate limit is given by the spatial and temporal coherence of the source. It relates to the size of the source and the energy spread of the emitted electrons, which is fundamentally limited only by the Heisenberg uncertainty relationship. In order to come close to this fundamental limit, which is associated with atomic resolution in 3 dimensions, a number of experimental issues need to be addressed and new technologies developed. They include: shielding the coherent electron source from external mechanical and electronic noise, developing a new two-dimensional detector for low energy electrons and improving the angular spread of the coherent electron wave-fronts by adsorbing C_{60} clusters onto the atomic point-source. The numerical work of Tatiana Latychevskaia is directed towards the important second step in holography, namely the reconstruction. This implies employing appropriate coherent optics schemes for reconstructing the 3-dimensional structure of the nanometer-sized object from its experimental electron hologram record.

10.3 Cryogenic LEEPS microscopy

This project primarily aims at improving the resolution of room-temperature LEEPS-microscopy, taking advantage of the extraordinary mechanical stability of cryogenic instruments and the possibility of utilizing novel schemes to effectively reduce the energy spread of the electron point source.

The project began in February 2002, and we have completed the construction of the instrument in June 2003. Since then we have been testing the microscope. The specially designed piezo stepping motor system, together with the computer control system have been thoroughly tested at room temperature as well as at cryogenic temperatures down to 4.2 K. The difficulty of using a micro-channel plate (MCP) at cryogenic temperatures made it necessary to search for an alternative detector. A post-acceleration detection system utilizing a micron-scale metallic mesh has been successfully developed in collaboration with diploma student Thomas Rusterholz[1]. With this detection system we obtained reasonable image quality at an emission current of 10 nA. We have also observed electron interference fringes near carbon fibers at room temperature, and we expect to see interference fringes at cryogenic temperatures in the near future. The instrumental testing phase will be completed within a few months, and we can then move on to the scientific investigations of novel methods in electron microscopy and its application to biology.

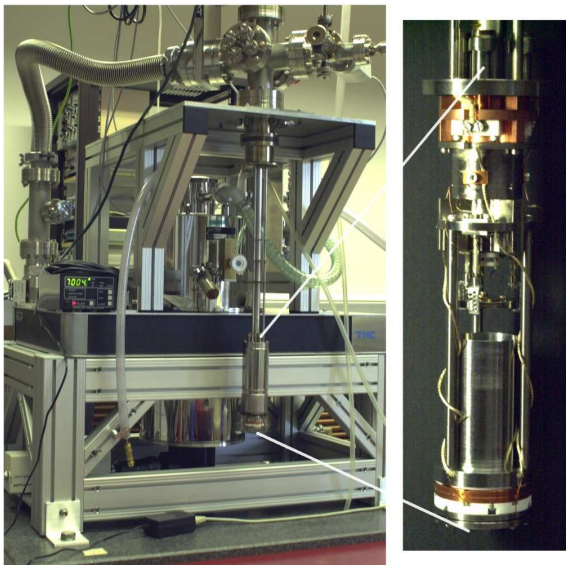

Figure 10.2: *The Cryogenic LEEPS microscope. - Hiroshi Okamoto*

[1] Thomas Rusterholz, *Ein neuer Detektor für Holographie mit langsamen Elektronen*, diploma thesis Physik-Institut der Universität Zürich, January 2004.

10.4 Structure of individual bio molecules

The purpose of this project is to develop tools and methods to image individual bio-molecules with a coherent low energy electron beam to obtain structural information. As a first step, novel methods need to be developed to attach individual macromolecules to surfaces. These investigations have begun with a filamentous phage called M13, which is to be attached to a carbon support film so that individual phage particles are suspended over holes in the film so they can be imaged using the low energy electron beam. The distribution of attached phage particles is being characterized using a transmission electron microscope (TEM).

Since beginning the project in November 2003, we have prepared a homogeneous suspension of M13 phage using a standard protocol and have developed a method for making holes of a desired size and shape in carbon support films using a focused ion beam. We have investigated ways of pre-treating the carbon film by glow discharge in air so as to impart a hydrophilic property to the surface that is necessary for attachment of M13 and other bio-molecules suspended in aqueous media.

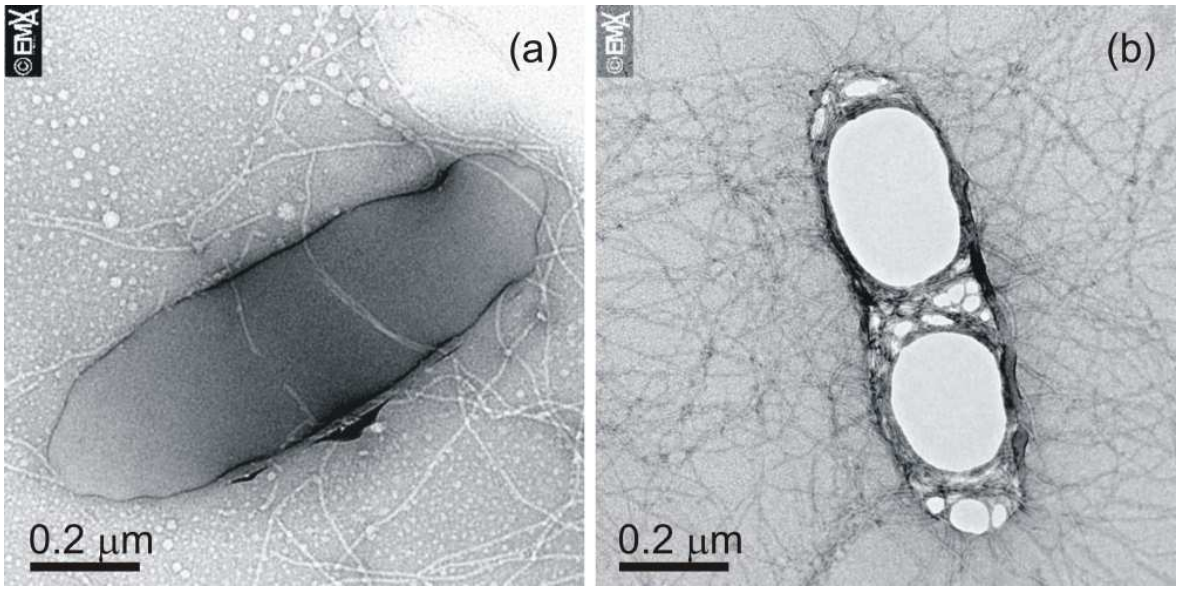

Figure 10.3: *TEM (Transmission Electron Microscopy) images of individual M13 phage particles suspended across holes in a carbon film. The samples were negatively stained with uranyl acetate, which has formedinto a film across the hole (a). In the case where the negative stain did not form a film across the hole (b), the M13 filaments were found to lie in bundles across and around the edge of the hole* [3]*. - Gregory Stevens.*

We have examined the dependence of phage concentration on the distribution of particles deposited onto carbon films and can obtain even distributions of particles at a preferred density. As shown in Fig. 10.3a, we have obtained TEM images of individual phage particles suspended across holes in a carbon film that were subsequently embedded in a film of negative stain. In cases where the negative stain film was absent, phage particles were found to adhere to the edge of the hole after drying, as shown in Fig. 10.3b. We have shown how surface tension in a water film is responsible for rearrangement of filaments that were previously suspended over holes, after part of the water film breaks during drying. In order to overcome such rearrangement during drying, we are currently investigating methods for rapidly freezing the specimen and then sublimating the surrounding ice under vacuum so that phage particles remain undisturbed.

We have begun to address concerns that bio-molecules may undergo significant conformational changes when placed in the vacuum environment of a LEEPS microscope by showing that Green Fluorescent Protein (GFP) retains its ability to fluoresce after several days in a vacuum. In future, GFP may be used for investigating the extent of radiation damage to biological material in the LEEPS microscope. We are currently examining the possibility of attaching lysine residues on the exterior of the phage coat to a gold surface using N-hydroxy-succinimide (NHS) chemistry. To this end, we have obtained a mutant of a related filamentous phage f1, which has been genetically engineered to have extra lysine residues on its surface. This might be useful for attaching gold nanoclusters of known size to the surface of the phage for purposes of calibrating images, or to prevent rearrangement of phages by strongly attaching them to a gold substrate film.

[3]We gratefully acknowledge the Institutes of Veterinary Anatomy and Virology, University of Zürich, for the use of their facilities in making these images.

10.5 Nanometer-sized structures for creating and investigating mesoscopic physics devices

This effort is directed towards directly observing the dynamics of individual charges in mesoscopic devices, like quantum dots, wires or single electron transistors. Single charges and their associated fields are expected to be visualized by holography with low energy electrons. What is needed for such a program is a quantum dot weakly coupled to at least two electrical leads by a tunnel barrier. Our focused ion beam appears to be invaluable in achieving that. Fig. 10.4 shows a carbon nanotube that has been cut using the focused gallium ion beam. The next step will be to trap an appropriate small metal cluster in this gap and to make sure that it is weakly coupled via two tunnel-barriers to the two nanotubes electrodes.
Another approach is to use highly oriented pyrolytic graphite (HOPG) sheets and the focused ion beam to in-situ fabricate quantum wires and measure their properties in particular in relation to ballistic electron transport. An example of this effort is shown in Fig. 10.5.

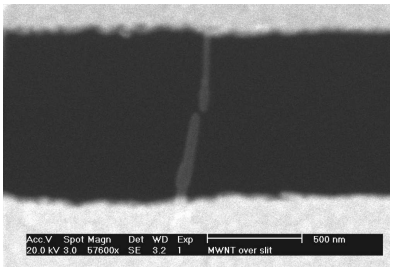

Figure 10.4:
A freestanding multi-wall carbon nanotube has been deposited over a slit in a SiN-membrane and subsequently been cut by a focused ion-beam.
- Michael Krüger.

While the preparation of the structure as well as the transfer to the microstructure with the integrated electrodes is now routinely possible, no current has yet be detected up to a bias of 70 V. Unfortunately, just as with molecular electronics structures, the contact resistances appear to be a particularly puzzling problem at this scale, which needs to be solved.

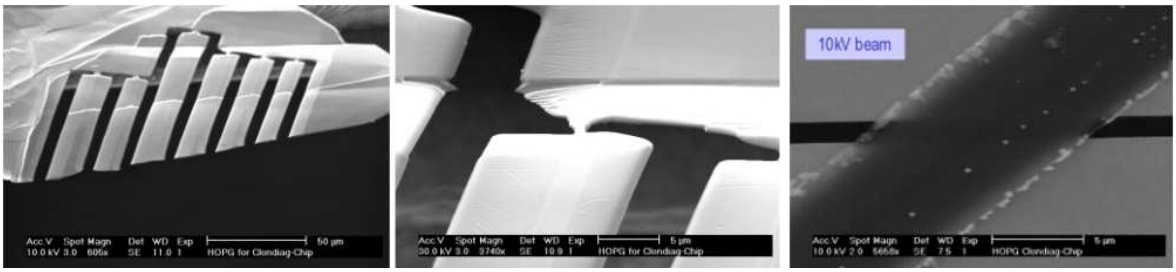

Figure 10.5: *HOPG sheets structured by a focused ion beam, removed by a precision manipulator and subsequently deposited onto a silicon device for electrical measurements.*

10.6 Field ion microscopy

Our field ion microscope, previously being used only to characterize our electron point sources, has now two dedicated purposes. They are being pursued by Sandra Thomann and Cornel Andreoli. The first and major goal is the investigation of the adsorption of single C_{60} clusters onto pyramidal tungsten tips, from which we expect to learn something about single molecule adsorption events as well as to obtain superior coherent electron sources. This work started in March 2004 and benefited from the expertise of the Institutes Surface Science group, in particular from Thomas Greber and Anna Tamai. Based on their experience in handling the sublimation of C_{60} clusters,Cornel Andreoli and Kurt Bösiger designed and build a C_{60} evaporator particular to our needs, namely in being free from disturbing light emission during sublimation of the clusters. The second project involving field

ion microscopy is the investigation of electrolyte tips for creating novel ion sources. Here the ion supply is provided by mobile bulk ions inside the electrolyte. This has distinct advantages over the ionisation from gas phase atoms. This work is carried out in collaboration with Dieter Pohl from the Physics Institute of Basel and had just started before the end of this report period. However, it already appears promising.

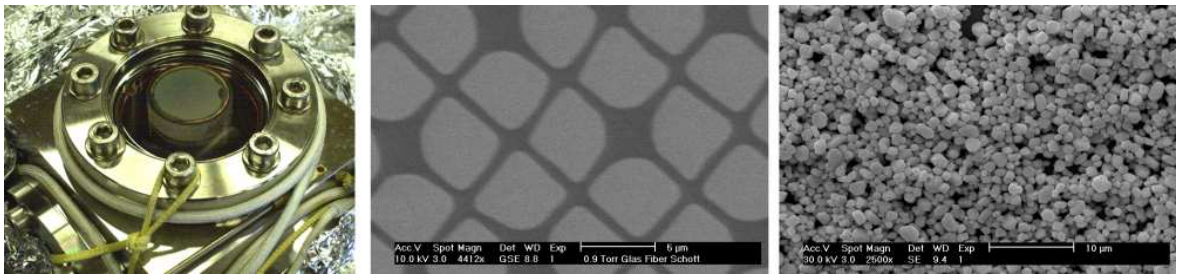

Figure 10.6: *Field emission microscope to study the diffusion of individual Cs atoms (left). Essential parts of the detector systems are a fiber optic plate (middle), donated to us by Shott-Glass with* 5 *micron thick fibers, and a fine phosphorous powder (right) of about 1 micron grain size, donated to us by the medical science division of Siemens. - Hiroshi Okamoto, Cornel Andreoli, Chan Mei Po (summer-student in 2003).*

10.7 Field emission microscopy to study the diffusion of Cs adsorbed on tungsten surfaces.

A field emission microscope is dedicated for students' experiments in association with the lecture series entitled "Physics on the Nanometer-Scale". It allows the students to measure the field emission current from a region of some 10 nm in diameter. The fluctuation of the current is directly related to the diffusion of Cs atoms entering or leaving the probe area. From the autocorrelation of this signal, the diffusion coefficient can be evaluated at different temperatures, starting at 80 K. This project is under the supervision of Hiroshi Okamoto who benefited from occasional help of summer students. With the assistance of the University glass blower Daniel Schnarwiler, Cornel Andreoli managed to build a quite original detector for this experiment, in as much as each fibre of the plate transmits a signal corresponding to a sub-nanometer region of the surface on which the motion of just a few Cs atoms takes place. The students can thus define a 10 nm diameter region to be probed by simply taking a black piece of paper with an appropriate hole of mm dimension at the atmospheric side of the detector. In this way they can probe the field emission current from a nanometer-sized region by using a photomultiplier to pick up the signal delivered from a few hundreds of these fibres.

The experiment is expected to become available to the students shortly after the first course on "Physics on the nanometer-scale" is completed, which is after the summer-semester 2004.

11 Computer Assisted Physics

C. Bersier, T. Mayer, P. F. Meier, E. Olbrich, S. Renold, and E. Stoll
guests: T. A. Claxton and H. U. Suter

In this report, we want to concentrate on the following research topics:

- Interpretation of the properties of high temperature superconductivity materials using spin-polarized *ab initio* calculations. The aim of this work is to provide insight into the particular microscopic electronic structure of cuprates.
- Non-linear dynamical study with particular reference to time series analysis of electroencephalograms in collaboration with two groups of the Medical Faculty.

We selectively report on the charge distribution in La_2CuO_4 before doping (11.1.1), muon sites and hyperfine fields in La_2CuO_4 and $Sr_2CuCl_2O_2$ (11.1.2), on the calculation of magnetic hyperfine coupling constants (11.1.3), and on results of time series analysis of sleep EEG (11.2).

11.1 Electronic structure of high-T_c materials

11.1.1 On the distribution of intrinsic holes in cuprates

La_2CuO_4 is insulating but becomes metallic and superconducting upon replacing a few percent of La^{3+} by Sr^{2+} or Ba^{2+}. The simplistic ionic model for the pure substance relies on the ions Cu^{2+}, O^{2-} and La^{3+}, the only hole in the electronic configuration being localized on Cu^{2+} in the $3d^9$ atomic configuration. The same assignment is made for the copper in the CuO_2 planes in $YBa_2Cu_3O_6$, the parent compound of the yttrium high-T_c family. To investigate the validity of this model we have performed first principles density functional calculations on the La_2CuO_4 crystal, simulated by using the Cu_5O_{26}/Cu_8La_{34} cluster (a picture of a similar cluster can be found in the next subsection) and have analyzed the charge distribution in detail.

There are 5 Cu atoms and 26 oxygen atoms in the cluster but for our discussion we select only those atoms at the center of the cluster for consideration. Those atoms close to the periphery of the cluster are not accounted for since these will include effects expected from the cluster edge. This cluster has five unpaired electrons leading to a choice of possible multiplicities, M = 2, 4 or 6. (M=6 corresponds to a "ferromagnetic" alignment of the spins, whereas M=4 leads to an "antiferromagnetic" alignment.) We list in Table 11.1 the total atom charges for the *central* copper and neighboring oxygen atoms in La_2CuO_4 which, in the present report, are for simplicity determined as averages of the charges resulting from multiplicities M=4 and M=6. A more detailed analysis may be found in Ref. [1].

Table 11.1: *Mulliken charges for Cu and for O_p and O_a, the planar and apical oxygens, respectively, for La_2CuO_4.*

Cu	O_p	O_a
1.16	-1.64	-1.94

Table 11.2: *Partial Mulliken populations for Cu and for O_p and O_a, the planar and apical oxygens, respectively.*

Cu			O_p		O_a
4s	$3d_{3z^2-r^2}$	$3d_{x^2-y^2}$	2s	$2p_{\|\|}$	$2p_z$
0.49	1.92	1.40	1.96	1.68	1.95

Furthermore, we present in Table 11.2 the corresponding Mulliken partial populations for those orbitals for which they deviate appreciably from the ionic picture.

The Mulliken charges in Table 11.1 suggest that 0.84 electrons are transferred to the oxygen atoms (Fig. 11.1). This result should be viewed with extreme caution if we continue to associate partial occupancy of orbitals with holes. For example using the Mulliken population data in Table 11.2 the hole is distributed 60% in the Cu $3d_{x^2-y^2}$ copper orbital, 9% in the $3d_{3z^2-r^2}$ copper orbital, 64% in the four planar oxygens $2p_{||}$ orbitals (parallel to the bond) and 10% in the two apical oxygen $2p_z$ orbitals, which is clearly nonsense.

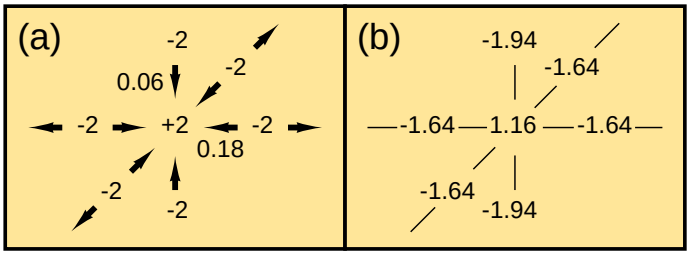

Figure 11.1: *(a) shows, using a simplistic model, the charge transfer of 0.84 electrons from oxygen anions (-2) to a copper cation (+2) as a result of covalent bonding. The charge transfers pointing away from the planar oxygen anions are to other planar copper cations which are not shown. Charges resulting from the hole transfer are given in (b).*

In order to proceed further we need to construct a molecular orbital energy diagram of the copper ion and its six nearest neighbor oxygen ions which leaves little room for doubt and explains the charge transfer observed. As is normal in similar circumstances we concentrate only on the frontier orbitals, the highest occupied, and for copper also at least the lowest unoccupied orbitals of the interacting ions. There is no difficulty with the Cu^{2+} ion since the qualitative orbital energy diagram has remained unchanged now for many years (see for example Ref. [2]) and is shown on the left hand side of Fig. 11.2 for O_h and D_{4h} symmetry. Note that we have added the copper $4s$ orbital, the unoccupied orbital of lowest energy .

In Table 11.2 only the four planar oxygen $2p_{||}$ orbitals and the two apical oxygen $2p_z$ orbitals have significantly reduced populations from complete occupancy, which indicates that only these oxygen frontier orbitals are significantly involved in bonding. We define each of these $2p$ orbitals in such a way that the phases of the lobes pointing towards the central copper atom are the same. Fortunately in O_h symmetry we can form six symmetry adapted orbitals easily. Let the symmetry adapted orbitals be represented by Φ and the $2p$ orbitals by ϕ so that

$$\mathbf{\Phi} = \mathbf{U}\phi$$

where $\mathbf{U}$ is a unitary 6×6 matrix. The moduli of the non-zero elements of each row of the matrix are all identical and so we only require the sign of these elements. These are given in Fig. 11.3 for each Φ. The energies increase as a function of the number of nodal planes in each selection. Φ_1 has no nodal planes, $\Phi_2,\ \Phi_3,\ \Phi_4$ have one nodal plane and $\Phi_5,\ \Phi_6$ have two nodal planes. These are drawn on the extreme right of Fig. 11.2, that also shows, immediately to the left, how the degeneracies are lifted for D_{4h} symmetry. Only the $4s$ (a_{1g}) and $3d_{x^2-y^2}$ (b_{1g}) orbitals on the copper are available for bonding

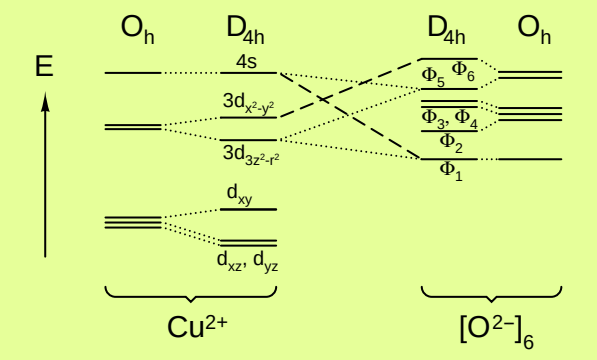

Figure 11.2: *Interaction of the atomic orbitals of copper with the symmetry combinations of the surrounding oxygen hybrid orbitals. The dashed lines indicate the primary interactions which remain even in O_h symmetry. The secondary (smaller) interactions are shown by dotted lines. Bonding and anti-bonding combinations of the orbitals of the primary interactions explain the occupancy of the 4s orbital and the transfer of the hole from the $3d_{x^2-y^2}$ orbital to oxygens (Φ_6 only).*

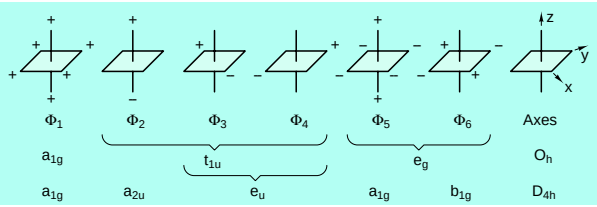

Figure 11.3: *The signs of the orbital coefficients for the various combinations of hybrid orbitals of the oxygen atoms. The absence of a sign indicates a zero coefficient. The hybrid orbitals are defined such that the phase pointing towards the copper atom have all the same sign.*

since these are not completely occupied. All the oxygen Φ orbitals are completely occupied and can only interact, if allowed by symmetry, by donating electrons into vacant or partially occupied orbitals on copper. The only interactions in O_h symmetry are $4s$–Φ_1 and $3d_{x^2-y^2}$–Φ_6. These are also allowed in D_{4h} symmetry and are regarded to be the dominant interactions. Secondary additional interactions arising from the reduction in symmetry to D_{4h} are $4s$–Φ_5, $3d_{3z^2-r^2}$–Φ_5 and $3d_{3z^2-r^2}$–Φ_1.

Since the hole, from the ionic model, originates from the $3d_{x^2-y^2}$ copper orbital there is *only one* interaction involving the hole: $3d_{x^2-y^2}$–Φ_6. This uniquely restricts the transfer from the copper to the planar oxygen $2p_\parallel$ orbitals (see definition of Φ_6 in Fig. 11.3). The Mulliken population analysis clearly indicates that 40% of the hole has been transferred to the planar oxygens (see Fig. 11.4 for more detail), and none, by this mechanism to the axial oxygens leaving 60% on the copper. Since a hole transfer is accompanied by an electron charge transfer in the opposite direction we conclude that of the 0.84 electrons transferred from the oxygens to copper, 0.40 electrons have been accounted for by the hole transfer. The remaining 0.44 electrons correspond almost exactly to the Mulliken $4s$ orbital population of 0.49 electrons which can be associated with the dominant $4s$–Φ_1 interaction. The discrepancy of 0.05 electrons can be attributed to the secondary interactions which also involve the $3d_{3z^2-r^2}$ orbital.

As concern spin densities we note that p_{spin}[Cu(4s)] = 0.03. This can be interpreted as arising from a spin polarization stemming from the unpaired electron in the $3d_{x^2-y^2}$-Φ_6 anti-bonding orbital, rather than a direct involvement in the hole transfer. However the effect on the hyperfine coupling constant is disproportionately large. The resultant spin in the $4s$ orbital polarizes the electrons in the $3s$ and to a minor extent in the $2s$ and $1s$ orbitals. The on-site contact hyperfine field is negative (-1.78 a_B^{-3}) but there exists a positive field that is transferred from nearest neighbor copper ions (+0.71 a_B^{-3}). A detailed analysis of these calculated spin transfers has been given in [3; 4]. Here, we first note that the theoretical results are in very good agreement with the values derived from the NMR data [5; 6]. We further note that Pavarini et al. [7] have emphasized the importance of the $4s$ orbital in intra layer hopping.

The hole distribution, which is predominantly centered on the $3d_{x^2-y^2}$ orbital on copper, should sensitively affect the EFG at the copper nucleus (see reference [3]) since this property is dependent

on the $1/r^3$ function.
The relatively high symmetry (D4h) of the immediate oxygen anion environment of copper cations, represented by the distorted octahedral cluster CuO_6^{10-} in La_2CuO_4, enables the hole distribution to be uniquely and unambiguously associated with the Cu $3d_{x^2-y^2}$ orbital and the symmetry adapted oxygen orbital Φ_6 from a qualitative molecular orbital energy diagram. The diagram also allows for the participation of the formerly unoccupied Cu $4s$ orbital in receiving electrons directly from two doubly occupied oxygen orbitals, without spin preference. It should now be clear that analysis of charge alone cannot determine the hole distribution. These results are in agreement with, and provide an explanation for, the Cu $4s$ orbital population from both previous band structure and current cluster calculations.

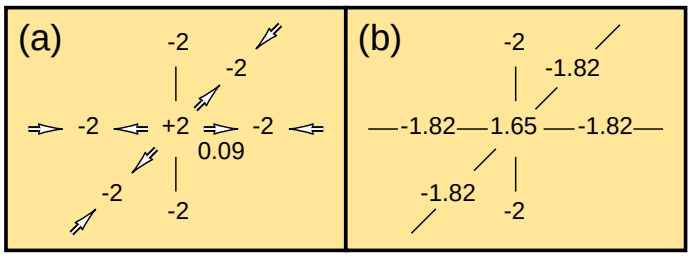

Figure 11.4: *(a) shows the transfer of 0.0875 holes from the copper cation to each of the planar oxygen anions arising from the bonding involving the Cu $3d_{x^2-y^2}$ orbital and the oxygen valence orbitals. The corresponding Mulliken charges resulting from the hole transfer is given in (b).*

11.1.2 Muon sites and hyperfine fields in La_2CuO_4 and $Sr_2CuCl_2O_2$

Positive muons are sensitive probes of local internal magnetic fields in solids and muon spin rotation (μSR) experiments have provided valuable insight into the microscopic nature of magnetism in a variety of substances, in particular also in cuprates. A disadvantage of the μSR method, however, is that the site in the crystallographic lattice at which the muon stops is not known. This is irrelevant for the study of the internal fields of flux line lattices where the distances between the flux cores are much larger than the dimension of the crystallographic unit cell. For the investigation of local magnetic fields in zero or small applied fields, however, a knowledge about the muon stopping site is necessary. Today, possible muon sites are estimated by comparing the measured local field with the dipolar field generated *in vacuo* by localized magnetic moments at the copper positions. The magnitude and directions of these moments are determined from neutron scattering data. The assumption that the local magnetic fields at muons result primarily from these remote moments, however still requires justification. We have therefore extended our cluster calculations on cuprates by inclusion of a muon at various sites and have determined the total energy allowing for lattice relaxation of neighboring atoms.

For the lanthanum compound La_2CuO_4 a small cluster, $\mu CuO_6/Cu_4La_{10}$, with only one copper atom in the core and a larger cluster, $\mu Cu_5O_{26}/Cu_8La_{34}$, which contains five copper atoms and is shown in Fig. 11.5 have been calculated. The smaller cluster was used to determine the relaxed geometry, whereas in the larger one the hyperfine parameters were calculated. The corresponding strontium clusters to simulate muons in $Sr_2CuCl_2O_2$ were also studied, namely $\mu CuO_4Cl_2/Cu_4Sr_{10}$ and $\mu Cu_5O_{16}Cl_{10}/Cu_8Sr_{34}$. The electronic structure calculation uses a hydrogen atom for the simulation of the muon, since the electronic wave function only depends on the charge and position of the atoms. Three muon sites were investigated. The first position, which is depicted in Fig. 11.5 and called site (A) is in the bond between the copper and the apical oxygen. Sites (B) and (C) which have been proposed before [8] are further away from the CuO_2 plane. The total energy, however, is lowest for site (A). The geometry optimisation resulted in pushing the Cu by 0.34 a_B (0.08) below the CuO_2 plane and moving the O upwards 0.43 a_B (0.52) (where the numbers in parentheses refer to $Sr_2CuCl_2O_2$).

Thus, contrary to the general belief, the bond centered position of the muon is preferred. A similar site has been attributed to the anomalous muonium in semiconductors. In the case of the lanthanum compound the muon is close to the appex oxygen atom, suggesting an $(O\mu)^-$ type species. From a chemical viewpoint one would interpret this configuration at this site as an $(OH)^-$ close to the Cu^{2+} ion. For the strontium compound this is not possible, therefore the muon is closer to the in–plane copper atom.
A comparison of the different geometries in the two materials shows that the calculated distance of the muon from the copper where the magnetic moments are centered, is larger in La_2CuO_4 than in $Sr_2CuO_2Cl_2$ by a factor of 1.21. Since both transferred and dipolar fields decrease with the third power of the distance, one expects from these geometries smaller fields in La_2CuO_4 than in $Sr_2CuO_2Cl_2$ by roughly a factor two. This compares favourably with the observed ratio of about three for the experimental hyperfine coupling constants of the two compounds and explains the larger frequencies found in the strontium compound.

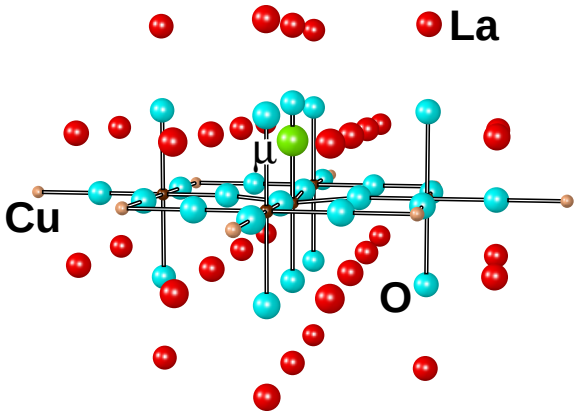

Figure 11.5: *The HCu_5O_{26}/Cu_8La_{34} cluster with the hydrogen (muon) at position A.*

We further note that the small mass of the muon implies a large spread of its quantum-mechanical ground-state wave function. This must be accounted for in more precise theoretical estimates of the spin densities at the muon.

In summary, the ab-initio cluster calculations show transferred hyperfine fields at muon sites in La_2CuO_4 which are in disagreement with the common interpretation of μSR experiments in cuprates. This is not completely surprising since a large amount of information about on–site and transferred hyperfine fields in cuprates is available: numerous nuclear magnetic resonance (NMR) experiments have been performed in the very same substances which were explored by μSR, yet it seems that the progress in understanding NMR data has so far been ignored by the μSR community.

11.1.3 Investigations into static NMR properties in cuprates

NMR measurements of the copper Knight shift in cuprates exhibit an amazing peculiarity. With the external magnetic field applied parallel to the CuO_2 planes the Knight shift declines in the superconducting state with decreasing temperature as is expected from the reduction in the spin susceptibility. With the field perpendicular to the planes, however, the shift is independent of the temperature in all compounds of the La- and Y- family irrespective of the doping level. This has been explained by an incidental cancellation of an on-site and a transferred hyperfine field at the copper nucleus. These quantities, however, depend on the lattice parameters and it is astonishing that the same coincidence should occur in both families.

Cluster calculations have the advantage that relative changes of magnetic hyperfine coupling constants (MHCC) upon changes in lattice parameters can be investigated. Therefore we have extended previous calculations of MHCC in La_2CuO_4 [9] and $YBa_2Cu_3O_7$ to include also $Sr_2CuO_2Cl_2$ and $YBa_2Cu_3O_6$.[10] Additional calculations have been performed in clusters with artificially stretched and squeezed planar lattice constant $a' = f \cdot a$ and $b' = f \cdot b$, with $f \in (0.99, 1.01)$. Furthermore, a La_2CuO_4 cluster was set up with an artifically buckled CuO_2 plane. In this way the behavior of the MHCCs under lattice distortions could be observed.

Selected results for the transferred hyperfine coupling, B, and the on-site dipolar interaction, $A^{\parallel}_{dip}$ at the planar copper nuclei are presented and plotted against the lattice constant in Figs. 11.6 and 11.7. As expected, the transferred hyperfine interaction drops in all compounds when increasing the lattice constant. However, in the yttrium based compounds, the transferred field is much smaller than in the other two compounds. Interestingly, B drops also upon an artificial buckling of the planes in the La compound as indicated by the red crosses.

The on-site dipolar interaction, $A^{\parallel}_{dip}$ gets also weaker when enlarging the unit cell and scales quite well with the lattice constant. It is seen that the buckling has only a minor effect on the dipolar interaction.

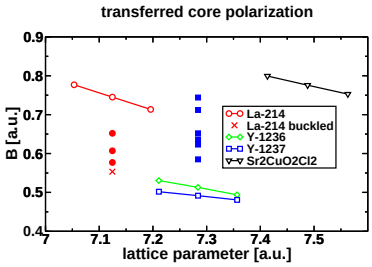

Figure 11.6: *Theoretical (open symbols) and experimental (closed symbols) values for the transferred copper hyperfine interaction (left panel) and for the on-site dipolar coupling (right panel) for various cuprates plotted against the lattice parameters.*

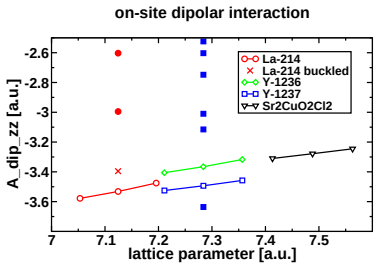

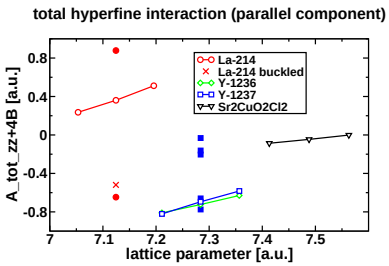

Figure 11.7: *Corresponding results for the total copper hyperfine interaction.*

As a conclusion, we think that the current explanation of a temperature independent Knight shift in c-direction may be in error. The proposal of a large residual shift at low temperatures could help in establishing a new understanding of the spin properties in cuprates.

In Fig. 11.7, the total hyperfine interaction along the c-axis is displayed. It is zero neither in the lanthanum compound nor in the yttrium compounds. The anisotropy of the total hyperfine interaction especially for $YBa_2Cu_3O_7$ ($[A^{\parallel}_{tot} + 4B]/[A^{\perp}_{tot} + 4B] \simeq 4$) shows that the non-zero hyperfine interaction should be observable in NMR experiments. Furthermore the buckling of the lanthanum compound drastically changes the total hyperfine interaction.

In conclusion, a cancellation of hyperfine fields for all cuprates cannot be corroborated by our calculations. The transferred interaction B has the largest influence on the anisotropy of the total hyperfine fields. Therefore, it seems reasonable to assume that - in a first approximation - the on-site hyperfine fields are essentially of the same size in all cuprates.

11.2 Time series analysis of EEG

Research on time series analysis of EEG data was centered on the further investigation of oscillatory events in the human sleep EEG. This research is conducted in close collaboration with the institute of pharmacology and toxicology.

Sleep oscillations, such as delta waves, K-complexes or sleep spindles are typical patterns in the sleep EEG, which are a main ingredient for the definition of sleep stages and might have an important function with regard to processes of synaptic plasticity during sleep, i.e. for learning and memory consolidation [11]. Therefore their detection, the characterization of their properties and appropriate models for their dynamics are important for a further understanding of their role in sleep.

Using a new algorithm for the detection of oscillatory events based on adaptive autoregressive modeling we studied the changes of their properties throughout the night. Fig. 11.8 shows an example of one night with the events denoted as dots at a particular time and frequency. In the lower panel the hypnogram, i.e. the sleep stages, are shown.

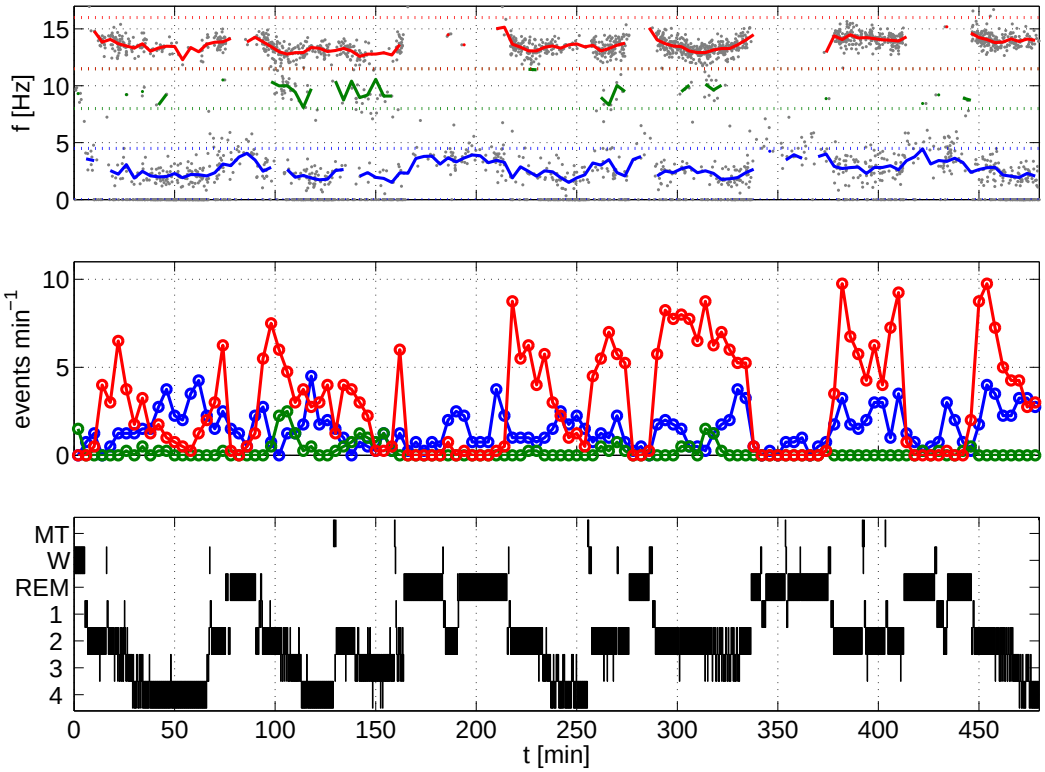

Figure 11.8: *Mean frequencies (top) and event densities (middle) of the oscillatory events for the three frequency bands for one night. The dotted lines in the upper panel denote the limits of the frequency bands. The grey points mark frequency and time for single events.*

We found that oscillatory events occurred essentially in three frequency bands: sigma (11.5-16 Hz, sleep spindles), alpha (8-11.5 Hz) and delta (0.75-4.5 Hz, delta waves and K-complexes). Their incidence showed only small intra- but large interindividual differences: the largest interindividual differences were found with respect to alpha events, we found individuals with a large amount of alpha events in sleep stages 3 and 4 (alpha-delta sleep), individuals with only a small amount of alpha events in REM sleep and sleep stage 1 and individuals with almost no alpha events at all.
The left panel of Fig. 11.9 illustrates the sleep stage dependencies of the mean event densities and their mean frequencies for the three types of events. The incidence of sleep spindles is maximal for sleep stage 2 and the incidence of delta events increases with the deepening of sleep. While this behavior is in agreement with standard knowledge the observed frequency behavior is less well known. The properties of the oscillatory events depend not only on the sleep stages but also on the time during the night, which can be studied by distinguishing the different REM-NREM cycles. See the hypnogram in Fig 11.8 for an example. This night shows five complete cycles. The right panel of Fig. 11.9 shows the results for sleep stage 2. The observed changes of the properties of oscillatory events during sleep are important for a deepening of our understanding of slow processes during sleep connected to synaptic plasticity.

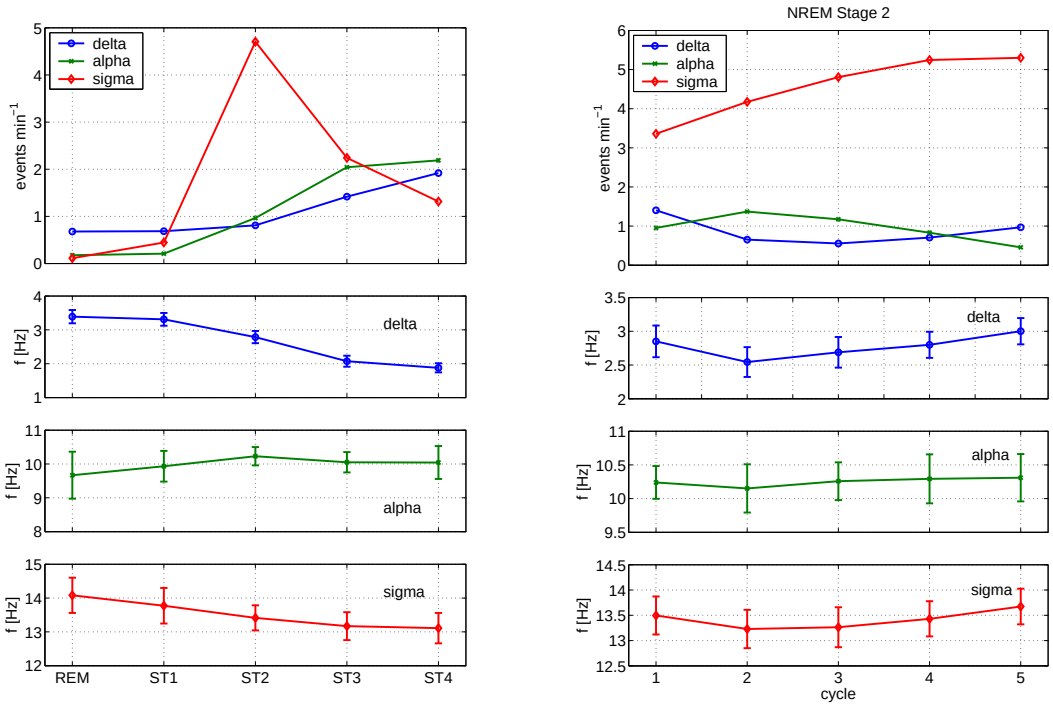

Figure 11.9: *Mean event densities (top) and mean frequencies (below) for the three frequency bands from a larger set of subjects and nights. The error bars denote the standard deviations with respect to the subjects. The left panel shows the sleep stage dependence and the right panel the influence of the sleep cycle, i.e. the time in the night.*

[1] E. P. Stoll, P. F. Meier, and T.A. Claxton, J. Phys.: Condens. Matter, **15**, 7881 (2003).

[2] H. H. Schmidtke in *Phys. Methods in Adv. Inorganic Chemistry*, edited by H. A. O. Hill and P. Day, Interscience London 1968, p. 107.

[3] E. P. Stoll, T. A. Claxton, and P. F. Meier, Phys.Rev.B **65**, 064532 (2002).

[4] P. F. Meier, T. A Claxton, P. Hüsser, S. Pliberšek, and E. P. Stoll, Z. Naturforschung **55 a**, 247 (2000).

[5] Y. Zha, V. Barzykin, and D. Pines, Phys.Rev.B **54**, 7561 (1996).

[6] T. Imai, J. Phys. Soc. Japan **59**, 2508 (1990).

[7] E. Pavarini, I. Dasgupta, T. Saha-Dasgupta, O. Jepsen, and O. K. Andersen, Phys.Rev.Lett.**87**, 047003 (2001).

[8] S. B. Sulaiman, N. Sahoo, T. P. Das, O. Donzelli, E. Torikai and K. Nagamine, Phys.Rev.B **44**, 7028 (1991).

[9] S. Renold and P. F. Meier, J. Supercond. Inc. Nov. Magn. **16**, 483 (2003).

[10] S. Renold, T. Heine, J. Weber, and P. F. Meier, Phys.Rev.B **67**, 024501 (2003).

[11] M. Steriade and I. Timofeev, Neuron review **37**, 563 (2003).

12 Mechanical Workshop

K. Bösiger, B. Schmid, B. Lussi, M. Schaffner, R. Meier (since October 2003), P. Treier, B. Wachter (left in October 2003), Ramon Caro (apprentice), A. Rochat (finished his apprenticeship and left in December 2003) and R. Reichen (apprentice)

Last year the workshop was mainly engaged in the development and construction of several new laboratory experiments for the medical students. We produced parts for experiments to illustrate the physical principles of the blood circulation system, the electrocardiogram, of ultrasound, of X-rays, the human eye and of an optical spectrometer. In particular, the construction of the blood circulation system was a time consuming and demanding job. Figure 12.1 shows the various assemblies. First, a prototype of each apparatus was built, tested and optimized. Then 15 pieces of each experiment were manufactured.

In fall 2003 a lathe was replaced with a new computer controlled machine (see Fig. 12.2). With the modern infrastructure of the mechanical workshop we are able to solve all kinds of demanding mechanical problems in relation to the projects described in this report. Projects from other institutes and private institutions are also worked on. These provide some income for the institute. In addition the workshop supplies over 30 institutes with metal and other technical material[4].

The blood circulation experiment.

Parts of the blood circulation experiment.

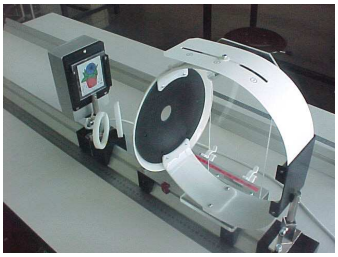

Optical bench with the model of the human eye. The focal distance is adjustable.

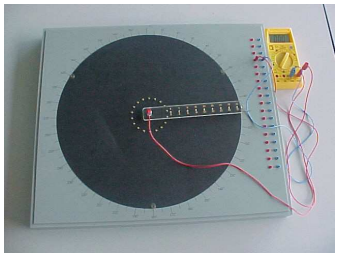

Setup which is used to measure the equipotential lines for different electrical field configurations.

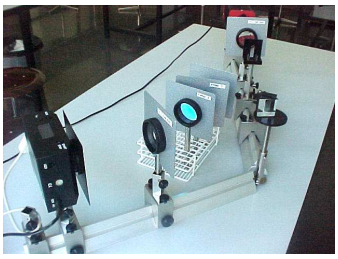

A prism optical spectrometer.

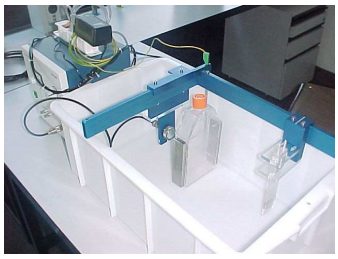

Setup to study ultrasonic sound.

Figure 12.1:
New laboratory experiments for medical students

The new lathe.

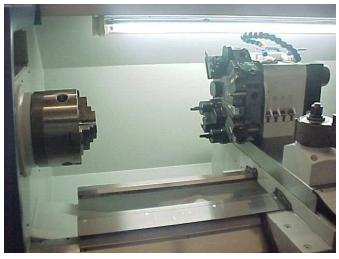

A closer look.

Figure 12.2: The new lathe

[4]For a catalogue see http://www.physik.unizh.ch/groups/werkstatt/dienstleistung.html

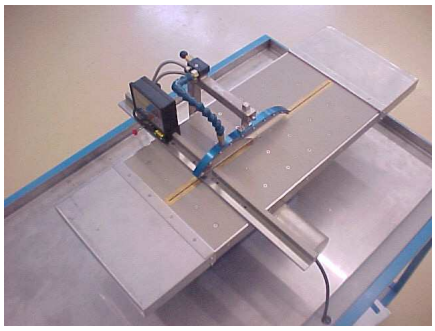

Figure 12.3: Total view of the circular saw on its stand.

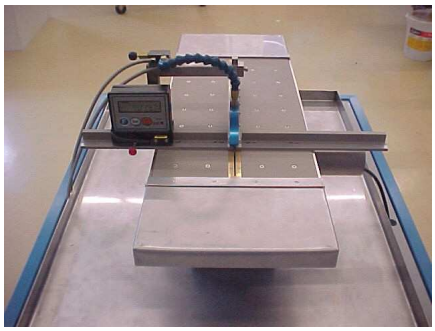

Figure 12.4: Closer look at the sawing table with the built in measuring system.

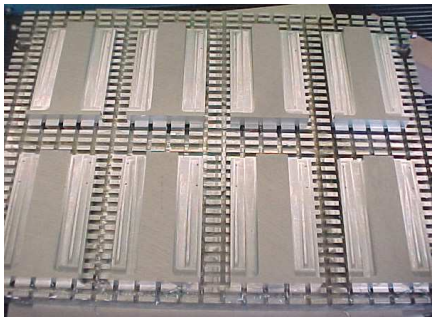

Figure 12.5: Support plate for the production of the cooling balconies of the LHCb inner tracker. Eight pieces are machined in parallel.

Figure 12.6: Gluing tool for the LHCb detector inner tracker during machining on the mill.

In the last report we presented the project of an apprentice exam work, which concludes the apprenticeship. The candidates have to do it in their home workshop. This work was successfully carried out in May 2003. Figures 12.3 and 12.4 show the completed circular saw with a diamond blade, which is now used in the workshop to cut special materials.
A selection of other finished and ongoing projects is listed below:

- *Surface Physics (Group Osterwalder, Sec. 9)*
  For this group the priorities were repair and maintenance work.

- *Physics of Biological Systems (Group Fink, Sec. 10)*
  Different mechanical infrastructure was manufactured and some test setups were built.

- *LHCb inner tracking detector (Group Straumann, Sec. 4)*
  Various parts for test stands were manufactured and the mass production of parts of the detector system was started at the end of 2003. So far, mainly cooling balconies and gluing tools are produced.

13 Electronics Workshop

W. Fässler, H.P. Meyer, P. Soland, K. Szeker

Apart from maintenance and repair work for the groups at the institute and some of their collaborators the workshop built equipment for the new medical student laboratory experiments. Several printed circuit boards were designed and manufactured. A current source, which can be used both in AC and DC mode and a filter preamplifier were developed and built (Fig. 13.1).
The workshop maintains and renews (together with L. Pauli and J. Seiler, who are responsible for the preparation of the experiments) also the equipment used for demonstration experiments in the lecture hall. Three lecture halls for the courses in experimental physics, including the one used for the medical students, have meanwhile been equipped with a flexible computerized readout system, which allows a clear presentation of the measurements. Figure 13.4 shows as an example the water vapour pressure curve, measured during a lecture on thermodynamics.

A selection of projects for the different groups is listed below:

- *Physics of Biological Systems (Group Fink, Sec. 10)*
  The control system for the high voltage supply used for a piezo drive was built.

- *Superconductivity and Magnetism (Group Keller, Sec. 7)*
  A laboratory spectrometer was equipped with a computer controllable motor power supply.

- *Surface Physics (Group Osterwalder, Sec. 9)*
  A solution for a GHz wideband amplifier was evaluated.

- *Particle Physics at DESY/HERA (H1) (Groups Straumann and Truöl, Sec. 3)*
  The workshop was involved in the production and integration of the new series of CIP readout electronics and the completion of the system. It also includes a crate controller for the low voltage power supply.

- *High-precision CP-violation Physics at LHCb (Group Straumann, Sec. 4)*
  Different test setups were built and the layout for a flexible printed circuit board with a fine pitch of 182 μm was designed.

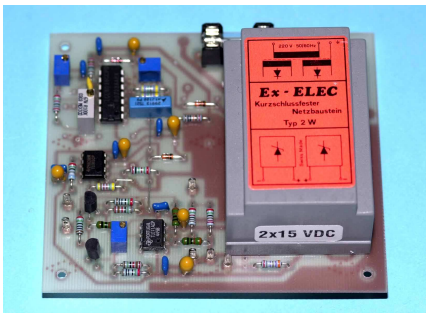

Figure 13.1: *AC-DC current source for the medical student laboratory experiments.*

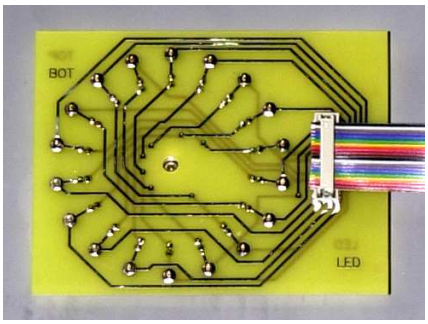

Figure 13.2: *Printed circuit board for the setup to measure equipotential lines.*

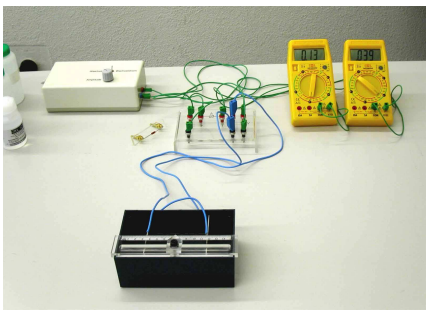

Figure 13.3: *Setup to measure the conductivity of different fluids.*

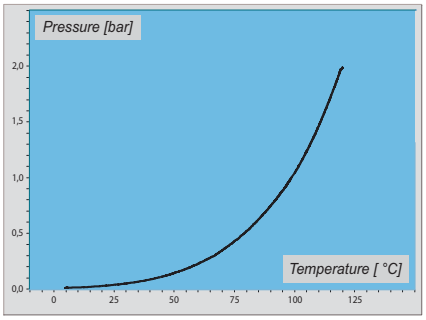

Figure 13.4: *Vapour pressure curve measured during a lecture on thermodynamics.*

14 Publications

14.1 Research group of Prof. C. Amsler

Articles

- *Positron plasma diagnostics and temperature control for antihydrogen production*
  M. Amoretti et al. (ATHENA Collaboration), Phys.Rev.Lett.91 (2003) 055001.

- *Detection of antihydrogen annihilations with a cryogenic pure-CsI crystal detector*
  C. Regenfus, C. Amsler, A. Glauser, D. Grögler, D. Lindelöf, H. Pruys,
  Nucl.Instr.Meth.A 504 (2003) 343.

- *Limits on the neutrino magnetic moment from the MUNU experiment*
  Z. Daraktchieva et al. (MUNU Collaboration), Phys.Lett.B 564 (2003) 190.

- *A measurement of the neutrino magnetic moment at the Bugey nuclear reactor*
  O. Link, Inaugural Dissertation, Universität Zürich, 2003.

- *The ATHENA antihydrogen apparatus*
  M. Amoretti et al. (ATHENA Collaboration), Nucl.Instr.Meth.A 518 (2004) 679.

- *Annihilation at rest of antiprotons and protons into neutral particles*
  C. Amsler et al. (CRYSTAL BARREL Collaboration), Nucl. Phys. A 720 (2003) 357.

- *Production and decay of $\eta'(958)$ and $\eta(1440)$ in $\bar{p}p$ annihilation at rest*
  C. Amsler et al. (CRYSTAL BARREL Collaboration), Eur.Phys.J.C 33 (2004) 23.

- *Mesons beyond the naive quark model*
  C. Amsler and N. A. Törnqvist, Physics Reports 389 (2004) 61.

- *High rate production of antihydrogen*
  M. Amoretti et al. (ATHENA Collaboration), Phys.Lett.B 578 (2004) 23.

- *Antihydrogen production temperature dependence*
  M. Amoretti et al. (ATHENA Collaboration), Phys.Lett.B 583 (2004) 59.

- *A cryogenic silicon microstrip and pure-CsI detector for detection of antihydrogen annihilations*
  C. Regenfus, Nucl.Instr.Meth.A 501 (2003) 65.

- *Development of APD readout for pure-CsI crystals at cryogenic temperatures*
  A. Glauser, Nucl.Instr.Meth.A 504 (2003) 347.

- *Study of the Hamamatsu avalanche photodiode at liquid nitrogen temperatures*
  A. Dorokhov, A. Glauser, Y. Musienk, C. Regenfus, S. Reucroft and J. Swain,
  Nucl.Instr.Meth.A 504 (2003) 58.

- *New Developments in Vertex Reconstruction for CMS*
  R. Frühwirth, K. Prokofiev, T. Speer, P. Vanlaer and W. Waltenberger,
  Nucl.Instr.Meth.A 502 (2003) 699.

- *Vertex reconstruction framework and its implementation for CMS*
  T. Boccali, R. Frühwirth, W. Waltenberger, K. Prokofiev, T. Speer, P. Vanlaer,
  Proc. Conf. on Computing in High Energy and Nuclear Physics, La Jolla (2003).

- *New vertex reconstruction algorithms for CMS*
  R. Frühwirth, W. Waltenberger, K. Prokofiev, T. Speer, P. Vanlaer, E. Chabanat, N. Estre, Proc. Conf. on Computing in High Energy and Nuclear Physics, La Jolla (2003).

- *The Atlas and CMS trackers*
  Thomas Speer, Proc. 5th Int. Conf. on Hyperons, Charm and Beauty Hadrons, Vancouver (2002), Nucl. Phys. (Proc. Suppl.) 115 (2003) 318.

- *First production and detection of cold antihydrogen atoms*
  M.C. Fujiwara et al. (ATHENA Collaboration), Proc. Int. Conf. on Low Energy Antiproton Physics (LEAP'03), Yokohama, Japan, Nucl.Instr.Meth.B 214 (2004) 11.

- *Temperature dependence of antihydrogen production in the ATHENA experiment*
  G. Bonomi et al. (ATHENA Collaboration), Proc. Int. Conf. on Low Energy Antiproton Physics (LEAP'03), Yokohama, Japan, Nucl.Instr.Meth.B 214 (2004) 17.

Articles in press

- *Tests of silicon sensors for the CMS pixel detector*
  A. Dorokhov et al., Nucl.Instr.Meth.A, preprint physics/0311050.

- *Position Dependence of Charge Collection in Prototype Sensors for the CMS Pixel Detector*
  T. Rohe et al., IEEE-TNS 7, preprint physics/0312009.

- *Detection of antihydrogen annihilations with a Si-microstrip and pure CsI detector*
  I. Johnson et al. (ATHENA Collaboration), World Scientific.

- *Design and Test of the CMS Pixel Readout Chip*
  M. Barbero et al., Nucl.Instr.Meth..

- *Study of antiproton annihilation on neutrons into* $\omega\pi^-\pi^0$
  C. Amsler et al. (CRYSTAL BARREL Collaboration), Phys. Lett. B.

- *Review of Particle Physics*
  S. Eidelman et al. (Particle Data Group), Phys. Lett. B.

- *Light exotic mesons*
  C. Amsler, Proc. Quark Confinement and the Hadron Spectrum V, Gargnano, 2002, World Scientific.

- *Vertex reconstruction in CMS*
  E. Chabanat et al., Proc. vertex 2003, Low Wood, Cumbria, UK, 2003, Nucl.Instr.Meth..

- *A Gaussian sum filter for vertex reconstruction*
  T. Speer, IX Int. Workshop on Advanced Computing and Analysis Techniques in Physics Research, ACAT03, Tsukuba, Japan, 2003, Nucl.Instr.Meth..

Invited Lectures

- C. Amsler: *Gluebälle*
  Invited talk, Physikalische Gesellschaft Zürich, 19.06.03.

- C. Amsler: *Experimental evidence for a large content of glue in the $f_0(1500)$ meson*
  Colloquium, Budker Institute of Nuclear Physics, Novosibirsk, 12.9.03.

- C. Amsler: *Antihydrogen*
  Colloquium, Budker Institute of Nuclear Physics, Novosibirsk, 19.9.03.

- C. Amsler: *Exotic mesons*
  Seminar, Laboratory of Theoretical Physics of Sobolev Institute for Mathematics, 24.9.03.

- C. Amsler: *Antihydrogen*
  Colloque, Université de Neuchâtel, 10.11.03.

- C. Amsler: *Fabrication d'antimatière au CERN*
  Conférence d'orientation, EPF-Lausanne, 28.1.04.

- V. Chiochia: *Tests of silicon sensors for the CMS Pixel Detector*
  Invited talk, 3rd Workshop on radiation hard semiconductor devices for very high luminosity colliders, CERN, 4.11.03.

- I. Johnson: *Detection of antihydrogen annihilations with a Si-micro-strip and pure CsI crystal detector*
  Invited talk, 8th ICATPP Conference on Astroparticle, Particle, Space Physics, Detectors and Medical Physics Applications, Como, Italy, 9.10.03.

- A. Dorokhov: *Tests of silicon sensors for the CMS pixel detector*
  Invited talk, 6th International Conference on Large Scale Applications and Radiation Hardness of Semiconductor Detectors, Florence, Italy 30.11.03.

- C. Regenfus: *Cold Antihydrogen for probing world antiworld symmetry*
  Colloque, Université de Fribourg, 21.5.03.

- V. Chiochia: *The CMS Pixel Detector: Overview and Test Beam results*
  Seminar, DESY, 5.12.03.

- T. Speer: *A Gaussian sum filter for vertex reconstruction*
  Invited talk, IX Int. Workshop on Advanced Computing and Analysis Techniques in Physics Research, ACAT03, Tsukuba, Japan, 4.12.03.

ATHENA Collaboration (2003):
M. Amoretti, C. Amsler, G. Bonomi, A. Bouchta, P. Bowe, C. Carraro, C. L. Cesar, M. Charlton, M. Doser, V. Filippini, A. Fontana, M. C. Fujiwara, R. Funakoshi, P. Genova, J. S. Hangst, R. S. Hayano, L. V. Joergensen, I. Johnson, V. Lagomarsino, R. Landua, E. Lodi Rizzini, M. Macri, N. Madsen, P. Montagna, H. Pruys, C. Regenfus, P. Riedler, J. Rochet, A. Rotondi, G. Rouleau, G. Testera, A. Variola, D. P. van der Werf

MUNU Collaboration (2003):
C. Amsler, M. Avenier, C. Broggini, J. Busto, C. Cerna, Z. Daraktchieva, G. Gervasio, P. Jeanneret,

G. Jonkmans, D.H. Koang, J. Lamblin, D. Lebrun, O. Link, F. Ould-Saada, G. Puglierin, A. Stutz, A. Tadsen, J.-L. Vuilleumier

CRYSTAL BARREL Collaboration (2003):
C. Amsler, C. A. Baker, B. M. Barnett, C. J. Batty, P. Blüm, K. Braune, V. Credé, K. M. Crowe, M. Doser, W. Dünnweber, D. Engelhardt, M.A. Faessler, R. P. Haddock, F. H. Heinsius, N. P. Hessey, D. Jamnik, H. Kalinowsky, P. Kammel, J. Kisiel, E. Klempt, H. Koch, M. Kunze, U. Kurilla, R. Landua, H. Matthäy, C. A. Meyer, F. Meyer-Wildhagen, R. Ouared, K. Peters, B. Pick, M. Ratajczak, C. Regenfus, J. Reinnarth, A. Sarantsev, U. Strohbusch, M. Suffert, J. S. Suh, U. Thoma, S. Wallis-Plachner, D. Walther, U. Wiedner

PARTICLE DATA Group (2003):
K. Hagiwara, K. Hikasa, K. Nakamura, M. Tanabashi, M. Aguilar-Benitez, C. Amsler, R.M. Barnett, P.R. Burchat, C.D. Carone, C. Caso, G. Conforto, O. Dahl, M. Doser, S. Eidelman, J.L. Feng, L. Gibbons, M. Goodman, C. Grab, D.E. Groom, A. Gurtu, K.G. Hayes, J.J. Hernandez-Rey, K. Honscheid, C. Kolda, M.L. Mangano, D.M. Manley, A.V. Manohar, J. March-Russell, A. Masoni, R. Miquel, K. Mönig, H. Murayama, S. Navas, K.A. Olive, L. Pape, C. Patrignani, A. Piepke, M. Roos, J. Terning, N.A. Törnqvist, T.G. Trippe, P. Vogel, C.G. Wohl, R.L. Workman, W.-M. Yao

14.2 Research group of Prof. H. Keller

Articles

- *Site-selective oxygen isotope effect on the magnetic field penetration depth in underdoped* $Y_{0.6}Pr_{0.4}Ba_2Cu_3O_{7-\delta}$
  R. Khasanov, A. Shengelaya, E. Morenzoni, M. Angst, K. Conder, I.M. Savić, D. Lampakis, E. Liarokapis, A. Tatsi, and H. Keller, Phys.Rev.B, **68**, 220506(R)-1-4 (2003).

- *Relevance of electron-lattice coupling in cuprate superconductors*
  T. Schneider, R. Khasanov, K. Conder, and H. Keller,
  J. Phys.: Condens. Matter **15**, L763-L769 (2003).

- *Observation of the Conduction Electron Spin Polarization in the Ag Spacer of a Fe/Ag/Fe Trilayer*
  H. Luetkens, J. Korecki, E. Morenzoni, T. Prokscha, M. Birke, H. Glückler, R. Khasanov, H.-H. Klauss, T. Slezak, A. Suter, E.M. Forgan, Ch. Niedermayer, and F.J. Litterst,
  Phys.Rev.Lett.**91**, 017204-1-4 (2003).

- *Vortex motion in type II superconductors probed by muon spin rotation and "SANS"*
  E.M. Forgan, D. Charalambous, P.G. Kealey, P.J.C. King, R. Khasanov, and A. Amato,
  Physica B **326**, 342-345 (2003).

- *Muonium formation at keV energies*
  T. Prokscha, E. Morenzoni, N. Garifianov, H. Glückler, R. Khasanov, H. Luetkens, and A. Suter,
  Physica B **326**, 51-54 (2003).

- *Low energy muons as probes of thin films and near surface regions*
  E. Morenzoni, R. Khasanov, H. Luetkens, T. Prokscha, A. Suter, N. Garifianov, H. Glückler, M. Birke, E. Forgan, H. Keller, J. Litterst, Ch. Niedermayer, and G. Nieuwenhuys,
  Physica B **326**, 196-204 (2003).

- *Diffusion of muons in metallic multilayers*
  H. Luetkens, J. Korecki, E. Morenzoni, T. Prokscha, N. Garifianov, H. Glückler, R. Khasanov, J. Litterst, T. Slezak, and A. Suter, Physica B **326**, 545-549 (2003).

- *Excess electron transport in cryoobjects*
  D.G. Eshchenko, V.G. Storchak, J.H. Brewer, S.P. Cottrell, and S.F.J. Cox,
  Low Temp. Phys. **29**, 185-195 (2003).

- *Excited muonium state in CdS*
  D.G. Eshchenko, V.G. Storchak, S.P. Cottrell, and S.F.J. Cox, Phys.Rev.B **68**, 073201-1-4 (2003).

- *Weakly bound muonium state in GaP*
  V.G. Storchak, D.G. Eshchenko, R.L. Lichti, and J.H. Brewer,
  Phys.Rev.B **67**, 121201(R)-1-4 (2003).

- *Relationship between the isotope effects on transition temperature, specific heat and penetration depths*
  T. Schneider, Phys.Rev.B **67**, 134514-1-7 (2003).

- *Three-Spin-Polarons and Their Elastic Interaction in Cuprates*
  B.I. Kochelaev, A.M. Safina, A. Shengelaya, H. Keller, K.A. Müller, K. Conder,
  Mod. Phys. Lett. B **17**, 415-421 (2003).

- *On the effect of heterovalent substitution in ruthenocuprates*
  P.W. Klamut, B. Dabrowski, S.M. Mini, M. Maxwell, M. Mais, I. Felner, U. Asaf, F. Ritter, A. Shengelaya, R. Khasanov, I. Savic, H. Keller, A. Wisniewski, R. Puzniak, I. Fita, C. Sulkowski, and M. Matusiak, Physica C **387**, 33-39 (2003).

- *Direct observation of the oxygen isotope effect on the in-plane magnetic field penetration depth in optimally doped* $YBa_2Cu_3O_{7-\delta}$
  R. Khasanov, D.G. Eshchenko, H. Luetkens, E. Morenzoni, T. Prokscha, A. Suter, M. Mali, J. Roos, K. Conder, and H. Keller, Phys.Rev.Lett.**92** 057602-1-4 (2004).

- *Estimation of the surface-d to bulk-s crossover in the macroscopic superconducting wave function in cuprates*
  K.A. Müller, J. Supercond. **17**, 3-6 (2004).

- *Finite-size effect in* $Bi_2Sr_2CaCu_2O_{8+\delta}$ *and* $YBa_2Cu_3O_{6.7}$ *probed by the in-plane and out-of-plane penetration depths*
  T. Schneider and D. Di Castro, Phys.Rev.B **69**, 024502-1-7 (2004).

- *Probing inhomogeneities in type II superconductors by means of thermal fluctuations, magnetic fields, and isotope effects*
  T. Schneider, J. Supercond. **17**, 41-48 (2004).

- *Coexistence of magnetism and superconductivity in* $Eu_{1.4}Ce_{0.6}RuSr_2Cu_2O_{10}$*: A muon spin rotation and magnetization study*
  A. Shengelaya, R. Khasanov, D.G. Eshchenko, U. Asaf, I.M. Savić, H. Keller and K.A. Müller, Phys.Rev.B **69**, 024517-1-6 (2004).

- *Two Band Superconductivity in* MgB_2*: Basic Anisotropic Properties and Phase Diagram*
  M. Angst and R. Puzniak, in *Focus on Superconductivity*, ed. B. P. Martines, Vol. **1** (Nova Science Publishers, New York, 2004) (pp. 1-49).

Articles in press

- *Anisotropic properties of MgB_2 by torque magnetometry*
  M. Angst, D. Di Castro, R. Puzniak, A. Wisniewski, J. Jun, S. M. Kazakov, J. Karpinski, S. Kohout, and H. Keller, Physica C.

- *The mystery of superconductivity in the cuprates evinced by London penetration depths measurements*
  T. Schneider, Proceedings of the International School of Physics, on *The Physics of Complex Systems (new advances and perspectives)*, Varenna, Italy, 1-11 July, 2003.

- *Granular superconductivity in the cuprates evinced by finite size effects in the specific heat and London penetration depths*
  T. Schneider, Proceedings of the Nato Advance Research Workshop on *Symmetry and Heterogeneity in High-Temperature Superconductors*, Erice, Italy, 4-10 October, 2003.

- *Evidence for granularity, anisotropy and lattice distortions in cuprate superconductors and their implications*
  H. Keller and T. Schneider, Proceedings of the Nato Advance Research Workshop on *Symmetry and Heterogeneity in High-Temperature Superconductors*, Erice, Italy, 4-10 October, 2003.

Diploma and PhD theses

- *Studies of the oxygen-isotope effect on the magnetic field penetration depth in cuprate superconductors*
  Rustem Khasanov, Dissertation, Physik-Institut, Universität Zürich, 2003.

- *Beobachtung einer metallischen Phase in schwach dotiertem $La_{2-x}Sr_xCuO_4$ anhand von elektronenparamagnetischer Resonanz*
  Maria Bruun, Diplomarbeit, Physik-Institut, Universität Zürich, 2003.

Conference reports

- *Anisotropic superconducting properties of MgB_2 by torque magnetometry*
  M. Angst, D. Di Castro, R. Puzniak, A. Wisniewski, J. Jun, S. M. Kazakov, J. Karpinski, S. Kohout, H. Keller,
  M2S-HTSC-VII 7th International Conference on Materials and Mechanisms of Superconductivity and High Temperature Superconductors, Rio de Janeiro, Brazil, 25-30 May, 2003.

- *Anisotropic superconducting properties of MgB_2 single crystals by torque magnetometry*
  M. Angst, R. Puzniak, A. Wisniewski, D. Di Castro, S. Kohout, H. Keller, J. Jun, S. M. Kazakov, J. Karpinski, MaNEP topical meeting: Materials: preparation, characterization and specific properties, Neuchâtel, Switzerland, 25-26 June, 2003.

- *Disorder driven phase transition of vortex matter in MgB_2*
  M. Angst, R. Puzniak, A. Wisniewski, J. Jun, S. M. Kazakov, J. Karpinski,
  Third International Conference on Magnetic and Superconducting Materials (MSM03), Monastir, Tunisia, 1-4 September, 2003.

- *Mixed state anisotropies of the two-band superconductor MgB_2*
  M. Angst, R. Puzniak, A. Wisniewski, D. Di Castro, S. Kohout, H. Keller, J. Jun, S. M. Kazakov, J. Karpinski, 2003 Swiss Workshop on Materials with Novel Electronic Properties, Les Diablerets, Switzerland, September 29 - October 1, 2003.

- *Study of the boron isotope effect on the magnetic penetration depth in MgB_2*
  D. Di Castro, M. Angst, D.G. Eshchenko, R. Khasanov, J. Roos, I.M. Savić, A. Shengelaya, S.L. Bud'ko, P.C. Canfield, K. Conder, J. Karpinski, S.M. Kazakov, R.A. Ribeiro, and H. Keller, 2003 Swiss Workshop on Materials with Novel Electronic Properties, Les Diablerets, Switzerland, September 29 - October 1, 2003.

- *Torque magnetometric measurements of Oxygen Isotope Effects in $La_{2-x}Sr_xCuO_4$ and $YBa_2Cu_4O_8$ single crystals*
  S. Kohout, D. Di Castro, M. Angst, J. Roos, J. Karpinski, K. Conder, T. Sasagawa, H. Keller, 2003 Swiss Workshop on Materials with Novel Electronic Properties, Les Diablerets, Switzerland, September 29 - October 1, 2003.

- *Pressure effect on in-plane magnetic field penetration depth in $YBa_2Cu_4O_8$*
  R. Khasanov, D.G. Eshchenko, D. Di Castro, D. Andreika, K. Conder, S. Kazakov, K. Pomjakushina, I. Savić, T. Straessle, R. Tetean, and H. Keller, 2003 Swiss Workshop on Materials with Novel Electronic Properties, Les Diablerets, Switzerland, September 29 - October 1, 2003.

- *Change of YBaCuO Cu nuclear quadrupole resonance parameters by immersion of YBaCuO powder grains into a nonconductive matrix*
  M. Mali, J. Roos, H. Keller, K. Conder, 2003 Swiss Workshop on Materials with Novel Electronic Properties, Les Diablerets, Switzerland, September 29 - October 1, 2003.

- *Low frequency charge fluctuations in the millikelvin temperature region exhibited by strong plane Cu nuclear quadrupole relaxation observed in $YBa_2Cu_4O_8$*
  M. Mali, J. Roos, H. Keller, A. Volodin, A. Egorov, A.V. Dooglav,
  2003 Swiss Workshop on Materials with Novel Electronic Properties, Les Diablerets, Switzerland, September 29 - October 1, 2003.

- *Measurements of superconducting properties on under- and overdoped $La_{2-x}Sr_xCuO_4$ single crystals by torque magnetometry*
  S. Kohout, T. Sasagawa, K. Conder, H. Keller,
  Annual meeting of the Swiss Physical Society, Neuchâtel, Switzerland, 3-4 March, 2004.

- *Single Crystal ^{11}B-NMR Study of Magnesium Diboride*
  S. Strässle, J. Roos, M. Mali, H. Keller, J. Karpinski,
  Annual meeting of the Swiss Physical Society, Neuchâtel, Switzerland, 3-4 March, 2004.

- *Anisotropy and internal field distribution of MgB_2 in the mixed state at low temperatures*
  D. Di Castro, M. Angst, R. Khasanov, D.G. Eshchenko, A. Shengelaya, I. Savic, S. Kohout, J. Roos, S. M. Kazakov, J. Karpinski, H. Keller,
  Annual meeting of the Swiss Physical Society, Neuchâtel, Switzerland, 3-4 March, 2004.

- *Site-selective oxygen isotope effect on the magnetic field penetration depth in underdoped $Y_{0.6}Pr_{0.4}Ba_2Cu_3O_{7-\delta}$*
  R. Khasanov, A. Shengelaya, E. Morenzoni, M. Angst, K. Conder, I.M. Savić, D. Lampakis, E. Liarokapis, A. Tatsi, H. Keller,
  Annual meeting of the Swiss Physical Society, Neuchâtel, Switzerland, 3-4 March, 2004.

- *Low energy muon study of $YBa_2Cu_3O_7/PrBa_2Cu_3O_7/YBa_2Cu_3O_7$ tri-layer*
  D.G. Eshchenko, R. Khasanov, E. Morenzoni, T. Proschka, A. Suter, H. Keller, Ø. Fischer, E. Koller, E. Treboux, P. Legendre,
  Annual meeting of the Swiss Physical Society, Neuchâtel, Switzerland, 3-4 March, 2004.

Invited lectures

- M. Angst: *Anisotropic properties of the two-band superconductor MgB_2 by torque magnetometry*
  Third International Conference on Magnetic and Superconducting Materials (MSM03), Monastir, Tunisia, 1-4 September, 2003.

- D. Eshchenko: *Muonium formation and ionization in semiconductors*
  LMU seminar, Laboratory for Muon-Spin Spectroscopy, Paul Sherrer Institut, Villigen, Switzerland, 12 June, 2003.

- H. Keller: *Oxygen-isotope effect on the magnetic penetration depth in cuprate superconductors*
  Shanghai, China, 3-5 April, 2003.

- H. Keller: *Oxygen-isotope effect on the magnetic penetration depth in cuprate superconductors*
  M2S-HTSC-VII 7th International Conference on Materials and Mechanisms of Superconductivity and High Temperature Superconductors, Rio de Janeiro, Brazil, May 25-30, 2003.

- H. Keller: *Unconventional isotope effects in cuprate high-temperature superconductors*
  Institut für Festkörper- und Werkstofforschung Dresden, Dresden, Germany, 7 July, 2003.

- H. Keller: *Unconventional isotope effects in cuprate high-temperature superconductors*
  Fifth General Conference of the Balkan Physical Union, Vrnjacka Banja, Serbia and Montenegro, 25-29 August, 2003.

- H. Keller: *Unconventional isotope effects in cuprate high-temperature superconductors*
  Nato Advance Research Workshop on *Symmetry and Heterogeneity in High-Temperature Superconductors*, Erice, Italy, 4-10 October, 2003.

- H. Keller: *Unconventional isotope effects in cuprate high-temperature superconductors*
  16th International Symposium on Superconductivity (ISS2003), Tsukuba, Japan, 27-29 October, 2003.

- H. Keller: *Unconventional isotope effects in cuprate high-temperature superconductors*
  Tohoku University, Institute for Material Research, Sendai, Japan, 30 October, 2003.

- H. Keller: *Oxygen-isotope effect on the magnetic penetration depth in cuprate superconductors*
  International Workshop on Fermi Surface and Lattice Effects in Cuprate High Temperature Superconductors (AIST), Tsukuba, Japan, 31 October, 2003.

- H. Keller: *Unconventional isotope effects in cuprate high-temperature superconductors*
  University of Geneva, DPMC, Geneva, Switzerland, 25 March, 2004.

- R. Khasanov: *Direct observation of the oxygen isotope effect on the in-plane magnetic field penetration depth in optimally doped $YBa_2Cu_3O_{7-\delta}$*
  2003 Swiss Workshop on Materials with Novel Electronic Properties, Les Diablerets, Switzerland, September 29 - October 1, 2003.

- M. Mali: *Temperature dependence of plane copper NQR linewidth in the $YBa_2Cu_4O_8$ superconductor*
  Specialized Colloque AMPERE on NMR and EPR Broad-Line Solids, Portoroz, Slovenia, 8-12 September, 2003.

- J. Roos: *Broad-line Cu-NQR studies in cuprate high-temperature superconductors*
  Specialized Colloque AMPERE on NMR and EPR Broad-Line Solids, Portoroz, Slovenia, 8-12 September, 2003.

- T. Schneider: *Probing Inhomogeneities in Type II Superconductors by Means of Thermal Fluctuations, Magnetic Fields, and Isotope Effects*
  Dynamic Inhomogeneities in Complex Oxides, Bled, Slovenia, 14-20 June, 2003.

- T. Schneider: *The mystery of superconductivity in the cuprates evinced by London penetration depths measurements*
  International School of Physics, Enrico Fermi Course CLV, The Physics of Complex Systems (new advances and perspectives), Varenna, Italy, 1-11 July, 2003.

- T. Schneider: *Granular superconductivity in the cuprates evinced by finite size effects in the specific heat and London penetration depths*
  Nato Advance Research Workshop on *Symmetry and Heterogeneity in High-Temperature Superconductors*, Erice, Italy, 4-10 October, 2003.

- T. Schneider: *Evidence for granularity, anisotropy and lattice distortions in cuprate superconductors and their implications*
  Nato Advance Research Workshop on *Symmetry and Heterogeneity in High-Temperature Superconductors*, Erice, Italy, 4-10 October, 2003.

- A. Shengelaya: *Microscopic phase separation driven by elastic interactions in $La_{2-x}Sr_xCuO_4$ as revealed by electron paramagnetic resonance*
  Dynamic Inhomogeneities in Complex Oxides, Bled, Slovenia, 14-20 June, 2003.

- A. Shengelaya: *A metallic phase in very low doped $La_{2-x}Sr_xCuO_4$ observed by electron paramagnetic resonance*
  2003 Swiss Workshop on Materials with Novel Electronic Properties, Les Diablerets, Switzerland, September 29 - October 1, 2003.

14.3 Research group of Prof. P. F. Meier

Articles

- *Synthesis of one monolayer of hexagonal boron nitride on Ni(111) from B-trichloroborazine $(ClBNH)_3$*
  W. Auwärter, H.U. Suter, H. Sachdev and T. Greber, Chemistry of Materials B **326**, 329 (2003).

- *Dynamics of human sleep EEG*
  E. Olbrich and P. Achermann, Neurocomputing **52-54**, 857 (2003).

- *Nonlinearity and nonstationarity in human sleep EEG data*
  E. Olbrich, P.F. Meier and P. Achermann, Sleep **26**, A394 (2003).

- *Influence of lattice parameter scaling on local electronic and magnetic properties in La_2CuO_4*
  S. Renold and P.F. Meier, J. Supercond. Inc. Nov. Magn. **16**, 483 (2003).

- *Nuclear magnetic resonance chemical shifts and paramagnetic field modifications in La_2CuO_4*
  S. Renold, T. Heine, J. Weber, and P.F. Meier, Phys. Rev. B **67**, 024501 (2003).

- *Dimensional complexity and spectral properties of the human sleep EEG*
  Y. Shen, E. Olbrich, P. Achermann, and P.F. Meier, Clin. Neurophysiol. **114**, 199 (2003).

- *Charge distribution in $La_{2-x}Sr_xCuO_4$*
  E. P. Stoll, T. A. Claxton, and P.F. Meier, Int. J. of Mod. Phys. B **17**, 3329 (2003).

- *On the distribution of intrinsic holes in cuprates*
  E.P. Stoll, T.A. Claxton, and P.F. Meier, J. Phys.: Condens. Matter **15**, 7881 (2003).

- *Muon sites and hyperfine fields in La_2CuO_4*
  H. U. Suter, E.P. Stoll, and P.F. Meier, Physica B: Condensed Matter **326**, 329 (2003).

- *Percolation, fractal behavior and high-T_c superconductivity*
  E.P. Stoll, J. Supercond. Inc. Nov. Magn. **17**, 79 (2004).

Diploma and PhD theses

- *First-principles studies of local electronic and magnetic properties in cuprates*
  S. Renold, PhD-thesis, University of Zurich (2004).

Articles in press

- *Oscillatory events in the human sleep EEG−detection and properties*
  E. Olbrich and P. Achermann, Neurocomputing, in Press, (2004).

- *From next nearest neighbour site percolation to continuum percolation: Application to high-Tc superconductors*
  E. P. Stoll, Int. J. of Mod. Phys. C **15**, in Press (2004).

Invited Lectures

- P.F. Meier: *Re-assessment of the interpretation of NMR and μSR data on cuprate superconductors*
  NATO Advanced Research Workshop on New Challenges in Superconductivity, University of Miami, 16.01.04.

- E. Olbrich: *Nonstationarity and nonlinearity in human sleep EEG data*
  Kolloquium: Aktuelle Themen der Schlafforschung, Institut für Pharmakologie und Toxikologie, Universität Zürich, 7.01.03.

- E. Olbrich: *Oszillatory events in the human sleep EEG*
  Computational Neuroscience Meeting 2003, Alicante, 06.07.03.

- S. Renold: *NMR Chemical shifts and paramagnetic field modifications in La_2CuO_4*
  MANEP-Conference, Les Diablerets 29.09.03.

- E. P. Stoll: *Inhomogeneities and percolation in complex high-T_c superconductors*
  Conference: Dynamic inhomogeneities in complex matter, Bled, Slovenia, 14-20.06.03.

Conference related contributions

- S. Renold: *NMR chemical shifts and paramagnetic field modifications in La_2CuO_4*
  2003 March Meeting of the American Physical Society, Austin, TX, 07.03.03.

- S. Renold: *Influence of lattice parameters on local electronic and magnetic properties in La_2CuO_4 and $Sr_2CuO_2Cl_2$*
  2003 March Meeting of the American Physical Society, Austin, TX, 07.03.03.

- S. Renold: *NMR chemical shifts and paramagnetic field modifications in La_2CuO_4*
  Annual meeting of the Swiss Physical Society, Basel 20.-21.03.03.

- E. P. Stoll: *Percolation, fractal behaviour and high-T_c superconductivity*
  Annual meeting of the Swiss Physical Society, Basel 20.-21.03.03.

14.4 Research group of Prof. J. Osterwalder

Articles

- *The electronic structure of a surfactant layer: Pb/Cu(111)*
  F. Baumberger, A. Tamai, M. Muntwiler, T. Greber, J. Osterwalder,
  Surf. Sci. 532-535, 82-86 (2003).

- *Optical recognition of atomic steps on surfaces*
  F. Baumberger, Th. Herrmann, A. Kara, S. Stolbov, N. Esser, T. S. Rahman, J. Osterwalder, W. Richter, T. Greber, Phys.Rev.Lett.90, 177402-1-4 (2003).

- *Density functional theory investigation of the geometric and spintronic structure of h-BN/Ni(111) in view of photoemission and STM experiments*
  G. B. Grad, P. Blaha, K. Schwarz, W. Auwärter, T. Greber, Phys. Rev. B 68, 085404-1-7 (2003).

- *Defect lines and two-domain structure of hexagonal boron nitride films on Ni(111)*
  W. Auwärter, M. Muntwiler, J. Osterwalder, T. Greber, Surf. Sci. 545, L735-L740 (2003).

- *Reinvestigation of the band structure of the Si(111)5x2-Au surface*
  I. Matsuda, M. Hengsberger, F. Baumberger, T. Greber, H. W. Yeom, J. Osterwalder,
  Phys. Rev. B 68, 195319-1-7 (2003).

- *Growth morphologies and defect structure in hexagonal boron nitride films on Ni(111): a combined STM and XPD study*
  J. Osterwalder, W. Auwärter, M. Muntwiler, T. Greber,
  e-J. Surf. Sci. Nanotech. 1, 124-129 (2003).

- *Remarks on the Generalized Solution of Electron Diffusion*
  A. Dolocan, Int. J. of Mod. Phys. B 17, 1043-1069 (2003).

- *X-Ray Propagation in Tapered Planar Waveguide*
  A. Dolocan, J.F. Van Der Veen, Int. J. of Mod. Phys. B 17, 2213-2257 (2003).

- *Step-lattice-induced band-gap opening at the Fermi level*
  F. Baumberger, M. Hengsberger, M. Muntwiler, M. Shi, J. Krempasky, L. Patthey, J. Osterwalder, T. Greber, Phys.Rev.Lett.92, 016803-1-4 (2004).

- *Boron nitride nanomesh*
  M. Corso, W. Auwärter, M. Muntwiler, A. Tamai, T. Greber, J. Osterwalder,
  Science 303, 217-220 (2004).

- *Synthesis of one monolayer of hexagonal boron nitride on Ni(111) from B-Trichloroborazine $(ClBNH)_3$*
  W. Auwärter, H. U. Suter, H. Sachdev, T. Greber, Chem. Mater. 16, 343-345 (2004).

Book chapter:

- *Structural effects in XPS and AES: Diffraction*
  J. Osterwalder, in *Surface Analysis by Electron Spectroscopy*, D. Briggs and J. Grant, eds., Surface Spectra Ltd and IM Publications (2003), p. 557-585.

Articles in press

- *Spin- and angle-resolved photoemission spectroscopy study of the Au(111) Shockley surface state*
  M. Muntwiler, M. Hoesch, V. N. Petrov, M. Hengsberger, L. Patthey, M. Shi, M. Falub, T. Greber, J. Osterwalder, J. Electron Spectrosc. Relat. Phenom. (in press).

- *One-dimensional chains of C_{60} molecules on Cu(221)*
  A. Tamai, W. Auwärter, C. Cepek, F. Baumberger, T. Greber, J. Osterwalder, Surf. Sci. (in press).

- *Localization of surface states in disordered step lattices*
  F. Baumberger, M. Hengsberger, M. Muntwiler, M. Shi, J. Krempasky, L. Patthey, J. Osterwalder, T. Greber, Phys.Rev.Lett.(in press).

Diploma and PhD theses

- *Extending the ESCALAB measurement capabilities and studying fundamentals for the spintronic candidate Mn on Ge(001)*
  Thomas Gresch, Diploma Thesis, Physik-Institut, Universität Zürich, 2003.

- *Nanostructured magnetic interfaces: case studies and new experiment control software*
  M. Muntwiler, Ph. D. Thesis, Physik-Institut, Universität Zürich, 2004.

Contributed conference presentations

- *Possible step lattice stabilisation by surface states (Poster)*
  T. Greber, Symposium on Surface Science, La Plagne, France, 1.4.03.

- *Development of a low-energy electron gun for pump-probe experiments (Poster)*
  M. Hengsberger, Workshop on Ultrafast Science with X-Rays and Electrons, Montreux, 9./10.4.03.

- *Spin-resolved Fermi surface mapping*
  M. Hoesch, Suga-Group Seminar, Osaka University, Japan, 13.5.03.

- *Ultraviolet photoelectron diffraction*
  M. Hoesch, Suga-Group Seminar, Osaka University, Japan, 10.6.03.

- *Angle- and spin-resolved photoelectron spectroscopy of the Au(111) surface state band (Poster)*
  M. Muntwiler, ICESS-9 Conference, Uppsala, Sweden, 30.6.03.

- *Growth and properties of epitaxial Cr-doped TiO_2 anatase and rutile*
  J. Osterwalder, Spintronics Workshop, Department of Physics, University of Washington, Seattle, WA, USA, 9.7.03.

- *Spin- and angle-resolved photoelectron spectroscopy of the surface state on Au(111)*
  M. Hoesch, 22nd European Conference on Surface Science, Prag, Czech Republic, 9.9.03.

- *One-dimensional chains of C_{60} molecules on Cu(221)*
  A. Tamai, 22nd European Conference on Surface Science, Prag, Czech Republic, 9.9.03

- *Boron nitride nanomesh (Poster)*
  M. Corso, 20th Annual Meeting of the SAOG (Schweizerische Arbeitsgemeinschaft für Oberflächen und Grenzflächen), Fribourg, 23.1.04.

- *C_{60} on h-BN/Ni(111): a molecular switch for electrons?*
  T. Greber, Symposium on Surface Science, St. Anton, Austria, 3.3.04.

- *Ultrafast space-charge dynamics with low-energy electron pulses*
  A. Dolocan, SPS Jahrestagung, Neuchatel, 3.3.04.

- *Boron nitride nanomesh*
  M. Corso, SPS Jahrestagung, Neuchatel, 4.3.04.

- *Doping dependent orientation of C_{60} molecules on Ag(111)*
  T. Greber, March Meeting of the American Physical Society, Montreal, Canada, 23.3.04.

- *One-dimensional C_{60} chains: molecular arrangement and electronic properties*
  A. Tamai, March Meeting of the American Physical Society, Montreal, Canada, 23.3.04.

- *Metal-insulator transition of monolayer C_{60} on a h-BN/Ni tunnelling junction*
  M. Muntwiler, March Meeting of the American Physical Society, Montreal, Canada, 23.3.04.

- *Nanomesh: self organization of boron nitride on Rh(111)*
  T. Greber, March Meeting of the American Physical Society, Montreal, Canada, 25.3.04.

Invited lectures

- M. Hoesch: *Spin-resolved Fermi surface mapping*
  NAIST Seminar, Nara Institute of Science and Technology, Nara, Japan, 4.6.03.

- J. Osterwalder: *One monolayer of hexagonal boron nitride on Ni(111): a model case for a magnetic metal-insulator-interface*
  Seminar, Environmental Molecular Sciences Laboratory, Pacific Northwest National Laboratory, Richland, WA, USA, 9.6.03.

- T. Greber: *h-BN/Ni(111): an atomically sharp interface*
  DFG Forschergruppenseminar "Ferromagnet-Halbleiter-Nanostrukturen", Regensburg, 27.6.03.

- M. Hoesch: *Spin-resolved Fermi surface mapping*
  HiSOR Seminar, Hiroshima Synchrotron Radiation Center, Hiroshima University, Japan, 8.7.03.

- M. Hoesch: *Spin-resolved Fermi surface mapping*
  Hasegawa-Group Seminar, University of Tokyo, Japan, 11.7.03.

- T. Greber: *How steps influence the electronic structure and vice versa*
  Seminar, Fritz-Haber-Institut, Berlin, 15.7.03.

- J. Osterwalder: *Spin-resolved Fermi surface mapping*
  Seminar, Advanced Light Source, Lawrence Berkeley Laboratory, Berkeley, CA, USA, 2.10.03.

- J. Osterwalder: *C_{60} fullerene monolayers: molecular arrangement, orientation and electronic structure*
  Shen-Group Seminar, Department of Applied Physics, Stanford University, Stanford, CA, USA, 2.10.03.

- J. Osterwalder: *Growth morphologies and defect structure in h-BN films on Ni(111): a combined STM and XPD study*
  4th International Conference on Atomic Level Characterization of New Materials and Devices, Kauai, HI, USA, 9.10.03.

- T. Greber: *Exploring the structural changes of not so small molecules on surfaces: from photoelectron diffraction towards near-node photoelectron holography*
  Swiss Light Source Users' Meeting, PSI Villigen, 30.10.03.

- M. Hoesch: *Spin-resolved Fermi surface mapping: the spin-orbit split surface state on Au(111)*
  Swiss Light Source Users' Meeting, PSI Villigen, 31.10.03.

- T. Greber: *Molecular valves for electrons: C_{60}/h-BN/Ni(111)*
  Seminar, Physik, Freie Universität Berlin, 3.11.03.

- J. Osterwalder: *Some tricks in photoelectron diffraction experiments for structural investigations at surfaces*
  50th American Vacuum Society Meeting, Baltimore, MD, USA, 4.11.03.

- M. Hoesch: *Spin-resolved Fermi surface mapping: the Fermi surface of bulk and ultrathin nickel*
  SRSES2003 Conference, Hiroshima, Japan, 19.11.03.

- T. Greber: *Steps: pivots on surfaces*
  High T_c workshop on novel materials and superconductivity, Planneralm, Austria, 27.2.04.

- J. Osterwalder: *About spin structures on Au surfaces, molecular chains and nanomeshes*
  Seminar, Fritz-Haber-Institut, Berlin, 1.3.04.

- J. Osterwalder: *Applications of synchrotron radiation techniques to surface science problems*
  4 hours of Lectures, HERCULES School 2004, Trieste, Italy, 18./19.3.04.

14.5 Research group of Prof. U. Straumann, (for H1 publications see Sec.14.6)

Articles

- *The CIP2K First-Level Trigger System at the H1 Experiment at HERA*
  M. Urban, J. Becker, S. Schmitt, U. Straumann, IEEE Trans.Nucl.Sci. 50:903-908, 2003.

- *A vertex detector for the future linear collider*
  Stefania Xella Hansen, Nucl.Instr.Meth.A 511 (2003) 229-234.

- *Flavour tagging at the future linear collider*
  Stefania Xella Hansen, Nucl.Instr.Meth.A 501 (2003) 106-110.

- *An orthotropic Magnesium-Carbon Composite as Lighweight Heat-guide Material with High Specific Stiffness and Radiation Transparency*
  S. Vaucher, O. Beffort, J. Kübler and F. Lehner, Adv. Eng. Mater. 5 (2003) 669-672.

- *Search for 3- and 4-Body Decays of the Scalar Top Quark in $p\overline{p}$ Collisions at $\sqrt{s}$=1.8 TeV*
  V. M. Abazov *et al.* [D0 Collaboration], Phys.Lett.B **B 581** (2004) 147-155.

- *Observation of diffractively produced W and Z Bosons in $p\overline{p}$ collisions at $\sqrt{s}$=1800 GeV*
  V. M. Abazov *et al.* [D0 Collaboration], Phys.Lett.B **574** (2003) 169-179.

- *Search for Large Extra Dimensions in the Monojet + Missing E(T) Channel at DØ*
  V. M. Abazov *et al.* [D0 Collaboration], Phys.Rev.Lett.**90** (2003) 251802.

- *Multiple Jet Production at low transverse energies in $p\overline{p}$ collisions at $\sqrt{s}$=1.8 TeV*
  V. M. Abazov *et al.* [D0 Collaboration], Phys.Rev.D **67** (2003) 052001.

- *$t\bar{t}$ Production cross section in $p\overline{p}$ collisions at $\sqrt{s}$=1.8 TeV*
  V. M. Abazov *et al.* [D0 Collaboration], Phys.Rev.D **67** (2003) 012004.

- *The LHCb Silicon Inner Tracker*
  F. Lehner, Nucl.Instr.Meth.A 501 (2003) 126-130.

- *The LHCb Silicon Inner Tracker*
  F. Lehner, Nucl.Instr.Meth.A 511 (2003) 43-47.

Diploma and PhD thesis

- *Simulation und Messung von Silizium-Streifen-Detektoren*
  Stefan Heule, Diplomarbeit, Physik-Insitut, Universität Zürich, 2003.

- *The new CIP2k z-Vertex Trigger for the H1 Experiment at HERA*
  Max Christoph Urban, PhD Thesis, Physik-Insitut, Universität Zürich, 2004.

- *A Measurement of the QED-Compton Cross-Section in Electron-Proton Scattering with the H1 Experiment at HERA*
  Nicolas Keller, PhD Thesis, Physik-Insitut, Universität Zürich, 2004.

- *Measurement of the Charged Current Cross Section in Positron-Proton Collisions at HERA*
  Nicole Werner, PhD Thesis, Physik-Insitut, Universität Zürich, 2004.

Conference contributions

- Nicole Werner: *Measurements of proton structure functions, alpha(s) and parton distribution functions at HERA*
  Talk on behalf of the H1 and ZEUS collaborations, 38th Rencontres de Moriond on QCD and High-Energy Hadronic Interactions, Les Arcs, Savoie, France, 22-29.03.2003. hep-ex/0305109.

- J. Becker *et al.*: *The first levvel trigger CIP2k for the H1 Experiment at HERA*
  8th Topical Seminar on Innovative Particle and Radiation Detectors, Siena, Italy, 21-24 Oct 2002, Nucl. Phys. Proc. Suppl. 125:277-281, 2003.

- Y. Ermoline: *LHCb Silicon Tracker infrastructure*
  Poster at the 9th Pisa Meeting on Advanced Detectors, La Biodola, Isola d'Elba, Italy, 25-31.05.2003.

- Peter Fierlinger: *Geant4 Simulations for Ultracold Neutron Experiments*
  Int. Conf. on Ultracold and Cold Neutrons Physics & Sources, St.Petersburg, Russia, June 2003.

- U. Straumann: *Silicon Strip Detectors with long strips and fast signal shaping for LHCb*
  talk presented at Imaging 2003, June 27, 2003, Stockholm, Sweden.

- F. Lehner, C. Lois, P. Vazquez:
  Caracterizacion de 15 detectores de micropistas de Silicio (5 GLAST2000, 5 OB2 CMS y 5 Hamamatsu LHCb Multi-Geometry) para la estacion TT del experimento LHCb
  XXIX Reunion Bienal de la Real Sociedad Espanola de Fisica, Madrid (Spain), July 7-11, 2003.

- M. Needham: *The LHCb Silicon Tracker*
  Int. Conf. on Large Scale Applications and Radiation Hardness of Semiconductor Detectors, September 30 - October 1, 2003, Firence, Italy.

- F. Lehner: *Investigation of Radiation Damage on Silicon Detectors for the D0 Run IIb Upgrade*
  Int. Conf. on Large Scale Applications and Radiation Hardness of Semiconductor Detectors, September 30 - October 1, 2003, Firence, Italy.

- A. Vollhardt: *The LHCb silicon tracker*
  Nuclear science symposium and medical imaging conference (IEEE), Portland, USA, October 19-25, 2003.

- M. Agari and O. Steinkamp: *Design of the LHCb Silicon Tracker*
  poster at the 10th Vienna Conference on Instrumentation (VCI 2004), February 16 - 21, 2004, Vienna, Austria.

Invited lectures and seminar talks

- Phillip Sievers: *The LHCb Silicon Inner Tracker*
  High Energy Physics Seminar, UCLA, Los Angeles, 29.01.2003.
- F. Lehner: *The Status of LHCb and its Inner Tracker detector*
  Experimental Particle Physics Seminar at Kansas State University, March 10, 2003, Manhatten, Kansas, USA.
- Stefan Schmitt: *H1 status and prospects*
  DESY-PRC open session, 30. Oktober 2003, http://www.desy.de/∼sschmitt/prc_oct_2003.pdf.gz.
- Stefan Schmitt: *Lepton beam polarisation for the HERA experiments ZEUS and H1*
  Seminar at MPI München, 9. Dezember 2003, http://www.desy.de/∼sschmitt/pol26_mpi.pdf.

Collaboration notes and technical reports

- *LHCb Reoptimized Detector Design and Performance*
  Technical Design Report, LHCb Collaboration,
  LHCb TDR 9, CERN/LHCC 2003-030, 9. September 2003.
- *Design of the LHCb Silicon Tracker*
  M. Agari *et al.*, LHCb Note 2004-010.
- *Simulation of Signal Generation in Silicon Micro-strip Detectors for the LHCb Silicon Tracker of the LHCb Experiment*
  St. Heule and F. Lehner, LHCb Note 2003-159.
- *Studies of the Beetle 1.2 Pipeline Homogeneity*
  M. Agari *et al.*, LHCb Note 2003-155.
- *The LHCb Silicon Tracker*
  A. Vollhardt, LHCb Note 2003-143.
- *The LHCb Silicon Tracker*
  M. Needham, LHCb Note 2003-142.
- *Layout and Expected Performance of the LHCb TT Station*
  J. Gassner, M. Needham, O. Steinkamp, LHCb Note 2003-140.
- *Prototype for an optical 12 input receiver card for the LHCb TELL1 board*
  G. Haefeli, U. Uwer, A. Vollhardt, D. Wiedner, LHCb Note 2003-137.
- *Characterization and Sample Testing of the LHC4913 Positive Voltage Regulator for the LHCb Silicon Tracker*
  A. Gafner and A. Vollhardt, LHCb Note 2003-128.
- *Test-Beam Measurements on Prototype Ladders for the LHCb TT Station*
  M. Agari *et al.*, LHCb Note 2003-082.
- *Capacitance Measurements on Silicon Micro-Strip Detectors for the TT Station of the LHCb Experiment*
  J. Gassner *et al.*, LHCb Note 2003-081.

- *Measurements of Prototype Ladders for the Silicon Tracker with Laser*
  R. Bernhard *et al.*, LHCb Note 2003-075.

- *Neutron Irradiation Results for the LHCb Silicon Tracker Data Readout System Components*
  A. Vollhardt, LHCb Note 2003-049.

- *A Prototype for the LHCb Silicon Tracker Data Readout System*
  A. Vollhardt, LHCb Note 2003-045.

- *Tracking Performance and Robustness Tests*
  M. Needham, LHCb Note 2003-020.

- *Silicon Tracker Simulation Performance*
  M. Needham, LHCb Note 2003-015.

14.6 H1 publications by the groups of Straumann and Truöl

Articles

- *Isolated Electrons and Muons in Events with Missing Transverse Momentum at HERA*
  H1-Collaboration, V. Andreev *et al.*,
  DESY 02 – 224, hep-ex/0301030, Phys.Lett.**B561** (2003), 241 - 257.

- *Measurement of Inclusive Jet Cross Sections in Photoproduction at HERA*
  H1-Collaboration, C. Adloff *et al.*,
  DESY 02 – 225, hep-ex/0302034, Eur.Phys.J.**C29** (2003), 497 - 513.

- *Measurement and QCD Analysis of Neutral and Charged Current Cross Sections at HERA*
  H1-Collaboration, C. Adloff *et al.*,
  DESY 03 – 038, hep-ex/0304003, Eur.Phys.J.**C30** (2003), 1 - 32.

- *Search for New Physics in $e^{\pm}q$ Contact Interactions*
  H1-Collaboration, C. Adloff *et al.*,
  DESY 03 – 052, hep-ex/0305015, Phys.Lett.**B568** (2003), 35 - 47.

- *Diffractive Photoproduction of J/Ψ Mesons with Large Momentum Transfer at HERA*
  H1-Collaboration, A. Aktas *et al.*,
  DESY 03 – 061, hep-ex/0306013, Phys.Lett.**B568** (2003), 205 - 218.

- *Multi-electron Production at High Transverse Momentum in ep Collisions at HERA*
  H1-Collaboration, A. Aktas *et al.*,
  DESY 03 – 082, hep-ex/0307015, Eur.Phys.J.**C31** (2003), 17 - 29.

- *Search for Single Top Quark Production in $e^{\pm}p$ Collisions at HERA*
  H1-Collaboration, A. Aktas *et al.*,
  DESY 03 – 132, hep-ex/0310032, Eur.Phys.J.**C33** (2004), 9 - 22.

- *Muon Pair Production in ep Collisions at HERA*
  H1-Collaboration, A. Aktas *et al.*,
  DESY 03 – 159, hep-ex/0311015, Phys.Lett.**B583** (2004), 28 - 40.

- *Inclusive Dijet Production at Low Bjorken-x in Deep Inelastic Scattering*
  H1-Collaboration, A. Aktas *et al.*,
  DESY 03 – 160, hep-ex/0310019, Eur.Phys.J.**C33** (2004), 477 - 493.

- *Observation of a Narrow Anti-Charmed Baryon State*
  H1-Collaboration, A. Aktas *et al.*,
  DESY 04 – 038, hep-ex/0403017, Phys.Lett.**B588** (2004), 17 - 28.

Articles in print

- *Measurement of Dijet Production at Low Q^2 at HERA*
  H1-Collaboration, A. Aktas *et al.*,
  DESY 03 – 206, hep-ex/0401010, Eur.Phys.J.**C** (2004), in print.

- *Search for Squark Production in R-Parity Violating Supersymmetry at HERA*
  H1-Collaboration, A. Aktas *et al.*.
  DESY 04 – 025, hep-ex/0403027, Eur.Phys.J.**C** (2004), in print.

- *Measurement of Anti-Deuteron Photoproduction and a Search for Heavy Stable Charged Particles in at HERA*
  H1-Collaboration, A. Aktas *et al.*,
  DESY 04 – 032, hep-ex/0403056, Eur.Phys.J.**C** (2004), in print.

- *Forward π^0 Production and Associated Transverse Energy Flow in Deep-Inelastic Scattering at HERA*
  H1-Collaboration, A. Aktas *et al.*,
  DESY 04 – 051, hep-ex/0404009, Eur.Phys.J.**C** (2004), in print.

H1-collaboration (1.5.2004)

A. Aktas, V. Andreev, T. Anthonis, A. Asmone, A. Babaev, S. Backovic, J. Bähr, A. Baghdasaryan, P. Baranov, E. Barrelet, W. Bartel, S. Baudrand, S. Baumgartner, J. Becker, M. Beckingham, O. Behnke, O. Behrendt, A. Belousov, Ch. Berger, N. Berger, T. Berndt, J.C. Bizot, J. Böhme, M.-O. Boenig, V. Boudry, J. Bracinik, G. Brandt, V. Brisson, H.-B. Bröker, D.P. Brown, D. Bruncko, F.W. Büsser, A. Bunyatyan, G. Buschhorn, L. Bystritskaya, A.J. Campbell, S. Caron, F. Cassol-Brunner, K. Cerny, V. Chekelian, J.G. Contreras, Y.R. Coppens, J.A. Coughlan, B.E. Cox, G. Cozzika, J. Cvach, J.B. Dainton, W.D. Dau, K. Daum, B. Delcourt, R. Demirchyan, A. De Roeck, K. Desch, E.A. De Wolf, C. Diaconu, J. Dingfelder, V. Dodonov, A. Dubak, C. Duprel, G. Eckerlin, V. Efremenko, S. Egli, R. Eichler, F. Eisele, M. Ellerbrock, E. Elsen, M. Erdmann, W. Erdmann, S. Essenov, P.J.W. Faulkner, L. Favart, A. Fedotov, R. Felst, J. Ferencei, L. Finke, M. Fleischer, P. Fleischmann, Y.H. Fleming, G. Flucke, G. Flügge, A. Fomenko, I. Foresti, J. Formánek, G. Franke, G. Frising, T. Frisson, E. Gabathuler, K. Gabathuler, E. Garutti, J. Garvey, J. Gayler, R. Gerhards, C. Gerlich, S. Ghazaryan, S. Ginzburgskaya, I. Glushkov, L. Goerlich, M. Goettlich, N. Gogitidze, S. Gorbounov, C. Goyon, C. Grab, H. Grässler, T. Greenshaw, M. Gregori, G. Grindhammer, C. Gwilliam, D. Haidt, L. Hajduk, J. Haller, M. Hansson, G. Heinzelmann, R.C.W. Henderson, H. Henschel, O. Henshaw, G. Herrera, I. Herynek, R.-D. Heuer, M. Hildebrandt, K.H. Hiller, P. Höting, D. Hoffmann, R. Horisberger, A. Hovhannisyan, M. Ibbotson, M. Ismail,

M. Jacquet, L. Janauschek, X. Janssen, V. Jemanov, L. Jönsson, D.P. Johnson, H. Jung, D. Kant, M. Kapichine, M. Karlsson, J. Katzy, N. Keller, I.R. Kenyon, C. Kiesling, M. Klein, C. Kleinwort, T. Klimkovich, T. Kluge, G. Knies, A. Knutsson, V. Korbel, P. Kostka, R. Koutouev, A. Kropivnitskaya, J. Kroseberg, K. Krüger, J. Kückens, M.P.J. Landon, W. Lange, T. Laštovička, P. Laycock, A. Lebedev, B. Leißner, R. Lemrani, V. Lendermann, S. Levonian, L. Lindfeld, K. Lipka, B. List, E. Lobodzinska, N. Loktionova, R. Lopez-Fernandez,V. Lubimov, H. Lueders, D. Lüke, T. Lux, L. Lytkin, A. Makankine, N. Malden, E. Malinovski, S. Mangano, P. Marage, J. Marks, R. Marshall, M. Martisikova, H.-U. Martyn, S.J. Maxfield, D. Meer, A. Mehta, K. Meier, A.B. Meyer, H. Meyer, J. Meyer, S. Mikocki, I. Milcewicz-Mika, D. Milstead, A. Mohamed, F. Moreau, A. Morozov, J.V. Morris, M.U. Mozer, K. Müller, P. Mur'in, V. Nagovizin, K. Nankov, B. Naroska, J. Naumann, Th. Naumann, P.R. Newman, C. Niebuhr, A. Nikiforov, D. Nikitin, G. Nowak, M. Nozicka, R. Oganezov, B. Olivier, J.E. Olsson, D. Ozerov, C. Pascaud, G.D. Patel, M. Peez, E. Perez, D. Perez-Astudillo, A. Perieanu, A. Petrukhin, D. Pitzl, R. Plačakytė, R. Pöschl, B. Portheault, B. Povh, N. Raicevic, P. Reimer, B. Reisert, A. Rimmer, C. Risler, E. Rizvi, P. Robmann, B. Roland, R. Roosen, A. Rostovtsev, Z. Rurikova, S. Rusakov, F. Salvaire, D.P.C. Sankey, E. Sauvan, S. Schätzel, J. Scheins, F.-P. Schilling, S. Schmidt, S. Schmitt, C. Schmitz, M. Schneider, L. Schoeffel, A. Schöning, V. Schröder, H.-C. Schultz-Coulon, C. Schwanenberger, K. Sedlák, F. Sefkow, I. Sheviakov, L.N. Shtarkov, Y. Sirois, T. Sloan, P. Smirnov, Y. Soloviev, D. South, V. Spaskov, A. Specka, B. Stella, J. Stiewe, I. Strauch, U. Straumann, V. Tchoulakov, G. Thompson, P.D. Thompson, F. Tomasz, D. Traynor, P. Truöl, G. Tsipolitis,I. Tsurin, J. Turnau, E. Tzamariudaki,A. Uraev, M. Urban, A. Usik, D. Utkin, S. Valkár, A. Valkárová, C. Vallée, P. Van Mechelen, N. VanRemortel, A. VargasTrevino, Y. Vazdik, C. Veelken, A. Vest, S. Vinokurova, V. Volchinski, B. Vujicic, K. Wacker, J. Wagner, G. Weber, R. Weber, D. Wegener, C. Werner, N. Werner, M. Wessels, B. Wessling, C. Wigmore, G.-G. Winter, Ch. Wissing, E.-E. Woehrling, R. Wolf, E. Wünsch, S. Xella, W. Yan, V. Yeganov, J. Žáček, J. Zálešák, Z. Zhang, A. Zhelezov, A. Zhokin, J. Zimmermann, H. Zohrabyan, and F. Zomer

14.7 Research group of Prof. P. Truöl (for H1 publications see Sec.14.6)

Articles

- *J/Ψ Production via χ_c Decays in 920 GeV pA Interactions*
  HERA-B Collaboration, I. Abt *et al.*,
  DESY 02 – 187, hep-ex/0211033, Phys.Lett.**B561** (2003), 61 - 72.

- *Inclusive V^0 Production Cross Section from 920 GeV Fixed Target Proton-Nucleus Collisions*
  HERA-B Collaboration, I. Abt *et al.*,
  DESY 02 – 213, hep-ex/0212040, Eur.Phys.J.**C29** (2003), 181 - 190.

- *High Statistics Measurement of K_{e4} Decay Properties*
  E865-Collaboration, S. Pislak *et al.*,
  hep-ex/0301040, Phys.Rev.**D67** (2003), 072004-1 - 072004-15.

- *New, High Statistics Measurement of the $K^+ \to \pi^0 e^+ \nu_e$ (K_{e3}) Branching Ratio*
  E865-Collaboration, A. Sher *et al.*,
  hep-ex/0305042, Phys.Rev.Lett.**91** (2003), 261802-1 - 261802-4.

- *Summary WG2 part 2: rare muon decays*
  A. van der Schaaf, Proc. NuFACT'01, Tsukuba, Japan (2001), Nucl.Instr.Meth.A503 (2003) 240.

- *μe Conversion experiments: status and prospects*
  A. van der Schaaf, Proc. NuFACT'01, Tsukuba, Japan (2001), Nucl.Instr.Meth.A503 (2003) 281.
- *SINDRUM II*
  A. van der Schaaf, Proc. NuFACT'02, London, U.K. (2002), Journal of Physics G29 (2003) 1503.
- *Muon physics at a neutrino factory*
  A. van der Schaaf, Journal of Physics G29 (2003) 2755.

Report in print

- *ECFA studies of a European neutrino factory complex*
  A. Blondel, J. Ellis, F. Dydak, J.J. Gomez-Cadenas, G. Giudice, A. van der Schaaf, M. Mangano, G. Buchalla, P. Janot, H. Haseroth, H. Ravn, H. Schonauer, R. Garoby, A. Lombardi,
  CERN Yellow Report, 2004.

Diploma and PhD Theses

- *An improved limit on the decay $K^+ \to \pi^+\mu^+e^-$*
  Aleksey Sher, PhD Thesis, Universität Zürich, 2003.
- *Entwicklung von Szintillationszählerprototypen für das KOPIO Experiment*
  Simon O. Scheu, Diploma Thesis, Universität Zürich, December 2003.

E865-collaboration

R. Appel, G.S. Atoyan, B. Bassaleck, D.R. Bergman, N. Cheung, S. Dhawan, H. Do, J. Egger, S. Eilerts, W.D. Herold, V.V. Issakov, H. Kaspar, D. Kraus, D. Lazarus, P. Lichard, J. Lowe, J. Lozano, H. Ma, W. Majid, S. Pislak, A.A. Poblaguev, A. Sher, Aleksey Sher, P. Rehak, J.A. Thompson, P. Truöl, and M.E. Zeller